Technical Annals

Vol 1, No 5 (2024)

Technical Annals

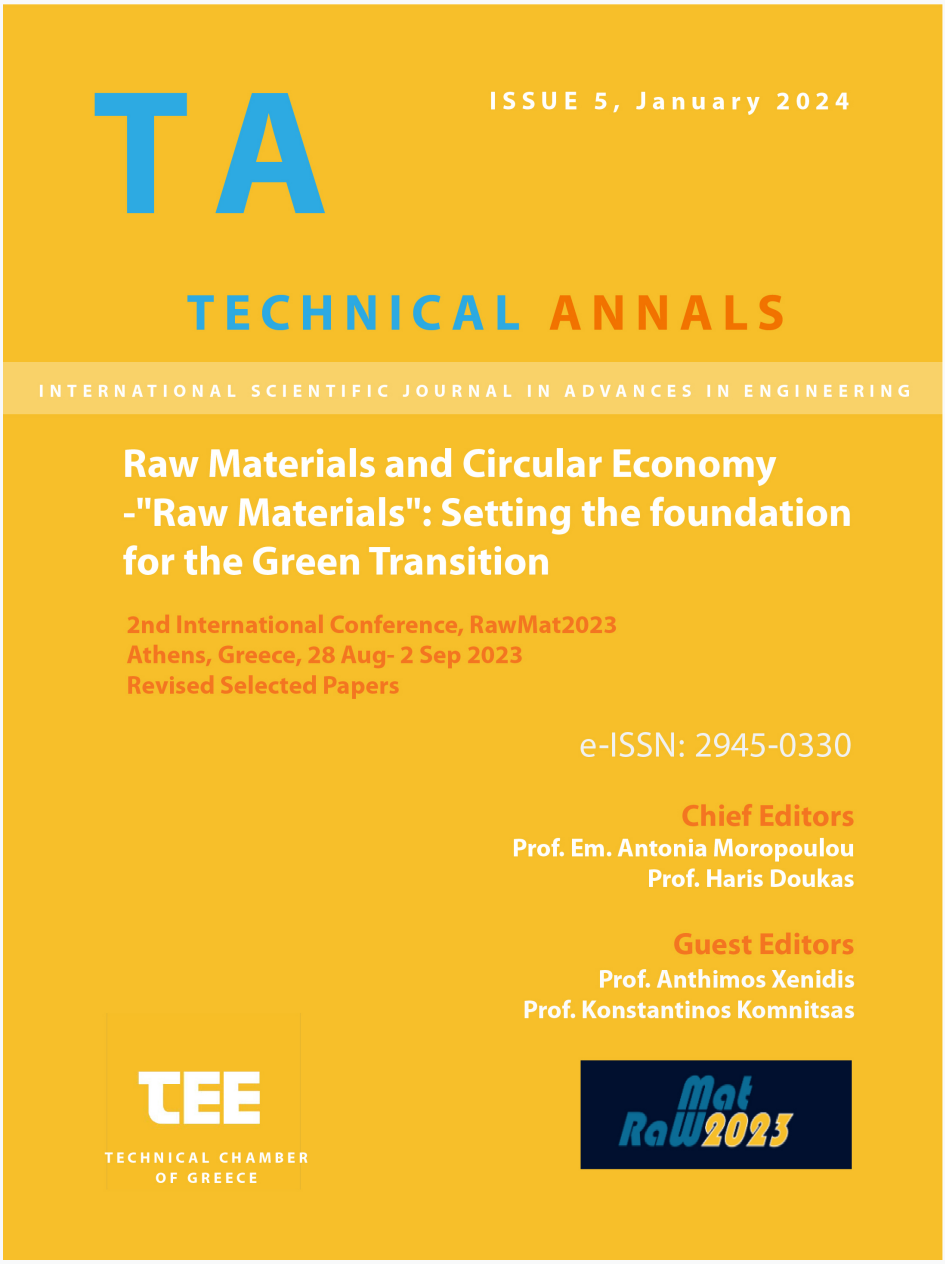

TA

ISSUE 5, January 2024

TECHNICAL ANNALS

INTERNATIONAL SCIENTIFIC JOURNAL IN ADVANCES IN ENGINEERING

Raw Materials and Circular Economy -"Raw Materials": Setting the foundation for the Green Transition

2nd International Conference, RawMat2023
Athens, Greece, 28 Aug- 2 Sep 2023
Revised Selected Papers

e-ISSN: 2945-0330

Chief Editors
Prof. Em. Antonia Moropoulou
Prof. Haris Doukas

Guest Editors
Prof. Anthimos Xenidis
Prof. Konstantinos Komnitsas

TEE
TECHNICAL CHAMBER OF GREECE

MatRaW2023

Technical Annals

Journal of the Technical Chamber of Greece

Disclaimer

Technical Chamber of Greece (TCG) makes every effort to ensure the accuracy of all the information (the Content) contained in our publications. However, TCG makes no representations or warranties whatsoever as to the accuracy, completeness, or suitability for any purpose of the Content. Any opinions and views expressed in this publication are the opinions and views of the authors and are not the views of TCG. The accuracy of the Content should not be relied upon and should be independently verified with primary sources of information. TCG shall not be liable for any losses, actions, claims, proceedings, demands, costs, expenses, damages, and other liabilities whatsoever or howsoever caused arising directly or indirectly in connection with, in relation to or arising out of the use of the Content. Terms and Conditions of access and use can be found at https://ejournals.epublishing.ekt.gr/index.php/ta/

Submitting to Technical Annals

For more information about the journal and guidance on how to submit, please see
https://ejournals.epublishing.ekt.gr/index.php/ta/

.

Contents

Technical Annals

Editorial Board Members

Panas Antonios

Dr. Civil Engineer

Pla-Karidi Danae

Dr. Electrical and Computer Engineer, Post Doctoral Researcher

Athina Research Center

Scientific Council Members

Triantafyllou Savvas

Dr. Civil Engineer, Assistant Professor

National Technical University of Athens - School of Civil Engineering

Klabatsea Irene

Dr. Architect Engineer, Assistant Professor

National Technical University of Athens - School of Architecture

Ioannidis Charalambos

Dr. Rural and Surveying Engineer, Professor

National Technical University of Athens - School of Rural, Surveying and Geoinformatics Engineering

Manolakos Dimitrios

Dr. Mechanical Engineer, Professor

National Technical University of Athens - School of Mechanical Engineering

Mansour Gabriel

Dr. Mechanical Engineer, Professor

Aristotle University of Thessaloniki - Department of Mechanical Engineering

Christodoulou Christos

Dr. Electrical and Computer Engineer, Adjunct Professor

University of Thessaly - Department of Electrical and Computer Engineering

Xenidis Anthimos

Dr. Mining and Metallurgical Engineer, Professor

National Technical University of Athens - School of Mining and Metallurgical Engineering

Loizidou Maria

Dr. Chemical Engineer, Emeritus Professor

National Technical University of Athens - School of Chemical Engineering

Ventikos Nikolaos

Dr. Naval Engineer, Assistant Professor

National Technical University of Athens - School of Naval Architecture and Marine Engineering

Gerogiannis Vasileios

Dr. Computer Engineer and Informatics, Professor

University of Thessaly - Department of Digital Systems

Tselios Vassilis

Dr. Regional Planning and Development Engineer, Associate Professor

Panteion University of Social and Political Sciences - Department of Economic and Regional Development

Saratsis Georgios

Dr. Mineral Resources Engineer, Laboratory Teaching Staff

Technical University of Crete - School of Mineral Resources Engineering

Akratos Christos

Dr. Envirovmental Engineer, Assistant Professor

Democritus University of Thrace - Department of Civil Engineering

About

With particular joy, respect and commitment to the history of TEE (TCG), to the future of the scientific role of the Chamber and to the work of Greek Engineers as a whole, the Technical Chamber of Greece is proceeding with the publication of an international scientific journal. After several years without regular scientific publications, due to the special economic situation of the country, but having as a source of our history the TECHNICAL ANNALS, published by the TCG for decades, we undertake this role again to give another scientific podium to the Engineering community.

More specific, the Governing Committee of TCG, in accordance to Decisions No A14/Σ39/2021, A16/Σ7/2022 and A41/Σ16/2022, proceeded to publish of the Scientific Journal entitled «Technical Annals» by the Technical Chamber of Greece (TCG) concerned with Advances in Engineering, in English language. The content of the journal will be available electronically and via Open Access, through the e-Publishing service of the National Documentation Centre (EKT).

The Governing Committee of the TCG assigned the responsibility of the publication to the Editorial Board and the Scientific Board of the Journal.

We inform all Engineers IN Greece and in the World, the Academic and Research Community that we are proceeding with this publication in order to give the floor for communication, publicity and recognition, by the International Community, of the Research and Innovation that Engineers produce in practice, on construction sites,in urban space, in regional areas, in industry, in development, in environment, in energy, in the digital world, in universities, in research centers, in startups, in businesses, etc.

We aspire to attract your interest, find in you critical readers, feed your scientific work and publish the results of your research through the International Scientific Journal of TCG.

Looking forward to an important publication that we'd like to become everyone's business.

Topics

The scope of the journal will include all Fields of Engineering:

1. Civil Engineering
2. Architectural Engineering
3. Mechanical Engineering
4. Electrical & Computer Engineering
5. Rural & Surveying Engineering
6. Chemical Engineering
7. Mining & Metallurgical Engineering
8. Naval Architecture & Marine Engineering
9. Electronic Engineering
10. Engineering of Urban Planning & Regional Development
11. Environmental Engineering
12. Mineral Resources Engineering
13. Production & Management Engineering

Furthermore, it will be concerned with Interdisciplinary Thematic Areas, which are at the cutting edge of Research and Innovation, such as:

Agricultural Engineering and Food Processing, Artificial Intelligence, Aerodynamics, Bioengineering, Circular Economy, Climate Change, Cultural Heritage, Education and Learning Processes, Energy, Environment, Economy, Geoinformatics, Human Modelling, Industrial Symbiosis, Management and Quality Control, Material Science and Engineering, Naval Coastal and Maritime Design Engineering and

Planning, Spatial Planning, Sustainable Development, Systems' and Processes Engineering, Technology, Transportation, Processes, among others, and the thematic areas will be dynamically adjusted and determined taking into account both the progress of Science and Engineering, as well as future trends and the trending concerns and needs of Society.

Information for Volume Editors and Authors

Moreover, conferences, in which TCG is either co-organizing or participating in their Organizing and Scientific Committee, will be able to submit a request to publish their Proceedings (in either Greek or English language) always through the "e-Publishing" mechanism, as long as the request has been submitted to TCG and has the approval of TCG's Governing Bodies, either six months before the conference date *(in cases where the proceedings are to be published prior to the conference initiation)*, or three months before the conference date *(in cases where the proceedings are to be issued after the Conference)*.

The Governing Committee of the TCG assigned the responsibility of the publication to the Editorial Board and the Scientific Board of the Journal; the list of members of each board is herein attached.

Antonia Moropoulou · Haris Doukas · Anthimos Xenidis · Konstantinos Komnitsas

ISSUE

Raw Materials and Circular Economy - “Raw Materials”: Setting the foundation for the Green Transition

Editors

Antonia Moropoulou

Dr. Chemical Engineer, Emeritus Professor,

National Technical University of Athens - School of Chemical Engineering

Haris Doukas

Dr. Mechanical Engineer, Professor

National Technical University of Athens- School of Electrical and Computer Engineering

Anthimos Xenidis

Dr. Mining & Metallurgical Engineer, Professor

National Technical University of Athens - School of Mining and Metallurgical Engureering

Konstantinos Komnitsas

Dr. Mining & Metallurgical Engineer, Professor

Technical University of Crete - School of Mineral Resources Engineering

The Technical Chamber of Greece (TCG) decided to republish in English a Scientific International Open Access e-Journal. The "Technical Annals" - a journal which was counting decades of life following T.C.G. activities – will be edited by the T.C.G. through e-Publishing Platform at the EKT (National Documentation Centre) and will concern all the advancements in Engineering, referring to the disciplines:

- Civil Engineering
- Architect Engineering
- Mechanical Engineering
- Electrical & Computer Engineering
- Rural & Surveying Engineering
- Chemical Engineering
- Mining & Metallurgical Engineering
- Naval Architecture & Marine Engineering
- Electronic Engineering
- Engineering of Urban Planning & Regional Development
- Environmental Engineering
- Mineral Resources Engineering
- Production & Management Engineering

Referring also to interdisciplinary Thematic Areas at the forefront of Research and Innovation such as: Agricultural Engineering and Food Processing, Artificial Intelligence, Aerodynamics, Bioengineering, Circular Economy, Climate Change, Cultural Heritage, Education and Learning Processes, Energy, Environment, Economy, Geoinformatics, Human Modelling, Industrial Symbiosis, Management and Quality Control, Material Science and Engineering, Naval Coastal and Maritime Design Engineering and Planning, Spatial Planning, Sustainable Development, Systems' and Processes Engineering, Technology, Transportation, Processes, et al as dynamically will be defined by the progress of science and engineering, the future trends and the social needs.

Through the e-journal, TCG is aiming to publish at least three volumes per year, to connect Greek Engineers with the International Community of Engineering Science and Innovation, for the benefit of the public interest and the promotion of science through research, innovation, and development, in compliance with its constitutional targets.

Technical Annals is a peer-reviewed journal.

Preface

Raw materials are the silent enablers of modern civilization. They form the indispensable foundation for industrial production, technological innovation, economic growth, and the sustainable development of nations. From construction and transportation to energy systems and consumer electronics, raw materials underpin nearly every sector of the global economy.

In the 21st century, as the world advances deeper into the **digital age** and simultaneously pursues ambitious **climate and sustainability goals**, the importance of raw materials, particularly **critical and strategic raw materials (CRMs and SRMs),** has come into sharper focus. CRMs such as lithium, cobalt, nickel, rare earth elements, and graphite are essential for manufacturing batteries, semiconductors, wind turbines, electric vehicles, photovoltaic panels, and countless other technologies that are central to the **digital economy** and the **green transition**. Without a stable and sustainable supply of these materials, progress toward a low-carbon, technologically advanced, and resilient society is at risk.

The European Union's **Critical Raw Materials Act (CRMA)**, adopted in 2023, reflects the growing urgency to secure a sustainable and resilient raw materials supply. The CRMA identifies a list of CRMs and SRMs and sets ambitious targets for domestic extraction, processing, and recycling capacities. It emphasizes strategic autonomy, diversification of supply chains, promotion of innovation, and the development of international partnerships—factors essential for ensuring long-term access to these vital resources.

In this context, the **RawMat2023 – 2nd International Conference on Raw Materials and Circular Economy**, held in Athens, Greece, from August 28th to September 2nd, 2023, provided a timely and comprehensive forum for scientific and technical exchange. RawMat2023 brought together a diverse global community of researchers, industry professionals, technology developers, and policy makers to address the multifaceted challenges surrounding raw materials: resource scarcity, geopolitical risks, environmental impacts, and the urgent need for circular economy solutions.

This special issue of the Technical Annals presents a curated selection of peer-reviewed papers from RawMat2023, showcasing cutting-edge research and innovation across the entire raw materials value chain. The contributions cover a broad spectrum of topics of RawMat2023, including:

– **Sustainable mineral exploration and responsible mining**,
– **Innovative processing, beneficiation, and refining technologies**,
– **Recycling, urban mining, and secondary raw materials**,
– **Material substitution and product eco-design**,
– **Digitalization, AI, and data analytics in raw materials management**,
– **Lifecycle analysis, ESG considerations, and circular economy models**,
– **Strategic policies and global governance frameworks in line with CRMA objectives**.

These studies highlight the pivotal role of raw materials not only as industrial inputs, but as strategic assets essential for **economic growth**, **technological sovereignty**, **climate action**, and **societal resilience**. Countries and regions that invest in raw materials innovation, supply chain security, and sustainable practices will be better positioned to thrive in a resource-constrained and climate-challenged world.

We wish to thank the authors for their high-quality contributions, the reviewers for their valuable insights, and the RawMat2023 organizing committee for delivering a successful and impactful conference. This edition would not have been possible without the commitment of the TMM-CH editors of this volume (Antonia Moropoulou, Haris Doukas, Anthimos Xenidis, Komnitsas Konstantinos); as well as the valuable assistance of the editing team at Technical Annals managing by Mrs Lilly Athini (Fotini Kyritsi, Eleni Bairaktari, Evridiki

Karathanasi, Panagiotis Vrelos, Maria Sinigalia, Manolis Erotokritos, Isabella Tsavari, Dimitris Psarris, George Trachanas), to whom we are most grateful.

It is our hope that this special issue will serve as a meaningful reference for researchers, professionals, and decision-makers—and as a catalyst for continued collaboration in the field of raw materials science, technology, and policy.

Prof. Moropoulou, Chief editor, Prof. Anthimos Xenidis, Prof. Komnitsas Konstantinos, Editor´s

January 2024

Special Issue Contents

Circular Economy

Energy

Material Science and Engineering

Sustainable Development

Technical Annals
Issue 5
January 2025

Circular Economy

Hydrometallurgical recovery of EoL LFP batteries using oxalic acid as leaching agent

Rafaella-Aikaterini Megaloudi, Nikolaos Konsolas, Paschalis Oustadakis, Anthimos Xenidis

School of Mining and Metallurgical Engineering, National Technical University of Athens 9, Iroon Polytechniou st., 15780 Athens, Greece
axen@metal.ntua.gr

Abstract. The extraction of lithium (Li), iron (Fe), aluminum (Al), and copper (Cu) by oxalic acid solution from lithium iron phosphate (LFP) electric vehicle batteries was systematically investigated. Following battery disassembly, a comprehensive pretreatment scheme was employed, comprising shredding, crushing/grinding, sieving, and washing to reduce particle size and recover valuable battery materials in a stream collectively known as black mass. The black mass primarily contains the valuable components of the anode (graphite) and cathode ($LiFePO_4$), as well as impurities such as aluminum and copper foils used as current collectors. Leaching experiments were conducted by varying oxalic acid concentration, temperature, and leaching time. Lithium extraction reached 100% at an oxalic acid concentration of 0.7 M, a leaching temperature of 70 °C, a liquid-to-solid ratio of 10 l/kg, and a leaching time of 30 minutes. Under these conditions, iron from $LiFePO_4$ is initially dissolved but subsequently precipitated as iron oxalate and iron phosphate oxide, thereby limiting its overall extraction to very low levels (<5%). Nearly 100% of aluminum is dissolved, whereas copper dissolution remains relatively low (<2%). At lower oxalic acid concentrations, the extraction efficiencies of lithium and aluminum decrease, while remaining largely unaffected by temperature variations. Overall, the oxalic acid-based process demonstrates high efficiency for lithium extraction, effective separation from the solid matrix, and strong potential for subsequent lithium recovery from the leachate.

Keywords: LFP batteries, Li-ion batteries, leaching, oxalic acid

1 Introduction

Most of today's electric vehicles use lithium-ion batteries. To reduce costs, lithium iron phosphate ($LiFePO_4$) batteries are being considered as a more economical alternative. These batteries use cheaper electrode materials compared to other batteries in the same category and they are more reliable than the widely used NMC batteries (lithium, nickel, manganese, cobalt) [1].

The increasing demand for lithium batteries and their widespread use makes their

recycling imperative. The recycling of Li-ion batteries can be summarized in three different approaches: direct recycling, pyrometallurgy and hydrometallurgy [2]. Direct recycling presents limitations, especially regarding the continuous changes in the composition of the batteries [3]. Pyrometallurgy lacks due to the high energy consumption and strict environmental regulations that need to be followed [4]. On the other hand, hydrometallurgical methods are safer, with low energy consumption and sufficient metal recovery rates.

The hydrometallurgical processing of lithium-ion batteries has been extensively researched using both inorganic and organic acids. Inorganic acids such as HCl [5], HNO_3 [6,7], and H_2SO_4 [8], as well as organic acids such as citric acid [9,10], acetic acid [11,12], ascorbic acid [13], maleic acid [12], trichloroacetic acid and oxalic acid [14], with or without the simultaneous use of reducing agents [15], have been proposed or applied as leaching agents for lithium-ion batteries.

In this study, a hydrometallurgical method to recover Li from spent LFP batteries' cathodes involving pretreatment and leaching stages using oxalic acid as a leaching agent without the necessity of using an oxidizing agent or prior chemical or thermal pretreatment has been examined. The kinetics of the leaching and the impact of initial oxalic acid concentration and reaction temperature on the lithium, iron, aluminum and copper extraction were investigated.

2 Materials and Methods

2.1 Batteries pretreatment

A total of twelve cylindrical LFP battery cells, at the end of their lifecycle, were used in this study. These cells were collected by Bauer Energy, a Greek company specializing in the trade of small electric vehicles, primarily the Chinese BEEV cars. The batteries were fully discharged under the supervision of the company. Each battery cell weighs 144.61 g, including its plastic and metal casing.

Before proceeding with leaching experiments for element recovery from the active battery material, a detailed pretreatment process, illustrated in Fig. 1, was applied. Initially, the batteries were shredded using a shredder equipped with 15 mm-diameter blades. Then, after manual separation of the metal casing, plastic components, and paper, the material underwent further size reduction using a Pulverizer Mill LM2 by Labtechnics, followed by dry sieving, resulting in four particle size fractions: +5.6 mm, +1 mm, +0.5 mm, and -0.5 mm shown in Fig. 1.

These four fractions were processed separately to minimize the formation of metallic fines, thereby reducing their concentration in the final working sample. The -0.5 mm fraction was not further processed and constituted a part of the working sample, along with material derived from the other three fractions, as detailed in the following paragraphs.

After the first grinding, a second grinding stage of the +1 mm and +0.5 mm fractions was performed using the same equipment, followed by sieving with a 0.5 mm sieve to release and separate fine anodic or cathodic material attached to metals and plastics.

Dry magnetic separation was also applied to the +5.6 mm particle size fraction, aiming to remove any magnetic material present in the sample.

The three coarse fractions obtained from the three primary and secondary sieving processes were mixed and placed in water at a liquid to solid ratio 100 l/kg to separate plastics. Then, the pulp containing the heavy fraction was further sieved using 0.5 mm sieves to remove residual coarse (+0.5 mm) material attributed to metals, paper or residual heavy plastics. The slurry thus obtained containing the fine (-0.5 mm) fraction was further filtered. The liquid from filtration was collected and the solids were placed in an oven for drying at 100°C for 48 hours. The four fine fractions (-0.5 mm) obtained from both the primary and secondary sieving were then mixed to obtain the final working sample, as illustrated in Fig. 1.

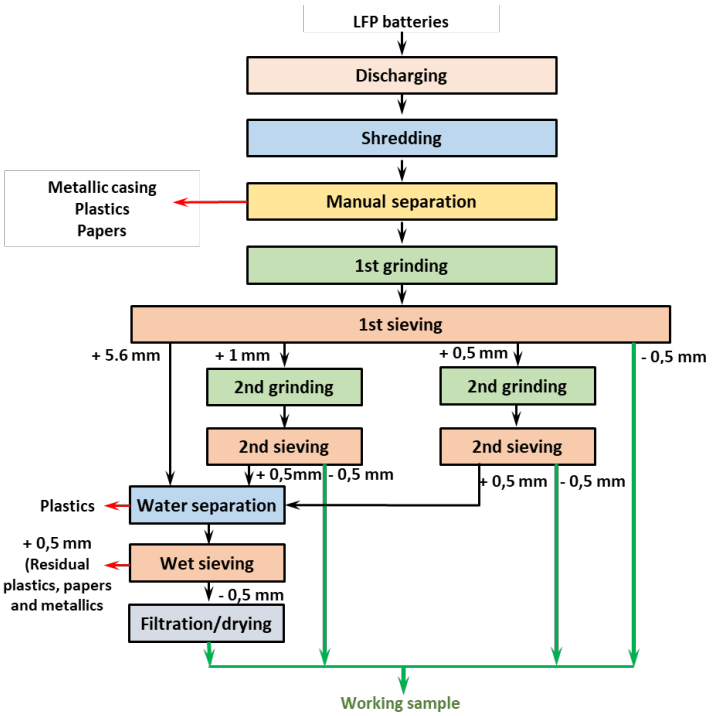

Fig. 1. LFP batteries pretreatment scheme

(a) (b) (c)

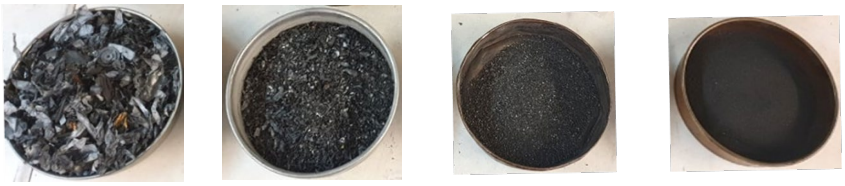

(d) (e) (f) (g)

Fig. 2. LFP batteries samples: (a) initial shredded sample (b) metallic casing, (c) material after metallics removal, (d)-(g) 1st sieving fractions ((d) +5.6mm, (e) -5.6 + 1 mm, (f) -1 + 0.5mm, (g) -0.5 mm)

2.2 Sample characterization

Chemical analysis of the working sample was conducted by fusion with borax of a finely ground subsample to a particle size of <75 μm, involving mixing of 0.1 g of the working sample with 1.5 g of a mixture of analytical grade potassium carbonate, sodium carbonate, and sodium tetraborate decahydrate at a molar ratio of 1:1:1. The mixture was then heated in a platinum crucible at 1000°C for 1 hour. The fused bead was transferred to a PTFE beaker, and an appropriate volume of diluted mineral acid (HCl) was added. The mixture was gently heated at 60–80°C under continuous stirring until fully dissolved. The resulting solution was diluted to a known volume with deionized water and analyzed by ICP-OES (Optima 7000, PerkinElmer, Akron, OH, USA) and atomic absorption spectroscopy (AAS) (PinAAcle 900T, PerkinElmer, Akron, OH, USA).

Mineralogical analysis was performed by X-ray diffraction analysis (XRD, D8 Focus, Bruker, Billerica, MA, USA) and scanning electron microscopy (SEM) using a Jeol 6380LV (JEOL Ltd., Tendo-shi, Japan).

2.3 Leaching experiments

A borosilicate round-bottom glass reactor with a total volume of 0.5 L, fitted with a five-port cap to accommodate various operational requirements, was used for the leaching experiments. The reactor was equipped with a thermomantle to ensure uniform heating and precise temperature control at 50, 70, or 90 °C. To mitigate excessive foaming observed during the reaction between the black mass and oxalic acid dihydrate ($C_2H_2O_4 \cdot 2H_2O$, >99%, Sigma-Aldrich), the reactor was loaded with only 300 mL of oxalic acid solution.

Leaching experiments were performed using oxalic acid solutions at concentrations of 0.1, 0.2, 0.5, and 0.7 M, with a fixed liquid-to-solid (L/S) ratio of 10 l/kg. Each experiment was conducted for 120 minutes under continuous stirring at 500 rpm. During the leaching process, four 5 mL aliquots were collected at 15, 30, 60, and 80 minutes. All samples, including the final bulk solution at the end of the experiment, were filtered, and the resulting filtrates were analyzed using atomic absorption spectroscopy (AAS) or inductively coupled plasma optical emission spectroscopy (ICP-OES). The pH of the final leachate was also measured. Solid residues were dried at

100 °C, weighed, and characterized by X-ray diffraction (XRD) and scanning electron microscopy (SEM).

Two experimental series were systematically conducted to investigate the effects of (i) oxalic acid concentration in the leaching solution and (ii) reaction temperature, on metals extraction under constant liquid-to-solid ratio of 10 l/kg, agitation speed of 500 rpm, and a residence time of up to 120 minutes, as summarized in the table below.

Table 1. Leaching conditions

Oxalic acid conc. (M)	Volume (ml)	Temperature (°C)	Pulp density (ml/g)	Time (min)
0.1	300	70	10	120
0.2	300	70	10	120
0.5	300	70	10	120
0.7	300	70	10	120
0.5	300	50	10	120
0.5	300	70	10	120
0.5	300	90	10	120

3 Results and Discussion

3.1 Mechanical Pretreatment

Table 1 presents the mass distribution of four particle size fractions obtained from twelve lithium-ion battery cells following shredding, removal of metal casings, plastic components, and separators, and subsequent sieving.

Table 2. Particle size fractions mass after the first crushing and sieving

Particle size	Weight (g)	Percentage (%)	Black mass (g)	Percentage (%)
+ 5.6 mm	244.04	26.6	10.55	1.69
-5.6 + 1 mm	104.04	11.3	65.20	10.45
-1 + 0.5 mm	82.54	9.0	61.20	9.80
-0.5 mm	487.26	53.1	487.26	78.06
Total	**917.88**	**100.0**	**624.21**	**100.00**

As shown in Table 2, 53% of the material obtained from the initial grinding process consists of particles smaller than 0.5 mm, which are classified as black mass, primarily composed of anodic and cathodic active materials. In addition, magnetic separation of the coarse fraction (>5.6 mm) revealed that 15.9% of this fraction is magnetic, representing 4.2% of the total mass of shredded batteries after the manual removal of metallic casings.

Following the treatment scheme outlined in Fig. 1, a total of 624.21 g of black mass was recovered, representing 68% of the battery mass after manual removal of metallic casings. This black mass served as the final working sample for subsequent leaching experiments with oxalic acid. The majority (78.06%) originated from the <0.5 mm fraction obtained during the first-stage screening, while the intermediate fractions (0.5–1 mm and 1–5.6 mm) contributed 9.80% and 10.45%, respectively. Only 1.69% of the black mass was recovered from the coarse fraction (>5.6 mm).

3.2 Sample Characterization

Chemical analysis of the working black mass sample is given in Table 3.

Table 3. Chemical analysis of the LFP batteries black mass

Element	Weight (g/100g)	Atomic (moles/100g)
Li	1.90	0.274
Al	4.66	0.173
Fe	15.26	0.273
Cu	6.82	0.107
PO_4^{3-}	25.80	0.272

As shown in Table 3, the molar ratio of Li:Fe:PO_4 is 1:1:1, consistent with the stoichiometry of $LiFePO_4$. The Al and Cu contents were 4.66% and 6.82%, respectively. The loss on ignition (LOI), determined after heating at 1000 °C for one hour, was 29.39%.

The X-ray diffraction (XRD) pattern is presented in Fig. 3. The primary crystalline phases identified were triphylite ($LiFePO_4$), graphite, and metallic copper.

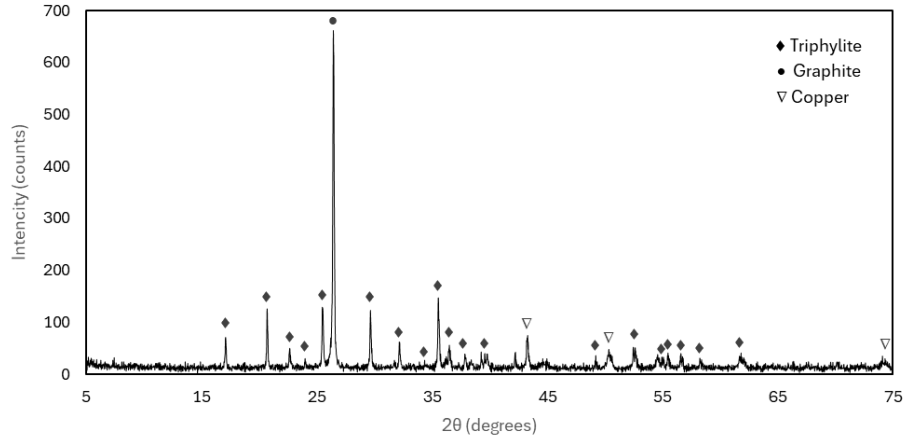

Fig. 3. XRD pattern of the working sample

The results of the SEM/EDS are shown in Fig. 4a-c. As seen in this figure, black mass consists of fine particles, approximately 25μm in size, as well as larger particles

with sizes around 500µm. Microanalyses conducted revealed the presence of LiFePO4 in various particle sizes, as well as metallic elements such as copper, typically found in larger particles and aluminum (Fig. 3c).

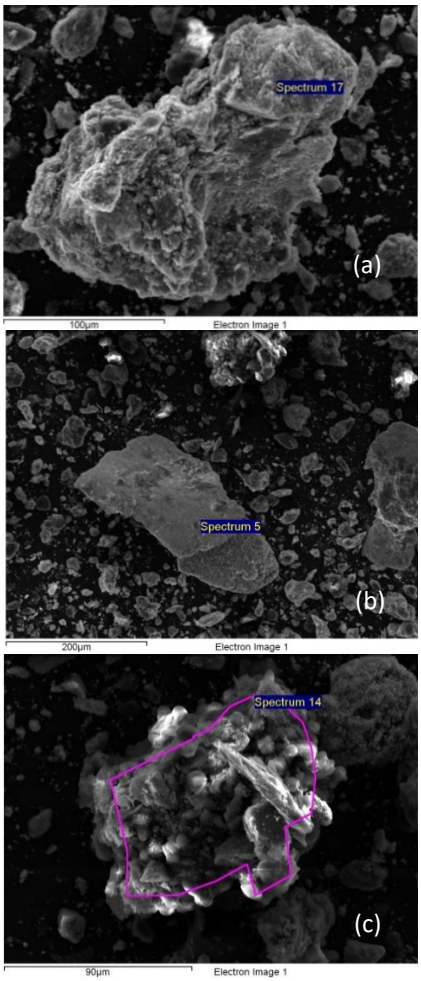

Element	Weight (%)	Atomic (%)
O	34.41	58.01
P	26.61	23.17
Fe	38.98	18.82
Totals	100.00	

Element	Weight (%)	Atomic (%)
O	1.74	6.52
Cl	0.90	1.52
Cu	97.36	91.96
Totals	100.00	

Element	Weight (%)	Atomic (%)
O	41.78	61.53
Al	21.66	18.91
P	12.21	9.29
Fe	24.35	10.27
Totals	100.00	

Fig. 4. SEM images and EDS results of the working sample (a): $LiFePO_4$, (b) metallic Cu, (c) aggregation of $LiFePO_4$ and metallic Al

3.3 Leaching tests

During black mass leaching, LiFePO4 dissolves in oxalic acid solutions with lithium remaining in the solution as lithium ions whereas Fe(II) of LiFePO4 will not oxidize and precipitate in the presence of oxalates to produce FeC2O4. The simplified reaction of LiFePO4 leaching with oxalic acid is:

$$LiFePO_{4(s)} + H_2C_2O_{4(aq)} \rightarrow Li^{+}{}_{(aq)} + FeC_2O_{4(s)} + PO_4^{3-} + 2H^{+}$$

Change of pH and redox potential. The results of pH and redox potential of the final leaching solution as a function of initial oxalic acid concentration are presented in Fig. 5.

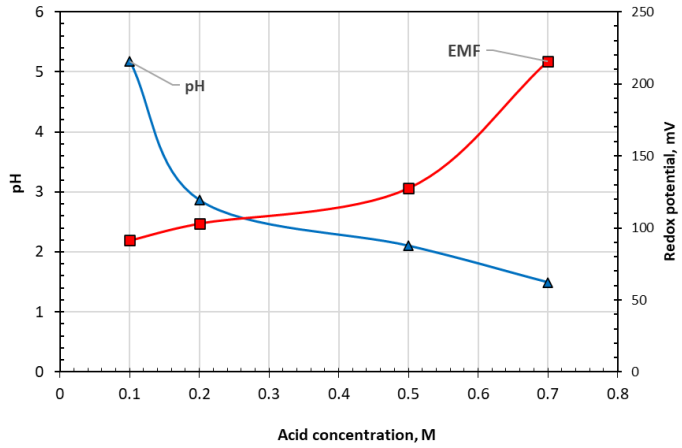

Fig. 5. Variation of final pH and redox potential as a function of oxalic acid concentration (time 120min, T=70°C , L/S 10 l/kg)

As shown in Fig. 5, the final pH of the leachate decreases with increasing oxalic acid concentration, while the redox potential increases correspondingly. Variation in temperature had no significant effect on the final pH of the leaching solution.

Effect of oxalic acid concentration. The influence of initial oxalic acid concentration and leaching time on the extraction efficiencies of Li, Fe, Cu, and Al is illustrated in Fig. 6–9. As shown in Fig. 6, complete Li extraction (100%) was achieved at an initial oxalic acid concentration of 0.7 M. At 0.5 M, Li extraction decreased to approximately 73–80%, while at 0.2 M it further declined to 30–35%. At the lowest tested concentration (0.10 M), lithium extraction was limited to around 20%.

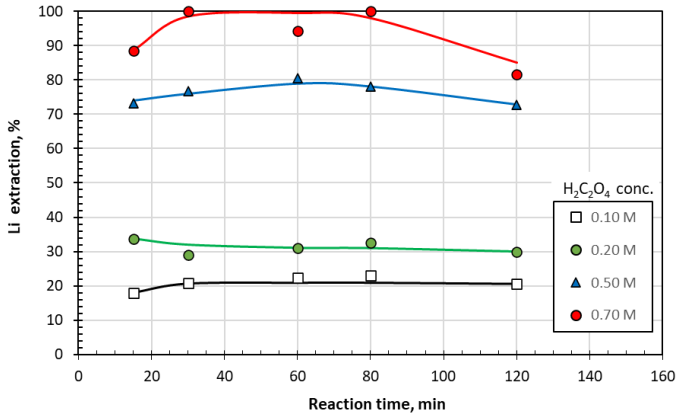

Fig. 6. Li extraction as a function of time and oxalic acid concentration (T=70°C)

In contrast, iron dissolution remained consistently low, lower than 5%, across all tested conditions and did not follow the same trend as Li (Fig 7). This behavior indicates the selective dissolution of $LiFePO_4$, likely accompanied by the reprecipitation of iron as solid iron oxalate as confirmed by the XRD patterns of the leaching residue to be presented in the following paragraphs.

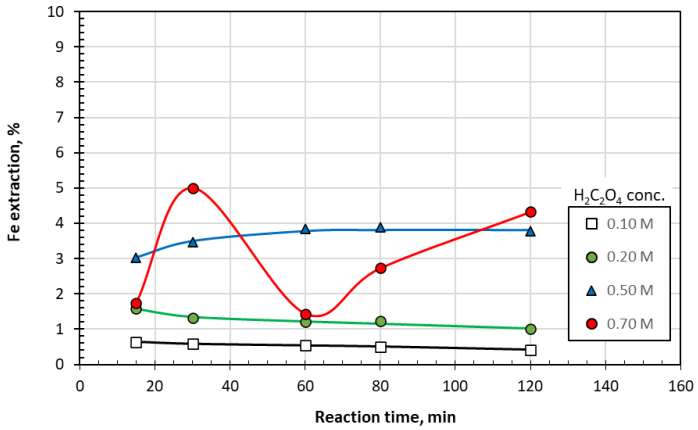

Fig. 7. Fe extraction as a function of time and acid concentration (T=70ºC)

Consequently, oxalic acid serves a dual function by providing the necessary acidity for the dissolution of $LiFePO_4$ and simultaneously by supplying oxalate ions that act as ligands, promoting the precipitation of iron as iron oxalate. The highest Li extraction efficiency was observed at an oxalic acid concentration of 0.7 M. However, the iron extraction profile over time at this concentration exhibited irregularities, suggesting that time-dependent dissolution and reprecipitation processes are occurring.

Copper extraction was minimal, with concentrations in the pregnant leach solution approaching the analytical detection limits under most conditions. An exception was observed at an oxalic acid concentration of 0.7 M, where copper recovery reached approximately 10% after 120 minutes of leaching, exhibiting an increasing trend (Fig. 8).

In contrast, aluminum exhibited high leachability, achieving extraction efficiencies of up to 100% at 0.7 M oxalic acid. At lower acid concentrations, aluminum extraction decreased significantly, with recoveries of approximately 78%, 12%, and 9% for oxalic acid concentrations of 0.5, 0.2, and 0.1 M, respectively (Fig. 9).

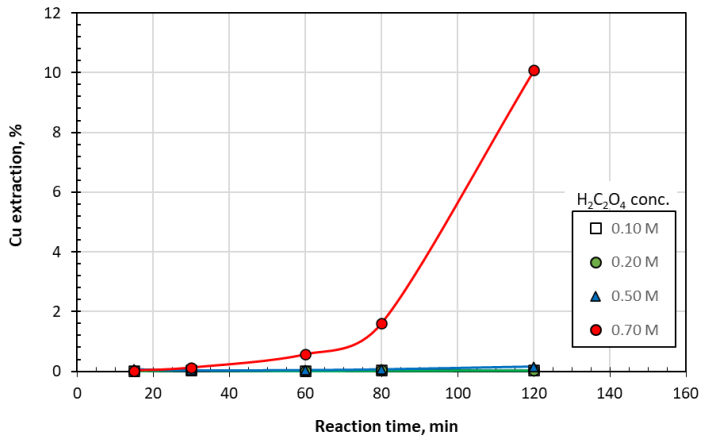

Fig. 8. Cu extraction as a function of time and oxalic acid concentration (T=70ºC)

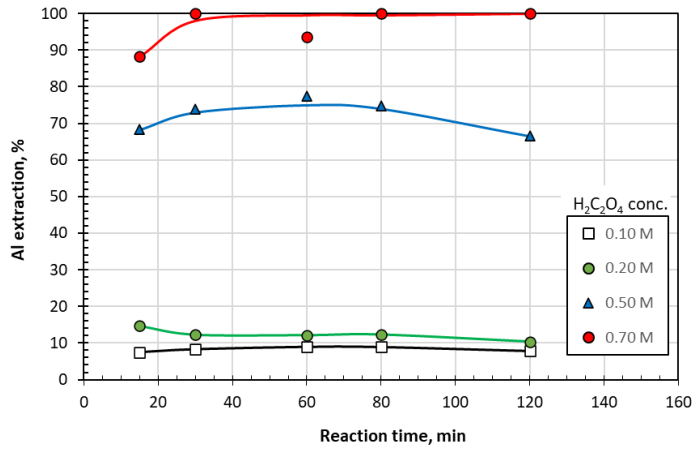

Fig. 9. Al extraction as a function of time and oxalic acid concentration (T=70ºC)

Effect of temperature. Leaching experiments were conducted at varying temperatures (50, 70 and 90 °C) while maintaining a constant oxalic acid concentration of 0.5 M. The effects of temperature on the extraction behavior of Li, Fe, Cu, and Al as a function of reaction time are presented in Figures 10–13.

As shown in these figures, increasing the temperature within the tested range had no significant effect on the extraction efficiencies of the target metals. Lithium extraction remained in the range of 75–80%, iron between 3–4%, copper below 0.2%, and aluminum between 70–80%

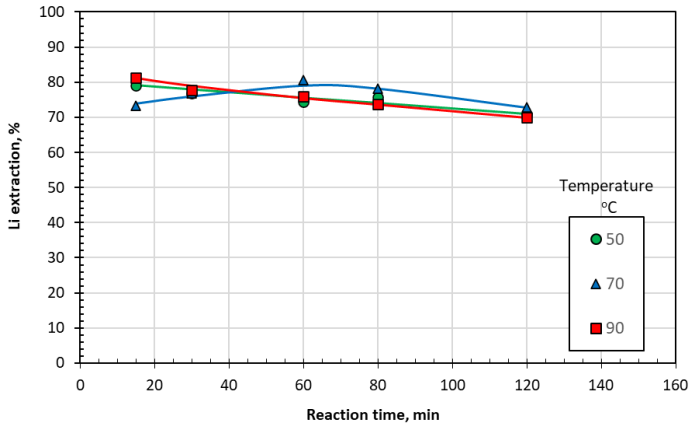

Fig. 10. Li extraction from LFP batteries as a function of time and temperature (0.5 M oxalic acid concentration)

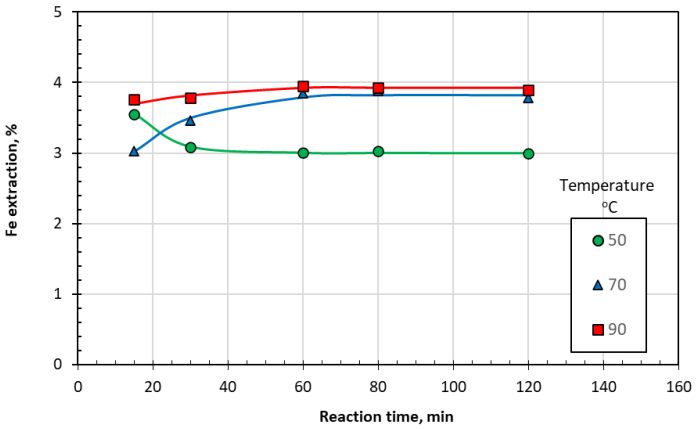

Fig. 11. Fe extraction from LFP batteries as a function of time and temperature (0.5 M oxalic acid concentration)

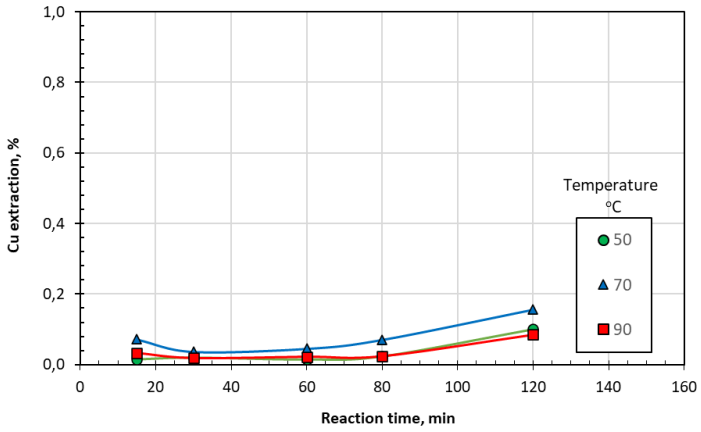

Fig. 12. Cu extraction from LFP batteries as a function of time and temperature (0.5 M oxalic acid concentration)

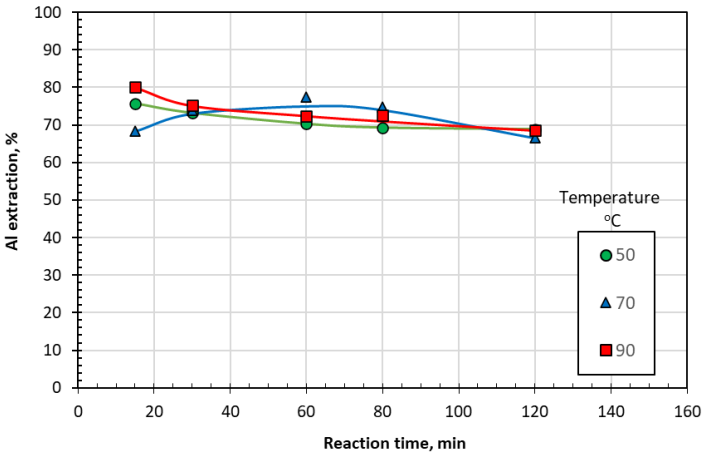

Fig. 13. Al extraction from LFP batteries as a function of time and temperature (0.5 M oxalic acid concentration)

Characterization of leaching solid residues. X-ray diffraction (XRD) analysis patterns performed on the solid leaching residues compared with that of the untreated initial sample, are shown in Fig. 14. As depicted, both the graphite phase and metallic copper remain detectable after leaching. $LiFePO_4$ was identified in residues from leaching conducted under mild conditions (oxalic acid concentrations of 0.1 and 0.2M). In addition, two new crystalline phases, absent in the original material, were identified in the leach residues: humboldtine (hydrated iron oxalate, $FeC_2O_4 \cdot 2H_2O$), which appeared in all residues, and iron phosphate oxide (Fe_3PO_7), which was detected at oxalic acid concentrations equal or greater than 0.5 M. The presence of these phases was further confirmed by scanning electron microscopy (SEM) analysis.

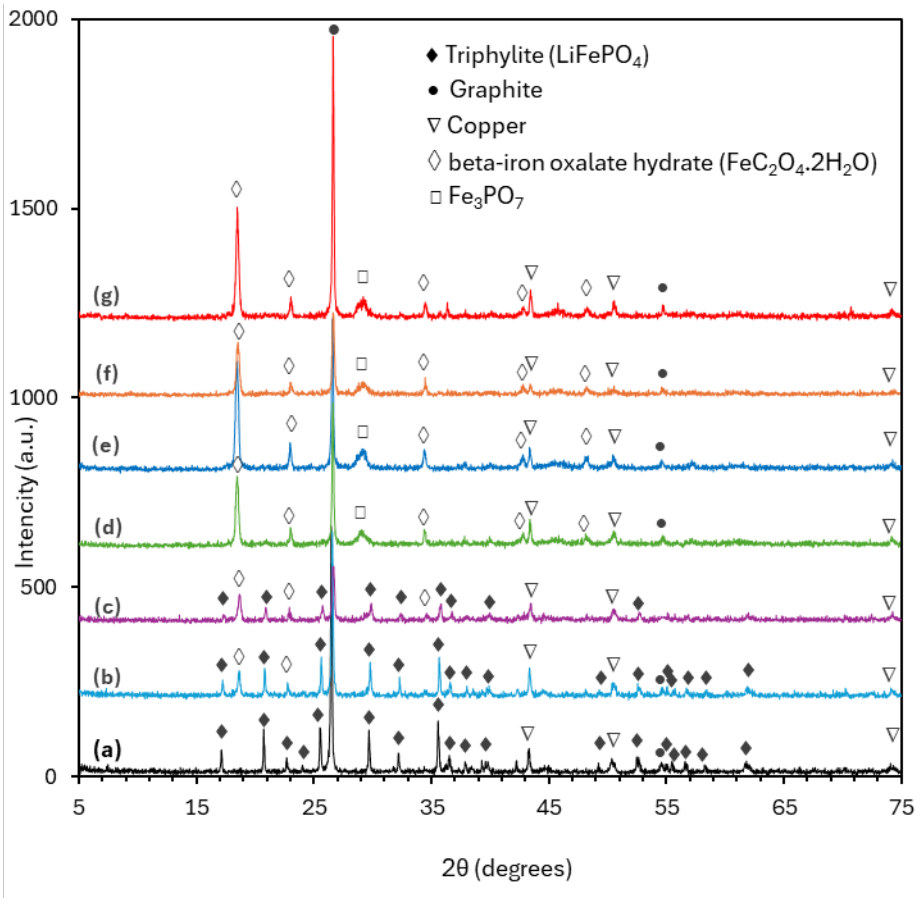

Fig. 14. RD patterns of the initial untreated sample (curve (a)) and solid residues obtained after leaching with oxalic acid under various conditions: curve (b) 0.1 M at 70°C, (c) 0.2 M at 70°C, (d) 0.5 M at 70°C, (e) 0.7 M at 70°C, (f) 0.5 M at 50°C, (g) 0.5 M at 70°C

Conclusions

A comprehensive treatment scheme for end-of-life (EoL) lithium iron phosphate (LFP) batteries was investigated, encompassing both pre-treatment and hydrometallurgical processing. The pre-treatment stage involved initial mechanical shredding and manual removal of the metallic casing, followed by successive crushing, grinding, and sieving steps. These were combined with water-based separation techniques to effectively eliminate plastic, organic, and metallic components. This process yielded a black mass primarily composed of anodic and cathodic active materials, along with residual metallic impurities, predominantly copper and aluminum originating from the current collectors.

Subsequent leaching experiments conducted using oxalic acid solutions at four concentrations (0.1, 0.2, 0.5, and 0.7 M) under controlled conditions: temperature of 70 °C, liquid-to-solid ratio of 10 l/kg, and reaction times of up to 120 minutes demonstrated complete lithium recovery (≈100%) at an oxalic acid concentration of 0.7 M. At 0.5 M, lithium extraction efficiency ranged from 73% to 80%. Lower concentrations resulted in significantly reduced extraction rates, with 30–35% lithium recovery at 0.2 M and approximately 20% at 0.1 M. Iron dissolution remained consistently low under all leaching conditions and did not correlate with lithium extraction. This behavior is attributed to the precipitation of iron following the dissolution of LiFePO4, primarily in the form of solid iron oxalate and iron phosphate oxide, as confirmed by X-ray diffraction (XRD) analysis of the solid residues. Copper extraction was minimal, with concentrations near the analytical detection limits, except at an oxalic acid concentration of 0.7 M, where extraction increased to approximately 10 percent after 120 minutes, indicating a slight upward trend. Aluminum demonstrated high leachability, with extraction efficiencies reaching up to 100 percent at 0.7 M oxalic acid. At lower concentrations of 0.5, 0.2, and 0.1 M, the extraction efficiencies declined to 78, 12, and 9 percent, respectively. Variations in leaching temperature between 50 °C and 90oC had no significant impact on the extraction efficiencies of lithium, iron, copper, or aluminum.

The composition of the solid leach residues was strongly dependent on the leaching conditions. At lower oxalic acid concentrations, unreacted components of the starting material, such as LiFePO4, copper, and graphite, remained present in the solid phase. In contrast, higher acid concentrations promoted the formation of secondary iron phases, including hydrated iron oxalate and iron phosphate oxide (Fe3PO7), as identified in the XRD patterns, along with residual graphite and copper.

In conclusion, leaching with 0.7 M oxalic acid proved effective for the selective extraction of lithium and its separation from the solid matrix, thereby enabling subsequent recovery from the leachate. Under these conditions, aluminum was co-dissolved to a significant extent, while iron and copper largely remained in the solid phase, limiting their co-dissolution.

References

1. Chen, X., Shen, W., Vo, T.T., Cao, Z., Kapoor, A.: An overview of lithium-ion batteries for electric vehicles. In Proceedings of the 10th International Power & Energy Conference (IPEC), Ho Chi Minh City, Vietnam, 230–235 (2012). https://doi.org/10.1109/ASSCC.2012.6523269
2. Baum, Z.J., Bird, R., Yu, X. and Ma, J.: Lithium-ion battery recycling-overview of techniques and trends. ACS Energy Letters 7(10), 3268-3269 (2022). https://doi.org/10.1021/acsenergylett.2c01888
3. Neumann, J., Petranikova, M., Meeus, M., Gamarra, J.D., Younesi, R., Winter, M., Nowak, S.: Recycling of lithium-ion batteries-current state of the art, circular economy, and next generation recycling. Adv. Energy Mater. 2102917, 1-26 (2022). https://doi.org/10.1002/aenm.202102917
4. Dunn, J.B., Gaines, L., Kelly, J.C., James, C., Gallagher, K.G.: The significance of li-ion batteries in electric vehicle life-cycle energy and emissions and recycling's role in its reduction. Energy Environ. Sci., 8, 158–68. https://doi.org/10.1039/C4EE03029J

5. Takacova, Z., Havlik, T., Kukurugya, F., Orac, D.: Cobalt and lithium recovery from active mass of spent Li-ion batteries: Theoretical and experimental approach. Hydrometallurgy 163, 9–17 (2016). http://dx.doi.org/10.1016/j.hydromet.2016.03.007
6. Lee, C.K. and Rhee, K.-I.: Preparation of LiCoO2 from spent lithium-ion batteries. J Power Sources 109, 17–21 (2002). https://doi.org/10.1016/S0378-7753(02)00037-X
7. Yuliusman, Fajaryanto, R., Nurqomariah, A., Silvia: Acid leaching and kinetics study of cobalt recovery from spent lithium-ion batteries with nitric acid. In 3rd i-TREC 2018, E3S Web of Conferences 67, 03025 (2018). https://doi.org/10.1051/e3sconf/20186703025.
8. Chen, X., Luo, C., Zhang, J., Kong, J., Zhou, T.: Sustainable recovery of metals from spent lithium-ion batteries: A green process. ACS Sustainable Chem. Eng. 3(12), 3104–3113 (2015). https://doi.org/10.1021/acssuschemeng.5b01000.
9. Chen, X., Zhou, T.: Hydrometallurgical process for the recovery of metal values from spent lithium-ion batteries in citric acid media. Waste Manag Res 32(11), 1083-93 (2014). https://doi.org/10.1177/0734242X14557380.
10. Li, L., Bian, Y., Zhang, X., Guan, Y., Fan, E., Wu, F., Chen, R.: Process for recycling mixed-cathode materials from spent lithium-ion batteries and kinetics of leaching. Waste Manag. 71, 362–371 (2018). http://dx.doi.org/10.1016/j.wasman.2017.10.028
11. Gao, W., Song, J., Cao, H., Lin, X., Zhang, X., Zheng, X., Zhang, Y., Sun, Z.: Selective recovery of valuable metals from spent lithium-ion batteries - Process development and kinetics evaluation. J of Cleaner Production 178, 833-845 (2018). https://doi.org/10.1016/j.jclepro.2018.01.040
12. Li, L., Bian, Y., Zhang, X., Yao, Y., Xue, Q., Fan, E., Wu, F., Chen, R.: A green and effective room-temperature recycling process of LiFePO4 cathode materials for lithium-ion batteries. Waste Management 85, 437–444 (2019). https://doi.org/10.1016/j.wasman.2019.01.012
13. Nayaka, G.P., Manjanna, J., Pai, K.V., Vadavi, R., Keny, S.J., Tripathi , V.S.: Recycling of valuable metal ions from the spent lithium-ion battery using aqueous mixture of mild organic acids as alternative to mineral acids. Hydrometallurgy 151, 73–77 (2015). https://doi.org/10.1016/j.hydromet.2014.11.006
14. Zeng, X., Li, J., Singh, N.: Recycling of spent lithium-ion battery: A critical review, Critical Reviews in Environmental Science and Technology, 44(10), 1129–1165 (2014). https://doi.org/10.1080/10643389.2013.763578
15. Meshram, P., Pandey, B.D., Mankhand, T.R.: Extraction of lithium from primary and secondary sources by pre-treatment, leaching and separation: A comprehensive review. Hydrometallurgy 150, 192–208 (2014). http://dx.doi.org/10.1016/j.hydromet.2014.10.012

Corrosion and Tensile Behavior of 304L Rebars under the Influence of a Concrete Additive and Migrating Corrosion Inhibitors

S. Tsouli[1] [0000-0002-5703-9403], S. Kleftakis[1], A.G. Lekatou[1,*] [/0000-0001-7951-4431]

[1]Laboratory of Applied Metallurgy, Department of Materials Science and Engineering, School of Engineering, University of Ioannina, 45110 Ioannina, Greece
*alekatou@uoi.gr

Abstract. This study examines the effect of a Ca-rich fly ash additive, a liquid migrating corrosion inhibitor (Inhibitor B), and a vapor phase inhibitor (Inhibitor C), individually and in combination, on the corrosion performance of 304L stainless steel rebars embedded in concrete cubes. This was assessed through open circuit potential (OCP) measurements over 1 m in an acid rain (AR) simulating electrolyte, salt spray testing for 4 m and tensile testing of 304L rebars following the corrosion tests. For 304L rebars embedded in concrete cubes containing fly ash (FA), Inhibitor B, Inhibitor C, and combinations of FA with Inhibitor B, immersed in AR for 1 m during OCP testing, there was more than a 90% probability that corrosion did not occur. Both Inhibitors B and C improved the corrosion resistance of the rebars in AR in the absence of FA, but when combined with FA, their inhibiting effects were neutralized. The 20 wt.% FA content improved the corrosion behavior of 304L rebars compared to 0 wt.% FA. After 1 m of OCP testing in AR, % elongation increased in all cases except without inhibitors. After 4 m of salt spraying, a slight decrease in strength was observed for the 304L reinforcement, both in the absence and presence of any inhibitors, though within standard deviation.

Keywords: 304L stainless steel rebars, Migrating Corrosion Inhibitors, Fly Ash, Salt Spray Test, Open Circuit Potential test.

1 Introduction

Steel reinforcement corrosion is the primary cause of reinforced concrete structure degradation, as it weakens the steel/concrete bond strength [1,2] and the concrete durability [3,4]. Various methods have been employed to mitigate this issue, including (i) alternative reinforcement materials and slab designs, (ii) barrier techniques, (iii) corrosion inhibitors and (iv) electrochemical procedures [5].

Among alternative reinforcement materials, stainless steel, molten zinc and epoxy-sprayed bars and stainless steel claddings offer the highest resistance to corrosion. However, solid stainless steel rebars provide superior structural properties [6]. Though more expensive than carbon steel, the long-term savings from reduced maintenance and

replacement costs often justify the initial investment on stainless steel rebars [1]. As a result, stainless steel rebars are increasingly used in new concrete constructions and renovations, especially in critical areas exposed to corrosive conditions [1], as well as in restoration works of ancient monuments and historical buildings like the ancient theater of Dodona in Epirus, Greece, where AISI 316L stainless steel is employed [7].

Barrier methods include partial replacement of cement with mineral additives, such as fly ash, silica fume, blast furnace slag, calcite laterites and microsilica, use of concrete overlays, waterproof membranes, concrete sealers and deep polymer impregnation [5]. The partial replacement of cement with mineral additives, such as fly ash (FA), has been a reliable, economic and environmentally friendly method to limit corrosion of reinforced concrete in aggressive environments including acidic [8, 9]. The addition of fly ash (FA) to concrete can enhance corrosion resistance by forming calcium silicate hydrate (C-S-H) through the pozzolanic reaction, which consumes the less stable calcium hydroxide (C-H) and fills concrete's capillary voids [8, 9]. FA also refines the concrete's pore structure by reducing pore volume, distribution, and critical pore size [9]. Furthermore, FA increases resistance to chloride, sulfate, sulfuric acid, and nitric acid attacks by forming pozzolanic products like Friedel's salt and ettringite, which decrease concrete permeability [8, 10].

Corrosion inhibitors can be a good alternative to other protection methods due to their low cost and ease of application [11]. They can be classified according to the electrochemical mechanisms of protection to: (a) anodic, (b) cathodic and (c) mixed, depending on whether they affect (a) the anodic reaction (steel dissolution), (b) the cathodic reaction on the steel surface or (c) both reactions by acting on both anodic and cathodic sites. They can also be classified according to the application methods to (a) admixed corrosion inhibitors (mixed into fresh concrete for new structures) and (b) migrating corrosion inhibitors - MCIs (applied onto the surface of hardened concrete, often to repair reinforced concrete) [11-13].

MCI molecules can migrate through concrete pores via liquid capillary action and gaseous phase diffusion onto the surface of the steel reinforcement, where they chemically interact with it and form a stable layer that shields both the anodic and cathodic sites of the rebars. [13, 14]. Active groups of MCIs can also adsorb chloride ions preventing them from directly accessing the steel [15]. Additionally, MCIs block surface pores in concrete, primarily at the surface rather than in the bulk, enhancing anti-corrosion effects without affecting the concrete's physical and mechanical properties [13, 16, 17]. In cases of pitting, inhibitors can function by [11]: a) forming a protective film before chloride ingress, b) stabilizing the pH in and around the pit, c) competing with aggressive ions for surface adsorption, and d) competing with aggressive ions for migration into the pit.

Amines, alkanolamines (AMA), and their salts with organic and inorganic acids are common inhibitors for protecting concrete steel reinforcement [11]. While MCIs are mostly considered to exert a mixed electrochemical action because they form a layer on both anodic and cathodic sites [11, 14], some studies suggest a mainly cathodic [18] or mainly anodic action [19]. The AMA-based inhibitors consist of a volatile aminoalcohol and an acid that forms a salt with the aminoalcohol [11]. Typical AMA

compounds include diethanolamine, dimethylpropanolamine, monoethanolamine, and dimethylethanolamine [17].

A main issue with MCIs is the difficulty of the surface applied volatile liquid to migrate through the concrete to the steel surface. For this reason, capsule-contained volatile (or vapor phase) corrosion inhibitors (VCIs or VPIs) have been developed, which can be inserted into drilled holes near the steel [20]. These capsules release volatile phases of varying vapor pressures ensuring a controlled release over time. These volatile phases diffuse to the metal surface, condense, physically adsorb onto it, and form a thin film of crystals. In the presence of even traces of moisture, the crystals dissolve, polarize and are attracted to the metal's anode and cathode, forming a protective layer that thickens over time by condensation of vapors [21]. Effective VCIs are typically salts of weak volatile acids and bases, like amine salts, ensuring both protection and volatility [22, 23]. The pH of the moisture film should be balanced, neither too acidic nor too alkaline [22].

Previous studies by the authors have demonstrated that high-calcium fly ash (FA) can replace both $Ca(OH)_2$ and Portland cement up to 20 wt.% enhancing the corrosion resistance of 316L and 304L stainless steel rebars in acid rain simulating solutions, seawater simulating solution and simulated saline environments attacked by acid rain [7, 24-29]. However, increasing FA to 25 wt.% reverses this trend owing to the formation of agglomerates that have reduced tendency for pozzolanic or cementitious reactions and also form differential aeration cells on the steel beneath them. The feasibility of using 304L stainless steel instead of 316L in critical applications, like historic monument restoration, was demonstrated. This substitution was achievable by incorporating low FA concentrations (10 or 15 wt.%) in both slightly acidic and strongly alkaline environment [26, 27]. Replacing cement with up to 25 wt.% FA in concrete had not any significant effect on the tensile properties of 316L and 304L rebars before and after 4 m of salt spraying [26, 28]. Additionally, FA, alone or combined with a liquid corrosion inhibitor, reduced porosity after salt spraying, with the most significant reduction observed at 15% and 25% FA content [30].

The current investigation is part of a broader initiative aimed at holistically exploring the potential of incorporating high-Ca fly ash in concrete members of critical applications. Studies assessing the performance of stainless steels embedded in concrete mixes containing high-calcium fly ash in acid rain environments are scarce, primarily due to concerns regarding the utilization of high-calcium fly ash. The latter contains elevated levels of free CaO and S, which are considered to negatively impact volume stability and concrete durability [31]. Additionally, high Ca-FAs contain significant quantities of Al_2O_3 in their glassy phase, which may react with C-H produced during cement hydration to form calcium aluminate hydrate (C-A-H); interaction with sulfate-rich environments, may lead to the formation of heavily hydrated ettringite causing expansion-related cracking [10]. On the other hand, certain mineralogical characteristics of high-calcium fly ash, such as engagement of Al_2O_3 in inert phases, supersulfation of concrete, selective nucleation of the corrosion resistant C-S-H on the surface of the $CaCO_3$ contained in the fly ash, can counteract the adverse effects mentioned earlier; further details can be sought in [27].

Within the above framework, the present effort focuses on the effect of FA, combined with a liquid inhibitor and a gas phase inhibitor, on: (a) the corrosion performance of 304L rebars embedded in concrete cubes during open circuit potential (OCP) measurements over a period of 1 m in an electrolyte simulating acid rain, and (b) the mechanical properties of 304L rebars embedded in concrete cubes subjected to salt fog testing for 4 m. The main motivation for this effort stems from the fact that several investigations have suggested that the amine-based inhibitors have a limited effect on corrosion inhibition [15, 32]. Also, a combination of two or more types of inhibitors could offer an effective strategy for enhancing corrosion protection [14, 15].

2 Experimental

304L stainless steel corrugated rebars having nominal composition in wt.%: Fe, 0.03% C, 18.20% Cr, 8.51% Ni, 0.75% Si, 2.00% Mn, 0.045% P, 0.03% S, diameter of 6 mm and length of 12 cm were embedded in concrete cubes. The concrete cubes ($7\times7\times7$ cm^3) contained Portland cement (CEM II/A-M 42.5R), CEN Standard silica sand and water (cement/sand/water: 450/225/1350 (g), according to BS EN 196-1). XRD analysis of the concrete mixture after hydration for 24 h detected the following hydration products along with calcite ($CaCO_3$): various C-S-H ($CaO\text{-}SiO_2\text{-}H_2O$) minerals that constitute the main hydration product of cement, other hydration minerals, like $CaO_2\cdot8H_2O$, C-H, C-A-Š-H ($CaO\text{-}Al_2O_3\text{-}SO_2\text{-}H_2O$) and C-A-H, and sulfoaluminates Aft (ettringite) and Afm (monosulfoaluminate) [27].

Pulverized class-C fly ash (FA) from the Hellenic Public Power Corporation lignite mines in Western Macedonia, Greece, was also added in the concrete mixture, FA replacing 20 wt.% of cement. The FA was mainly composed by CaO, SiO_2, Al_2O_3, SO_3, Fe_2O_3, and MgO [7]. A comprehensive mineralogical analysis of the FA is provided in [27]. In summary, the FA primarily consisted of calcite ($CaCO_3$), anhydrite ($CaSO_4$), quartz (SiO_2), lime (CaO), and hematite (Fe_2O_3). Minerals present in minor quantities included brownmillerite ($Ca_2(Al,Fe)_2O_5$), periclase (MgO), merwinite ($Ca_3Mg(SiO_4)_2$), portlandite ($Ca(OH)_2$), K-Al-silicates like K-feldspars and illite, and traces of plagioclase. Amorphous phases including glass and residual clay minerals from lignite, were also identified. Among the aforementioned minerals, anhydrite, lime, brownmillerite, periclase, and portlandite are reactive minerals, while quartz, hematite, and K-Al silicates are inert [33]. Consequently, the high content of reactive minerals (particularly anhydrite and lime) along with glassy phases in the fly ash imparts it with hydraulic and pozzolanic properties, making this fly ash a potentially effective binding agent [34].

Inhibitor B, a liquid MCI inhibitor with a mixed electrochemical action, based on alkanolamine, was applied by brush on the concrete surface. Besides its corrosion inhibition by molecule migration, as described in the Introduction, it is claimed to restore the alkalinity of the concrete and maintain it stable [35]. Inhibitor C, a third generation VCI inhibitor, released in three stages, was inserted in concrete cubes, as a 10 ml capsule. Inhibitor C is made up of a complex blend of three vapour phase corrosion inhibitors of fast (24 h), medium (48 h) and long (12-48 m) term protection, resulting in the building of a protective passive film around the reinforcement. Inhibitor C works as a

migrating corrosion inhibitor of anodic and cathodic action by building a vapour density within an enclosed space. [36].

The open circuit potential (OCP test) of reinforced concrete cubes immersed in an acid rain simulating electrolyte ((g/L H_2O): H_2SO_4: 0.032, HNO_3: 0.015, $(NH_4)_2SO_4$: 0.046, Na_2SO_4: 0.032, $NaNO_3$: 0.021 and NaCl: 0.084, pH = 3.1 [37]) was recorded every 10 min for 1 m. The stainless steel /concrete junction of the free surface was coated by an epoxy glue. The naked part of the rebar was connected with the ACM Gill AC potentiostat using a three electrode cell (reference electrode: Ag/AgCl/3.5 M KCl, counter electrode: Pt-gauge). The pH value of the electrolyte was regularly measured.

The reinforced concrete cubes also underwent salt spraying for 4 m in a Vötch chamber using a fog of 5 wt.% NaCl at 35 ºC according to ASTM B117-97.

Prior to and after salt spray and OCP tests, the rebars were carefully removed from the concrete cubes and were subjected to tensile testing at the Galdabini uniaxial testing machine (100 kN, cross-head speed: 1.30 mm/min, ASTM E8/E8M-09).

Polished cross sections of 304L after the OCP and salt spraying tests were examined by Scanning Electron Microscopy and Energy Dispersion X-ray Spectroscopy (SEM/EDX) at the JeoL JSM 6510 LV system, equipped with an X-act (Oxford Instr.) EDX analyzer.

3 Results and discussion

3.1 OCP test

Figs. 1a-e illustrate the variation of the OCP values of 304L rebars embedded in concrete cubes containing FA (0 wt.% & 20 wt.%) and/or Inhibitors B and C. It should be noted that the OCP test is an electrochemical technique that does not provide any information about the corrosion kinetics, but identifies the existence of corrosion or passivation [38]. In all cases, the OCP values are more positive than -160 mV (Ag/AgCl), indicating a greater than 90% probability that the rebars are in a non-corroding state [38, 39]. The only exception is the case of "304L - 0 wt.% FA + Inhibitor C" during the first three to four days of immersion (Fig. 1c,e), after which the OCP ennobles, following a continuously increasing trend. As reported in the Experimental section, this ennoblement coincides with the vaporization of the medium term component of Inhibitor C, which strengthens the bonding of the surface film with the steel.

The intensive fluctuations in the OCP values in Fig. 1, provide evidence of the alternating formation and dissolution of surface products on steel surface sites that are most susceptible to pitting, like strain-hardened martensitic ribs and sulfide inclusions. Nevertheless, pitting is metastable and has led to repassivation, since OCP > -160 mV (Ag/AgCl). Pitting in 304L steel is usually associated with MnS inclusions [40].

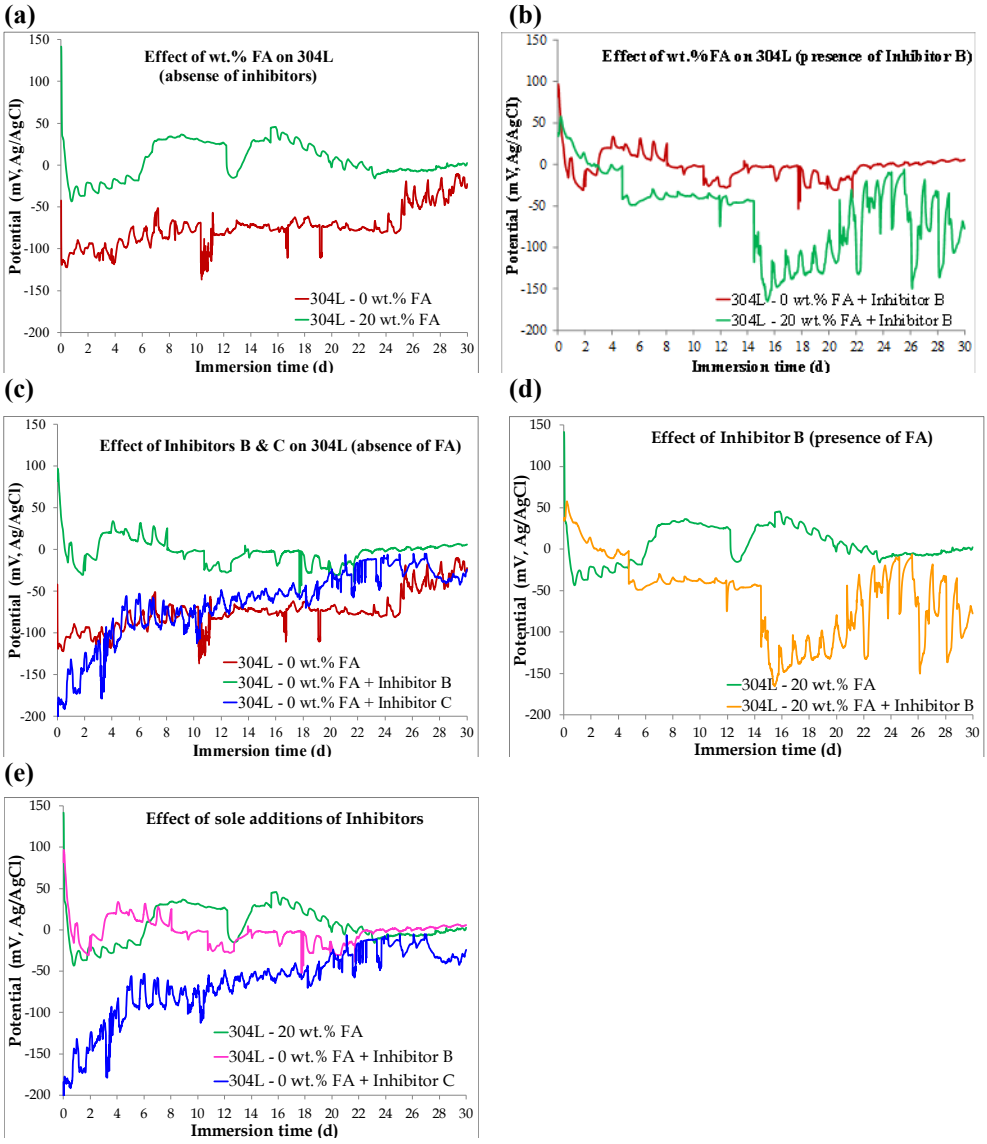

Fig. 1. Open circuit potential measurements of concrete embedded 304L rebars immersed in a simulating acid rain solution (pH = 3.1)

In Fig. 1b, the notably higher OCP values and reduced OCP fluctuations indicate that the 20 wt.% FA content has a beneficial effect on the corrosion behavior of 304L rebars compared to 0 wt.% FA. This observation aligns with previous studies by the authors, which elaborate on the beneficial role of FA [7, 24-30]. The beneficial role of FA under AR attack can be attributed to its high content of reactive phases with hydraulic and pozzolanic properties. Additionally, a significant portion of Al_2O_3 in FA

has been shown to be bound in inert K-Al silicate minerals, which limits the availability of alumina to form ettringite [27]. Ettringite ($C_3A(CS)_3H_{32}$) is a compound that can expand nearly sevenfold in volume leading to internal stresses and subsequent cracking of concrete [26].

Fig. 1c shows that both Inhibitors B and C improved the corrosion behavior of 304L concrete reinforcement in the absence of FA, with Inhibitor B demonstrating the best resistance to corrosion for up to 20 d of immersion. After this period, Inhibitors B and C led to similar corrosion performances. It should be emphasized that the long term component of Inhibitor C had not been released by the end of the test; hence, its full potential had not been realized.

Conversely, the combination of FA with Inhibitor B for 304L rebars shows worse corrosion performance compared to the use of Inhibitor B alone (Fig. 1b) or FA alone (Fig. 1d) in terms of lower OCP values and more intensive OCP fluctuations. Hence, it is drawn that the combination of Inhibitor B with FA has negated the individual inhibiting effects of both FA and Inhbitor B, as sole additions. This conclusion is compatible with previous research by the authors, which showed that the combination of FA with Inhibitor B slightly increases the porosity of concrete compared to the sole addition of FA, although within statistical error [30]. A similar conclusion was drawn in that study for the combination of FA with Inhibitor C. Fig. 1e shows that the OCP values in the presence of inhibitors B, C and FA, converge after 22 d of immersion. It should again be noted that the long term component of Inhibitor C had not been released by the end of the OCP test.

3.2 Tensile testing after salt spray and OCP tests

Fig. 2 shows the macroscopic state of concrete cubes reinforced with 304L rebars after having been subjected to a salt spray test for 4 m. The concrete cubes in Fig. 1a,b contain 20 wt.% FA and are coated by Inhibitor B, whereas in Fig. 1c,d contain 20 wt.% FA and Inhibitor C. Both cases manifest excellent surface states without any visible signs of corrosion. Fig. 3 presents the stress-strain curves of 304L rebars extracted from concrete cubes, which either contained 20 wt.% FA (Fig. 3a, b) or did not (Fig. 3c, d), and were either coated with Inhibitor B (Fig. 3b, d) or not (Fig. 3a, c), before and after 4 m of salt spray testing. The only notable difference in Fig. 3 is the decreased strain in the specimens after salt spraying. Fig. 3d shows that the decreasing trend in the strain is consistent over the time span from 0 to 4 m. Similarly, Fig. 4 presents the stress-strain curves of 304L rebars extracted from concrete cubes, which either contained 20 wt.% FA (Fig. 4a, b) or did not (Fig. 4c, d), and were either coated with Inhibitor B (Fig. 4b, d) or not (Fig. 4a, c), before and after 1 m of OCP testing. The only noticeable difference in Fig. 4 is the increased strain of the specimens removed from the cubes containing 20 wt.% FA and/or Inhibitor B, after OCP testing, in contrast to the slightly decreased strain of the specimens removed from the concrete cube free of any inhibitors (the latter is observed in Fig. 4c). This increase is in contrast with the decreased strain after salt spraying. Table 1 compares the effect of FA, Inhibitor B and their combination on the tensile property values of 304L rebars removed from concrete cubes after salt spray testing (4 m) and OCP testing (1 m). It can be seen that after salt spray test and after OCP test, the presence of 20 wt.% FA and/or Inhibitor B does not have any

statistically significant effect on the tensile properties of 304L rebars. Table 2 presents the effect of time on the tensile properties of 304L rebars removed from concrete cubes prior to and after salt spray testing (4 m) and OCP testing (1 m).

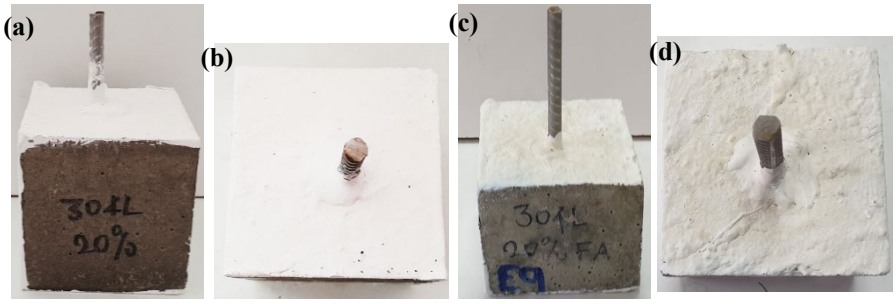

Fig. 2. Concrete cubes reinforced by 304L rebars after salt spraying for 4 m: (a), (b): 20 wt.% fly ash + Inhibitor B; (c), (d): 20 wt.% fly ash + Inhibitor C

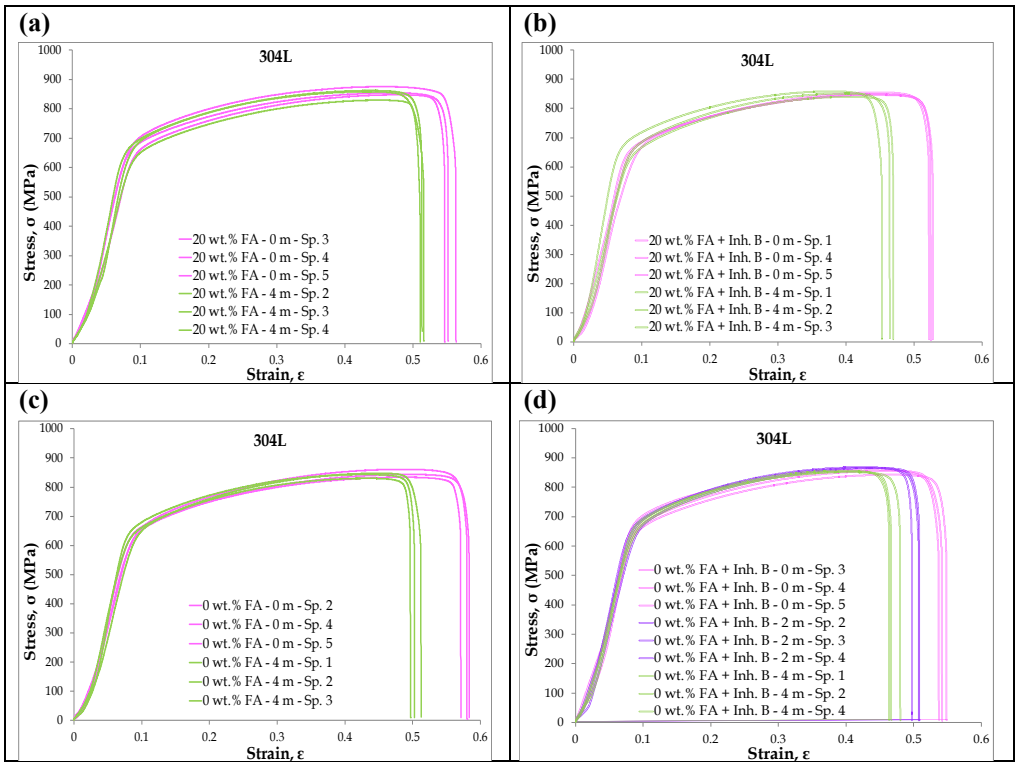

Fig. 3. Stress-strain curves of 304L corrugated bars reinforcing concrete that contained: (a) 20 wt.% fly ash, (b) 20 wt.% fly ash + Inhibitor B, (c) 0 wt.% fly ash, (d) 0 wt.% fly ash + Inhibitor B, before (0 m) and after salt spraying for 4 m (4 m)

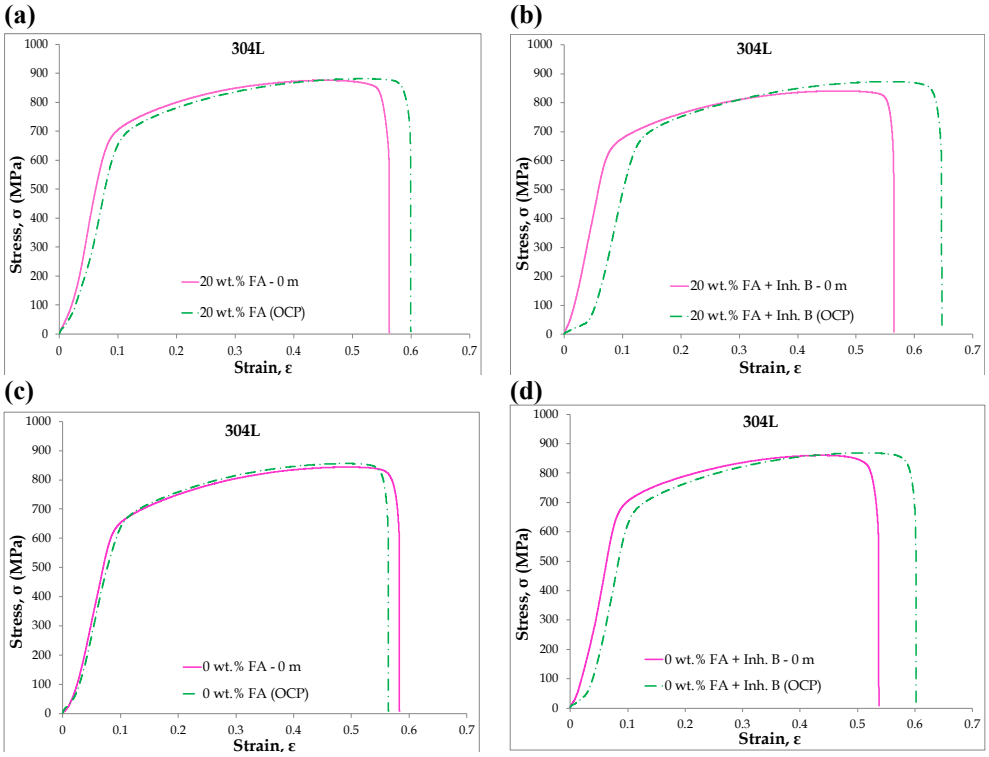

Fig. 4. Stress-strain curves of 304L corrugated bars reinforcing concrete that contained: (a) 20 wt.% fly ash, (b) 20 wt.% fly ash + Inhibitor B, (c) 0 wt.% fly ash, (d) 0 wt.% fly ash + Inhibitor B, before (0 m) and after OCP testing for 1 m (OCP)

Table 1. Effect of fly ash, inhibitor B and their combination on the tensile properties of 304L rebars after salt spray testing (4 m) and OCP testing (1 m)

Inhibitor	Test	Duration, m	0.2% yield strength, MPa	Tensile strength, MPa	Fracture strength, MPa	% el
0FA, 0B	Salt spray	4	537±18	702±17	718±13	38±1
20FA	Salt spray	4	571±56	738±71	680±47	40±4
B	Salt spray	4	509±61	662±61	631±62	34±1
20FA+B	Salt spray	4	546±43	706±47	666±47	34±1
0FA, 0B	OCP	1	540±36	699±40	699±60	41±2
20FA	OCP	1	551±38	713±55	713±54	44±2
B	OCP	1	552±47	714±51	714±37	45±2

Table 2. Effect of time on the tensile properties of 304L rebars prior to and after salt spray testing (4 m) and OCP testing (1 m).

Inhibitor	Test	Duration, m	0.2% yield strength, MPa	Tensile strength, MPa	Fracture strength, MPa	% el
0FA, 0B	Salt spray	0	597±15	780±28	751±40	44±1
0FA, 0B	Salt spray	4	573±11	739±14	718±13	37±1
20FA	Salt spray	0	586±15	754±16	707±9	43±1
20FA	Salt spray	4	571±56	738±71	680±47	40±4
B	Salt spray	0	583±44	751±51	717±40	43±1
B	Salt spray	4	509±61	662±61	631±62	34±1
20FA+B	Salt spray	0	554±36	709±32	678±33	42±2
20FA+B	Salt spray	4	546±43	706±47	666±47	36±1
0FA, 0B	OCP	0	572±25	747±36	712±42	43±1
0FA, 0B	OCP	1	540±36	699±40	699±60	41±2
20FA	OCP	0	543±59	680±50	643±45	40±2
20FA	OCP	1	551±38	713±55	713±54	44±2
B	OCP	0	543±50	680±50	643±45	40±2
B	OCP	1	552±47	714±51	714±37	45±2
20FA+B	OCP	0	554±36	709±32	678±33	42±2

Table 2 shows that after 4 m of salt spraying, 304L reinforcement presented a slight decrease in the strength values, though within standard deviation. The drops in the strength values were larger in the case of single use of Inhibitor B than the drops in the cases of 20FA and 20FA+Inhibitor B. Small decreases % elongation (with or without inhibitors) were also observed. The drops in the % elongation were statistically significant in all cases but 20 wt.% FA. The above observations are in compatibility with Lee et al. [40] and Apostolopoulos et al. [41], who observed that the corrosion effect on the elongation of concrete steel rebar is more intensive compared to its yield strength and tensile strength. The decrease in elongation has been associated with embrittleness due to pitting, as microcracking initiates at pits [40].

The largest drop in %el after salt spraying, occurred when FA was absent from the concrete (cases 0FA-0B, 0FA-B). The smallest drop in %el occurred in the cases of 20FA-0B (especially) and 20FA-B. This observation is consistent with the decrease in the concrete porosity after four months of salt spraying, realized by the addition of FA in the concrete (either alone or combined with inhibitor B) [30]. Previous authors' work has demonstrated that high Ca-FA as a concrete additive boosts the pozzolanic reactions in the concrete through the formation of Ca-Al-Fe-silicate hydroxides that are more stable than $Ca(OH)_2$ [27]. As the curing time increases with salt spraying, more

hydration products are formed that can protect by simply reducing the concrete porosity (e.g. just forming $Ca(OH)_2$ [42]) or by both reducing the concrete porosity and forming stable compounds.

Despite the small drop in %el. after salt spraying, Fig. 5 does not reveal any significant differences in the fracture modes of 304L rebars before and after salt spraying for 4 m. The rebars have been removed from concrete cubes containing 25 wt.% FA and being coated by inhibitor B. The low magnification images (for a more objective observation) reveal that the ductile mode of fracture has been retained after 4 m of salt spraying. The fracture surfaces are characterized by numerous dimples, a result of the stretching and thinning of the material during deformation [43]. Elongated dimples have been formed by microvoid coalescence.

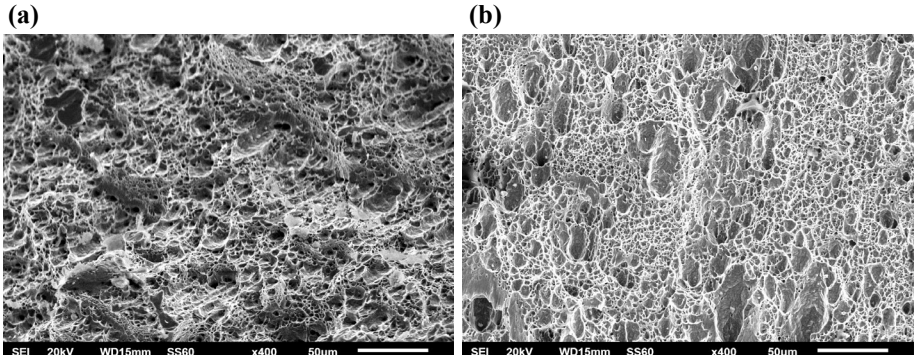

Fig. 5. Fracture surfaces of 304L concrete rebars after tensile testing (a) before and (b) after 4 m of salt spraying. The rebars have been removed from concrete cubes containing 25 wt.% fly ash and coated by inhibitor B.

Table 2 shows that after 1 m in OC state in the AR simulating electrolyte, the strength values of 304L rebars in the absence of inhibitors and FA, showed small decreases, though within standard deviation. The tensile properties of 304L, in the sole presence of 20 wt.% FA concrete additive or Inhibitor B, showed a statistical but consistent increase. In the case of combined "20 wt.% FA + Inhibitor B", the strength values remained practically unchanged. All the same, in all cases, % el. has increased.

In the case of FA addition, previous authors' work has shown that high Ca-FA as a concrete additive has led to formation of new phases, such as aluminum sulfate/sulfite hydrates that supersulfate the concrete, inhibiting its reaction with the sulfate ions of acid rain to form expansive compounds that may lead to concrete cracking [27].

In the case of Inhibitor B, one or more of the mechanisms reported in the Introduction can be considered responsible for this slight improvement in the tensile properties. For instance, Fig. 6 shows that the presence of Inhibitors B and C, induce small increases in the pH of the electrolyte compared to the sole addition of 20 wt.% FA. Although this result is not conclusive, it indicates that Inhibitors B and C can stabilize the pH within the pit's immediate environment. Other potential beneficial mechanisms of the inhibitors will be discussed in conjunction with the SEM/EDX examination in the next section.

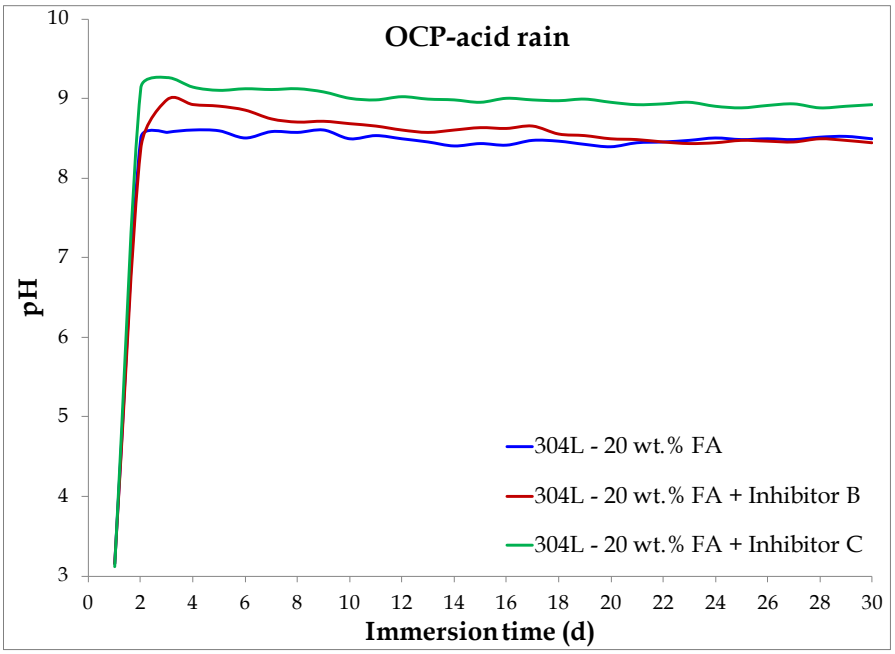

Fig. 6. Variation of pH in the acid rain-simulating electrolyte during OCP testing of concrete cubes containing 20 wt.% fly ash with or without the addition of Inhibitors B and C

3.3 Microstructural inspection of the corroded rebars

Fig. 7 and Fig. 8 illustrate the SEM cross-sectional micrographs of 304L rebars extracted from concrete cubes the after salt spray test and OCP test, respectively. The concrete cubes contained (a) 20 wt.% FA, (b) Inhibitor B, and (c) Inhibitor C. At this low magnification, an objective overview is provided, showing fine surface states without any signs of corrosion beneath the surfaces.

The excellent performance of the 304L reinforcement under both salt fog and acid rain conditions is evident in Figs. 9 and 10, which manifest the formation of compact and dense CaO-rich surface films containing Si, Al and Mg. The participation of FA in the surface film cannot be discerned, as Ca, Si, Al and Mg are also constituent elements of Portland cement and siliceous sand. However, previous publications concerning electrolytes simulating concrete pore solutions that contained FA and were exposed to saline and acid rain environments, have proven the participation of FA in the surface film and its interaction with the active ions of the electrolytes [7, 24-30]. Furthermore, it is highly likely that the detection of Mg in the surface films shown in Figs. 9 and 10, is owing to the participation of FA in the surface film, as MgO was not detected in the XRD pattern of the concrete used in this study [27].

The participation of Inhibitors B and C in the surface films also cannot be confirmed. However, a hint of nitrogen enrichment on the steel surface can be discerned in Fig. 10a. It should also be noted that nitrogen was automatically detected by the EDX detector. The above observations are in compatibility with Dong et al. [44], who suggested

that inhibitors containing amino groups are more likely to be adsorbed on passive films rather than bare metals, through oxygen vacancies within the passive films that attract the electronegative lone-pair electrons of the nitrogen atom.

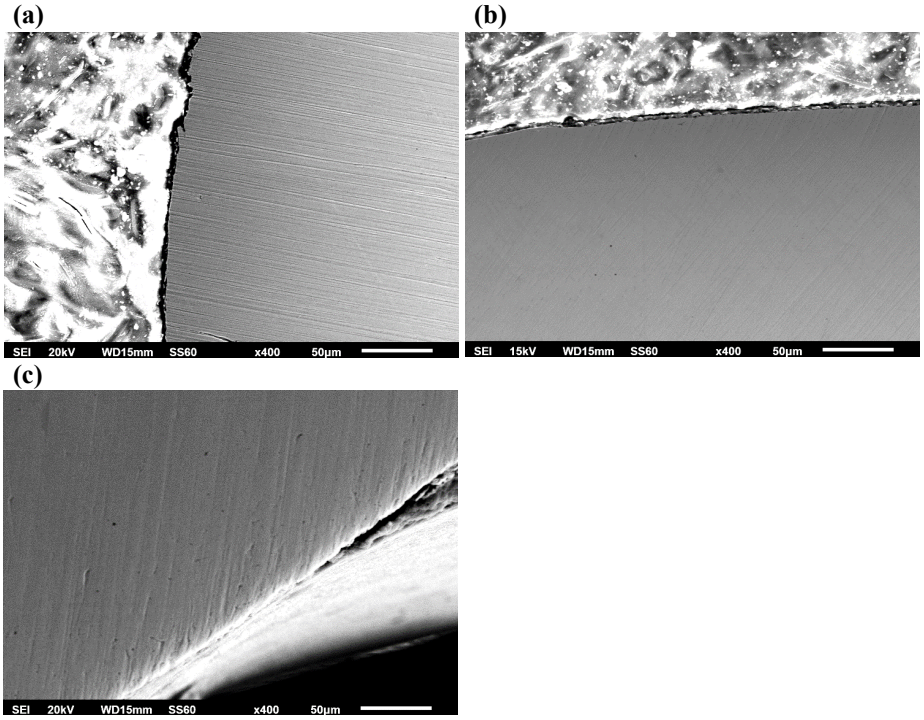

Fig. 7. SEM images (cross-sections) of 304L rebars removed from concrete cubes containing (a) 20 wt.% FA, (b) Inhibitor B, (c) Inhibitor C, after salt spraying for 4 m

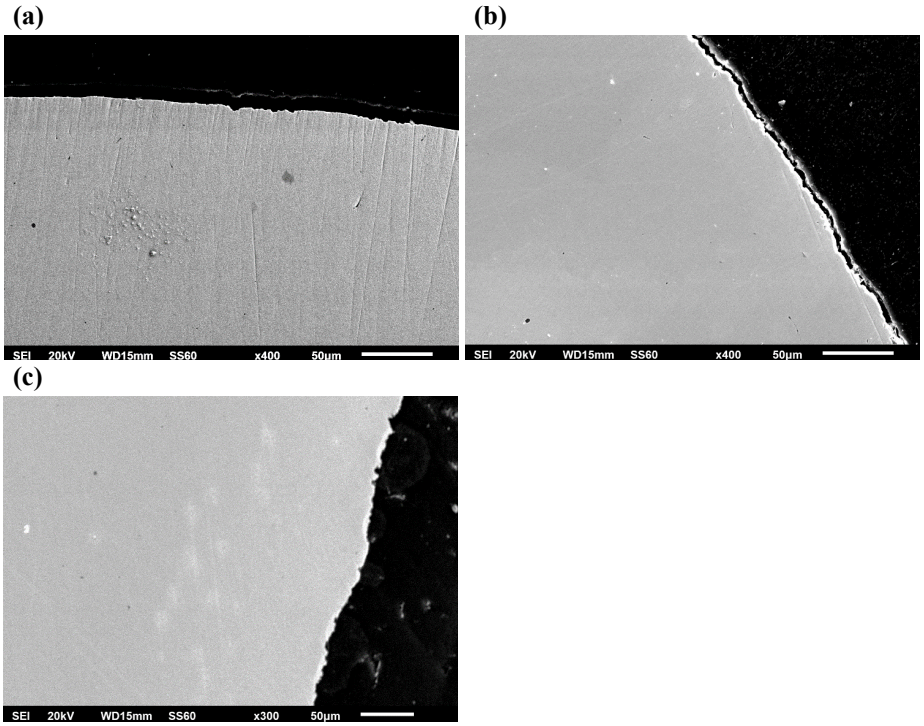

Fig. 8. SEM images (cross-sections) of 304L rebars removed from concrete cubes containing (a) 20 wt.% FA, (b) Inhibitor B, (c) Inhibitor C, after OCP testing for 1 m.

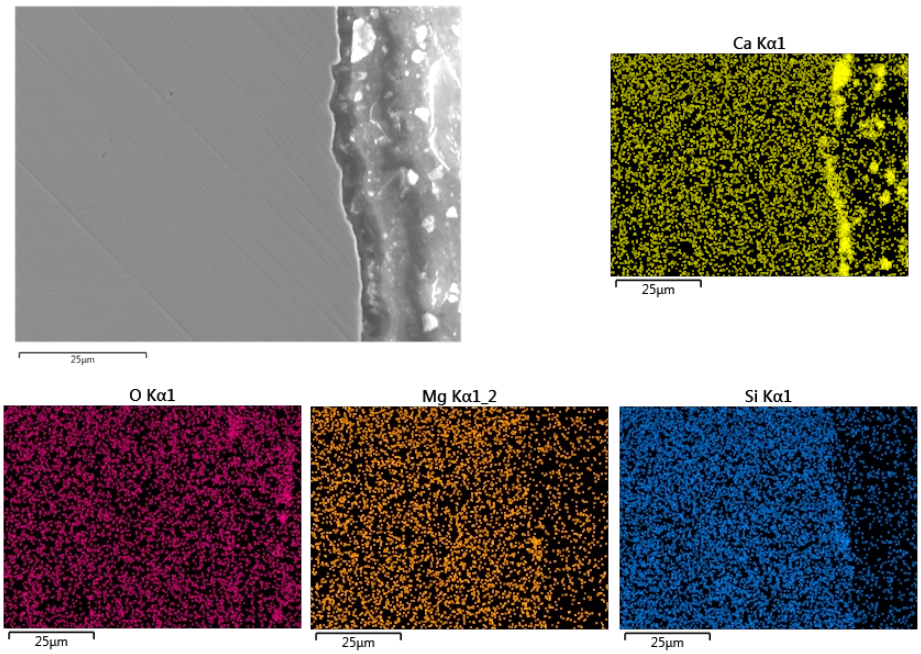

Fig. 9. SEM images (cross-sections) of 304L rebar after salt spraying for 4 m (20 wt.% FA + Inhibitor B) and EDX elemental maps.

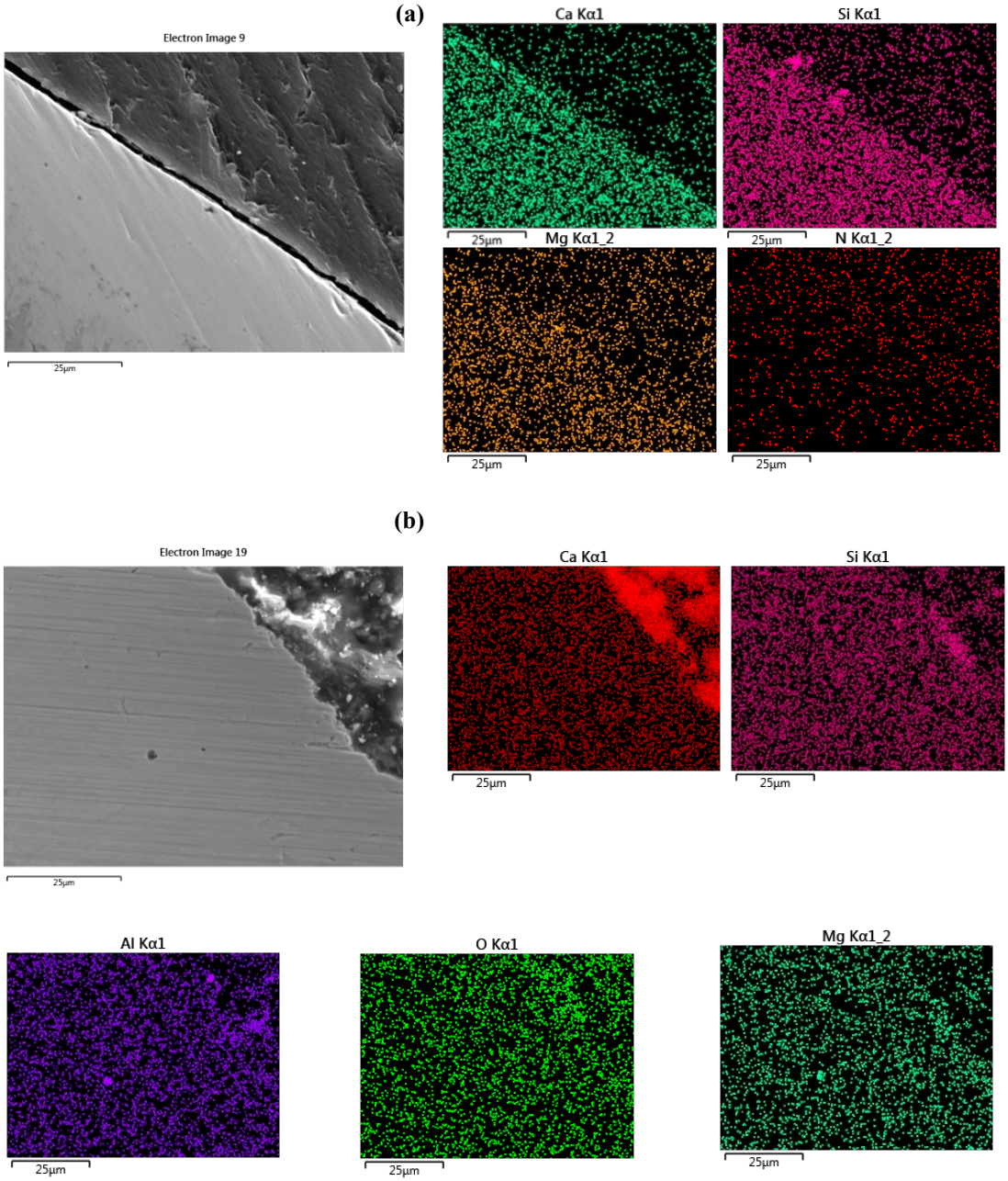

Fig. 10. SEM images (cross-sections) of 304L rebars after OCP testing for 1 m. (a) 20 wt.% FA + Inhibitor B, (b) 20 wt.% FA + Inhibitor C, and corresponding EDX elemental maps.

4 Conclusions

1. For 304L stainless steel corrugated rebars embedded in concrete cubes containing fly ash (FA), Inhibitor B, Inhibitor C, as well as combinations of FA with Inhibitor B, and immersed in an acid rain (AR) simulating solution for 30 d during an Open Circuit Potential (OCP) test, there is more than a 90% probability that corrosion did not occur.
2. Both Inhibitors B and C improved the corrosion performance of 304L reinforced concrete cubes in AR in the absence of FA. However, when combined with FA, both inhibitors negated the inhibiting effect of FA and vice versa.
3. The 20 wt.% FA content had a beneficial effect on the corrosion behavior of 304L rebars compared to 0 wt.% FA.
4. After an OCP test for 30 d in an AR-simulating electrolyte and after a salt spray test for 4 m (5 wt.% NaCl, 35°C), the presence of 20 wt.% FA combined or not with Inhibitor B did not have any statistically significant effect on the tensile properties of 304L rebars.
5. After 4 m of salt spraying, the 304L reinforcement showed a slight decrease in the strength values, both in the absence and presence of any inhibitors, though within standard deviation. Small decreases in the percent elongation (with or without inhibitors) were also observed. The decreases in percent elongation were statistically significant in all cases except for 20 wt.% FA.
6. After 1 m of OCP testing in the AR simulating electrolyte, the strength values of 304L rebars in the absence of inhibitors and FA, showed small decreases, though within standard deviation. The tensile properties of 304L rebars, in the presence of 20 wt.% FA or Inhibitor B, showed a statistically insignificant but consistent increase. In the case of combined 20 wt.% FA + Inhibitor B, the strength values remained practically unchanged. In all cases except for the absence of any Inhibitors, % elongation increased.
7. Macroscopic examination revealed that the concrete cubes reinforced with 304L rebars, with or without the addition of fly ash and Inhibitors B and C, remained free of corrosion indications after the salt spray and OCP tests. Similarly, cross-sections of the 304L reinforcements did not present any signs of corrosion.
8. Longer OCP testing of reinforced concrete in AR-simulating electrolyte is needed to fully explore the potential of Inhibitor C.

References

1. Wang, X., Nguyen, M., Stewart, M.G., Syme, M., Leitch, A.: Analysis of Climate Change Impacts on the Deterioration of Concrete Infrastructure. Part 1: Mechanisms, Practices, Modelling and Simulations - A Review. CSIRO, Canberra, Australia (2010).
2. Yalciner, H., Marar, K.: Experimental study on the bond strength of different geometries of corroded and uncorroded reinforcement bars. Journal of Materials in Civil Engineering 29(7), 05017002-1–05017002-10 (2017) https://doi.org/10.1061/(ASCE)MT.1943-5533.0001914.

3. Maia, L., Alves, S.: Low durability of concrete elements due to steel corrosion - cases wherein the steel reinforcing bars acted as an internal clock bomb. Procedia Structural Integrity 5, 139–146 (2017) https://doi.org/10.1016/j.prostr.2017.07.082.
4. Li, Z., Jin, Z., Zhao, T., Wang, P., Zhao, L., Xiong C., Kang, Y.: Service life prediction of reinforced concrete in a sea-crossing railway bridge in Jiaozhou bay: A case study. Applied Sciences 9(7), 1–18 (2019) https://doi.org/10.3390/app9173570.
5. Kepler, J.L., Darwin, D., Locke C.E., Jr.: Evaluation of corrosion protection methods for reinforced concrete highway structures. Structural Engineering and Engineering Materials SM Report No. 58, University of Kansas Center for Research, Inc. Lawrence, Kansas (2000) https://hdl.handle.net/1808/20463.
6. Head, M., Ashby-Bey, E., Edmonds, K., Efe, S., Grose, S., Mason, I.: Stainless steel prestressing strands and bars for use in prestressed concrete girders and slabs. MD-13-SP309B4G Report, Morgan State University, Department of Civil Engineering and Maryland State Highway Administration, Office of Policy & Research (2015).
7. Tsouli, S., Lekatou, A.G. Kleftakis, S.: The effect of fly ash on the corrosion performance of AISI 316L stainless steel reinforced concrete for application to restoration works of ancient monuments. In: Koui, M., Zezza, F., Kouis, D. (eds.) 10th International Symposium on the Conservation of Monuments in the Mediterranean Basin (MONUBASIN), pp. 171–178. Springer, Cham, Switzerland (2018) https://doi.org/10.1007/978-3-319-78093-1_17.
8. Barbhuiya, S., Kumala, D.: Behaviour of a sustainable concrete in acidic environment. Sustainability 9, 1–13 (2017) https://doi.org/10.3390/su9091556.
9. Yu, Z., Ye, G.: The pore structure of cement paste blended with fly ash. Construction and Building Materials 45, 30–35 (2013) https://doi.org/10.1016/j.conbuildmat.2013.04.012.
10. Ghafoori, N., Najimi, M., Diawara, H., Islam, M.S.: Effects of class F fly ash on sulfate resistance of Type V Portland cement concretes under continuous and interrupted sulfate exposures. Construction and Building Materials 78, 85–91 (2015) https://doi.org/10.1016/j.conbuildmat.2015.01.004.
11. Söylev, T.A., Richardson, M.G.: Corrosion inhibitors for steel in concrete: State-of-the-art report. Construction and Building Materials 22(4), 609–622 (2008) https://doi.org/10.1016/j.conbuildmat.2006.10.013.
12. Lee, H.S., Saraswathy, V., Kwon, S.-J., Karthick, S: Corrosion inhibitors for reinforced concrete: A review. In: Aliofkhazraei, M. (ed.), Corrosion inhibitors, principles and recent applications, Chapter 5, IntechOpen, pp. 95–120 (2018) https://doi.org/10.5772/intechopen.72572.
13. Ormellese, M., Bolzoni, F., Goidanich, S., Pedeferri, M.P., Brenna, A.: Corrosion inhibitors in reinforced concrete structures. Part 3 - migration of inhibitors into concrete. Corrosion Engineering, Science and Technology 46(4), 334–339 (2011) https://doi.org/10.1179/174327809X419230.
14. Batis, G., Pantazopoulou, P., Routoulas, A.: Corrosion protection investigation of reinforcement by inorganic coating in the presence of alkanolamine-based inhibitor. Cement and Concrete Composites 25(3), 371–377 (2003) https://doi.org/10.1016/S0958-9465(02)00061-6.
15. Zomorodian, A., Behnood, A.: Review of corrosion inhibitors in reinforced concrete: Conventional and green materials. Buildings 13, 1–20 (2013) https://doi.org/10.3390/buildings13051170.
16. Shi, W., Wang, T.-Z., Dong, Z.-H., & Guo, X.P.: Application of wire beam electrode technique to investigate the migrating behavior of corrosion inhibitors in mortar.

Construction and Building Materials 134, 167–175 (2017) https://doi.org/10.1016/j.conbuildmat.2016.12.036.
17. Elsener, B., Angst, U.: Corrosion inhibitors for reinforced concrete, In: Aïtcin, P.C., Flatt, R.J. (eds.), Science and Technology of Concrete Admixtures, Chapter 14, pp. 321–339, Elsevier (2016).
18. Rawat, A., Karade, S.R., Thapliyal, P.C.: Mechanism of inhibitors in control of corrosion of steel in concrete. Materials Today: Proceedings, 1–7 (2023) https://doi.org/10.1016/j.matpr.2023.06.210.
19. Fouda, A.S., Elewady, G.Y., Shalabi, K., Abd El-Aziz, H.K.: Alcamines as corrosion inhibitors for reinforced steel and their effect on cement based materials and mortar performance. RSC Advances 46(5), 36957–36968 (2015) DOI https://doi.org/10.1039/C5RA00717H.
20. Banks L., Hosgood H.: Inhibiting corrosion in reinforced concrete. UK Patent No. WO/1987/006958 (1997).
21. Boyle, B.: A look at developments in vapor phase corrosion inhibitors. Metal Finishing 102(5), 37–41 (2004) https://doi.org/10.1016/S0026-0576(04)90182-1.
22. Bastidas, D.M., Cano, E., Mora, E.M.: Volatile corrosion inhibitors: a review. Anti-Corrosion Methods and Materials 52, 71–77 (2005) https://doi.org/10.1108/00035590510584771.
23. Sherif, El-Sayed M.: The role of corrosion inhibitors in protecting metallic structures against corrosion in harsh environment. In: Fanun, M. (ed.), The role of colloidal systems in environmental protection, Chapter 20, pp. 509–526, Elsevier (2014) https://doi.org/10.1016/B978-0-444-63283-8.00020-X.
24. Tsouli, S., Lekatou, A.G., Kleftakis, S., Matikas, T.E., Dalla, P.T.: Corrosion behavior of 304L stainless steel concrete reinforcement in acid rain using fly ash as corrosion inhibitor. Procedia Structural Integrity 10, 41–48 (2018) https://doi.org/10.1016/j.prostr.2018.09.007.
25. Tsouli, S., Lekatou, A.G., Nikolaidis, C., Kleftakis, S.: Corrosion and tensile behavior of 316L stainless steel concrete reinforcement in harsh environments containing a corrosion inhibitor. Procedia Structural Integrity 17, 268–275 (2019) https://doi.org/10.1016/j.prostr.2019.08.036.
26. Lekatou, A.G., Tsouli, S., Nikolaidis, C., Kleftakis, S., Tragazikis, I.K., Matikas, T.E.: Effect of fly ash on the corrosion performance and structural integrity of stainless steel concrete rebars in acid rain and saline environments. Frattura ed Integrità Strutturale 50, 423–437 (2019) https://doi.org/10.3221/IGF-ESIS.50.36.
27. Lekatou, A.G., Tsouli, S.: Cyclic polarization of corrugated austenitic stainless steel rebars in acid rain: Effect of fly ash, pH and steel type. Corrosion and Materials Degradation 3(1), 75–100 (2022) https://doi.org/10.3390/cmd3010005.
28. Tsouli, S., Lekatou, A.G., Siozos, E., Kleftakis, S.: Accelerated corrosion performance of AISI 316L stainless steel concrete reinforcement used in restoration works of ancient monuments. MATEC Web of Conferences 188(03003), 1–8 (2018) https://doi.org/10.1051/matecconf/201818803003.
29. Tsouli, S., Lekatou, A.G., Goutzos, P., Kleftakis, S.: Effect of fly ash on the electrochemical performance of 316L stainless steel concrete reinforcement in saline environments attacked by acid rain. MATEC Web of Conferences 349(02015), 1–8 (2021) https://doi.org/10.1051/matecconf/202134902015.
30. Tsouli, S., Lekatou, A.G., Kleftakis, S., Gkoutzos, P., Tragazikis, I.K., Matikas, T.E. Combined corrosion inhibitors and mechanical properties of concrete embedded steel

(AISI 316L) during accelerated saline corrosion test. Materials Proceedings 5(1), 1–7 (2021) https://doi.org/10.3390/materproc2021005072.
31. Fu, Y., Ding, J., Beaudoin, J.J.: Expansion of Portland cement mortar due to internal sulfate attack. Cement and Concrete Research 27(9), 1299–1306 (1997) https://doi.org/10.1016/S0008-8846(97)00133-6.
32. Martín, D., Seyhan, E.: Protection of reinforced concrete steel exposed to a marine environment - A preliminary onsite study of the performance of a new generation of surface-applied corrosion inhibitors. Corrosion and Materials Degradation 3(4), 628–645 (2022) https://doi.org/10.3390/cmd3040034.
33. Kostakis, G.: Characterization of the fly ashes from the lignite burning power plants of northern Greece based on their quantitative mineralogical composition. Journal of Hazardous Materials 166(2-3), 972–977 (2009) https://doi.org/10.1016/j.jhazmat.2008.12.007.
34. Filippidis, A., Georgakopoulos, A.: Mineralogical and chemical investigation of fly ash from the Main and Northern lignite fields in Ptolemais, Greece. Fuel 71(4), 373–376 (1992).
35. MuCis-mia-200, Technical datasheet, https://sintecno.gr/wp-content/uploads/2023/03/MuCis%C2%AE-mia-200.pdf, last accessed 2024/10/05.
36. QED Margel-580 VPi: Vapour phase Migrating Corrosion Inhibitor in capsule form by Sintecno - Prevention & protection of reinforced concrete structures, https://sintecno.gr/en/diacheomenos-anastoleas-diavrosis-aerias-drasis-se-morfi-kapsoylas-apo-tin-sintecno-prolipsi-amp-prostasia-kataskeyon-oplismenoy-skyrodematos, last accessed 2024/10/05.
37. Ragab, Kh.A., Abdel-Karim, R., Farag, S., El-Raghy, S.M., Ahmed, H.A.: Influence of SiC, SiO_2 and graphite on corrosive wear of bronze composites subjected to acid rain. Tribology International 43(3), 594–601 (2010) https://doi.org/10.1016/j.triboint.2009.09.008.
38. Pérez-Quiroz, J.T., Terán, J., Herrera, M.J., Martínez M., Genescá, J.: Assessment of stainless steel reinforcement for concrete structures rehabilitation. Journal of Constructional Steel Research 64(11), 1317–1324 (2008) https://doi.org/10.1016/j.jcsr.2008.07.024.
39. ASTM International: ASTM C876- 15 Corrosion potentials of uncoated reinforcing steel in concrete, USA (2015).
40. Lee, H., Cho, Y.: Evaluation of the mechanical properties of steel reinforcement embedded in concrete specimen as a function of the degree of reinforcement corrosion. International Journal of Fracture 157(1-2), 81–88 (2009) https://doi.org/10.1007/s10704-009-9334-7
41. Apostolopoulos, Ch.A., Demis, S., Papadakis, V.G.: Chloride-induced corrosion of steel reinforcement - Mechanical performance and pit depth analysis. Construction and Building Materials 38, 139–146 (2013) https://doi.org/10.1016/j.conbuildmat.2012.07.087.
42. Papadakis, V.G.: Effect of fly ash on Portland cement systems: Part II. High-calcium fly ash. Cement and Concrete Research 30(10), 1647–1654 (2000) https://doi.org/10.1016/S0008-8846(00)00388-4.
43. Kerlins, V.: Modes of fracture. In: Schroeder, C.J., Parrington, R.J., Maciejewski, J.O., Lane, J.L. (eds.), ASM Metals Handbook, Volume 12: Fractography, pp. 12-71, ASM International (1987).
44. Dong, Z.H., Shi, W., Zhang, G.A., Guo, X.P.: The role of inhibitors on the repassivation of pitting corrosion of carbon steel in synthetic carbonated concrete pore solution.

Electrochimica Acta 56(17), 5890–5897 (2011)
https://doi.org/10.1016/j.electacta.2011.04.120.

Energy

Integrated Raw Material Approach to Sustainable Geothermal Energy Production: Harnessing CO_2 for Enhanced Resource Utilization

Sofianos Panagiotis Fotias[1,*], Spyros Bellas[2] and Vassilis Gaganis[1,2]

[1]School of Mining and Metallurgical Engineering, National Technical University of Athens, Athens 157 73, Greece
[2]Institute of Geoenergy, Foundation for Research and Technology (IG/FORTH), Chania, 73100, Greece
sfotias@metal.ntua.gr

Abstract. CPG (CO_2 Plume Geothermal) has recently emerged as a promising technology that combines the extraction of geothermal energy with underground CO_2 storage, thus aligning with the energy objectives of Greece according to the National Energy and Climate Plan. The concept of CPG revolves around treating CO_2 as a raw material, recycling it through continuous injection and production to and from a subsurface reservoir, taking advantage of the discrete plume that forms on top of the subsurface formation. As CO_2 is injected, it contacts the hot formation and captures thermal energy which is eventually transferred from the reservoir to the surface facilities where it gets exploited in thermal plants. The CO_2 flow system is closed thus offering the permanent storage option. Despite the favorable aspects of this technology, such as reduced energy requirements for fluid recycling, improved mobility and a smaller environmental footprint, there are also challenges that require careful consideration. CO_2 is less viscous and lighter than resident brine, thus fingering effects are more prominent than sweeping displacement. As a result, CO_2 breakthrough appears soon, even at wells designed for pressure maintenance through brine extraction. This highlights the need for a thorough study of the geological field and reservoir, along with the optimization of the production system's design. This study presents a comprehensive analysis of a geothermal reservoir and covers an optimized dynamic simulation for a combined geothermal, CO_2 storage and CPG system. Results demonstrate that a sustainable carbon-negative energy-producing power plant is possible. Such systems can also be implemented in already existing industries, providing a source of energy for secondary operations while also positioning the operators more strongly in the carbon tax market.

Keywords: CO_2 Plume Geothermal, Reservoir simulator, CO_2 injection

1 Introduction

The incessant rise in carbon dioxide (CO_2) emissions, particularly at the industrial

level, has become a pressing global concern, propelling the exploration of innovative strategies for mitigation. Industries, traditionally significant contributors to greenhouse gas emissions, are now compelled to reassess their environmental impact. Carbon Capture and Utilization (CCU) [1] has emerged as a beacon in this pursuit, providing a dual-pronged solution. The capture element involves deploying advanced technologies to intercept CO_2 emissions at their source, curbing their release into the atmosphere and thereby mitigating climate change. This approach not only aligns with environmental goals but also positions industries as proactive participants in the global transition toward sustainable practices.

As the emphasis on reducing carbon footprints intensifies, the concept of CCU extends beyond emission handling, delving into the realm of CO_2 utilization as a raw material [2]. Captured CO_2 is transformed from a perceived environmental liability into a valuable resource. Chemical utilization techniques offer a diverse array of possibilities, ranging from the production of synthetic fuels and chemicals to carbonating concrete. By integrating CO2 into various industrial processes, CCU not only minimizes environmental impact but also drives innovation, paving the way for a more sustainable and circular economy. This chemical utilization aspect of CCU represents a transformative step toward turning emissions into assets, fostering economic growth while simultaneously mitigating climate change [3]. As a result capture and utilization (Figure 1) allow CO_2 to be considered as a raw material rather than as an environmentally detrimental waste product.

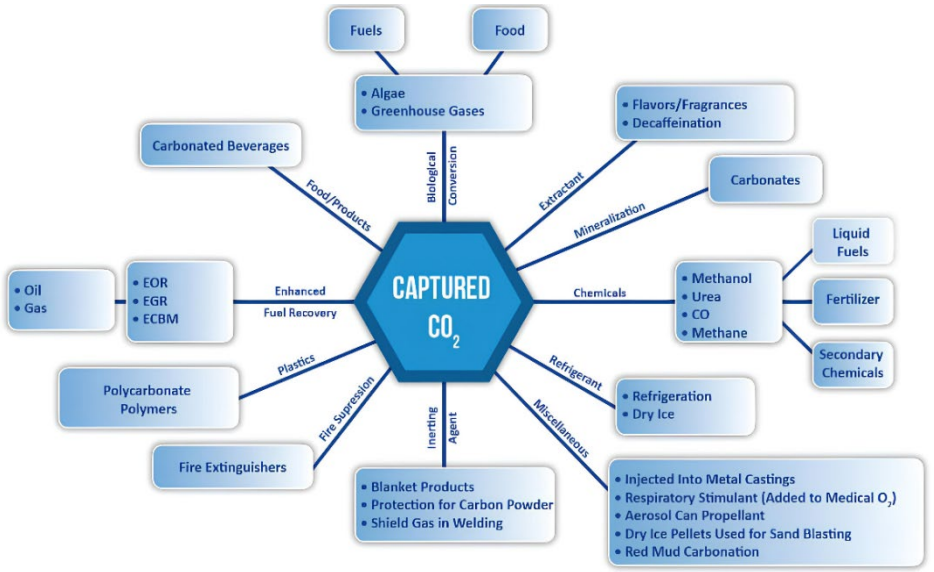

Figure 1 Classification of CO_2 utilisation options (Provided by the US Department of Energy's National Energy Technology Laboratory)

Fig. 1. CO_2 utilization
[https://www.linkedin.com/pulse/carbon-capture-utilization-conference-ccon4-final-bookings-laverty/]

In the context of sustainable energy practices, CO2 Plume Geothermal (CPG) emerges as a pioneering method that seamlessly intertwines carbon capture with the

efficient utilization of Earth's geothermal resources by utilizing CO2 as the processing material. Resources are defined as naturally occurring substances or phenomena that can be used for economic gain. When it comes to geothermal energy, resources refer to the geothermal heat available in the Earth's crust that can be harnessed for power generation.

Usually as we move from the earth's surface towards the core, temperature increases as a result of heat transfer from the much hotter interior of it to the outer layers, a parameter named geothermal gradient. While the average values of it are around 3 degrees per km, at specific areas, the geothermal gradient is much higher, enabling for utilization of it as geothermal energy in relatively medium to deep depths. Geothermal power plants, in their classic framework, harness the temperature gradient between the Earth's heated subsurface rock and the cooler surface to generate electricity. These systems transfer thermal energy from below the ground to the surface using a working fluid, which then undergoes a partial conversion of its thermal energy to electricity in a power plant. The cooled working fluid is usually reinjected into a subsurface reservoir to maintain hydraulic sustainability. Conventional geothermal energy technologies use hot brine as the working fluid. Subsequently, geothermal power plants are usually constructed in regions with active tectonic or volcanic activity, where the temperature gradient is exceptionally high [4]. These areas are referred to as high enthalpy fields and are exploited for power generation. In Greece, for instance, most of them are directly linked to the well-known subduction of the African lithospheric plate beneath the Aegean microplate and the subsequent formation of the South Aegean Active Volcanic Arc (SAAVA). Geothermal fields associated with the volcanic activity are found in the Cyclades group of Islands (such as the established Milos and Nisyros fields) and in the broader vicinity of Lesvos Island (the former location of the arc that has now shifted southwards) [5]. Additionally, within the same region, shallow-depth, low-temperature geothermal fields also exist, as seen in the case of Santorini Island, classified as "probable". In the context of geothermal energy, "probable" refers to areas where geothermal activity is suspected but not yet fully confirmed or exploited. Additionally, in northern continental Greece, particularly within the sedimentary basins of Strymon in the Deltas of Evros and Nestos Rivers and in the Island of Samothrace, low, medium and high enthalpy resources, exploitable down to depths of 2 to 3km have been reported [6]. The latter potential fields located in the wider area of Alexandroupolis city, may very well be suitable for the dual-purpose of CPG, since they are deep geothermal energy carriers near highly populated cities that need this kind of green-generated power. Nevertheless, these unique thermal resources are limited in terms of both size and location, necessitating the development of innovative technologies to tap into the abundant thermal energy within the Earth's crust.

Enhanced Geothermal Systems (EGS) have been proposed as a way to extend the reach of geothermal resources by artificially creating reservoirs in regions lacking suitable conditions [7]. These systems typically entail injecting cold pressurized water to hydraulically fracture a subsurface formation. The injected water absorbs heat and is then brought back to the surface.

As opposed to conventional geothermal energy extraction, which relies on water as a heat transfer medium, CPG leverages captured CO_2 as the working fluid. This not only

addresses the need for emission reduction but also enhances the efficiency of geothermal energy extraction. By utilizing CO_2 in this geothermal context, the technology demonstrates its versatility in contributing to both environmental stewardship and sustainable energy generation. The integration of CPG represents a noteworthy stride toward achieving a balance between carbon capture and geothermal energy utilization. Apart from its environmental footprint, CO_2 has been suggested as an alternative working fluid thanks to it being abundant and possessing non-flammable properties [8]. CPG systems utilize CO_2 as the primary subsurface working fluid in naturally permeable sedimentary basins or EGS, creating a large-scale CO_2 plume. Additionally, a buoyancy-driven thermosiphon can be established by exploiting variations in CO_2 density between injection and production wells. This approach eliminates the need for costly pumping, which is commonly associated with conventional hydrothermal setups.

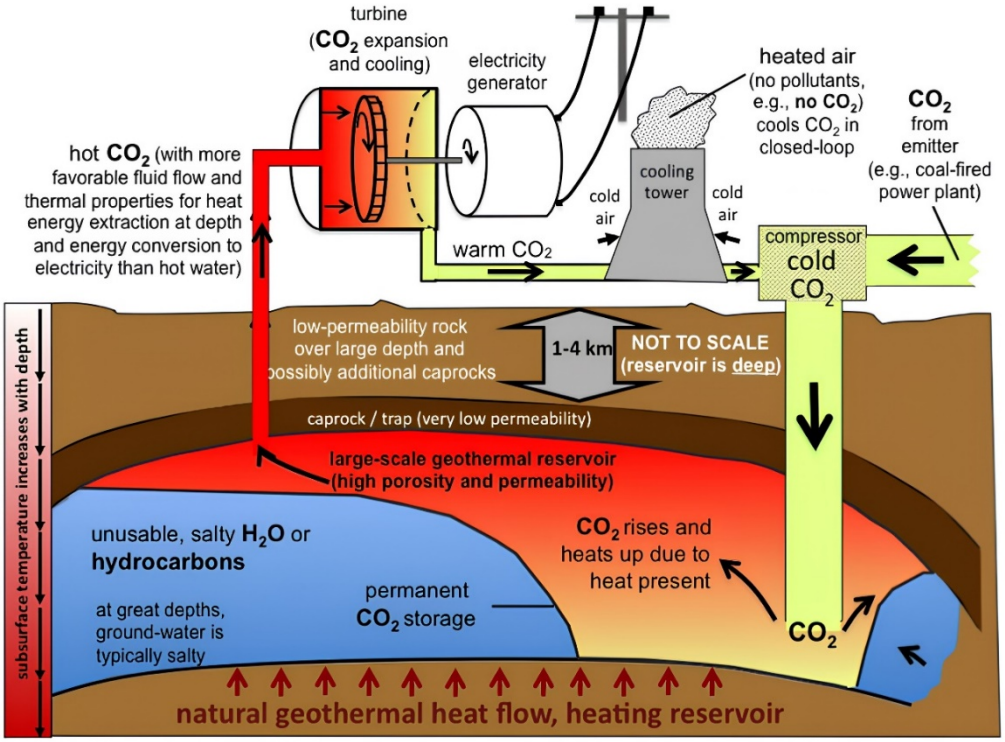

Fig. 2. CPG system
[https://www.thinkgeoenergy.com/cpg-systems-storing-co2-for-geothermal-energy-production/]

Sedimentary basins suitable for CPG systems are found worldwide [9]. These basins often consist of aquifers with excessive salinity, making them unsuitable for drinking or industrial purposes. They may also include partially depleted oil and gas fields utilized for Enhanced Oil Recovery (EOR) operations [10]. In a CPG system, the buoyant CO_2 needs to be confined by very low-permeability or fully impervious caprock beds covering the permeable reservoirs. CPG systems can be seamlessly integrated with CO_2

Capture and Storage (CCS) sites [11], [12], [13], enabling the simultaneous generation of electricity and heat while securely sequestering CO_2. This integration ensures reservoir stability by mitigating overpressurization concerns associated with standalone CCS operations, which could trigger human-induced seismicity and CO_2 leakage. Furthermore, a combined CPG-CCS system can enhance the economic viability of CCS, thereby supporting global initiatives to address climate change. However, challenges associated with using CO_2, such as its reduced density at reservoir conditions and potential environmental impact in case of leakage, require further research and development. To address the risks linked with employing CO_2, CPG (Figure 2) energy systems have been recently introduced and developed [14], [15], [16].

A meticulously designed CPG development plan is required for industries characterized by substantial CO_2 emissions, reminiscent of operational dynamics found in cement plants, refineries, or offshore oil rigs. At the heart of the plan lies the integration of a carbon-negative energy-producing subsystem, leveraging advanced carbon capture technologies to convert emissions into valuable resources while simultaneously generating clean energy. For example, within the cement industry, captured CO_2 [17] is harnessed in chemical processes like synthetic fuel production or concrete carbonation, not only minimizing the industry's environmental footprint but also fostering a circular economy. Offshore oil rigs, benefit from reduced carbon tax liabilities by securely storing captured emissions underground. The stored CO_2 is repurposed for Enhanced Oil Recovery (EOR) or other industrial processes, creating an additional revenue stream and contributing to a more sustainable energy landscape. This strategic approach seamlessly applies to energy-intensive manufacturing sectors such as steel production [18], where advanced carbon capture technology enables the creation of valuable chemicals or the generation of green hydrogen. This contributes significantly to the broader shift towards sustainable energy sources. Moreover, the integration of a carbon-negative subsystem not only tackles environmental issues but also boosts the economic feasibility of these operations. Through the active production of clean energy, this approach not only reduces emissions but also diminishes dependence on conventional energy sources, thereby establishing a more robust and eco-friendly energy provision for these industries. Crucially, the carbon-negative subsystem positions these industries strategically within the carbon tax market. By proactively managing emissions, generating clean energy, and offering storage services to other sectors, these industries not only reduce their carbon tax liabilities but also capitalize on the burgeoning carbon market, creating new revenue streams. This cross-industry utilization of captured CO_2 exemplifies a holistic strategy, transforming emissions into valuable resources, producing clean energy, and positioning industries as active contributors to global climate change mitigation. By embracing environmental responsibility and strategically placing themselves in the carbon tax market, these industries not only ensure regulatory compliance but also foster sustainable and circular industrial practices for a greener and more resilient future.

In this work, a joint CPG-CCS plan is designed, in continuation to our previous work [19], to showcase its operational stability as an energy producing subsystem of a greater industrial plant. The basis of the operation is a deep anisotropic saline aquifer that is expansive, closed and inclined while being fully saturated with brine. The elevated temperature of the aquifer exceeds typical thermal gradient expectations, attributable to

underlying magmatic activity. Additionally, the aquifer exhibits slight underpressurization, suggesting that the total stored CO_2 mass may surpass initial estimates before reaching the fracturing pressure. The high and isotropic permeability of the aquifer results in a nearly uniform pressure distribution across all its cells. Monitoring the pressure within the aquifer becomes crucial to ensure that the fracturing limit, which could lead to undesired rock fractures, is not exceeded. Numerical solutions are employed to solve the mass, momentum, and energy differential equations governing fluid flow in the porous medium. Nevertheless, various analytical solutions, corroborated by numerical simulations, have been proposed to address related issues such as cap rock uplift [20], plume pressure buildup [21], and the analysis of flow regimes [22].

The rest of the paper is organized as follows. In Section 2, the most important aspects of Carbon Capture Utilization and Storage (CCUS) processes are explored. The subsurface system along with the injection/production schedules followed will be presented in detail in Section 3. Results and discussion are facilitated in Section 4. Finally conclusions are drawn in Section 5.

The units used throughout the text and their conversion factors are shown in Table 1.

Table 1. Unit conversion

Property	**Name**	**Symbol**	**SI conversion**
Pressure	pounds per square inch	psi	$6,894.76\,Pa$
Temperature	Fahrenheit	F	$(K-273.15)\cdot 9/5$
Depth	feet	ft	$0.348\,m$
Permeability	milliDarcy	mD	$10^{-15}\ m^2$
Gas volume	cubic feet	cf	$0.028\,m^3$
Liquid volume	stock tank barrel	STB	$0.16\,m^3$
Mass	pounds	lbm	$0.45\,kg$

2 CCUS

2.1 Carbon capture

Carbon capture is the first in a series of steps contributing to the global effort to mitigate climate change, as it plays a pivotal role in reducing greenhouse gas emissions. The process involves capturing CO_2 emissions from various sources, preventing their release into the atmosphere and contributing to the accumulation of greenhouse gases. According to the Global Carbon Project, in 2022, human activities released approximately 37 billion metric tons of CO_2 into the atmosphere [23]. These emissions originated from industrial facilities, power plants, cement factories, as well as natural sources like wildfires and volcanic activity. Given their contribution to the greenhouse effect, the significant scale of these emissions underscores the urgent need for effective carbon capture strategies to address the escalating levels of greenhouse gases and mitigate their impact on climate change. A major issue arises from the fact that CO_2 typically occupies

a small fraction of the emitted streams typically of the order of 10%. Therefore, developing economically viable methods to capture a nearly pure stream of CO_2 from emissions remains an ongoing area of research.

One of the most widely studied and implemented methods for CO_2 capture is post-combustion capture (PCC) shown in Figure 3. In the context of power plants, PCC involves capturing CO_2 emissions after the combustion of fossil fuels, mainly aiming to remove the CO_2 along with other combustion byproducts such as nitrogen oxides (NO_x) and sulfur oxides (SO_x). Amine-based solvents, such as monoethanolamine (MEA), are frequently employed in PCC systems due to their high affinity for CO_2 [24]. These solvents absorb CO_2 from flue gas streams, facilitating its separation. Another technique in PCC involves the utilization of advanced sorbents, such as supported amine sorbents. These solid sorbents, with amine groups immobilized on a solid substrate, offer advantages such as reduced energy requirements and potentially lower operating costs compared to liquid solvents. Supported amine sorbents exhibit high CO_2 capture capacity and can be regenerated for multiple cycles, making them an attractive option for PCC applications [25].

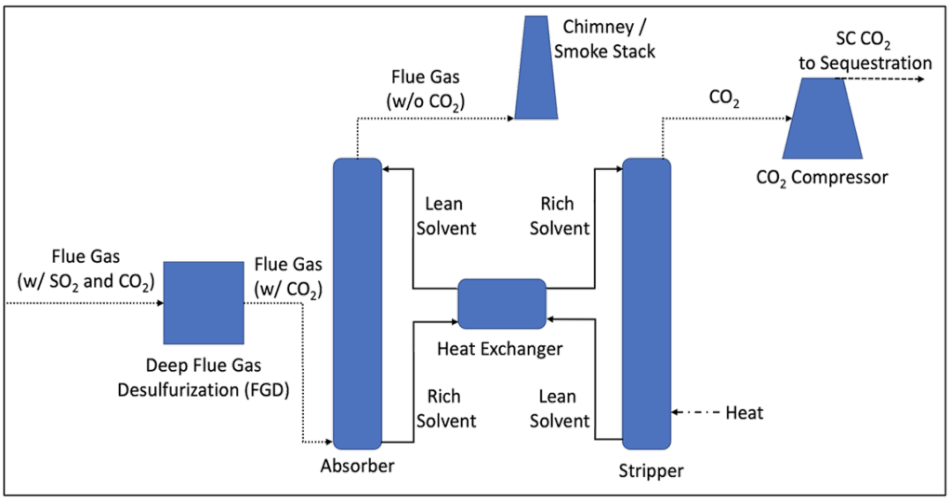

Fig. 3. Post combustion capture
[https://www.long-intl.com/blog/post-combustion-capture/]

On the other hand, pre-combustion capture seen in Figure 4, involves the removal of CO_2 before the combustion of fossil fuels, commonly associated with Integrated Gasification Combined Cycle (IGCC) power plants [26]. In IGCC, fossil fuels are gasified to produce a syngas, from which CO_2 can be captured before combustion, allowing for the more efficient capture as the fuel gas contains a higher concentration of CO_2 compared to the overall combustion products.

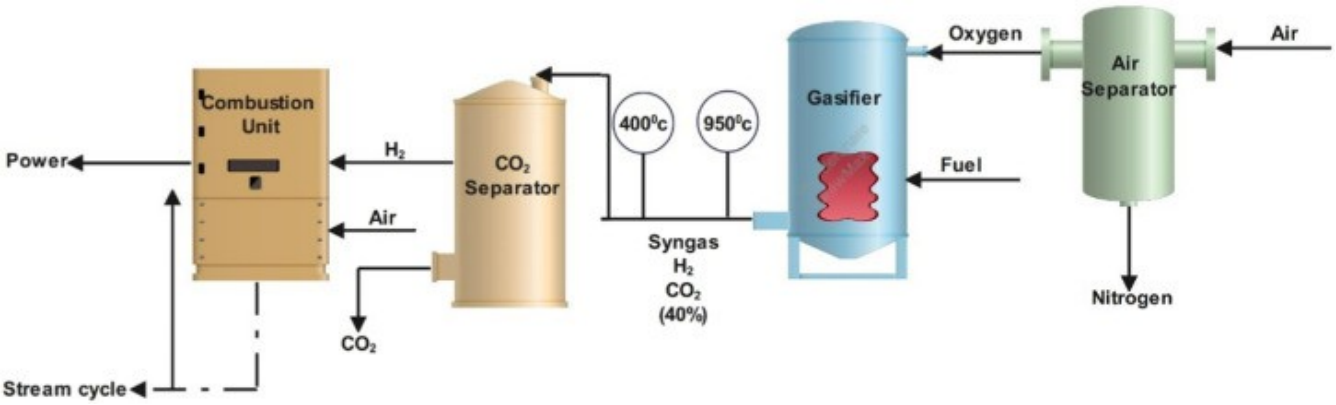

Fig. 4. Pre combustion capture [27]
[https://www.sciencedirect.com/topics/earth-and-planetary-sciences/pre-combustion-capture]

Finally, oxyfuel combustion involves burning fossil fuels in an oxygen-rich environment, resulting in a flue gas predominantly composed of CO_2 and water vapor rather than N_2 (see Figure 5). Thanks to its rich concentration, the CO_2 stream can be easily captured. This method is often considered for its compatibility with existing combustion technologies [28].

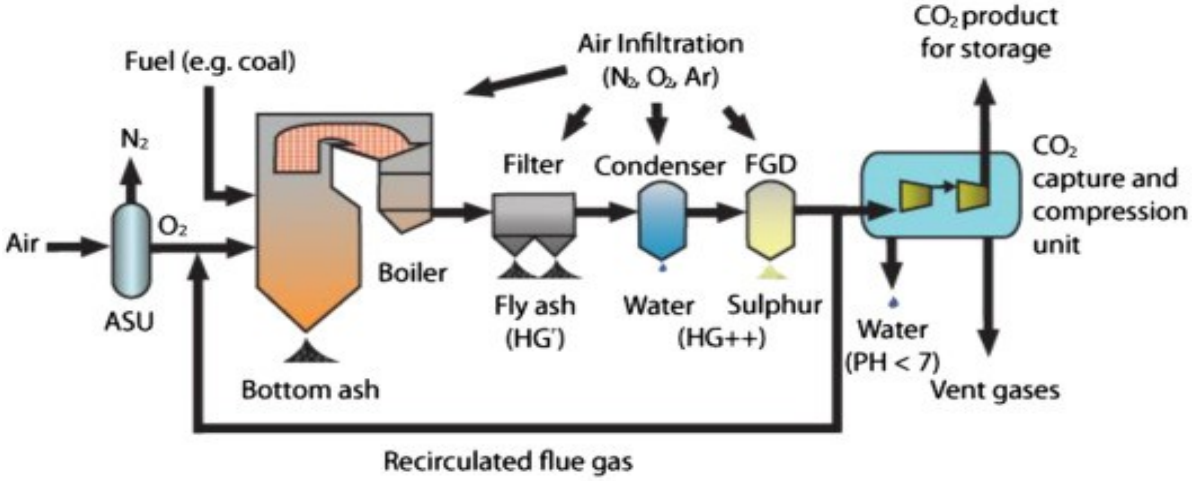

Fig. 5. Oxyfuel combustion capture [27]
[https://www.sciencedirect.com/topics/engineering/oxyfuel-combustion]

2.2 Carbon Utilization

Carbon utilization, or carbon capture and utilization (CCU), stands as a pivotal approach in the global initiative to combat climate change by considering CO_2 as a raw material which can be converted into valuable products. This strategy offers an alternative to traditional emission reduction methods and contributes to the establishment of a circular carbon economy. Diverse pathways within carbon utilization have been explored, each offering distinctive opportunities for sustainable carbon management.

One significant avenue in carbon utilization involves incorporating CO_2 into chemical synthesis processes to produce valuable compounds, such as chemicals, polymers, and fuels. Catalytic processes, for instance, can convert CO_2 into methane or ethylene, showcasing the potential for reducing emissions while generating useful materials [29]. Biological carbon utilization represents a sustainable avenue, where microorganisms can be engineered to utilize CO_2 for the production of biofuels, chemicals, and other bioproducts, offering a nature-inspired solution to carbon management challenges [30]. In the realm of electrochemical conversion, technologies such as electrochemical reduction enable the conversion of CO_2 into valuable products using renewable energy sources. This approach presents a promising tool for synthesizing fuels like methane or ethylene [31]. Additionally, while the production of certain products from CO_2 may result in emissions of other greenhouse gases or pollutants, comprehensive lifecycle analyses and strict environmental regulations can help minimize these unintended consequences and ensure that the net impact on the environment remains positive. In summary, carbon utilization strategies offer promising pathways to transform CO_2 from a pollutant into a valuable resource. Continued research and innovation are essential for developing efficient processes, optimizing economic viability, and promoting widespread adoption of carbon utilization technologies across various industries.

2.3 Carbon storage

Carbon storage is a critical component of global efforts to mitigate climate change by preventing CO_2 emissions from entering the atmosphere. CCS involves the capture of CO_2 emissions from industrial processes and power generation, followed by liquefaction transportation and secure storage underground. This technology plays a crucial role in achieving carbon neutrality and addressing the challenges of reducing greenhouse gas emissions. The most significant approach within carbon storage is probably the geological option, where captured CO_2 is injected into geological formations such as depleted oil and gas reservoirs, deep saline aquifers, or unmineable coal seams. These subsurface formations, are usually high pressure environments where CO_2 can be injected and stay as a supercritical fluid. In such conditions, CO_2's density is much higher than its gaseous phase and it is comparable to that of oil, taking up much less volume than it would at surface. These formations provide a secure and stable environment for long-term carbon storage, preventing CO_2 from contributing to the greenhouse effect [32]. Eventually, mineralization of CO_2 into stable carbonates takes place. CO_2 is transformed into a geologically stable form so as its release into the atmosphere under seismic or other geological events is prevented, mitigating the potential for environmental harm and contributing to long-term carbon sequestration efforts. The storage of CO_2 in geological

formations, such as depleted oil and gas reservoirs or deep saline aquifers, is a well-established technique [33]. Ongoing research and interdisciplinary collaboration are essential for refining existing methods, exploring new approaches, and optimizing the overall efficiency of carbon capture processes.

Another avenue is ocean storage, which involves injecting liquid CO_2 into the deep ocean since it can dissolve and disperse gases. When liquid CO_2 is released into the deep ocean, it encounters high pressures and low temperatures. At these conditions, supercritical CO_2 is heavier than seawater and will sink to the bottom of the ocean [34]. In the long term, CO_2 will be dissolved into the surrounding seawater. The dissolution process involves the physical interaction between CO_2 molecules and water molecules, forming carbonic acid (H_2CO_3). The carbonic acid can then further dissociate into bicarbonate ions (HCO_3^-) and hydrogen ions (H^+). This dissolution mechanism allows the CO_2 to be stored in the ocean in a dissolved form rather than as a separate gas phase. While this approach can be effective in removing CO_2 from the atmosphere, it raises environmental and ecological concerns, necessitating careful consideration of potential impacts on marine ecosystems [35].

In summary, carbon storage technologies are diverse and multifaceted, offering solutions to capture and sequester CO_2 emissions. Each one presents unique opportunities and challenges. Continued research, innovation, and international collaboration are essential to advancing these technologies and integrating them into comprehensive climate change mitigation strategies.

3 CPG plan

To demonstrate the potential of utilizing captured CO_2 as the working fluid in geothermal applications, a thorough CPG plan is studied by conducting simulations that integrate plans for concurrent CO_2 storage and geothermal energy production. The simulations involve modeling of the dynamic interactions between the injected CO_2 plume and geothermal fluids within a subsurface, deep aquifer. The aquifer is highly permeable and slightly heterogeneous with an abnormally high temperature justifying the CPG application. Through careful optimization, best injection strategies were devised, aimed at maximizing the benefits of both CO_2 storage and enhanced geothermal energy extraction. The coupling of CO_2 storage with geothermal operations demonstrated promising results, showcasing improved heat transfer efficiency and increased geothermal energy production. The integration not only provided a sustainable means of reducing CO_2 emissions but also offered a dual-purpose solution by harnessing renewable geothermal energy.

3.1 The aquifer

The characteristics of the subsurface system are presented in Table 2.

Table 2. Aquifer characteristics

Parameter	Value	Units
Average pressure (P)	3,800	Psi
Temperature (T)	360	$^{\circ}F$
Porosity (ϕ)	0.25	
Average depth (D)	10,180	ft
Average xy permeability (k)	300	mD
Bulk volume (V)	$2.5 \cdot 10^{11}$	cf
Water in place	$1.1 \cdot 10^{10}$	STB

3.2 Aquifer flow simulation

The primary objective of the schedule optimization is to address a hydraulic problem within the aquifer by fine-tuning the well placements and flow rates. A reasonable key assumption is made regarding a uniformly distributed specific heat capacity throughout the aquifer. This assumption simplifies the consideration of thermal dynamics, implying consistent heat absorption or release capabilities across the entire system. Moreover, there are no designated zones or boundaries within the aquifer serving as thermal sources. Therefore, the adjustment of well placements is influenced solely by inclination and not by specific thermal considerations.

To properly solve the fluid flow problem, reservoir simulation is utilized through the commercial software Reveal [36] by Petroleum Experts. Simulation is a crucial tool in the field of reservoir engineering that aids in modeling and predicting fluid flow behavior within subsurface reservoirs. The primary objective is to simulate the complex interactions among various components, such as rock, fluids, and wells. One of the fundamental principles underlying reservoir simulation is Darcy's law, which describes the flow of fluids through porous media, relating fluid velocity to the pressure gradient, permeability, and fluid viscosity [37].

Combined to mass conservation, the Darcy equation is a second-order partial differential equation (PDE), derived from homogenization of the Navier-Stokes equations and can be analytically solved only under severe assumptions. However, when modelling realistic subsurface formations, these assumptions do not hold. In this case, the discretization of the equation through linearization is essential. This process involves dividing the reservoir into a grid to represent the spatial distribution of rock properties and fluid flow. Common methods for discretization include finite differences, finite volumes, and finite elements. Finite volumes [38], in particular, are widely used in reservoir simulation due to their simplicity and efficiency. Gridding (Figure 6) plays a vital role in the discretization process, involving defining the size and shape of the cells within the reservoir grid. Various types of grids, such as Cartesian, corner-point, and unstructured grids, may be used based on the geological complexity of the reservoir, whereas the choice of grid impacts the accuracy and computational efficiency of the simulation.

Petrophysical fluid properties, including porosity, permeability, fluid saturations, compressibility and relative permeability are crucial inputs for reservoir simulation.

Accurate characterization of these properties is essential for realistic simulation results. Furthermore, the incorporation of phase behavior models is required to capture the complex interactions between brine and CO_2 including phase expansion and solubility. Expanding beyond this scope, thermodynamic properties of the fluids were derived using the CoolProps software [39], to estimate the specific enthalpy of both CO_2 and brine

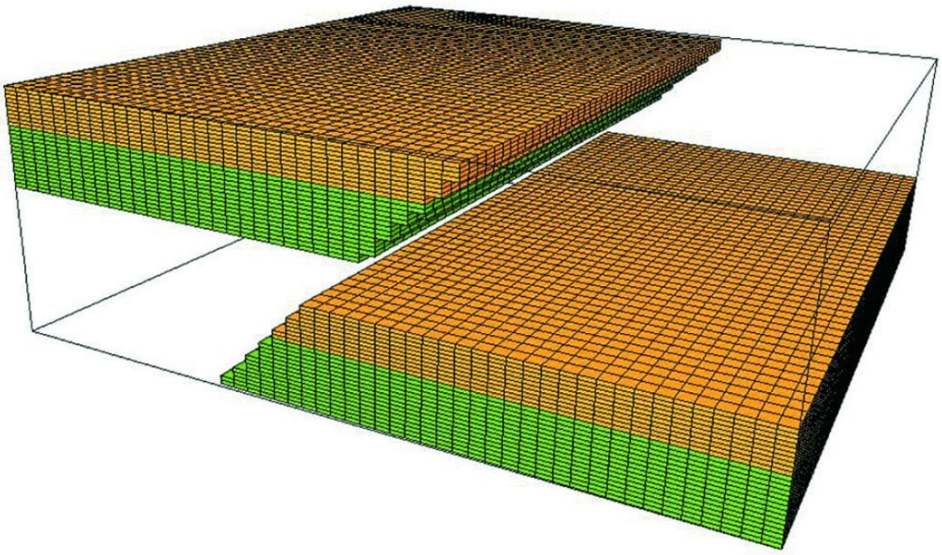

Fig. 6. Discretization of anticline reservoir
[https://csegrecorder.com/articles/view/improving-the-reservoir-modeling-of-compressional-structures]

3.3 Schedule

The schedule for achieving carbon sequestration and energy generation relies heavily on strategic well placement and precise control of injection and production rates. Placing injection wells close to emission sources like industrial facilities reduces transportation costs and logistic challenges. Furthermore, well placement and rate control directly influence pressure buildup within reservoirs and the delay of breakthrough events. Managing injection rates ensures optimal CO_2 storage while balancing pressure dynamics. Similarly, controlling production rates maximizes energy extraction without compromising storage integrity. Continuous monitoring and advanced modeling inform rate adjustments, minimizing breakthrough risks and optimizing operational efficiency. CCS operations optimization has been extensively explored in the literature [40]. However, in this study, a more conventional fine-tuning approach was employed by utilizing engineering intuition to space the wells along the aquifer and manually changing flow rates when deemed necessary.

After taking into account all of those parameters, the resulting schedule is delineated into three distinct phases, as illustrated in Figure 7, which align with the project's goals. Each phase represents a specific stage in the system's implementation, with tailored actions and parameters designed to simultaneously achieve carbon sequestration and geothermal energy generation.

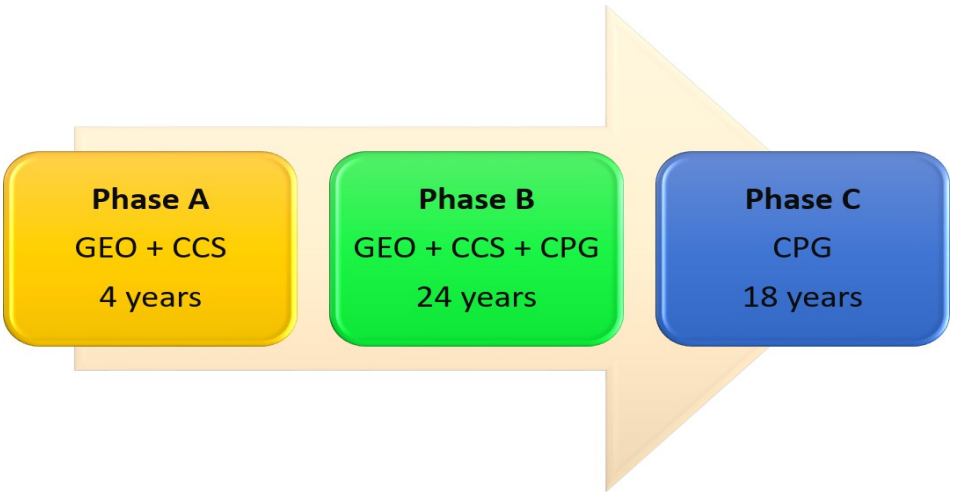

Fig. 7. Schedule phases. GEO stands for geothermal production with brine

As the system is closed, pressure buildup while injecting CO2 for CCS must be managed by simultaneous brine production (phase A). Note that, an open system with stratigraphic traps would maintain pressure through brine migration to adjacent formations. Since CO2 is lighter than brine, even when in supercritical phase, the configuration depicted in Figure 8 can be effectively harnessed. Therefore, the brine producers need to be drilled at the reservoir's bottom and perforated solely in the lowest layers, while CO2 be injected at the crest, to achieve maximum breakthrough delay. The density difference between the two fluids results in an expanding CO2 plume within the upper layers, enabling it to reach the deeper production well's upper layers. However, due to the limited vertical permeability (compared to the horizontal one $k_z \approx 0.1 \cdot k_x$), the migration of the CO_2 plume to the brine producers' perforations is slowed down. This phase involves controlling brine extraction rates in each well to maintain the overall constant brine production for as long as possible, thus ensuring stable power output. Subsequently, brine is utilized for energy production and treated for safe disposal.

The Voidage Replacement Ratio (VRR), defined as the ratio between the downhole volume of the injected and the produced fluid, exhibits variations during the process due to reservoir temperature and pressure changes, drastically influencing the injected fluid's density as well as the occurrence of CO_2 breakthrough in the latter stages. On average, the VRR in the optimized schedule maintains a value of 267%, resulting in a steady but controlled increase in reservoir pressure of about 800 psi/year. This phase is designed to last for four years.

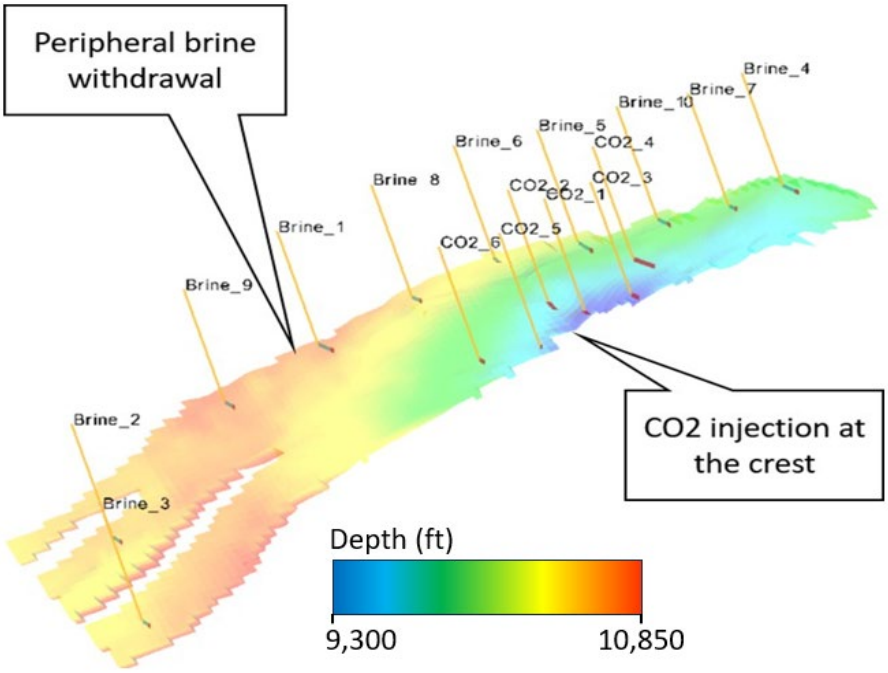

Fig. 8. Aquifer inclination and wells placement

Once brine can no longer be produced at the selected constant rate due to the risk of breakthrough, its production is slowed down and phase B is initiated. However, reduced brine production leads to a decline in the power output of the geothermal system. This situation is unfavorable and to counterbalance the system's power output loss, some CO_2 injectors are converted into producers to initiate CPG. This phase is characterized by controlling both brine and CO_2 production rates to level the system's power output to phase A. Furthermore, system pressure buildup is more easily controlled in this phase due to the increase in controllable parameters. This transitional phase where brine production is steadily decreased and CO_2 saturation is increased may last up to 24 years.

Finally, once breakthrough has reached all brine producers, the system transitions to phase C. The power output of the geothermal plant depends solely on CPG, while CCS and brine production are minimized. This phase was simulated [36] for 18 years, although the steady state flow conditions achieved can be extended arbitrarily long.

4 Discussion and Results

Selecting an appropriate CO_2 storage schedule is a nontrivial task. Unlike primary or secondary oil production, where the objective is to maximize the hydrocarbons recovery factor "as much and as fast as possible", this development plan involves various targets and limitations. It is crucial for power output to remain constant throughout the

resource utilization, as a power plant, whether autonomous or a subsystem of a larger facility, must consistently meet specific energy demands over time. Several trade-offs have to be considered for the case study in this work. Firstly, higher production rates are inversely correlated with breakthrough time. Secondly, the minimum CO_2 storage mass rate needs to remain higher than the mass rate produced from the carbon storage facilities, allowing space for excess CO_2 needs to be met through the market. The trade-off here is that an increased mass rate leads to sooner pressure buildup and faster breakthrough.

CCS takes place during in phases A and B, spanning a 28-year timeframe in this aquifer. Therefore, operators must identify and develop plans for more subsurface formations or target other storage operators to store emissions after this period. Development plans, especially in the case of CPG, needed to be engineered to suitably space CO_2 injectors, as once transformed into producers, CO_2 must be reheated sufficiently to serve as a geothermal fluid. In the plan presented in this work, the schedule was developed based on the expertise of the research team, and results may not be globally optimized.

The most important results obtained are the total mass of CO_2 sequestered, as depicted in Figure 9, and the geothermal power output that can be extracted from the produced CO_2 before it is recycled as shown in eq. (1)

$$E = \left(h_{prod}^{wh} - h_{inj}^{wh}\right) \cdot \dot{m} \tag{1}$$

where $h_{prod}^{wh}, h_{inj}^{wh}$ is the specific enthalpy of CO_2 at the wellhead conditions in the production and injection wells respectively and $\dot{m}$ is the mass flow rate. Clearly, the enthalpy difference corresponds to the heat load utilized by the steam turbine, taking off system losses that occur due to the selection of the thermodynamic cycle, as well as the cooling and pressurization of the CO_2 effluent from the turbine and prior to the injection well.

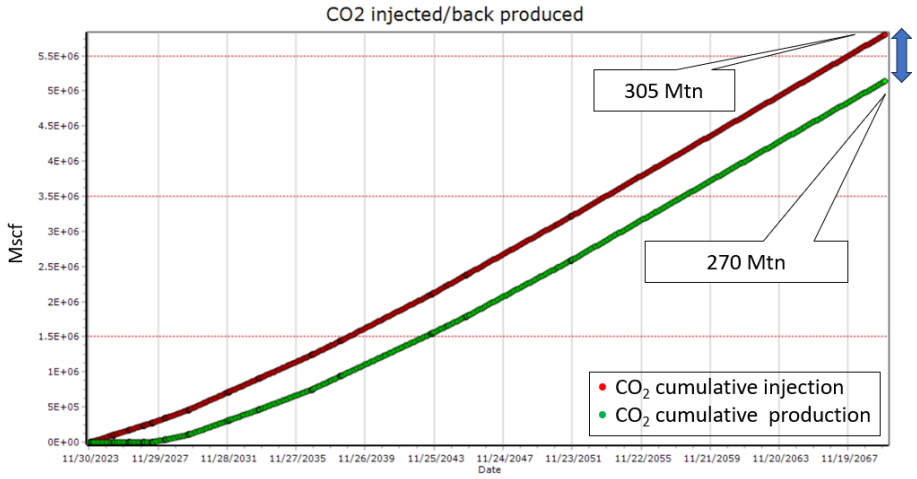

Fig. 9. Cumulative CO_2 injection/production rates

After phase B is completed, the total mass of CO_2 that has been sequestered within the reservoir is estimated at 35 Mtn (Figure 9). To calculate the power output, the produced CO_2 and brine mass rate are directly obtained from the simulation for each phase (Figures 10, 11).

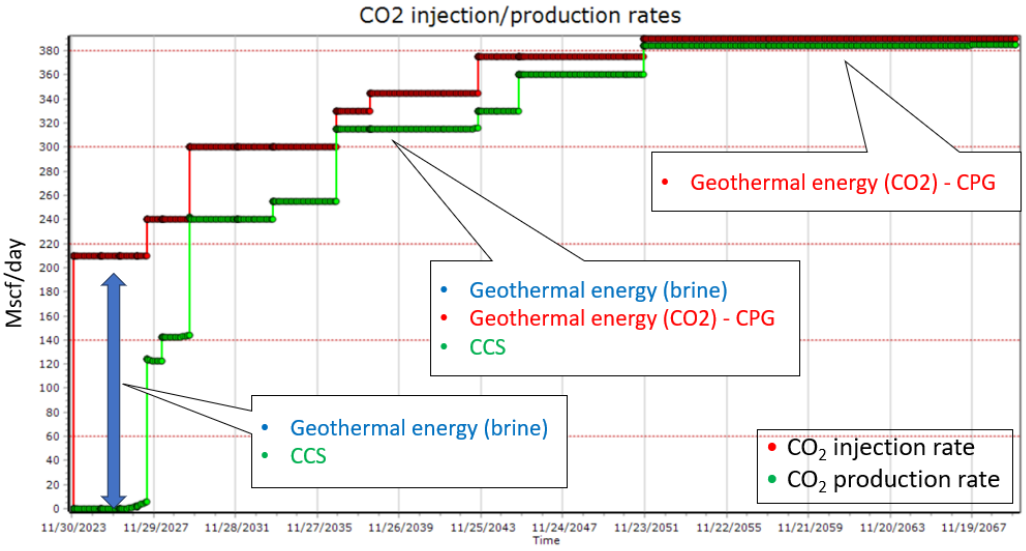

Fig. 10. CO2 injection/production mass rates

High enthalpy wells, can be considered near isenthalpic, implying that fluid enthalpy remains almost constant along the well as long as the CO_2 remains in a supercritical state. The power output can be calculated straightforwardly as the sum of the enthalpy differences of the two produced fluids at each phase and is determined to vary between $41 - 46\,MW$. The variability in power output, is attributed to fluctuations in the project's schedule and the need for long-term integrity.

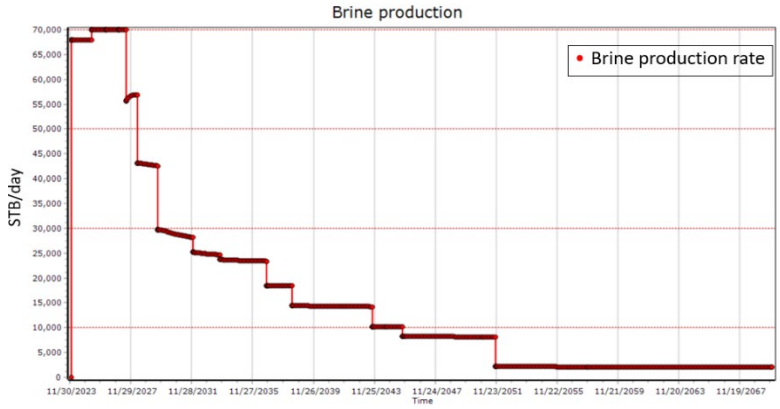

Fig. 11. Brine production mass rates

To further boost power output in phase C, injection and production rates can be increased as needed and additional CO_2 wells may be drilled. There is no need for global concern regarding average pressure increase, as the fluid is injected and produced simultaneously at similar bottomhole rates thus creating a closed loop system. Additionally, there is low only concern regarding pressure buildup due to the high and isotropic permeability of the reservoir. When considering increasing the recycling rates, the primary consideration is the time it takes for the returned fluid to reach the reservoir's temperature. Ideally, it would be preferable for the fluid to reach the aquifer's temperature before being produced, as the density of supercritical CO_2 decreases with an increase in temperature, maximizing geothermal energy retrieval.

With the flow rates simulated in this study, the temperature of the produced fluid converges to a value close to the temperature of the aquifer. Nevertheless, there are many control options to be exploited to optimize production temperature, such as horizontally perforating existing wells, drilling new ones as mentioned earlier, or even temporarily halting CPG for a few hours every day to allow the fluid to reach the aquifer's temperature. This may be a common practice in industrial cases, as power plant needs vary throughout the day.

5 Conclusions

In the broader landscape of carbon management, the utilization of CO_2 as a raw material in industry holds considerable significance. CO_2, often considered a byproduct of various industrial processes, can be repurposed for various applications. Industries can capture and utilize it as a feedstock in the production of chemicals, fuels and materials, contributing to a more circular and sustainable approach. This not only mitigates emissions by preventing the release of CO_2 into the atmosphere but also transforms it into a valuable resource for industrial processes, aligning with the principles of a circular carbon economy.

In conclusion, the CPG-CCS joint system emerges as a highly promising approach, seamlessly integrating energy generation with carbon-negative emissions. This study concentrated on a deep saline aquifer situated within a basin characterized by substantial subsurface magmatic activity. Over the course of 28 years, our results showcase the successful sequestration of over 35 million tonnes of CO_2. Concurrently, a geothermal system was established, harnessing the sequestered CO_2 and produced brine to yield noteworthy energy outputs. The implementation of this innovative system offers quantifiable benefits. Firstly, it contributes significantly to carbon negativity, securely storing a substantial amount of CO_2 and thereby mitigating environmental impact. Secondly, it facilitates energy extraction through the geothermal system, resulting in a notable increase in overall energy production. By combining carbon sequestration and geothermal energy, our findings underscore the potential for a system that not only achieves carbon negativity but also contributes positively to overall energy production. To enhance practical implications, our study prompts consideration of real-world applications. Addressing potential challenges, exploring economic feasibility, and evaluating scalability are crucial steps toward understanding the practicality and applicability of the CPG-CCS joint system. While acknowledging the limitations inherent in our study, such as

uncertainties in modeling approaches and site-specific factors, we envision a roadmap for future research and development. Our primary emphasis centered on optimizing the fluid flow problem. Further research is warranted to conduct a comprehensive technical and economic analysis, considering factors such as the efficiency of the thermodynamic cycle employed, the increased cost associated with CO_2 wells necessitating non-corrosive materials, and the incorporation of a heat exchanger to mitigate energy loss in turbine working fluids. Addressing these challenges can pave the way for widespread adoption and further refinement of the CPG-CCS joint system. In a broader context, the CPG-CCS joint system aligns with global efforts to combat climate change. Its potential role in achieving carbon neutrality should be seen as part of a larger strategy, contributing not only to local sustainability but also to international climate goals and agreements. Emphasizing long- term sustainability, we highlight the resilience of the CPG-CCS joint system to changing environmental conditions and its ongoing effectiveness in carbon storage and energy production. This reinforces the system's viability as a sustainable solution over the long run.

Credit author statement. Conceptualization, S.F., S.B and V.G.; methodology, S.F.; software, S.F.; validation, S.F. and V.G.; resources, S.F.; writing—original draft preparation, S.F.; writing—review and editing, S.F., S.B. and V.G.; visualization, S.F. All authors have read and agreed to the final version of the manuscript.

References

1. Turgut M Gu¨r. Carbon dioxide emissions, capture, storage and utilization: Review of materials, processes and technologies. Progress in Energy and Combustion Science, 89:100965, 2022.
2. Chih-Hung Huang, Chung-Sung Tan, et al. A review: Co2 utilization. Aerosol and Air Quality Research, 14(2):480–499, 2014.
3. Cameron Hepburn, Ella Adlen, John Beddington, Emily A Carter, Sabine Fuss, Niall Mac Dowell, Jan C Minx, Pete Smith, and Charlotte K Williams. The technological and economic prospects for co2 utilization and removal. Nature, 575(7781):87–97, 2019.
4. Ronald DiPippo. Geothermal power plants: principles, applications, case studies and environmental impact. Butterworth-Heinemann, 2012.
5. M Fytikas. Updating of the geological and geothermal research on milos island. Geothermics, 18(4):485–496, 1989.
6. Dimitrios Mendrinos, Ioannis Choropanitis, Olympia Polyzou, and Constantine Karytsas. Exploring for geothermal resources in Greece. Geothermics, 39(1):124–137, 2010.
7. Katrin Breede, Khatia Dzebisashvili, Xiaolei Liu, and Gioia Falcone. A systematic review of enhanced (or engineered) geothermal systems: past, present and future. Geothermal Energy, 1:1–27, 2013.
8. Donald W Brown. A hot dry rock geothermal energy concept utilizing supercritical co2 instead of water. In Proceedings of the twenty-fifth workshop on geothermal reservoir engineering, Stanford University, pages 233–238, 2000.
9. Julie K Langenfeld and Jeffrey M Bielicki. Assessment of sites for co2 storage and co2 capture, utilization, and storage systems in geothermal reservoirs. Energy Procedia, 114:7009–7017, 2017.

10. Barry Freifeld, Steven Zakim, Lehua Pan, Bruce Cutright, Ming Sheu, Christine Doughty, and Timothy Held. Geothermal energy production coupled with ccs: a field demonstration at the secarb cranfield site, cranfield, mississippi, usa. Energy Procedia, 37:6595–6603, 2013.
11. Edesio Miranda-Barbosa, Bergur Sigfu´sson, Johan Carlsson, and Evangelos Tzimas. Advantages from combining ccs with geothermal energy. Energy Procedia, 114:6666–6676, 2017.
12. Global CCS Institute. Global ccs institute 2022 status report. https://status22. globalccsinstitute.com/2022-status-report/introduction/, 2022.
13. Hon Chung Lau, Seeram Ramakrishna, Kai Zhang, and Adiyodi Veettil Radhamani. The role of carbon capture and storage in the energy transition. Energy & Fuels, 35(9):7364–7386, 2021.
14. Jimmy B Randolph and Martin O Saar. Combining geothermal energy capture with geologic carbon dioxide sequestration. Geophysical Research Letters, 38(10), 2011.
15. Jimmy B Randolph and Martin O Saar. Coupling carbon dioxide sequestration with geothermal energy capture in naturally permeable, porous geologic formations: Implications for co2 sequestration. Energy Procedia, 4:2206–2213, 2011.
16. Benjamin M Adams, Thomas H Kuehn, Jeffrey M Bielicki, Jimmy B Randolph, and Martin O Saar. A comparison of electric power output of co2 plume geothermal (cpg) and brine geothermal systems for varying reservoir conditions. Applied Energy, 140:365–377, 2015.
17. Adina Bosoaga, Ondrej Masek, and John E Oakey. Co2 capture technologies for cement industry.
18. Energy procedia, 1(1):133–140, 2009.
19. Mar P´erez-Fortes, Jos´e Antonio Moya, Konstantinos Vatopoulos, and Evangelos Tzimas. Co2 capture and utilization in cement and iron and steel industries. Energy Procedia, 63:6534–6543, 2014.
20. Sofianos Panagiotis Fotias, Spyridon Bellas, and Vassilis Gaganis. Optimizing geothermal energy extraction in co2 plume geothermal systems. Materials Proceedings, 15(1):52, 2023.
21. Elias Gravanis and Ernestos Sarris. A working model for estimating co2-induced uplift of cap rocks under different flow regimes in co2 sequestration. Geomechanics for Energy and the Environment, 33:100433, 2023.
22. Ernestos Sarris and Elias Gravanis. Flow regime analysis of the pressure build-up during co2 injection in saturated porous rock formations. Energies, 12(15):2972, 2019.
23. Sarris Ernestos, Gravanis Elias, and Papanastasiou Panos. Investigation of self-similar interface evolution in carbon dioxide sequestration in saline aquifers. Transport in porous media, 103(3):341– 359, 2014.
24. Pierre Friedlingstein, Michael O'sullivan, Matthew W Jones, Robbie M Andrew, Luke Gregor, Judith Hauck, Corinne Le Qu´er´e, Ingrid T Luijkx, Are Olsen, Glen P Peters, et al. Global carbon budget 2022. Earth System Science Data Discussions, 2022:1–159, 2022.
25. Zhiwu Liang, Kaiyun Fu, Raphael Idem, and Paitoon Tontiwachwuthikul. Review on current advances, future challenges and consideration issues for post-combustion co2 capture using amine- based absorbents. Chinese journal of chemical engineering, 24(2):278–288, 2016.
26. Arunkumar Samanta, An Zhao, George KH Shimizu, Partha Sarkar, and Rajender Gupta. Post- combustion co2 capture using solid sorbents: a review. Industrial & Engineering Chemistry Re- search, 51(4):1438–1463, 2012.

27. Anamaria Padurean, Calin-Cristian Cormos, and Paul-Serban Agachi. Pre-combustion carbon dioxide capture by gas–liquid absorption for integrated gasification combined cycle power plants. International Journal of Greenhouse Gas Control, 7:1–11, 2012.
28. Toheeb A Jimoh, Fredrick O Omoarukhe, Emmanuel I Epelle, Patrick U Okoye, Emmanuel Oke Olusola, Alivia Mukherjee, and Jude A Okolie. Introduction to carbon capture by solvent-based technologies. In Elsevier Reference Collection in Earth Systems and Environmental Sciences. Elsevier, 2023.
29. Rohan Stanger, Terry Wall, Reinhold Sp¨orl, Manoj Paneru, Simon Grathwohl, Max Weidmann, Gu¨nter Scheffknecht, Denny McDonald, Kari My¨oh¨anen, Jouni Rit-vanen, et al. Oxyfuel combustion for co2 capture in power plants. International journal of greenhouse gas control, 40:55–125, 2015.
30. Abass A Olajire. Valorization of greenhouse carbon dioxide emissions into value-added products by catalytic processes. Journal of CO2 Utilization, 3:74–92, 2013.
31. Frederic D Meylan, Vincent Moreau, and Suren Erkman. Co2 utilization in the perspective of industrial ecology, an overview. Journal of CO2 Utilization, 12:101–108, 2015.
32. Sichao Ma, Paul JA Kenis, et al. Electrochemical conversion of co2 to useful chemicals: current status, remaining challenges, and future opportunities. Current Opinion in Chemical Engineering, 2(2):191–199, 2013.
33. Franklin M Orr Jr. Storage of carbon dioxide in geologic formations. Journal of Petroleum Technology, 56(09):90–97, 2004.
34. Vyacheslav Romanov, Yee Soong, Casey Carney, Gilbert E Rush, Benjamin Nielsen, and William O'Connor. Mineralization of carbon dioxide: a literature review. ChemBioEng Reviews, 2(4):231– 256, 2015.
35. Kurt Zenz House, Daniel P Schrag, Charles F Harvey, and Klaus S Lackner. Permanent car- bon dioxide storage in deep-sea sediments. Proceedings of the National Academy of Sciences, 103(33):12291–12295, 2006.
36. Nianzhi Jiao, Gerhard J Herndl, Dennis A Hansell, Ronald Benner, Gerhard Kattner, Steven W Wilhelm, David L Kirchman, Markus G Weinbauer, Tingwei Luo, Feng Chen, et al. Microbial production of recalcitrant dissolved organic matter: long-term carbon storage in the global ocean. Nature Reviews Microbiology, 8(8):593–599, 2010.
37. Petroleum Experts. Ipm suite.
38. Stephen Whitaker. Flow in porous media i: A theoretical derivation of darcy's law. Transport in porous media, 1:3–25, 1986.
39. Robert Eymard, Thierry Gallou¨et, and Rapha`ele Herbin. Finite volume methods. Handbook of numerical analysis, 7:713–1018, 2000.
40. Ian H. Bell, Jorrit Wronski, Sylvain Quoilin, and Vincent Lemort. Pure and pseudo-pure fluid thermophysical property evaluation and the open-source thermophysical property library coolprop. Industrial & Engineering Chemistry Research,53(6):2498–2508,20
41. Ismail Ismail., Gaganis Vassilis. Carbon Capture, Utilization, and Storage in Saline Aquifers: Subsurface Policies, Development Plans, Well Control Strategies and Optimization Approaches—A Review. Clean Technol. 2023, 5, 609-637.https://doi.org/10.3390/cleantechnol5020031

Material Science and Engineering

Compressive strength of concrete containing rubber particles from recycled car tires confined with textile reinforced mortar (TRM) jackets

Ioanna Skyrianou[1][0000-0002-0231-9387], Christos G. Papakonstantinou[1][0000-0001-9165-8307] and Lampros N. Koutas[1][0000-0002-7259-6910]

[1]Department of Civil Engineering, University of Thessaly,
Pedion Areos, GR-38334, Volos, Greece
iskyrianou@uth.gr, cpapak@uth.gr, koutas@uth.gr

Abstract. This study examines the mechanical characteristics of concrete incorporating recycled rubber aggregates as a partial substitute for natural aggregates. The concrete is confined with fibre textile jackets using an inorganic mortar. Systems like this are known as textile reinforced mortars (TRM) or fibre reinforced cementitious mortars (FRCM). The experimental program includes studying the mechanical properties of concrete containing recycled aggregates compared to conventional concrete, through uniaxial compression tests of cylindrical specimens of 100 mm diameter and 200 mm height. Furthermore, the mechanical properties of confined concrete specimens with one or two layers of basalt fibre mesh in a cementitious matrix are examined. The findings underscore a significant reduction in the compressive strength of concrete when substituting natural aggregates with rubber, accompanied by an augmented deformation capacity. The incorporation of an inorganic matrix proves effective in enhancing compressive strength up to 38%, particularly with the addition of more confinement layers. These results collectively suggest the feasibility of employing this environmentally friendly "green" concrete with TRM in applications prioritizing high deformability.

Keywords: Green concrete, confinement, TRM, rubber, recycled tires.

1 Introduction

According to the European Commission, the construction industry contributes to annual gaseous pollutant emissions in the range of 5-12% of the total emissions in the European Union. Remarkably, a reduction of up to 80% can be achieved by incorporating recycling and recovery practices into the production of construction materials [1]. Concrete stands out as a fundamental and extensively utilized material in the construction sector. As efforts intensify to curtail gaseous pollutant emissions associated with concrete production, the utilization of recycled aggregates has garnered significant attention. Recent research has been dedicated to exploring the feasibility and benefits of integrating aggregates sourced from recycled materials into concrete formulations.

This approach aligns with the broader goal of mitigating the environmental impact of the construction industry. In recent years, there has been a notable emphasis on researching the utilization of aggregates derived from recycled rubber, particularly sourced from the recycling of car tires. Within the European Union, the recycling and reuse of car tires have achieved a commendable rate, reaching 91% of tires removed from end-of-life vehicles. This trend highlights a growing interest in sustainable practices and the circular economy, with a specific focus on repurposing materials from discarded automotive components to contribute to more environmentally friendly construction methods [2].

Recent studies have delved into the substitution of natural aggregates with recycled rubber granules [3, 4]. The outcome of this replacement is a considerable decrease in the compressive strength of the concrete, a factor influenced by both the size and the content of recycled rubber aggregates in the concrete mix [5]. Despite the reduction in compressive strength, an observable increase in toughness is noted, stemming from a significant rise in deformations, both axial and lateral [6,7].

Due to the adverse impact of rubber on the compressive strength of concrete, the application of this "green" concrete has been constrained to uses with lower compressive strength requirements, such as in pavement construction [8]. This limitation reflects the ongoing challenge of balancing environmental considerations with the structural performance demands of different construction applications. In an attempt to counteract the adverse effect, the use of composite jackets to confine the concrete has been considered. At present, research has focused on confinement using Fibre-Reinforced Polymers (FRPs) or steel tubes [9-11].

The utilization of FRP confinement for concrete, incorporating rubber granules, has demonstrated notable effectiveness in contrast to traditional concrete practices. This is attributed to the substitution of a portion of natural aggregates with recycled rubber granules, resulting in heightened lateral deformations of the concrete [12, -13]. Simultaneously, the application of FRP enhances the maximum axial deformation capacity. This capacity increases with the increase of FRP layers and rubber content, while concurrently mitigating the adverse impact on compressive strength [14].

Over time, the adoption of Textile Reinforced Mortars (TRM) has surpassed that of FRPs, aiming to address the limitations associated with organic matrices. The inorganic matrix presents an appealing alternative characterized by lower costs, increased resistance to high temperatures, and the capability to be applied to wet surfaces. Furthermore, studies indicate that the effectiveness of TRM confinement is comparable to that of FRP [15]. However, the application of TRM as confinement for concrete containing recycled rubber aggregates remains unexplored as of now.

2 Experimental programme

Initially, the mechanical properties of concrete containing recycled rubber aggregates were examined and compared with those of conventional concrete. For this purpose, cylindrical specimens with a diameter of 100 mm and a height of 200 mm were prepared from a mixture of conventional concrete and a mixture in which part of the

natural aggregates has been replaced with recycled rubber at a rate of 42% by volume. A total of eight specimens of each mixture were examined, in three of which the axial strain was measured. Subsequently, six specimens from each mix were reinforced with TRM jackets using a basalt mesh in a cementitious matrix. Three specimens were reinforced using one layer of TRM and three specimens using two layers. All specimens were tested in uniaxial compression.

2.1 Materials

For all the concrete mixtures, Type II Portland cement with a characteristic strength of 42.5 MPa and crushed limestone aggregate (referred to as natural aggregate) with a nominal maximum size of 16 mm were used. For the conventional concrete (CM) mix, crushed limestone aggregates with a maximum diameter of 16 mm divided into 6 gradations were used. The mix design proportions of conventional concrete mixture are provided in Table 1. A small quantity of high range water reducing admixture, based on modified polycarboxylic ether polymers, was used in all mixtures to regulate the workability of the concrete. A ratio of water to cement equal to W/C = 0.4 was used.

Table 1. Mix design of control concrete

Material		Quantity (kg/m^3)
Cement		365.8
Water		145.2
Limestone Aggregates	8-16 mm	507.9
	4-8 mm	432.7
	2-4 mm	357.5
	1-2 mm	169.3
	0.5-1 mm	169.3
	0-0.5 mm	244.9
Superplasticizer		2

The recycled rubber employed in the study originated from a tire recycling plant in Drama, Greece, where the rubber undergoes separation from other tire materials such as linen and steel. The separated rubber is then processed into granules of diverse grades. Specifically, in the concrete with recycled aggregates (RuC), the natural aggregates with a gradation of 2-8 mm (refer to Figure 1) were completely replaced by recycled rubber of identical diameter, accounting for 100% substitution. It was determined that the overall content of recycled rubber in the mixture constituted 42% of the total volume of aggregates.

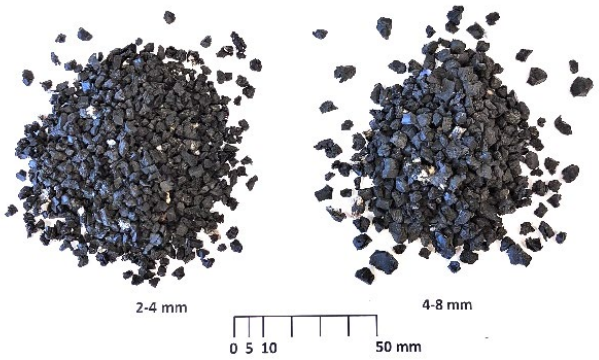

Fig. 1. Rubber particles used as natural aggregate replacement

A two-way basalt grid (Figure 2a) with a 6 mm pitch, a nominal thickness of 0.039 mm per fibre direction and a weight (with the coating) of 250 g/m2 was used for TRM confinement. The tensile strength of the textile was 1542 MPa and the modulus of elasticity 89 GPa, according to the manufacturer. The cementitious mortar used contains fine aggregates with a maximum grain diameter of 1.3 mm and polypropylene fibres (Figure 2b). According to measurements made on prismatic samples of the mortar with dimensions of 40x40x160 mm, the 28-day compressive and flexural strengths were found to be 22.6 MPa and 4.0 MPa, respectively.

(a) (b)

Fig. 2. (a) Basalt textile used for confinement (b) Cementitious mortar

The cylindrical concrete specimens (Figure 3) were subjected to uniaxial monotonic compression, while two linear displacement sensors were used on each specimen to measure axial strain. These sensors were positioned vertically at a length of 160 mm, diametrically opposed to each other, as illustrated in Figure 4.

(a) (b) (c)

Fig. 3. (a) Conventional concrete cylinder, (b) rubberised concrete and (c) confined rubberised concrete cylinder using 2 layers of TRM

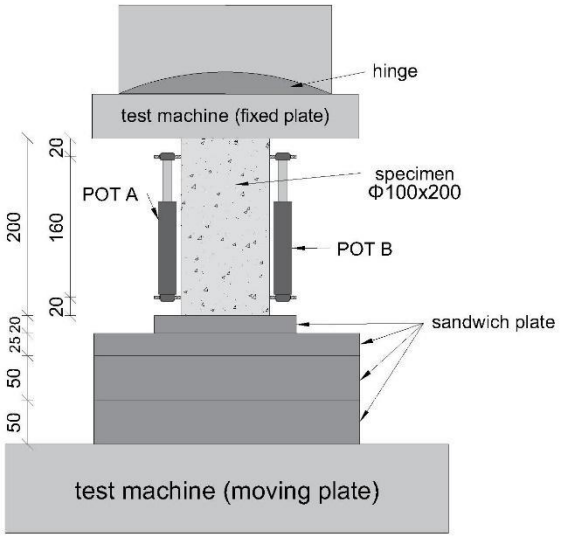

Fig. 4. Experimental Setup (dimensions in mm)

3 Results and discussion

3.1 Compressive Strength

Based on the experimental results, the compressive strength of each specimen is shown in Figure 5. The compressive strength of conventional concrete (CM) was 33.7 MPa for unconfined specimens and increased to 39.0 MPa and 41.0 MPa for confined specimens with 1 and 2 layers respectively. In contrast, the addition of recycled rubber to concrete (RuC) significantly reduced its compressive strength, which was 7.4 MPa for the unconfined specimens, while for the 1- and 2-layer confined specimens it reached 10.0 MPa and 10.2 MPa respectively. This suggests that while TRM confinement does improve strength in rubberized concrete, the improvement is less pronounced than in conventional concrete. Similar findings were reported by Gesoğlu et al. [16], who observed that replacing natural aggregates with recycled rubber resulted in a substantial reduction in compressive strength. In their study, the compressive strength decreased by up to 50% when using a 50% rubber aggregate substitution. However, they noted that the use of external confinement, specifically FRP jackets, helped mitigate the reduction in strength to some extent, aligning with the effects seen in our study with TRM confinement. Furthermore, Siddique and Naik [17] also reported a reduction in compressive strength across different rubberized concrete mixtures. Their research highlighted the importance of the size and content of rubber particles in determining the extent of strength reduction, a factor confirmed by the high rubber content (42%) used in our research.

Moreover, it is observed that in the case of concrete containing recycled rubber, the use of 2 layers of TRM does not result in a significant increase in strength compared to the use of 1 layer. This disparity can be attributed to the elevated content of rubber in the concrete (42%), exerting a significant influence on the mechanical properties of the concrete.

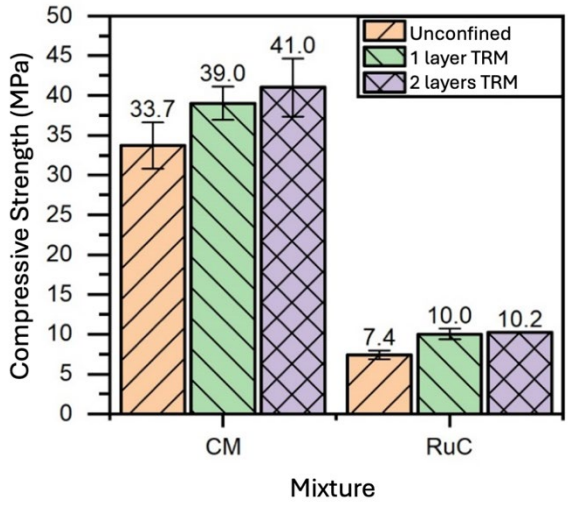

Fig. 5. Concrete compressive strength comparison

3.2 Stress-Strain curves

During the uniaxial compression tests axial strains were recorded using the axial transducers. Using the recoded loads (from the load cell) and deformations typical stress-strain diagrams for both unconfined (Unc - unconfined) and confined (1L - 1 layer, 2L - 2 layers) specimens from the two concrete mixes were drawn. The resulting diagrams are displayed in Figure 6. Failure was conventionally defined as the point where the load dropped by 20% after the maximum value was reached. The conventional failure point is indicated on the curves of Figure 6 with dots.

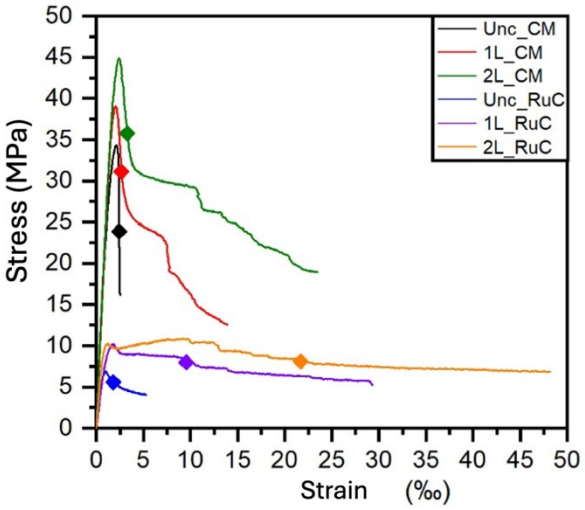

Fig. 6. Stress vs strain curves

It is evident from the stress-strain diagram that in the case of conventional concrete, the confinement increased the compressive strength, but without an appreciable increase in the axial strain up to failure. This occurs due to the premature failure of the TRM jacket at the ends of the specimen, as a result of which the confinement does not have time to fully activate and, by extension, the load drops. In the context of concrete with recycled rubber, TRM confinement demonstrated superior effectiveness, notwithstanding premature failure at the edges. This superiority can be attributed to the substantial swelling of the concrete caused by the rubber, triggering a quicker activation of the confining jacket. Consequently, the confined specimens experienced failure at significant values of maximum axial strain. Furthermore, it was observed that the utilization of 2 layers of TRM further increased the axial strains compared to the use of 1 layer of TRM. Similar findings were reported by Aiello et al [18], who reported that.

The stress-strain behavior of rubberized concrete under confinement in this study demonstrated that TRM was more effective in increasing axial strain in concrete containing recycled rubber than in conventional concrete. Similar behavior has been observed in other studies. More specifically, Güneyisi et al. [19] found that rubberized concrete exhibited increased lateral expansion when confined, leading to earlier

activation of confining jackets, a phenomenon particularly notable in concrete with a higher rubber content. Additionally, Xue and Shinozuka [20] noted that as rubber content increased, axial strain also increased. However, they observed diminishing returns in strain improvement beyond a certain rubber content level.

3.3 Toughness

Toughness is defined as the area enclosed by the curve of the stress-strain diagram until failure and expresses the ability of concrete to absorb energy during compression until fracture. This measurement reflects the concrete's capacity to absorb energy throughout the compression process until it eventually fractures. In essence, the greater the area under the stress-strain curve, the higher the toughness of the material, indicating its ability to withstand deformation and absorb energy prior to failure.

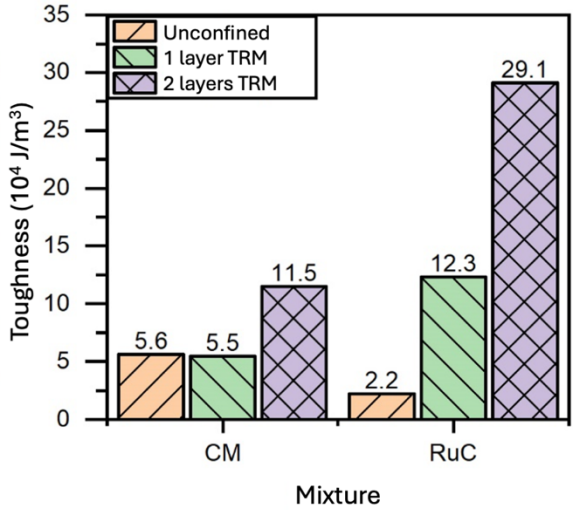

Fig. 7. Comparison between geopolymer and cement-based mortar strength

As shown in Figure 7, the toughness of unconfined concrete with recycled rubber is lower than that of conventional concrete, as the very low compressive strength significantly affects the energy absorption capacity. However, the use of confinement significantly increases the toughness of the rubberised concrete specimens, especially as the layers increase. Similar findings have been reported in other studies [21,22].

It is evident that the toughness of unconfined rubberized concrete decreases when natural aggregates are replaced with rubber particles, primarily due to the reduced compressive strength and weak bonding between rubber and the cement matrix, which limits the material's energy absorption capacity during axial compression. This observation aligns with findings from other studies, such as those by Güneyisi et al. [18] and Li et al. [21], who also reported a decrease in toughness in rubberized concrete compared to conventional concrete. Although rubberized concrete exhibits higher deformability, it cannot absorb as much energy as conventional concrete due to its lower compressive

strength. However, the application of confinement techniques, such as FRP or Textile Reinforced Mortars (TRM), significantly improves the toughness by enhancing both strength and deformability, as observed in this study.

Specifically, as observed in this study, the use of TRM jackets on rubberized concrete specimens results in a notable increase in toughness, particularly with the use of two layers of TRM, which significantly boosts the energy absorption capacity compared to unconfined specimens. This improvement is attributed to the confinement's ability to restrain the lateral expansion of the concrete, delaying failure and enabling higher axial strains. Previous research, such as that by Güneyisi et al. [18] and Razagpur et al. [22], supports these findings, showing that FRP confinement techniques effectively enhance the toughness of rubberized concrete by preventing premature failure and allowing for greater deformation under load. The increase in toughness with confinement, especially with multiple layers, demonstrates the potential of rubberized concrete for applications requiring high deformability and toughness, such as in seismic structural elements.

4 Conclusions

In this study, the impact of incorporating recycled rubber in concretewas examined, along with the effects of using TRM (Textile-Reinforced Mortar) jackets for confinement.

Based on the results, the following conclusions can be drawn:

- The incorporation of recycled rubber as an aggregate in concrete led to a notable decrease in compressive strength.
- The application of TRM jackets increased the deformability and toughness of rubberized concrete.
- Confined concrete containing recycled rubber demonstrated enhanced confinement effectiveness, primarily due to the lateral dilation caused by the rubber particles, which activated the TRM jacket more effectively.

Based on these findings, it is recommended to further explore the use of confined rubberized concrete in applications requiring high deformability, such as seismic-resistant structures. However, optimizing the concrete mix design is crucial to mitigate the reduction in compressive strength. Additionally, care must be taken to optimize the application of TRM jackets to prevent premature failures and to ensure consistent performance.

References

1. European Commission, https://ec.europa.eu/growth/industry/sustainability/buildings-and-construction_en, last accessed 2024/12/10/
2. European Tyre & Rubber Manufactures' Association https://www.etrma.org/library/europe-91-of-all-end-of-life-tyres-collected-and-treated-in-2018/, last accessed 2024/10/12

3. Su, H., Yang, J., Ling, T.C., Ghataora, G.S, Dirar, S.: Properties of concrete prepared with waste tyre rubber particles of uniform and varying sizes. Journal of Cleaner Production 91, 288–296 (2016)
4. Papakonstantinou, C.G., Tobolski, M.J.: Use of waste tire steel beads in Portland cement concrete. Cement and Concrete Research 36, 1686–1691(2006)
5. Youssf, O., Mills, J. E., Hassanli, R. (2016). Assessment of the mechanical performance of crumb rubber concrete. Construction and Building Materials, 125, 175–183. https://doi.org/10.1016/j.conbuildmat.2016.08.040
6. Eldin, N.N, Senouci, A.B.: Rubber-Tire Particles as Concrete Aggregate. Journal of Materials in Civil Engineering 5(4), 478–496 (1993)
7. Angoraj-Taghavi, H., Nematzadeh, M., Mirhosseini, S.M.: Compressive stress-strain response of freshly compressed rubberized concrete: An experimental and theoretical study. Structures 69, 107386 (2024)
8. Turatsinze, A., Measson, M., Faure, J.P.: Rubberised concrete: from laboratory findings to field experiment validation. International Journal of Pavement Engineering 19(10), 883–892 (2018)
9. Wang, Z., Hajirasouliha, I., Guadagnini, M., Pilakoutas, K.: Axial behaviour of FRP-confined rubberised concrete: An experimental investigation. Construction and Building Materials 267, 121023 (2021)
10. Cao, Y., Li, L., Liu, M., Wu, Y.: Mechanical behavior of FRP confined rubber concrete under monotonic and cyclic loading. Composite Structures 272, 114205 (2021)
11. Mujdeci, A., Guo, Y.T., Bompa, D.V., Elghazouli, A.Y.: Axial and bending behaviour of steel tubes infilled with rubberised concrete. Thin-Walled Structures 181, 110125 (2022)
12. Bompa, D.V., Elghazouli, A.Y.: Stress–strain response and practical design expressions for FRP-confined recycled tyre rubber concrete. Construction and Building Materials 237: 117633 (2020)
13. Raffoul, S., Garcia, R., Escolano-Margarit, D., Guadagnini, M., Hajirasouliha, I., Pilakoutas, K.: Behaviour of unconfined and FRP-confined rubberised concrete in axial compression. Construction and Building Materials 2017, 147, 388–397
14. Chan, C.W., Yu, T., Zhang, S.S., Xu, Q.F.: Compressive behaviour of FRP-confined rubber concrete. Construction and Building Materials 211, 416–426 (2019)
15. Bournas, D.A., Lontou, P.V., Papanicolaou, C.G., Triantafillou, T.C.: Textile-Reinforced Mortar versus Fiber-Reinforced Polymer Confinement in Reinforced Concrete Columns. ACI Structural Journal 104(6), 740–748 (2007)
16. Gesoğlu, M., Güneyisi, E., Hansu, O., İpek, S., & Asaad, D. S. (2010). Influence of waste rubber on the mechanical properties of conventional and self-consolidating concretes. Construction and Building Materials, 24(10), 1878-1887
17. Siddique, R., & Naik, T. R. (2004). Properties of concrete containing scrap-tire rubber – an overview. Waste Management, 24(6), 563-569
18. Güneyisi, E., Gesoğlu, M., & Özturan, T. (2014). Properties of rubberized concretes containing silica fume. Cement and Concrete Research, 34(2), 2309-2317
19. 19. Aiello, M. A., Leuzzi, F., Centonze, G., & Maffezzoli, A. (2009). Use of steel fibres recovered from waste tyres as reinforcement in concrete: Pull-out behaviour, compressive and flexural strength. Waste Management, 29(6), 1960-1970
20. Xue, J., & Shinozuka, M. (2013). Rubberized concrete: A green structural material with enhanced energy dissipation capability. Construction and Building Materials, 42, 196-204

21. Li, X., & Li, Y. (2004). "Effect of tire rubber on the mechanical properties of concrete." Journal of Materials in Civil Engineering, 16(2), 118-124
22. Razaqpur, A. G., Zhang, L., & Lu, X. (2015). "Behavior of rubberized concrete confined with FRP." Construction and Building Materials, 74, 146-156

Sustainable Use of Extractive Wastes in Continuous Surface Coal Mines: The case of Anyntaion Mine, Greece

Ariadni Sokratidou[1], Nikolaos Paraskevis[2][0009-0004-1892-6896], Aikaterini Servou[2][0000-0001-7814-706X], Francis Pavloudakis[3][0000-0002-9492-1032], Christos Roumpos[2][0000-0001-9394-8041]

[1]Environment Department, Public Power Corporation of Greece, 104 32 Athens, Greece
[2]Department of Mining Engineering and Closure Planning, Public Power Corporation of Greece, 104 32 Athens, Greece
[3]Mineral Resources Engineering Department, School of Engineering, University of Western Macedonia, 501 00 Kozani
c.roumpos@ppcgroup.com

Abstract. Continuous surface coal mines are related to large amounts of extracted overburden or interburden waste material. One of the main objectives of the strategic mine planning of such mines is to optimize the coal production, considering the waste-to-ore ratio in combination with the optimal allocation of the waste material to the outside and inside dumping areas. Further to other uses of waste material, the suitable sustainable reclamation of mining land is directly associated with the sustainable use of waste dumping sites for post-mining activities. This study investigates the main issues related to extractive waste management in continuous surface coal mining projects, focusing on a long-term strategic mining planning and scheduling model and the post-mining utilization of waste dumping areas. As a case study, the basic geospatial parameters of the waste dumping areas of the Amyntaion lignite mine in North Greece are examined based on the results of a long-term experimental design of water and soil sampling and monitoring program. The applied methods include a model for validating lignite production and waste extraction and dumping scheduling, and the geotechnical, hydrogeological, and geochemical spatial analysis of the waste material considering the post-mining land uses and the circular economy principles. The findings indicate the geotechnical and geochemical stability of the examined areas and the suitability of mining land to transition to post-mining activities, mainly related to renewable energy systems.

Keywords: Waste Management, Circular Economy, Closure, Reclamation, Post-Mining

1 Introduction

The optimal reclamation and post-mining exploitation of a continuous surface coal mining project is directly related to the long-term strategic mine planning and scheduling and the suitable management of waste mine lands. Considering the phase-out of such projects, the sustainable reclamation planning of the mined-out and waste

dumping areas is an indispensable part of mine closure and post-mining activities, incorporating circular economy principles [1].

Extractive waste generation is an unavoidable procedure in the mining industry, so the respective companies try to face the issue in a sustainability context. Coal mining is accompanied by its geological history and the respective rock formations through time, which gives information about the type of rocks and the respective geological environments. This type of information is beneficial for selecting the methods that would be followed for waste management. A percentage of approximately 45% of total extracted material annually is estimated to be waste for each of the leading coal production countries in both open-pit and underground mining (United States, China, India, and Australia) [2]. Among the aggregated industrial sectors, European countries' highest extractive waste generation is observed in the mining and quarrying sector compared with manufacturing, energy supply [3].

Regarding the mining industry, the circular economy model tends to replace the linear economy model of traditional coal production, meaning “take, make, and dispose”. This linear model includes a closed system with constantly increasing entropy [4]. It has been observed that the studies concerning mining waste have an increasing trend, especially those for sustainable management, accounting for approximately 40% of the total [5]. The study for the best possible waste management is fundamental to complete sustainable mine planning. The ideal concept is the implementation of circular economy priorities on post-mining land uses in surface mining operations to achieve the viability and sustainability of mining projects [6]. In particular, the waste materials generated during the operation of mines are investigated, considering specific parameters. For instance, in the hard coal mining region of Ostrava-Karvina of the Czech Republic, mining waste is used as reclamation material [7,8] Other scientific works focus on waste management as a resource and recycling materials [7].

In recent years, the circular economy concept has gained interest, including all the procedures that can ensure a harmonious coexistence of industry, society, and the environment. These procedures are summarized in the 4 R framework of the European Union (EU) Waste Framework Directive, meaning Reduce, Reuse, Recycle, and Recover [8,9]. According to the European Commission, this concept aims to decompress natural resources and enhance new sustainable growth and employment. Particularly, the generated mining residues are reused for filling excavation voids for rehabilitation and construction purposes [10]. In this context, the circular economy deals with waste management of industrial operations. The circular economy concepts are distinguished into three different levels depending on the related actions: the macro (city, country, and more), micro (products, companies, consumers, etc.), and mezzo level (defined as the regional level, e.g., eco-industrial parks) [9]. As it was concluded in [11] the management of extractive waste in coal surface mining projects can be effectively combined with circular economy principles.

The post-mining areas’ release is a complex procedure that is followed by each country’s legislation and affects the economic, social, and environmental sectors. In a sustainable framework, the post-mining areas are designed considering the most economically valuable land uses. For the most efficient mine closure, some fundamental criteria for taking into consideration are the following: physical and chemical stability, hydrogeological and hydrological conditions, geographical and climate conditions, local characteristics, land uses, required resources for the closure, socioeconomic parameters

[12]. In this context, several studies are conducted by the coal mining companies, including geotechnical, geochemical, and hydrogeological ones.

The sustainable use of extracted materials from the mining exploitation constitutes one of the basic stages of waste management. Usually, the extracted waste materials are used for filling the mining gaps that are created during the mining exploitation. However, alternative uses could be applied depending on the physicochemical composition of these materials. Some of the sustainable uses of waste materials are considered for the spatial configuration of squares and yards, for the stabilization of excavation and dumping slopes, while they could be used for the road configuration and construction, even in larger construction projects [13]. In addition, desulfurization is one possible use of limestone in wet flue gas desulfurization systems of coal-fired power plants to control sulfur dioxide emissions.

The waste dumping site operation might last for some decades, but the waste materials will remain on the site after the end of the mining operations. In the framework of the mine closure phase, the waste dumps have been reclaimed for several land uses, such as agriculture, forests, and water bodies (lakes), according to the approved environmental terms. However, considering the principles of the Circular Economy, some decisions about land use may be changed. For instance, areas that were proposed for typical land uses for reclaimed surface mining areas, such as forests and agricultural land, will finally be used for the development of activities [14] that add more value in terms of socio-economic development and environmental protection, such as the installation of renewable energy systems [15].

In this study, the main procedures that follow the gradual land release are investigated. More specifically, for the environmental monitoring and decision-making regarding post-mining land use proposals, land properties must be determined. The main parameters of interest are the soil and water properties of the reclaimed mining areas, as well as the atmosphere, noise, vibrations, and slope stability conditions.

The main research questions are:

(a) Is the allocation of the extracted waste material to outside and inside waste dumping areas compatible with the strategic mine planning and post-mining land uses of the Amyntaion mine?
(b) How does the spatial variability of the main hydrogeological, geochemical, and other environmental parameters affect the suitability of mining land to transition to post-mining activities?
(c) How can the concepts of circular economy be incorporated into the transformation of mining areas to new land uses?

The investigation is based on the quantitative analysis of the waste material in the outside and inside dumping areas, and the results of the experimental water and soil sampling and monitoring.

2 Materials and Methods

2.1 The Amyntaion Mine

The waste material and dumping areas of the exhausted Amyntaion lignite mine, North Greece, are investigated. Most part of the mine area is located in the Florina

Prefecture, whereas a small part is in the Kozani Prefecture of Western Macedonia region. Being in the southern part of Amyntaion city, the main mining sites are situated among the Filotas, Perdikkas, and Olympias villages (Fig. 1). The elevation values of the area range between 407 m and 1200 m, with mean elevation in the +625 m. Public Power Corporation of Greece (PPC) mines, have elevation values ranging from 400 to 600 m. Three individual fields delineate the Amyntaion lignite mining complex: the main Amyntaion mine, the Anargiri mine, and the Lakkia mine. The total area included in the Environmental Permit Limits of the Amyntaion Lignite Mining complex is 61.83 km2.

The excavation work began in 1984, whereas the lignite production in 1986. In the main Amyntaion mine, the excavation works began in 1989 while the lignite production began in a limited amount in 1990 and full operational scale in 1991. A large amount of the waste materials that were excavated from the Amyntaion and Anargyri mines were deposited in the outside dumping site, while the remaining in the inside dumping site. In 2013, the excavation works began in the Lakkia mine, which is operating today in the initial excavation mining sites. On the 10th of June 2017, a landslide event occurred in the southwest slopes of Amyntaion mine, and since then the operation works include only configuration and restoration works, which were completed in July of 2020. In 2018, the EIA was modified concerning the remaining small part of the Amyntaion mine, while the exploitation planning for the Lakkia mine was not differentiated.

The complex deposit geometry of the Amyntaion mine, is obvious in the Digital Elevation Maps (Fig. 2) where three different mining phases are presented: the initial surface before the excavation works, the technical mine bottom declaring the excavation areas, and the final surface after the mining operation works.

The final post-mining land use planning of the study area does not follow the initial planning according to the EIA and the Waste Management Plan, because of the new energy planning following the phase-out of electricity generation by lignite.

2.2 Waste Management Framework

Waste management in surface mining projects constitutes one of the early stages of mine planning and exploitation. It could be distinguished into four fundamental pillars: (i) mineral exploration, (ii) mine planning strategy, (iii) immediate utilization of waste materials, and (iv) spatial utilization of waste dumping materials. Mineral exploration constitutes one of the primary stages of the whole mining exploitation. It includes the exploration of the spatial distribution of the lignite deposits and the overburden and interburden materials. More specifically, this stage of waste management includes the mapping of the area hosting the mineral, the assessment of borehole findings, the assessment of the material volumes that will be dumped, as well as their geological composition.

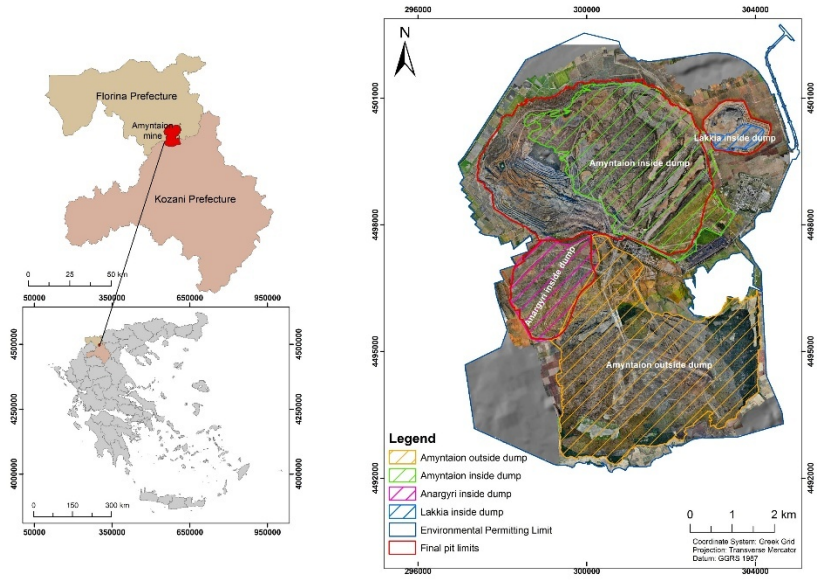

Fig. 1. General overview of the Amyntaion mine and the four investigated dumping sites

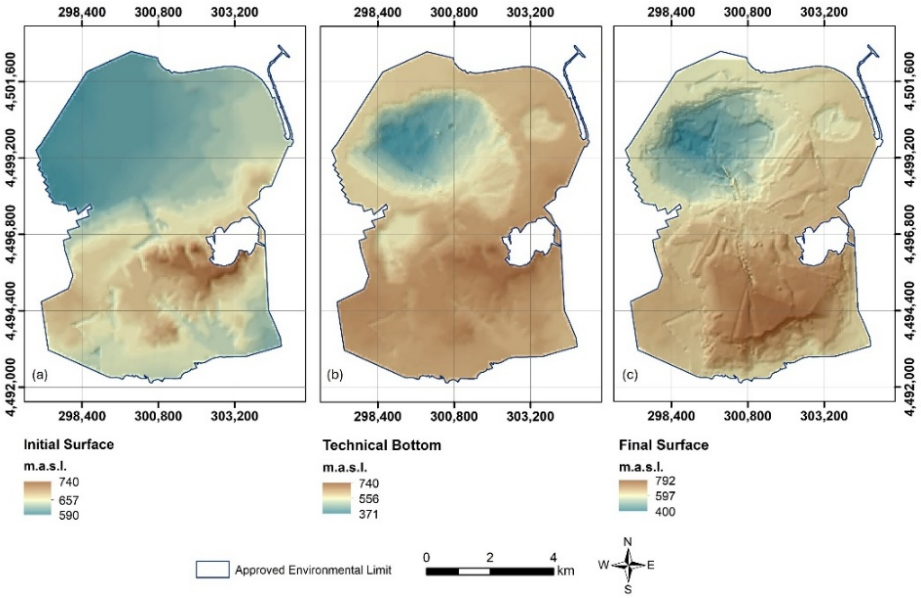

Fig. 2. Digital Elevation Maps of three different phases in Amyntaion mines: (a) initial surface before the excavation works, (b) the technical bottom declaring the excavation areas, and (c) the final post-mining surface

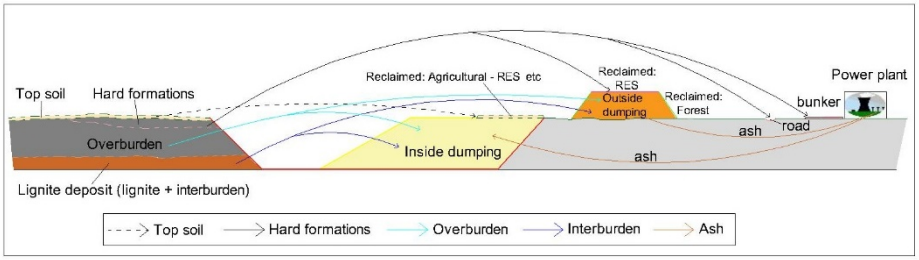

Fig. 3. Spatial representation of waste management in a surface coal mine

At the same time, the mine planning should have already been prepared and focused on the optimal way of the initial excavation and the planning of exploitation progress, aiming to deposit as little extractive waste as possible in the outside dumping areas. An essential part of the mine planning is the spatial definition of the outside dumping limits following the material volume intended to be deposited. It is worth noticing that the definition of the critical start point of the inside dumping is of high importance for achieving the minimum volume of waste materials outside deposition and, as a result, the configuration of a successful and safe mine operation. Inside dumping is the process of dumping waste materials within the void of the mine, while outside dumping refers to the practice of dumping waste materials outside the boundaries of the mine. Figure 3 depicts the whole procedure of waste management.

In the same context of mine planning and scheduling, the necessary configuration of the slopes and dumps is included to ensure geochemical and geotechnical stability. In particular, ash deriving from lignite Power Stations as a by-product is used as a stabilizer material in the outside dumping areas. Furthermore, the type of waste materials and their spatial arrangement are two components that need to be investigated. In this framework, geochemical and geotechnical attributes of the waste materials were investigated to classify the suitability of materials for several land uses. Additionally, the groundwater quality was investigated to clarify if there are any environmental consequences from the extractive procedure. More specifically, a sampling campaign was scheduled, and chemical analyses of soil and water samples were conducted for the determination of some critical parameters (pH, electrical conductivity, $CaCO_3$ content, soil organic substances, nitrates, and ammonium ions, etc.). Electrical conductivity and pH were measured electrometrically using a soil saturated paste based on WCC-103 Publication WREP-125, 2nd Edition. From the geotechnical aspect, slope stability analyses and systematic site monitoring concerning possible land movements were employed. It is worth noticing that the slope stability analyses and the site monitoring are in a continuous process to ensure the required mining safety.

Figure 3 also shows the allocation of waste material and the waste management system from a circular economy perspective. Initially, the upper beds of the soil system, namely the topsoil, are transferred to areas that are intended to be reclaimed for agricultural use, as they carry all the necessary ingredients for agricultural development. In turn, the hard formations are moved to outside dumping or/and are used as material for road construction, slope stability, and the configuration of bunkers, as their mechanical strength permits it. The overburden and interburden materials are moved for outside and inside dumping, as they could be materials of several compositions. These materials

are also used for the preparation and suitable spatial configuration of areas that aim to be reclaimed for post-mining land uses (e.g., agricultural, forest land use, industrial areas, recreation parks, and photovoltaic parks). In addition, the lignite processing in the power plants produces ash, which could be used to improve slope dumps and the cohesion of the dumping materials.

2.3 Volume Calculation of Waste Materials

Several methods could employ volume calculation. In the present study, volume calculation to validate the planning of the waste material allocation was employed via the triangulation method. This method is based on Triangulated Irregular Network (TIN) surfaces and calculates the signed volume defined by two TIN surfaces declaring the elevation differences between the two surfaces [16]. This method differs from the grid-based and cross-section volume routines. Compared with the other methods, the triangulation method is considered faster and more accurate because it considers actual TINs. In general, the volume calculations among the TIN surfaces are usually employed through interpolation methods like Inverse Distance to a Power (k=1 and k=2), Point Kriging, Minimum Curvature, Modified Shepard's Method, Natural Neighbor, Nearest Neighbor, Polynomial Regression (simple planar surface), Multiquadratic Radial Basis Function, Triangulation with Linear Interpolation [17]. The type of triangulation that was applied in the framework of this study was the Linear Interpolation.

3 Results and Discussion

In the Amyntaion lignite mining area, three surface lignite mines had been in operation: the Anargyroi Mine (1984-2010), the Amyntaion Mine (1989-2020), and the Lakkia Mine (2013-2021). The mining exploitation completed in 2021, and a total of 232 million tons of lignite has been extracted, with total excavations of 1.817 million m3 and a mining ratio (waste materials to lignite) of 7:1 m3/t. Concerning the changes in land uses in the broader area of the Amyntaion mine, Figures 4 and 5 show the land uses in 2000, almost a decade after the opening phase of the main Amyntaion mine field, and in 2018, three years before the closure of the lignite extraction phase.

Considering the validation of lignite production and waste extraction and dumping scheduling, Figure 6 shows a graphical representation model including the excavations rate and the waste dumping allocating into the outside and inside dumping areas as a function of the lignite production, according to a long-term master plan, conducted in 1996 and revised later, and the actual data of total excavations, outside dumping and total waste dumping. On the x-axis of Fig. 6 the accumulated lignite reserves are shown. On the y-axis, the positive volumes represent the excavation site of the mine. The minimum and maximum total excavations (T.E.Min. and T.E.Max.) depend on (a) the required lignite production to meet the needs of the corresponding power plant and (b) the design of the excavation mine sectors according to the pit slope which ensures the stability of excavation site based on the geotechnical investigation). The negative volumes correspond to the dumping site of the mine (D.V.Min. and D.V.Max. are the

minimum and the maximum dump volume requirements taking into account the swell factor).

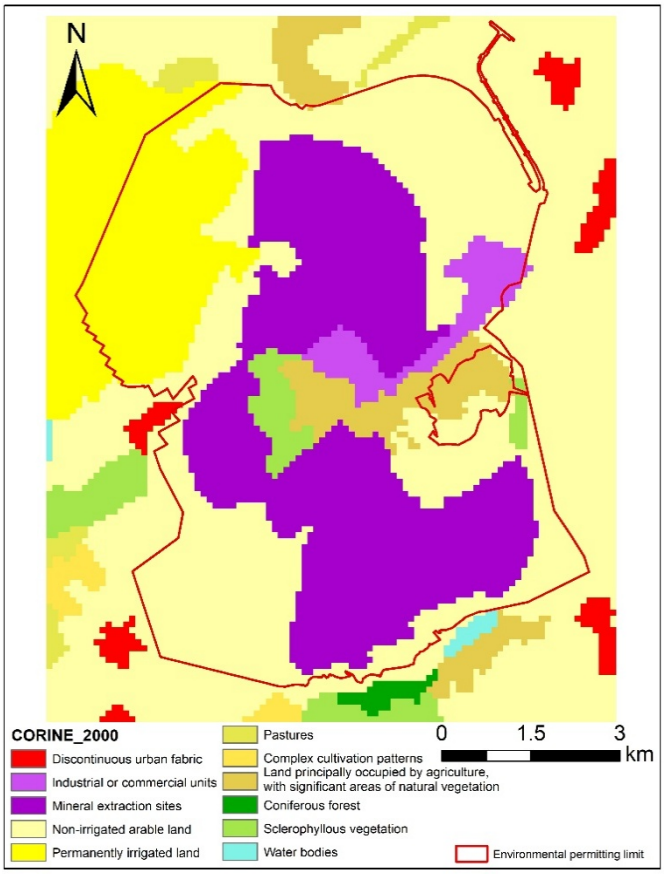

Fig.4. Land uses in the Amyntaion mining area in 2000

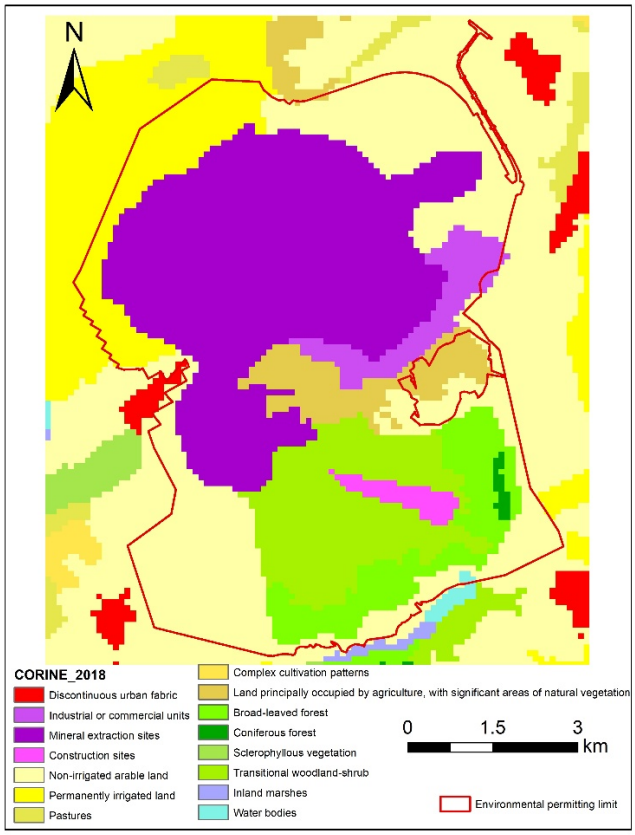

Fig. 5. Land uses in the Amyntaion mining area in 2018

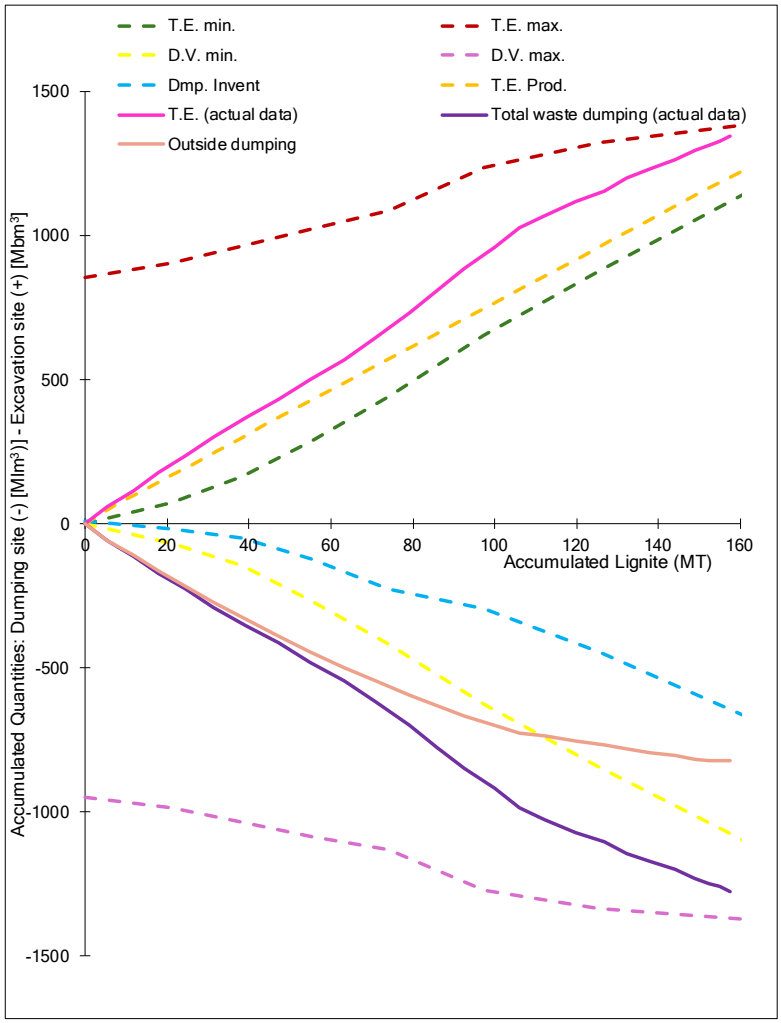

Fig. 6. A graphical representation model for the long term mine planning of the Amyntaion mine to validate the lignite production and waste extraction and dumping scheduling (T.E.Min.: minimum total excavations, T.E.Max.: maximum total excavations, T.E. Prod.: Total scheduled excavations V.Min.: minimum dump volume requirements, Dmp Invent.: dump space inventory on the inside dump, and D.V.Max.: maximum dump volume requirements according to a master plan, and T.E., Total waste dumping and Outside dumping: the actual production data respectively)

The dump volume is further increased by the deposition of ash (and possibly other materials to be dumped in the mine). The dump space inventory on the inside dump (Dmp Invent.) of the mine is determined by deducting the accumulated volume of the inside dump sectors (based on the appropriate design of dumping sectors) from the

minimum dump volume requirements (D.V.Min.). The minimum of this graph (Dmp Invent.) is the minimum outside dump volume.

Considering the actual total excavations volumes and the actual outside and total waste dumping volumes shown in Fig. 6, it is concluded that (i) the total actual excavations ranged between the scheduled limits, (ii) the actual excavations pit slopes had less inclination than the initially designed excavation faces, and (iii) the actual outside and total waste dumping volumes were increased compared with the initial calculations. Therefore, the allocation of the extracted waste material to outside and inside waste dumping areas is compatible with the strategic mine planning and post-mining land uses of the Amyntaion mine.

Figure 7 presents the distribution of waste materials in the inside and outside dumping areas, while Figures 8-11 show the excavation and dumping sites of the Amyntaion mine, the spatial distribution of the waste material, and the spatial differences of the initial and final topography in the Amyntaion mining areas. It is observed that in the middle of material dumping, in 2004, the inside dumping began to increase while the outside dumping materials began to decrease significantly. In addition, a normal distribution appears for both materials deposited in outside dumping during 1990-2009 and those deposited in inside dumping during 2004-2019. This indicates a balance of material disposal, which in turn is attributed to a feasible mining design. The primary dumping materials are waster interburdens in the lignite seams, consisting of stiff clays, usually with medium (15-35%) to high (35-50%) carbonate content (marls), while the thinner waste interburdens are present in the lignite blocks.

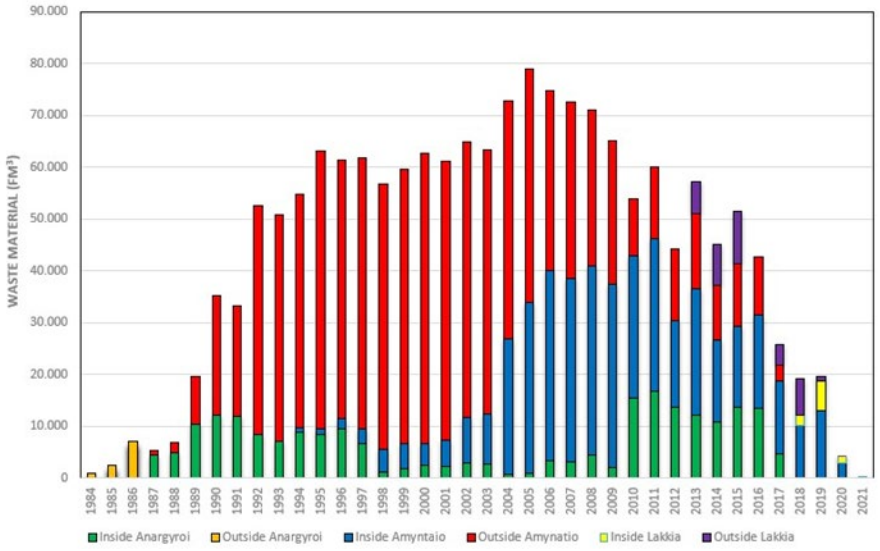

Fig. 7. Waste material distribution in the inside-outside dumping area

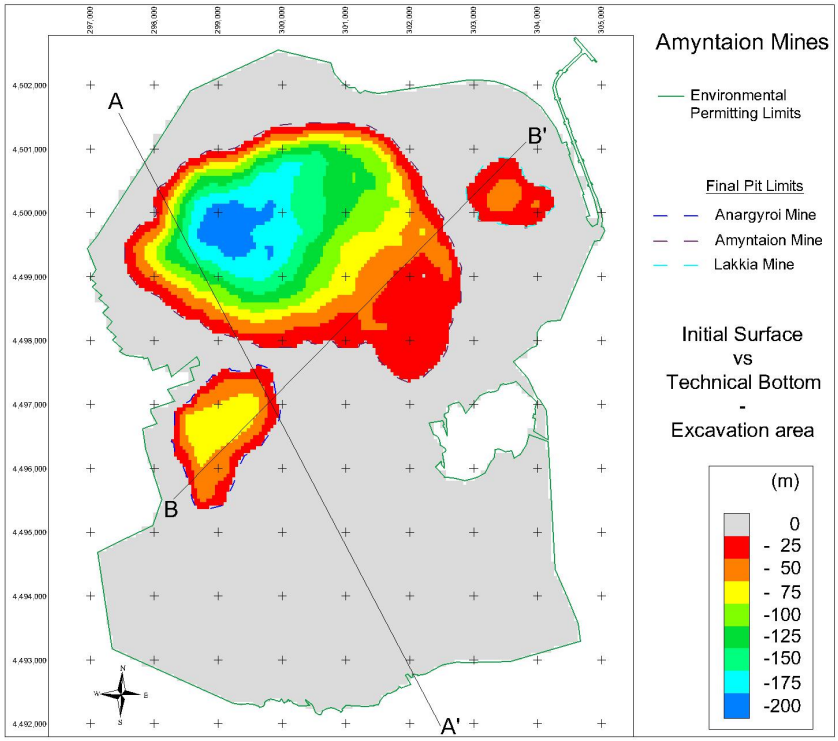

Fig. 8. Excavation sites of the Amyntaion mines

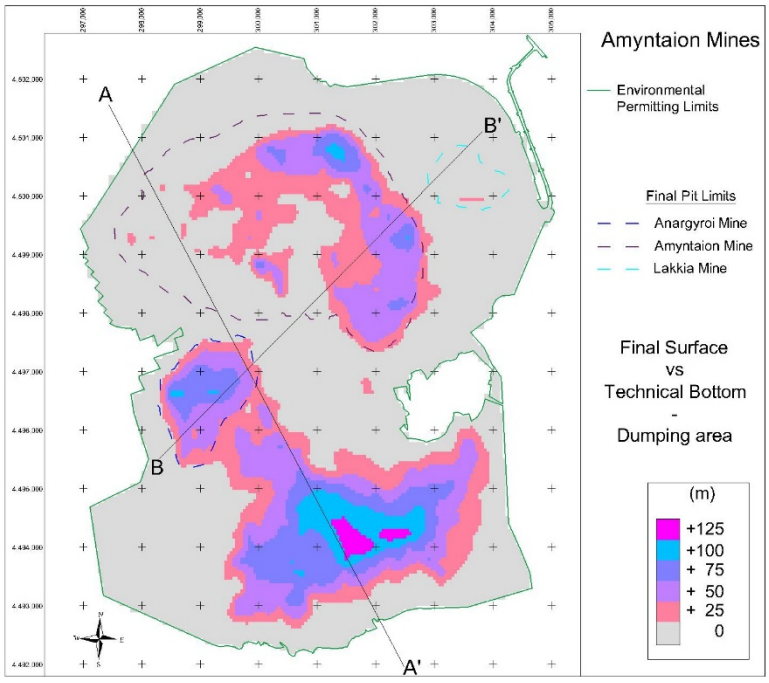

Fig. 9. Waste material distribution in the inside-outside dumping areas

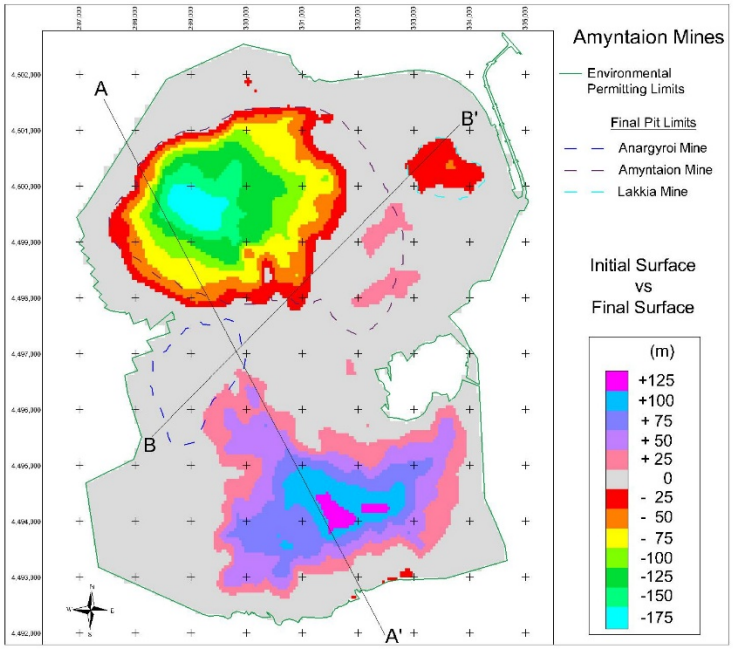

Fig. 10. Spatial differences of the initial and final topography in the Amyntaion mining areas

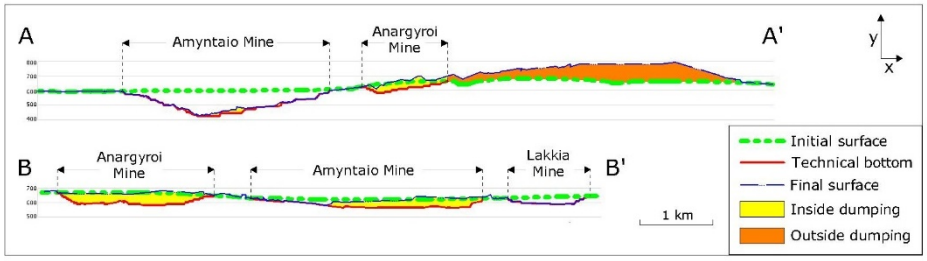

Fig. 11. Cross sections A-A' and B-B' showing the mining sequence

Furthermore, considering the spatial distribution of the waste dumping materials and the planning of post-mining land uses in the waste dumping areas, Figure 12 shows the land uses according to an old planning, the new land uses according to a just transition development plan, and the overlay of the two land uses plans indicating the revised planning based on a sustainable land use planning towards the energy transition in combination with a variety of different uses placing emphasis on the biodiversity. The Just Transition Plan aims to ensure a fair development transition of the lignite area, which is based on three pillars: employment protection, compensation of the socio-economic impact of the transition and energy self-sufficiency of lignite areas and the country at large [18].

Regarding the long-term experimental design for the investigation of the geochemical stability of the waste dumping sites and the perimeter area of the excavation sites, Figure 13 shows the locations of soil and water sampling points. Indicative results of the soil sampling analysis are shown in Figures 14-16.

The soil chemical analyses were conducted in the waste dumping area for systematic measurements of 15 years (2005-2019). The concentration analyses in mineral and non-mineral materials showed that the mining excavation works did not affect the dumping sites, and the soils were not polluted. More specifically, the soil analyses showed that the pH values range from 6.8 to 8.9 with a mean value of 7.3, while the mean electrical conductivity ranges from 120 to 5050 mS/cm, with a mean value of 950 mS/cm. The soil content in $CaCO_3$ ranges from 0.38 to 9.73%, with a mean value of 4.58%. The soil organic content is between less than 0.17 and 2.10%, with a mean value of 0.59% and the NO^{-3} and NH^{+4} concentrations range from 33.33 to 266.67 mg/kg (mean:115.69 mg/kg) and from 5.93 to 230.89 mg/kg (mean: 28.23 mg/kg), respectively. The geotechnical characteristics of the waste dumping materials regard the cohesion with a value range c=0-10 kPa, internal friction angle, φ=22-35° and $\varphi_{residual}$= 10-20°. The unconfined compression strength (Q_u) ranges from 50 to 150 kPa, while the undrained shear strength (C_u) ranges from 25 to 75 kPa.

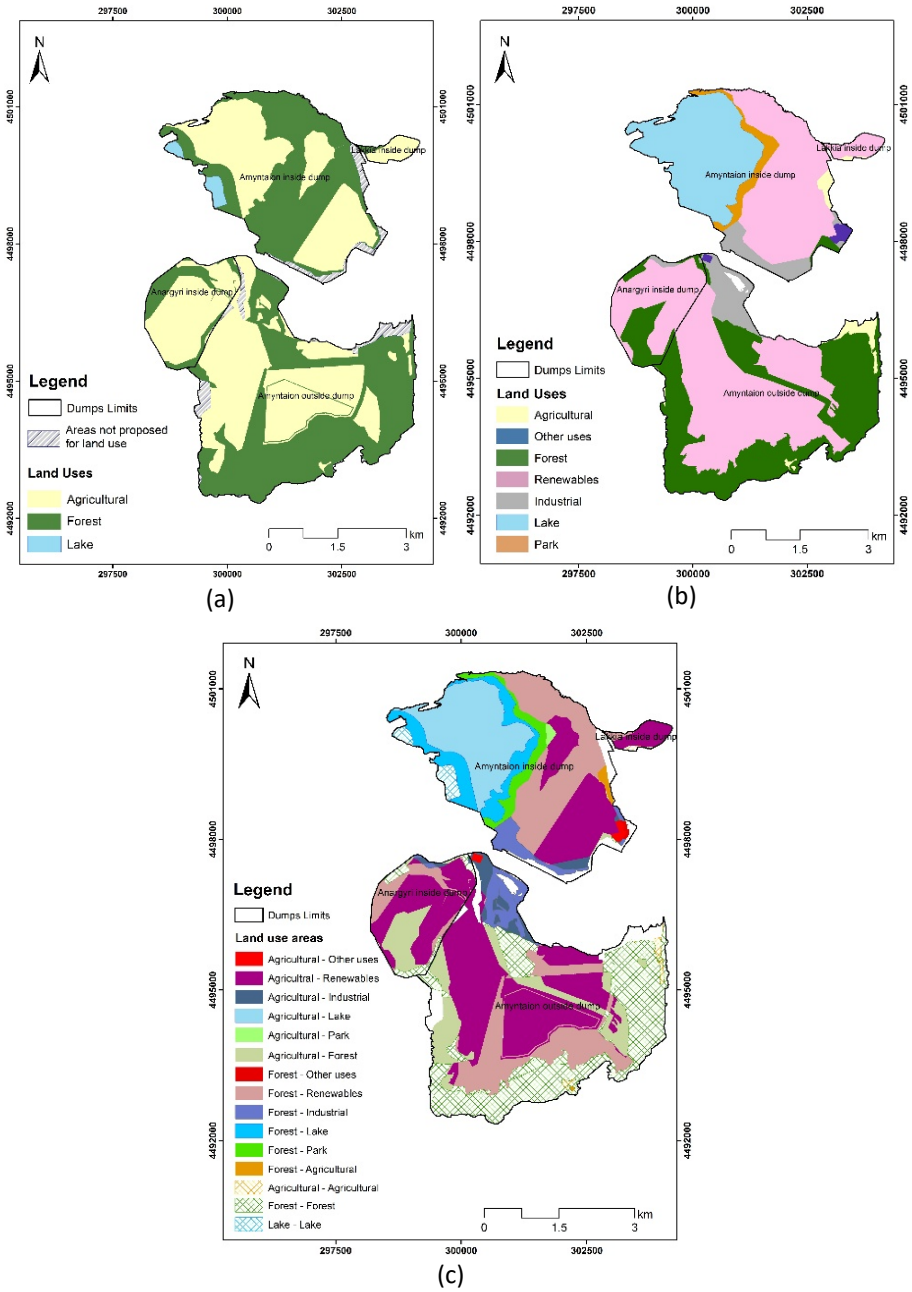

Fig. 12. (a) Land uses according to an old planning, (b) new land uses according to a transition development plan, (c) Overlay of the two land uses plans (only waste dumping sites of the Amyntaion mine)

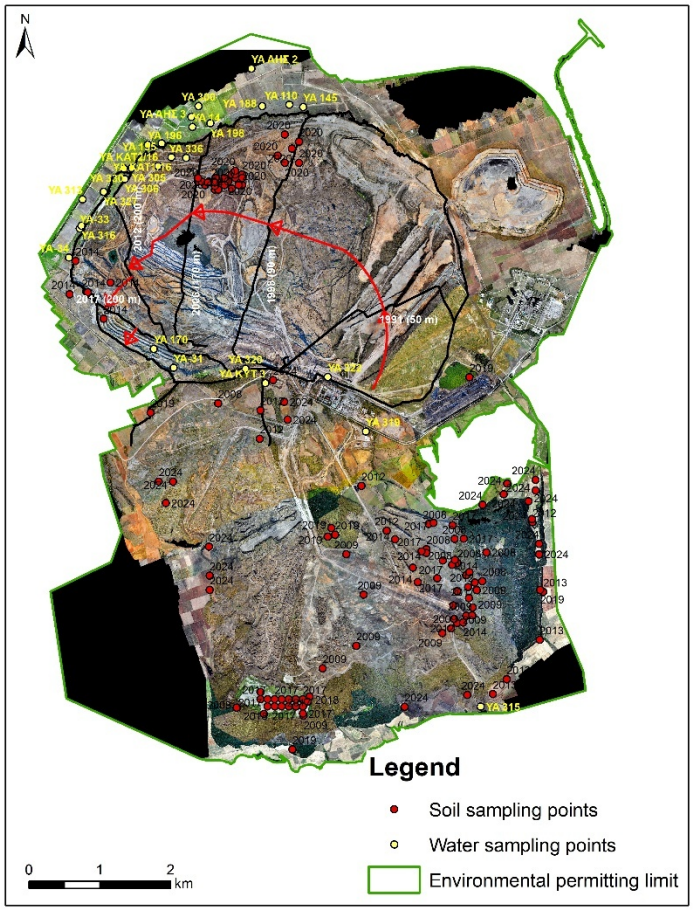

Fig. 13. Experimental design of water and soil sampling and monitoring program (the year in the soil sampling points denotes the starting year of the sampling)

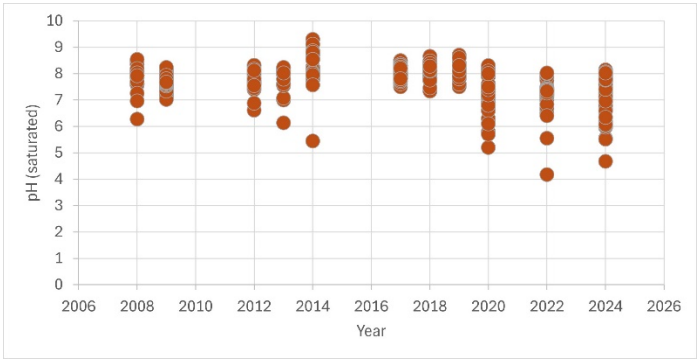

Fig. 14. pH values resulted from soil sampling

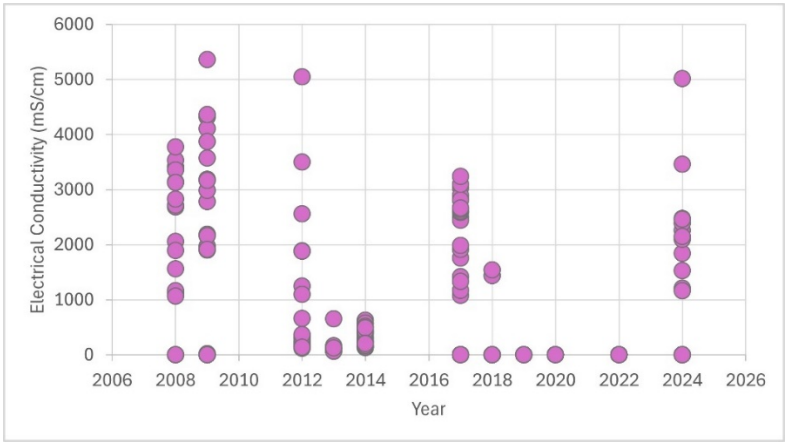

Fig. 15. Electrical conductivity values (mS/cm) resulted from soil sampling

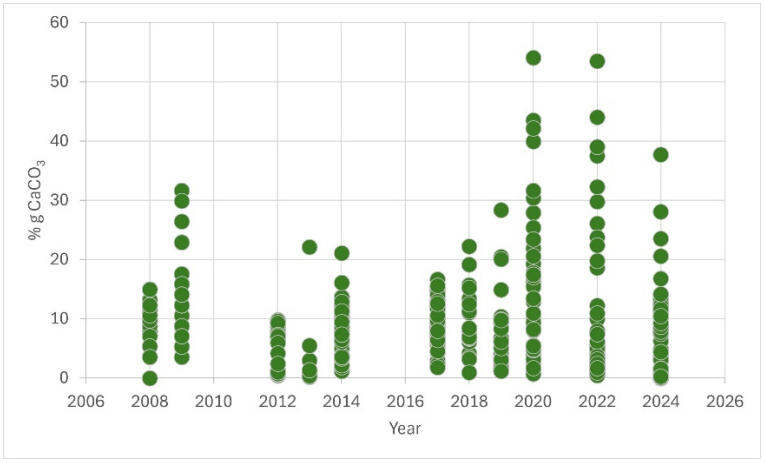

Fig. 16. $CaCO_3$ (%) values resulted from soil sampling

Regarding the groundwater quality, indicative results are shown in Figures 17-21. The results showed that the physicochemical parameters (pH, electrical conductivity, As, Cd, Pb, Hg, Ni, Cr, nitrates, chloride and sulfate ions, ammonium) concentration are inside the legislation's thresholds. For instance, the pH values range from 7 to 8.3, and the electrical conductivity ranges from 500 to 2000 μS/cm, while the bottom and upper threshold for pH are 6.5 and 9.5, respectively, and the upper threshold for electrical conductivity is 2500 μS/cm [10].

From the environmental aspect, all the procedures follow the Approved Environmental Terms. For example, the priority of dumping procedures is to fill the created voids in the exhausted mines and then start the outside dumping. The study of Pavloudakis et al. [19] showed that the air quality parameters correlate better with the total excavations than with the lignite production. In addition, this study showed that the

excavation pits and the dumps of Amyntaion mines are unlikely to cause many pollution episodes.

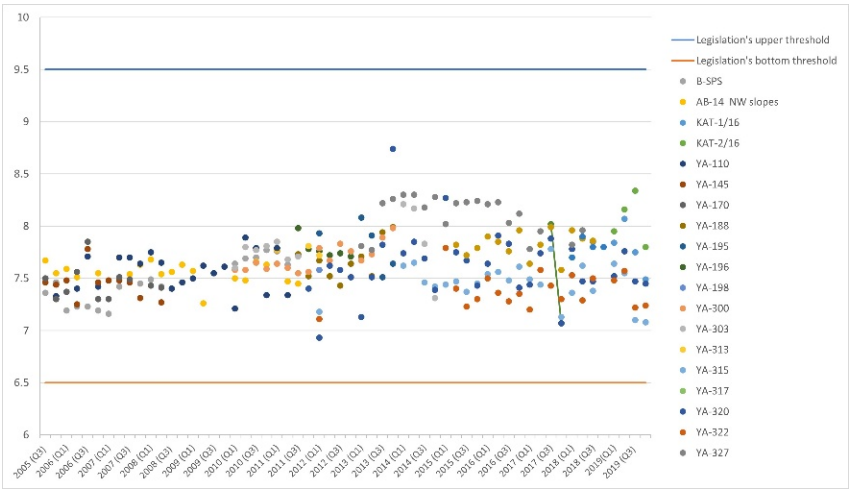

Fig. 17. The values variance of pH resulted from water sampling in water boreholes

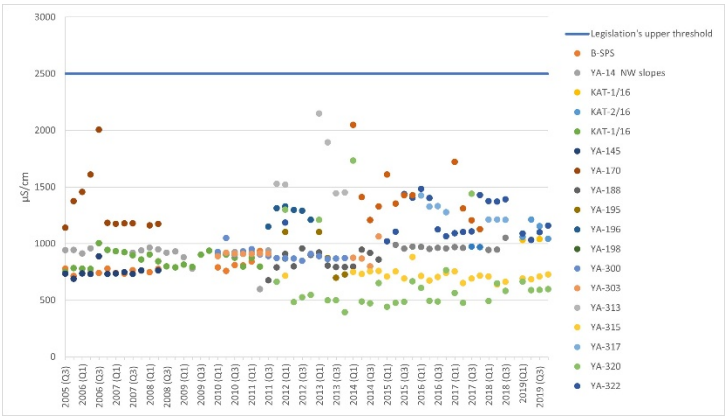

Fig. 18. The values variance of electrical conductivity resulted from water sampling in water boreholes

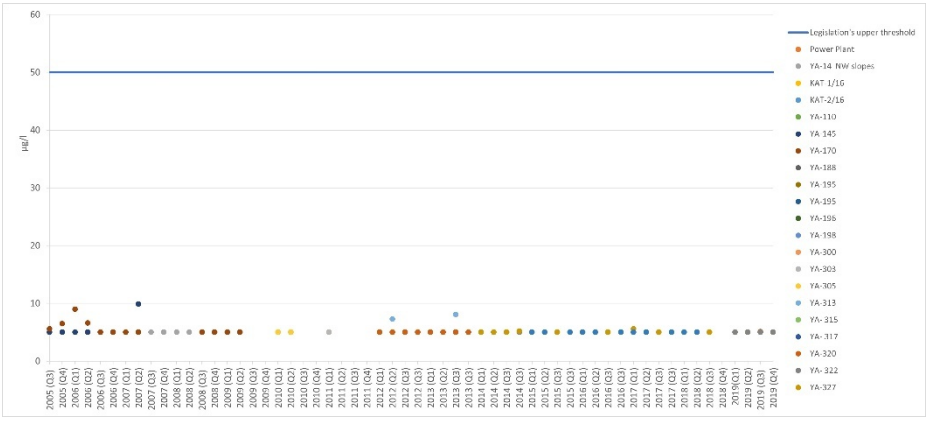

Fig. 19. The values variance of total Cr resulted from water sampling in water boreholes

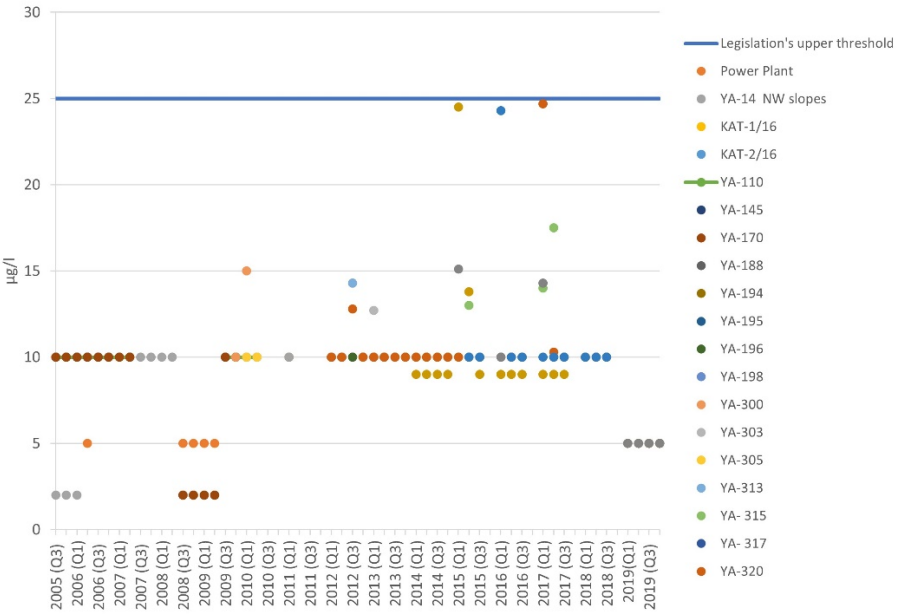

Fig. 20. The values variance of Pb resulted from water sampling in water boreholes

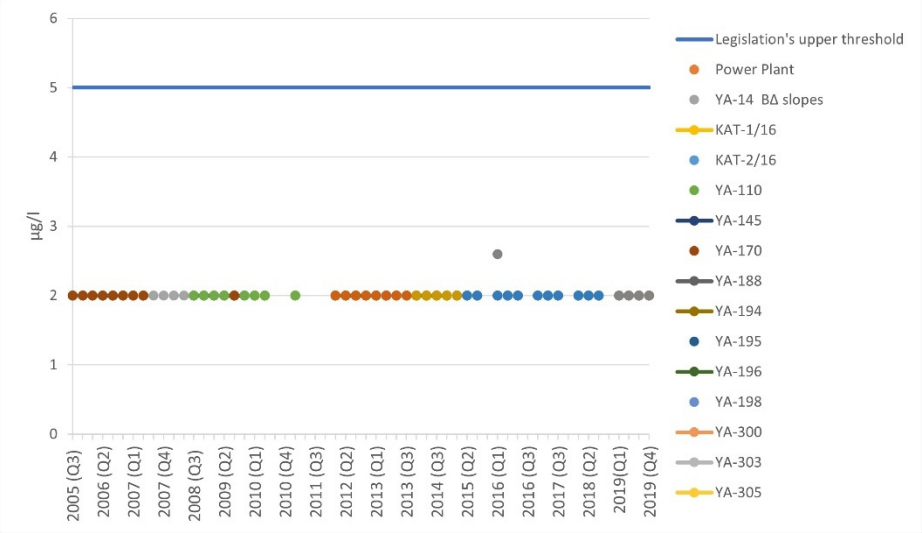

Fig. 21. The values variance of Cd resulted from water sampling in water boreholes

From the results of the soil and water sampling analysis and the geotechnical, hydrogeological, geochemical, and other environmental parameters, the various land uses of post-mining areas are planned based on their suitability to the transition to post-mining activities, emphasizing renewable energy projects. The decision-making process was based on the physical, chemical, biological, and hydrological and hydrogeological stability of the final excavations faces and waste materials dumping sites, as well as on socio-economic considerations. In addition, the transformation of the mining areas to new land uses incorporates circular economy concepts, considering the optimal exploitation of the final topography of the mining areas.

4 Conclusions

Sustainable post-mining waste management in continuous surface coal mines based on circular economy concepts is an essential part of mine closure planning towards a transition to other land uses of mining lands. The planning and scheduling of post-mining activities follows the early stages of strategic mine planning, based on the optimal allocation of the waste material into the outside and inside dumping areas. The success of the long-term mine planning and the following short-term modifications can be validated by suitable mine scheduling models. In the investigated case study of the Amyntaion mine, the physical, chemical, biological, geotechnical, hydrological and hydrogeological stability of the final excavations faces and waste materials dumping sites can be based on a carefully designed sampling and monitoring program. The circular economy principles adopted for this study are based mainly on the utilization of the dumping materials and on the suitable spatial arrangement of the reclamation works which favor

the alternative uses, placing emphasis on renewables in combination with other uses ensuring the biodiversity of the broader mining area.

References

1. Pavloudakis, F., Roumpos, C., Spanidis, PM.: Planning the Closure of Surface Coal Mines Based on Circular Economy Principles. Circ.Econ.Sust. 4, 75–96. https://doi.org/10.1007/s43615-023-00278-x (2024)
2. Fecko, P.; Tora, B.; Tod, M. Coal Waste: Handling, Pollution Impacts and Utilization. In The Coal Handbook: Towards Cleaner Production; Elsevier, 2013; pp. 63–84 ISBN 978-1-78242-116-0 (2013)
3. Eurostat: Total Amount of Waste Generated by Households and Businesses by Economic Activity According to NACE Rev. 2, Mining and Quarrying, (2020)
4. Ru-yin, L., and Xiao-ting, Z.: Negative Entropy Mechanism of the Circular Economy Development Countermeasures in Mining Area. Procedia Environ. Sci. 1 (1): 1678–85. https://doi.org/10.1016/j.proeps.2009.09.258 (2009)
5. Aznar-Sánchez, J., García-Gómez, J., Velasco-Muñoz, J., Carretero-Gómez, A.: Mining Waste and Its Sustainable Management: Advances in Worldwide Research. Minerals 2018, 8, 284, doi:10.3390/min8070284 (2018)
6. Pavloudakis, F., Roumpos, C., Karlopoulos, E., Koukouzas, N.: Sustainable Rehabilitation of Surface Coal Mining Areas: The Case of Greek Lignite Mines. Energies 2020, 13, 3995, doi:10.3390/en13153995 (2020)
7. Kalisz, S., Kibort, K., Mioduska, J., Lieder, M., Małachowska, A.: Waste Management in the Mining Industry of Metals Ores, Coal, Oil and Natural Gas - A Review. J. Environ. Manag 2022, 304, 114239, doi:10.1016/j.jenvman.2021.114239 (2022)
8. European Commission: Circular Economy Action Plan for a Cleaner and More Competitive Europe (2008)
9. Kirchherr, J., Reike, D., Hekkert, M.: Conceptualizing the Circular Economy: An Analysis of 114 Definitions. Resour. Conserv. Recycl. 2017, 127, 221–232, doi:10.1016/j.resconrec.2017.09.005 (2017)
10. European Commission. Directorate General for Environment., Vito: Study Supporting the Development of General Guidance on the Implementation of the Extractive Waste Directive: Final Report.; Publications Office: LU (2021)
11. Sokratidou, A.; Roumpos, C.; Paraskevis, N.; Servou, A.; Pavloudakis, F. Extractive Waste Management in Coal Surface Mining Projects—A Circular Economy Approach. Mater. Proc. 2023, 15, 13. https://doi.org/10.3390/materproc2023015013 (2023)
12. Garbarino E., Orveillon G., Savey H.G.M, Barthe P. & Eder P.: Best available techniques (BAT) reference document for the management of waste from extractive industries, in accordance with Directive 2006/21/EC. JRC science policy report EUR28963 (MWEI BREF). Available at: http://publications.jrc.ec.europa.eu/repository/bitstream/JRC109657/jrc109657_mwei_bref_-_for_pubsy_online.pdf (2018)
13. Vo, T.L., Nash, W., Del Galdo, M., Rezania, M., Crane, R., Nezhad, M.M., Ferrara, L.: Coal mining wastes valorization as raw geomaterials in construction: A review with new perspectives, J. Clean. Prod., 336, 130213, https://doi.org/10.1016/j.jclepro.2021.130213 (2022)
14. Mborah, C., Bansah, K.J. Boateng, M.K.: Evaluating alternate post-mining land-uses: A review. Environ Pollut, 5(1), pp.14-22 (2016).
15. Al Heib, M., Cherkaoui: A. Assessment of the Advantages and Limitations of Installing

PV Systems on Abandoned Dumps. Materials Proceedings, 5(1), 68. https://doi.org/10.3390/materproc2021005068 (2021)
16. Tengler S, Sehnal D.: Method of Solving the Volume Between Triangulated Mesh Surfaces. In: Świątek J, Borzemski L, Grzech A, Wilimowska Z, editors. Information Systems Architecture and Technology: Proceedings of 36th International Conference on Information Systems Architecture and Technology – ISAT 2015 – Part III, vol. 431, Cham: Springer International Publishing; 2016, p. 53–62. https://doi.org/10.1007/978-3-319-28564-1_5 (2016)
17. Yilmaz N. Volume Calculation Through Using Digital Elevation Models Created by Different Interpolation Methods. FIG Congress 2018, Embracing our smart world where the continents connect: enhancing the geospatial maturity of societies, Istanbul, Turkey (2018)
18. Ministry of Environment and Energy. (2020). Just Transition Development Plan of lignite areas. https://www.sdam.gr/sites/default/files/consultation/Master_Plan_Public_Consultation_ENG.pdf
19. Pavloudakis, F., Sachanidis, C., Roumpos, C.: The Effects of Surface Lignite Mines Closure on the Particulates Concentrations in the Vicinity of Large-Scale Extraction Activities. Minerals 2022, 12, 347, doi:10.3390/min12030347 (2022)

The application of data science and machine learning techniques in predicting the compressive strength of confined concrete

C. G. Papakonstantinou [1][0000-1111-2222-3333], M. Valasaki[1][0000-0002-2597-8027]
F. Sofos[2][0000-0001-5036-2120], T. Karakasidis[2][0000-0001-9580-0702]

[1]Department of Civil Engineering, University of Thessaly, Volos, Greece
[2]Department of Physics, University of Thessaly, Volos, Greece
cpapak@uth.gr

Abstract. The integration of machine learning (ML) techniques into industrial and manufacturing applications has seen great growth in recent years. Various numerical and analytical models have been proposed, based either on experimental results or simulation results, and have helped to understand phenomena that take place during the life cycle of a material. In this direction, a large experimental data set to determine the compressive strength of fiber reinforced polymer (FRP) confined concrete specimens has been used as a basis in this work. The obtained measurements are correlated with the mechanical and structural properties of the material and fed into a ML model. The model is trained on the experimental values and can provide predictions for conditions within or outside the value range of the input data. Various ML algorithms are implemented and studied for their prediction accuracy, and the results show that ML can be an important computational tool, which can act as a complement to expensive experiments or time-consuming simulations in engineering sciences.

Keywords: Machine Learning, Data Science, Confined Concrete, Compressive Strength, FRP

1 General

Property extraction in materials science has seen a significant shift in the last decade towards the adoption of techniques based on data science. The large amount of experimental data generated and stored in various databases has enabled scientists and engineers to incorporate this information into innovative statistical techniques and methods. This integration aims to propose new methodologies and materials with enhanced properties, which is especially crucial for technological and scientific advancement. The majority of data-driven methods are based on concepts from artificial intelligence (AI) and machine learning (ML).

The term ML refers to the implementation of a computational model of complex non-linear data-driven relationships and AI is the framework for decision-making and

actions based on ML [1]. ML uses statistical approaches to analyze data with the help of appropriate algorithms and lead to predictions. The two main categories of ML are supervised and unsupervised learning. In supervised ML, the characteristics of the input data are known in advance, while in unsupervised ML, no information is available and the characteristics of the input data need to be searched [2].

Particularly in the field of engineering and construction, ML techniques have been used to predict concrete properties that affect quality measures such as the compressive strength [3,4]. The compressive strength of concrete can indeed be influenced by either the proportions of the constituent materials in the mix or by their mechanical properties. Both factors play a crucial role in determining the overall strength and durability of the concrete structure [5-7]. In this study, we investigate a database where the concrete compressive strength (f_{cc}) is modeled as a function of the mechanical properties of concrete using ML (machine learning) methods. The workflow, depicted in Figure 1, involves normalizing the experimental data and training an ML algorithm. By employing both linear and non-linear approximations, the model determines how input parameters map to the output variable, enabling predictions even when input information is scarce.

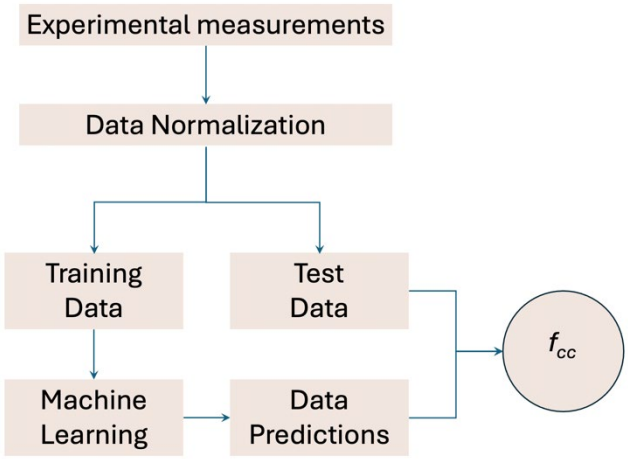

Fig. 1. Property prediction model with ML methods

2 Data Handling

2.1 Database

The dataset comprises experimental records from various concrete specimens, which were confined using different FRP materials—including carbon, glass, and aramid. These specimens span a range of concrete strengths, from low to high. The practice of reinforcing concrete with composite materials has been shown to significantly enhance compressive strength [8] and is widely adopted in construction.

There are eight crucial input parameters related to the mechanical properties of the concrete specimens and the physical and mechanical characteristics of the composites. These parameters directly impact the confined compressive strength. For a detailed breakdown of each parameter, refer to Table 1.

2.2 Data Pre-processing

A total of 1476 experimental measurements are split into two subsets: one for training the ML model and the other for comparison. The division ratio is 80% for training and 20% for comparison. Before feeding the input data to the ML algorithm, it undergoes preprocessing. This preprocessing includes checking for empty or problematic records and applying a normalization step. The normalization aims to restrict the range of input values and is expressed by the following relation:

$$\bar{x} = \frac{x - x_{min}}{x_{max} - x_{min}} \tag{1}$$

In summary, the data is carefully prepared before training the ML model, ensuring its quality and suitability for the algorithm.

Table 1. Description of 8 input parameters and output f_{cc}.

Parameter	Description
D	Concrete specimen diameter (mm)
H	Concrete specimen height (mm)
E_f	Fiber modulus of elasticity (commercial value)
e_{fu}	FRP ultimate axial strain at failure
f'_{co}	Unconfined concrete compressive strength (MPa)
f_{frp}	Ultimate axial FRP stress $f_{frp} = E_{frp}\,\varepsilon_{frp}$ (MPa)
t	Total FRP thickness (mm)
L	FRP number of layers
f_{cc}	Confined compressive concrete strength (MPa)

3 Machine Learning Algorithms

Linear regression, decision trees, and artificial neural networks stand out as some of the most extensively employed machine learning algorithms in the realms of science and technology. This study will scrutinize these three cases by inputting our data, evaluating their performance based on the coefficient R2, mean absolute error (MAE), and mean square error (MSE). The implementation leverages the Python library, sci-kit learn [9].

3.1 Multiple Linear Regression

Linear regression pertains to a method of analyzing the relationship between a dependent variable and a single independent variable. When dealing with multiple input variables, the model is denoted as multiple linear regression (MLR) [9] . In MLR we consider n independent input variables, linearly combined to derive the dependent variable Y as:

$$Y = \sum_{i=1}^{n} w_i X_i \tag{2}$$

Where $w_1, w_2, \ldots, w_n$ are the weight for each independent input $X_1, X_2, \ldots, X_n$. The method is shown graphically in Figure 2(a).

3.2 Decision Trees

The Decision Trees (DT) algorithm operates in the structure of a tree diagram, encompassing nodes, branches, and leaves (Figure 2(b)). Each node signifies a test conducted on a feature, and each branch represents the outcome of that test. The DT model's response follows the decisions made from the initial node to the terminal node (leaf). The feature space undergoes recursive partitioning based on the partition feature. A value is assigned to each terminal region for estimating the target output. Despite its ease of implementation, it's worth noting that input from other statistical methods may be required to prevent overfitting in the DT algorithm [11]. The use of decision trees can be advantageous compared to other algorithms, since decision trees are relatively robust to outliers, as the splitting criteria focus on dividing the data into homogenous sets. They are quite simple but powerful tools that model decisions and their potential outcomes. Techniques like pruning and ensemble methods can be used to address their limitations and increase their efficiency. Decision trees are adaptable, easy to understand, and user-friendly machine learning algorithms, that are effective for both classification and regression tasks.

3.3 Perceptron Algorithm

When arranged in multiple layers, such as input, output, and various internal hidden layers (Figure 2(c)), the conventional perceptron evolves into a neural network commonly known as a multi-layer perceptron (MLP). The determination of the number of hidden layers typically involves an iterative trial-and-error process. The data flow between neurons is contingent upon activation functions applied to each internal node and a weight function imposed on each input. These weights undergo adjustments to ensure that the predicted output closely resembles the expected output with minimal error. The training of the multi-layer perceptron (MLP) occurs iteratively, employing a backward calculation process. Despite being the favored choice in concrete property prediction applications, MLPs remain widely popular due to their effectiveness in minimizing error prediction through iterative adjustments [12,13], their multiparameter implementation can create difficulties in model convergence, trapping in local minima and over-

modelling [14]. In this study, a neural network comprising three hidden layers, each consisting of 20 nodes (20,20,20), was employed.

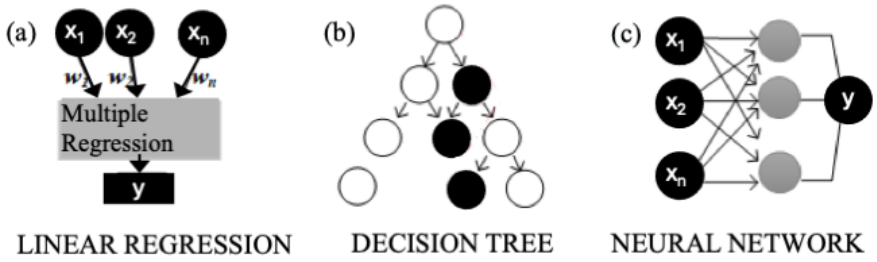

Fig. 2. ML algorithms, a) multiple linear regression, b) decision tree, c) neural network

4 Results and Discussion

Following the application of the three representative machine learning algorithms to predict the compressive strength behavior based on eight distinct mechanical and structural material characteristics, the regression results are presented in Figure 3. The accuracy of the predictions is contingent on the distance of the data points from the central 450 line.

The linear regression model (Figure 3a) demonstrates moderate performance, whereas the neural networks (Figure 3c) exhibit notably accurate results, achieving an R2 value of 0.927. The highest level of accuracy, however, is observed in the decision tree model, attaining an R2 value of 0.960. (Figure 3b). Additional measures of accuracy (mean absolute error and mean squared error) are given in Table 2. Based on these criteria, decision trees emerge as the optimal choice for handling this particular type of input data.[15].

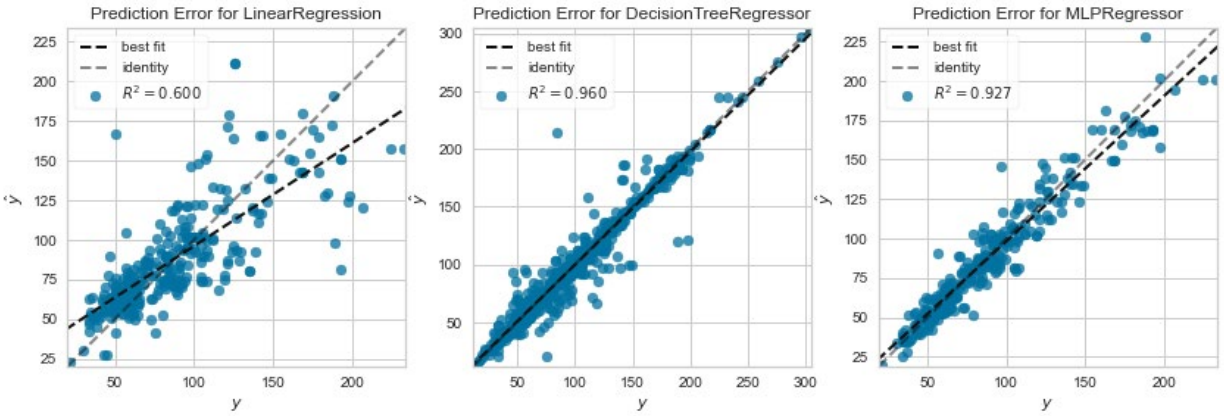

(a) (b) (c)

Fig. 3. Regression results for the ML algorithms, a) multiple linear regression, b) decision tree, c) neural network, showing the fit of the experimental value (y) to the predicted value ($\hat{y}$).

Table 2. Accuracy measures for each ML method

Model	MAE	MSE
MLR	18.05	667.46
DT	9.33	233.48
MLP	10.27	236.63

5 Conclusions

Machine Learning Algorithms presented in this paper have shown that they are able to provide accurate predictions of compressive strength based on an eight-variable parameter space, even in the presence of significant noise in the observations, due to the experimental measurements. Additionally, we have demonstrated that machine learning algorithms based on decision trees exhibit strong performance when compared to conventional linear models. Due to their ease of implementation in contrast to intricate neural network architectures, decision tree-based models can be seamlessly integrated into comparable applications.

In conclusion, it becomes clear that statistical and machine learning techniques could potentially be applied to many real-life applications, overcoming the traditional route, which, most of the time, requires either expensive experiments or time-consuming, computationally intensive techniques. Along with knowledge of the physical problem, ML could contribute to the development of existing techniques and thus could be integrated into traditional scientific and technological methods.

References

1. Dimiduk DM, Holm EA, Niezgoda SR. Perspectives on the Impact of Machine Learning, Deep Learning, and Artificial Intelligence on Materials, Processes, and Structures Engineering. Integrating Materials and Manufacturing Innovation 2018; 7(3): 157–172. DOI: 10.1007/s40192-018-0117-8
2. Wang T, Zhang C, Snoussi H, Zhang G. Machine Learning Approaches for Thermoelectric Materials Research. Advanced Functional Materials 2020; 30(5): 1906041. DOI: https://doi.org/10.1002/adfm.201906041
3. Cook R, Lapeyre J, Ma H, Kumar A. Prediction of Compressive Strength of Concrete: Critical Comparison of Performance of a Hybrid Machine Learning Model with Standalone Models. Journal of Materials in Civil Engineering 2019; 31(11): 04019255. DOI: 10.1061/(ASCE)MT.1943-5533.0002902
4. Sofos F, Papakonstantinou CG, Valasaki M, Karakasidis TE. Fiber-Reinforced Polymer Confined Concrete: Data-Driven Predictions of Compressive Strength Utilizing Machine Learning Techniques. Applied Sciences. 2023; 13(1):567. https://doi.org/10.3390/app13010567
5. Young BA, Hall A, Pilon L, Gupta P, Sant G. Can the compressive strength of concrete be estimated from knowledge of the mixture proportions?: New insights from statistical analysis and machine learning methods. Cement and Concrete Research 2019; 115: 379–388. DOI: 10.1016/j.cemconres.2018.09.006
6. Asteris PG, Skentou AD, Bardhan A, Samui P, Pilakoutas K. Predicting concrete compressive strength using hybrid ensembling of surrogate machine learning models. Cement and Concrete Research 2021; 145: 106449. DOI: 10.1016/j.cemconres.2021.106449
7. Słoński M. A comparison of model selection methods for compressive strength prediction of high-performance concrete using neural networks. Computers & Structures 2010; 88(21): 1248–1253. DOI: 10.1016/j.compstruc.2010.07.003
8. Papakonstantinou, C.G. Fiber Reinforced Polymer (FRP) Confined Circular Columns: Compressive Strength Assessment. Journal of Engineering Science & Technology Review 13.6, 2020.DOI: 10.25103/jestr.136.01
9. Pedregosa F, Varoquaux G, Gramfort A, Michel V, Thirion B, Grisel O, et al. Scikit-learn: Machine Learning in Python. Journal of Machine Learning Research 2011; 12(85): 2825–2830
10. Sofos F, Karakasidis TE. Machine learning techniques for fluid flows at the nanoscale. Fluids 2021; 6(3). DOI: 10.3390/fluids6030096
11. Schmidt J, Marques MRG, Botti S, Marques MAL. Recent advances and applications of machine learning in solid-state materials science. Npj Computational Materials 2019; 5(1): 1–36. DOI: 10.1038/s41524-019-0221-0
12. Ikumi T, Galeote E, Pujadas P, de la Fuente A, López-Carreño RD. Neural network-aided prediction of post-cracking tensile strength of fibre-reinforced concrete. Computers & Structures 2021; 256: 106640. DOI: 10.1016/j.compstruc.2021.106640
13. Roberson MM, Inman KM, Carey AS, Howard IL, Shannon J. Probabilistic neural networks that predict compressive strength of high strength concrete in mass placements using thermal history. Computers & Structures 2022; 259: 106707. DOI: 10.1016/j.compstruc.2021.106707
14. Nguyen H, Vu T, Vo TP, Thai HT. Efficient machine learning models for prediction of concrete strengths. Construction and Building Materials 2021; 266: 120950. DOI: 10.1016/j.conbuildmat.2020.120950

15. Sofos F, Stavrogiannis C, Exarchou-Kouveli KK, Akabua D, Charilas G, Karakasidis TE. Current Trends in Fluid Research in the Era of Artificial Intelligence: A Review. Fluids 2022; 7(3): 116. DOI: 10.3390/fluids7030116

Sustainable Development

Gold recovery from pressure oxide residues using thiosulfate

Christiana Mystrioti[1*], Konstantina Kousta[1], Nymphodora Papassiopi[1], Katerina Adam[1], Maria Taxiarchou[1], Ioannis Paspaliaris[1]

[1]School of Mining and Metallurgical Engineering National Technical University of Athens.
*chmistrioti@metal.ntua.gr

Abstract. Considering the toxicity and environmental problems created using cyanide in industrial applications of gold extraction, intensive research has been developed during the decades for identifying new effective reagents able to replace cyanide in gold extraction operations. The high thermodynamic stability of gold complexes with certain compounds is the first prerequisite for the selection of a promising extractant. The stability of gold-thiosulphate complex, though considerably lower than that of cyanide, is the highest amongst other alternative ligands, and for this reason it has been thoroughly investigated with laboratory and pilot scale tests. Ca-thiosulphate salt was selected for evaluation in the framework of the present work, as a promising cyanide-free alternative for obtaining the recovery of gold from the pressure oxidation (POX) residue of gold bearing sulfide concentrates. Thiosulfate leaching experiments were carried out, examining variables including initial thiosulfate concentration, initial pH, temperature, and solid-liquid mixing ratio (S/L). Findings reveal promising gold recovery rates with potential optimization through parameter adjustments. The objective of this research is to offer valuable insights into the feasibility of employing thiosulfate as a gold recovery agent, advocating environmentally conscious practices in the metallurgical industry and addressing challenges linked to pressure oxidation residues.

Keywords: calcium thiosulfate; gold extraction; pressure oxidation residues; gold bearing sulfide concentrates, cyanide free gold recovery.

1 Introduction

Cyanide was the ultimate gold extractant for many years until the environmental concerns surrounding its use, particularly its toxicity to humans and aquatic life, came to light. As a result of these risks, many countries have banned the use of cyanide in gold mining. In the United States, for example, the Environmental Protection Agency (EPA) has banned the use of cyanide in new gold mining operations by 1979[1,2]. The search for cyanide-free lixiviants for gold recovery has gained significant momentum in recent years due to the environmental concerns associated with cyanide usage [3-5]. A plethora of alternative lixiviants have emerged as promising replacements for

cyanide, offering potential advantages in terms of environmental friendliness, safety, and applicability to a wider range of ores. Thiosulfate, thiourea, ammonia, thiocyanate, citric and ascorbic acid have been evaluated as alternative agents [6,7].

Among these alternative lixiviants, thiosulfate stands out as a prominent candidate. Thiosulfate exhibits low toxicity, biodegradability, and the ability to leach gold from various ore types, including refractory sulfide ores that are challenging to treat with cyanide [3-5]. Additionally, thiosulfate-based processes have demonstrated promising economic viability. Thiosulfate is already being used in some gold mining operations, and it is likely to become more common in the future. Barrick Gold's (Goldstrike mine in Nevada, USA) developed a commercial scale, thiosulfate-based process for gold extraction, in 2015 [8]. Compared to cyanide leaching, the thiosulfate system exhibits increased complexity in its underlying chemistry. However, through meticulous control of key parameters such as redox potential (Eh), pH, and the concentrations of thiosulfate, oxidant, and oxygen within the leaching solution, it is possible to achieve high levels of gold extraction with comparatively low reagent consumption for certain types of ore [9].

The investigation of the thiosulfate system for gold extraction has encompassed a diverse array of oxidants. These potential oxidizing agents include molecular oxygen, copper(II) ammine complexes, cobalt(III) ammine complexes, and various iron(III) complexes [5]. In solutions with alkaline or neutral pH values, containing thiosulfate, gold exhibits gradual dissolution in the presence of an oxidizing agent [5,10]. This dissolution of gold is an electrochemical phenomenon, characterized by the involvement of oxygen as the oxidant and thiosulfate as the ligand [5,11]:

$$4Au + 8\,S_2\,O_3^{2-} + \,O_2 + \,2H_2O = \,4Au\,(S_2O_3)_2^{3-} + 4\,OH^- \quad (1)$$

The oxidation of metallic gold to the aurous Au+ ion in 0.10 M ammoniacal thiosulfate in the presence of Cu(II) occurs at Eh of 0 V and can be simply represented by the following reactions:

$$Au + 5\,S_2O_3^{2-} + \,Cu(NH_3)_4^{2+} = Au\,(S_2O_3)_2^{3-} + 4\,NH_3\, + Cu\,(S_2O_3)_3^{5-} \quad (2)$$

and

$$4\,Cu\,(S_2O_3)_3^{5-} + \,16NH_3 + \,O_2\, + \,2H_2O \\ = 4\,Cu\,\,(NH_3)_4^{2+} + 4OH^- + 12{S_2O_3}^{2-} \quad (3)$$

The mechanism involves the formation and absorption of mixed Cu(II) ammonia thiosulfate complexes on the gold surface with simultaneous oxidation of gold [12-16]. Cu(II) is used as a catalyst for this reaction at concentrations 10-3 to 10-4 M (60-6 ppm) [17], with oxygen acting to reoxidize Cu(I) to Cu(II). Nevertheless, the dissolution of gold by thiosulfate is subject to passivation, influenced by the presence of various cations (e.g. Fe and Ag) and chemical species such as humic acid or ammonia in the leaching solution. This passivation occurs mainly due to the accumulation of sulfur coatings resulting from the decomposition of thiosulfate on the gold surface [5, 18-20]. The use of CaS2O3 salt instead of NaS2O3 or (NH4)2S2O3 salt in the leaching has beneficial effects on gold extraction, where calcium appears to prevent the formation of thiosulfate

degradation products on the gold surface and assists in the maintenance of a constant and high leaching rate during prolonged leaching [21]. The use of calcium thiosulfate and copper as catalyst without any ammonia is the basis of Barrick Gold's commercial-scale thiosulfate plant for treating carbonaceous ores [22, 23].

The dissolution rates of gold using calcium thiosulfate surpass those achieved with sodium thiosulfate, exhibiting considerable acceleration under all comparable conditions, particularly in the presence of Cu(II) and/or sulfide minerals. This can be explained by the stronger affinity between thiosulfate ions and the divalent cation Ca2+, resulting in the formation of ion pairs, which appears to be more robust compared to the interaction between thiosulfate ions and monovalent cations. Divalent cation-thiosulfate complexes exhibit higher equilibrium constants compared to their monovalent counterparts [13,14,24]. In the study by Feng and van Deventer (2010), enhanced gold recoveries were noticed when treating sulfide and pyrite concentrate using calcium thiosulfate salt [21]. Their experimental work involved the use of ammonium and Cu(II) at a pH of approximately 11.5. It should be mentioned that without ammonia, copper exists solely as Cu(I)-thiosulfate, lacking oxidizing properties. Consequently, the role of copper differs in the thiosulfate-oxygen system compared to the copper-ammoniacal thiosulfate system. In the latter, calcium interacts with anionic Cu(I)-S2O3 complexes in the solution, maintaining a higher solution potential. Calcium can also act as stabilizer before the formation of Au(S2O3)23- [16]. In another study, leaching tests were implemented by mixing pressure-oxidized carbonaceous ore residues (supplied by Goldstrike ore in Nevada, USA) with calcium thiosulfate and in presence of Cu(II) at a pH value of 8 and a temperature of 50°C [23]. The gold recovery was around 80% with addition of resin in leach. Conducting leaching tests for gold recovery in lower pH prevents gypsum formation and precipitation on ore particles in the presence of calcium. The evaluation of oxygen-calcium thiosulfate system using the electrochemical rotating disc technique to an oxide ore was investigated by Zhang et al. (2014) [25]. Results from this study indicated that a combination of Cu(II), high temperature, and the use of CaS2O3 over sodium enhanced the gold dissolution rate.

The chemistry of the thiosulfate system is relatively complicated. However, by properly maintaining and controlling the leaching parameters, high gold extractions can be achieved with low reagent consumption for some auriferous ores. Various additives have been suggested for inclusion in the thiosulfate leaching system to enhance gold recovery and decrease reagent consumption, but their success varies [5]. The use of CaS2O3 salt in the leaching stage has beneficial effects on gold extraction during the treatment of a sulfide and pyrite concentrate, as calcium appears to prevent the formation of thiosulfate degradation products on the gold surface and assists in the maintenance of a constant and high leaching rate during prolonged leaching. The effectiveness of applying thiosulfate to different ore types will vary, and the leaching conditions must be customized to accommodate each specific application [5].

Calcium thiosulfate was evaluated in the framework of the present study, as a promising non-cyanide reagent for the recovery of gold from the pressure oxidation (POX) residue of gold bearing sulfide concentrates. The investigated parameters included CaTS concentration, 0.05-0.15 M, initial pH of the slurry, 7- 10, temperature, 30-50oC, and solid to liquid ratio, 10-30%. All the experiments were carried out using a constant

Cu(II) concentration, 0.8 mM. The effect of treatment duration was also examined for all the above operating conditions, conducting tests with a total duration of 2, 6 and 24 hours.

2 Materials and Methods

2.1 Materials

Pressure oxidation residue (POX)

The gold recovery by CaTS was evaluated at a sample of the pressure oxidation residue from Olympias mixed concentrate produced by Metso-Outotec under the following conditions S/L=14%, T=200oC, pO2=400 kPa, t=3 h. The pressure oxidation residue and the mixed concentrate were characterized by X-ray diffraction (XRD) analysis and XRF analysis. The XRD analysis was performed using a Rigaku MiniFlex benchtop XRD and at a scan speed of 1° min -1. XRF analysis was conducted using SPECTRO XEPOS energy dispersive X-ray fluorescence (ED-XRF) spectrometer.

Chemicals

The following chemicals were used during the tests: calcium thiosulphate, pure 30-50% solution in water (Thermoscientific, Belgium), copper sulphate pentahydrate (ChemLab, Belgium), calcium hydroxide, >95% (ChemLab, Belgium). The reagents used for the determination of calcium thiosulphate (CaTS) concentration included the following chemicals: sodium thiosulphate pentahydrate >99% (Alfa Aesar, Germany), starch (ChemLab, Belgium), potassium iodate for analysis, (Sigma Aldrich, Canada), potassium iodide for analysis (Merck, Germnay). Some leaching experiments were carried out in the presence of resin (resin in leach tests). The type of resin used was Puromet MTA5011 and was kindly provided for free by Purolite Company.

2.2 Experimental conditions

The central operating conditions used during the experimental work were as follows: solid-liquid ratio, S/L=20% w/v, pH=7.0, initial concentration of calcium thiosulphate, CaTS, equal to 0.1 M, Cu(II) concentration 0.8 mM, temperature T=40oC.

The investigated parameters included the initial concentration of CaTS, 0.05, 0.10 and 0.15 M, the initial pH 7, 8.5 and 10, the solid to liquid ratio, 10, 20 and 30 % w/v and the operating temperature 30, 40 and 50oC. A resin in leach (RIL) test was also implemented at central experimental conditions by adding the anionic resin Purogold MTA5011 in the pulp (100 g/L), during the leaching of POX-mixed with CaTS.

All the experiments were carried out using a constant concentration of Cu(II)= 0.8 mM (50 mg/L). The effect of treatment duration was also investigated under all the examined conditions, by conducting tests with a total duration of 2, 6 and 24 hours. The experimental conditions are summarized in Table 1.

Table 1. Experimental conditions of leaching tests (Cu(II)= 0.8 mM, t=2, 6 and 24 hours)

No	S/L, %	T, ^{o}C	pH	CaTS, M	Other
1	20	40	7	0.1	
2	20	40	8.5	0.1	
3	20	40	10	0.1	
4	20	40	7	0.05	
5	20	40	7	0.15	
6	20	30	7	0.1	
7	20	50	7	0.1	
8	10	40	7	0.1	
9	30	40	7	0.1	
10	20	40	7	0.1	Resin in leach*

* Addition of Purogold MTA5011 (100 g/L)

2.3 Experimental procedure

The experiments were carried out in shaking flasks of 250 mL capacity. For the preparation of experimental slurries 20 g of POX were mixed with 50 mL of deionized water (DW). The pH of the slurry was raised to the target pH value, 7, 8.5 or 10, by adding dropwise a Ca(OH)2 solution (the supernatant of 1% w/v lime suspension). After that step, 10 mL of concentrated CaTS (0.5, 1 or 1.5 M) and 1 mL of 80 mM CuSO4 were added in the slurry. Deionized water (DW) was added until the final volume of leaching solution was equal to 100 mL. The conical flasks were placed into an incubator, maintaining constant temperature conditions, and applying an agitation of 250 rpm. After the end of predetermined leaching duration (2h, 6h and 24h), the shaking flasks were removed from the incubator and the solids were separated from the leachate by vacuum filtration. Some batch experiments were conducted in duplicates to evaluate the repeatability of leaching tests.

2.4 Sampling and Analyses

The leachate solution was analyzed for pH, oxidation reduction potential (ORP) and dissolved oxygen (DO). The pH of leachate solution was measured using the pH meter Metrohm 827 pH Lab, the dissolved oxygen was analyzed by Microprocessor oximeter (OXI 196, WTW) and the ORP was determined using Hach multipolymeter HQ40d. A part of the solution was kept for metal analysis (Au, Cu, Fe, As, Zn, Pb and Si) by using atomic absorption spectrometer, Perkin Elmer PinAAcle 900T. The calcium thiosulphate concentration in the leachate solution was analyzed by iodometric titration. Solid residues were washed with distilled water and were kept in the oven for 24 h, at 100oC, to be completely dried. The dried solid residues were analyzed for their Au content.

The Au at solid residues was determined by wet acid digestion method with aqua regia combined with solvent extraction with MIBK.

3 Results

Characterization of the Olympias concentr1ate and pressure oxidation residue

The composition of the Olympias mixed concentrate and of the POX residue is shown in Table 2. The gold content in the sulphide concentrate was close to 20 mg/t. A higher gold content in POX equal to 45.4g/t was determined.

Table 2. Chemical composition of Olympias concentrated and of the POX-residue

	Olympias concentrate	**POX-residue**
Element (%)		
Fe	33.9	20.5
As	11.1	14.9
S	33.3	
S(SO_4)		4.36
Ca	2.21	3.38
Pb	0.62	1.50
Au (g/t)	**19.9**	**45.4**

The crystalline phases identified in the sulphides were pyrite, arsenopyrite, calcite, dolomite and quartz (Table 3). The approximate content was calculated based on the chemical composition of the samples. In the pressure oxidation residues, the only arsenic containing phase detected in the XRD patterns was a compound reported as Basic Ferric Arsenate-Sulfate (BFAS, Fe(AsO4)(1-x)(SO4)x(OH)x) in the relevant literature.

Table 3. Crystalline phases identified by XRD and approximate modal composition of the feed material (Olympias concentrate**)** and pressure oxidized residue (POX)

Crystalline phases	Name	Pdf**		
Sulphides			**Olympias concentrate**	
FeS_2	Pyrite	71-1680	54.2	
FeAsS	Arsenopyrite	42-1320	22.3	
$CaCO_3$	Calcite	72-1652	3.77	
$CaMg(CO_3)_2$	Dolomite	75-1656	2.91	
SiO_2	Quartz	46-1045	11.1	
Oxidized residue				**POX**
$Fe(AsO_4)_{(1-x)}(SO_4)x(OH)x$	BFAS*	na		51.1
$H_3OFe_3(SO_4)_2(OH)_6$	H_3O-jarosite	36-0427		5.0
$Fe(OH)_3$	Bernalite	46-1436		9.79
$CaSO_4.2H_2O$	Gypsum	76-1746		14.5
$CaSO_4$	Anhydrite	37-1496		
SiO_2	Quartz	46-1045		19.6

* BFAS: Basic Ferric Arsenate Sulfate, XRD data from relevant publications (Papassiopi et al., 1994, Dutrizac & Jambor, 2007)

** Powder Diffraction File, produced by the International Centre for Diffraction Data (ICDD), in Crystallographica Search-Match (*CSM*) database

Effect of pH

Variation of pH as a function of time

The tests were carried out adjusting the initial pH at three different values, namely 7, 8.5 and 10. However, the pH was not maintained constant during the experiments. As shown in Figure 1, the trend of pH evolution was augmentative in the case of initial pH 7.0 and after 24 hours reached the value 8.0. The tests carried out with initial pH 8.5 presented a relatively small fluctuation as a function of time and after 24 hours the pH was equal to 8.3. The most important variation was observed in the case of initial pH 10, where pH dropped to 8.5 after 24 hours.

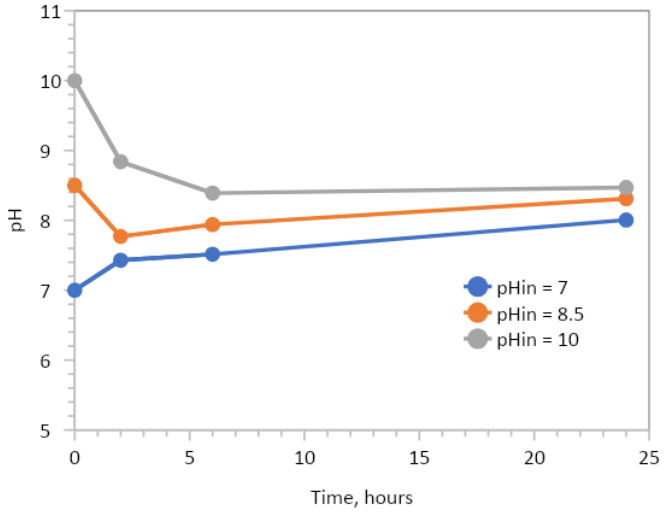

Fig. 1. Time evolution of pH in the tests carried out with different initial pH values (0.1M CaTS, 40°C, S/L = 20%)

Effect of initial pH on gold leaching

The extraction of gold as a function of time during the tests carried out with different initial pHs is shown in Figure 2. The highest extraction achieved was equal to 40.6% and was observed in the tests with initial pH 7.0 at 6 hours. When the duration of treatment extended from 6 to 24 hours, gold leaching decreased from 40.5% to 34.8%. When the initial pH was adjusted to higher values, i.e., 8.5 and 10, the kinetics of gold extraction was clearly slower.

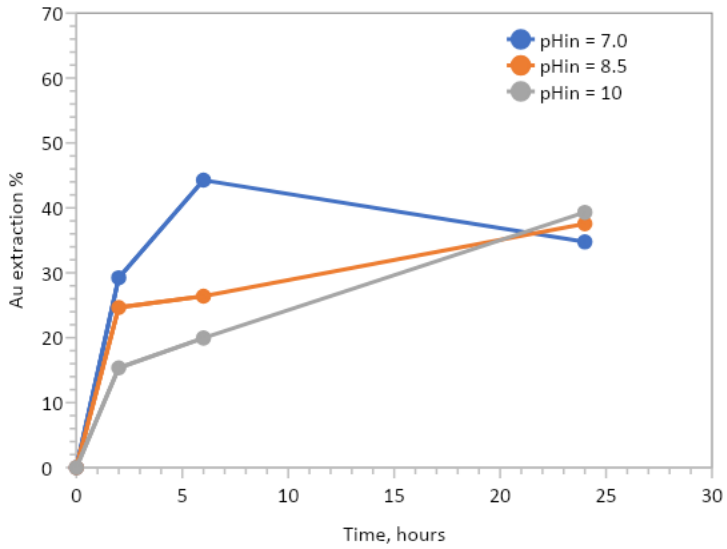

Fig. 2. Effect of initial pH on gold leaching (0.1M CaTS, 40°C, S/L = 20%)

Evolution of CaTS concentration

The evolution of thiosulphate concentration is shown in Figure 3. The observed fluctuations are partially due to the instability of titrations reagent. The results of 24 hours suggest a relative decrease of thiosulphate concentration, when the pH decreased from 10 to 7. Namely the concentration of thiosulphate remained constant in the test with initial pH 10, decreased by 10% in the test with initial pH 8.5 and by 20% in initial pH 7.

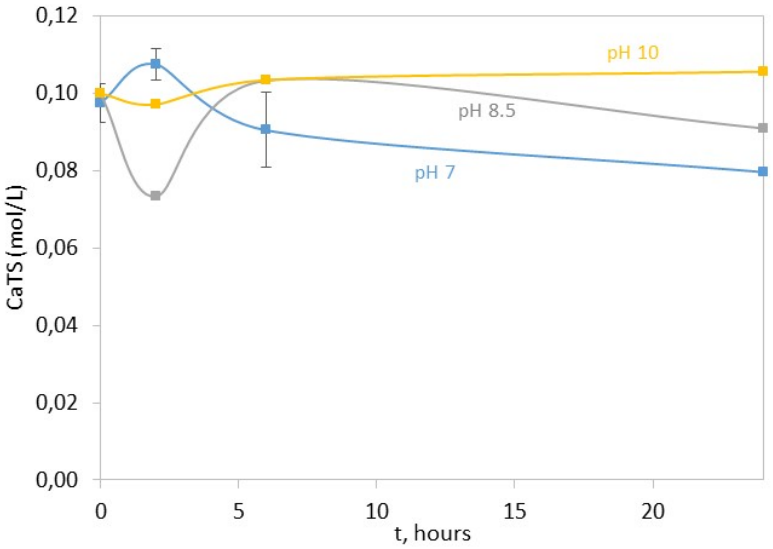

Fig. 3. Concentration of thiosulphates in the experiments with different initial pH (0.1M CaTS, 40°C, S/L = 20%)

Effect of initial pH on the release of arsenic

The concentrations of As in the tests carried out with different initial pHs are shown in Figure 4. After 6 hours, arsenic concentration ranged between 46 and 49 mg/L in the tests with initial pH 10, while in the tests with initial pH 7 and 8.5 ranged between 37 and 43 mg/L. Taking into consideration that POX-mixed contains 15% As and that the experiments were carried out with 20% pulp density it is calculated that As release is in the order of 0.12-0.16%.

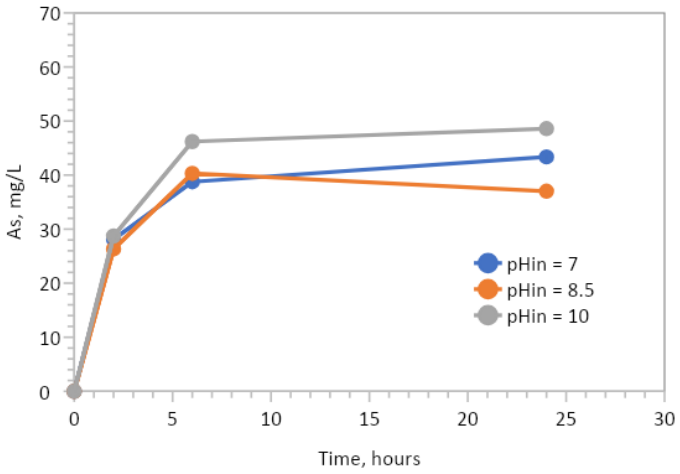

Fig. 4. Effect of initial pH on the release of As (0.1M CaTS, 40°C, S/L = 20%)

Concentration of Cu

All the tests were carried out with addition of 0.8 mM Cu(II), i.e. 50 mg/L. The concentrations measured in the leaching solutions at all treatment times and all initial pH values ranged between 2.1 and 3.1 mg/L (Figure 5.). The results suggest that copper is not maintained in solution in this specific system.

The catalytic role of Cu(II) during the leaching of gold with thiosulphate has been extensively studied [15,16,21]. In most studies, leaching was carried out in the presence of free ammonia, NH3, at levels varying from 0.4 up to 3 M. The catalytic role of Cu in the presence of NH3 is represented in equations (4) and (5).

$$Au + 5\ S_2O_3^{2-} + Cu(NH_3)_4^{2+} = Au(S_2O_3)_2^{3-} + 4\ NH_3 + Cu(S_2O_3)_3^{5-} \quad (4)$$

$$4\ Cu(S_2O_3)_3^{5-} + 16\ NH_3 + O_2 + 2\ H_2O = 4\ Cu(NH_3)_4^{2+} + 4OH^- + 12\ S_2O_3^{2-} \quad (5)$$

In the above studies, copper was added to the solution at levels varying between 0.5 and 10 mM (32-636 mg/L) and was maintained in solution, even at strong alkaline pHs, due to the formation of strong aqueous complexes with ammonia, as Cu(II), or with thiosulphates, as Cu(I).

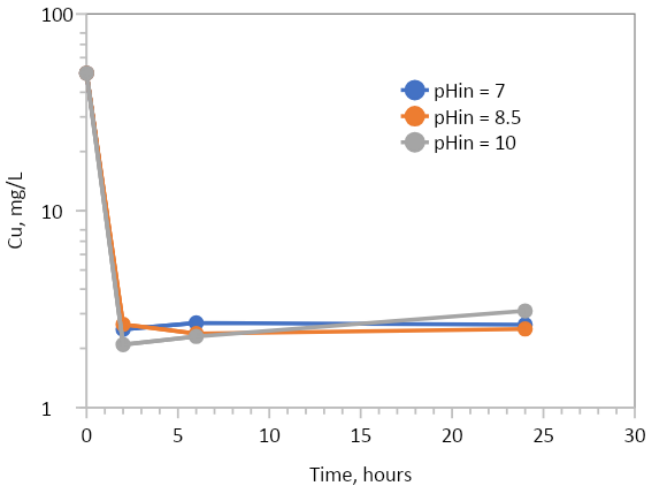

Fig. 5. Copper concentration (at logarithmic scale) in the tests with different initial pHs (0.1M CaTS, 40°C, S/L = 20%)

Thermodynamic calculations indicate that, at neutral and alkaline pHs and in the absence of ligands, such as ammonia or thiosulphates, divalent copper precipitates as Cu(OH)2 and monovalent copper as Cu2O (see Figure 6). In the presence of free NH3 both Cu(I) and Cu(II) can be maintained in the aqueous phase at levels as high as 400-8000 mg/L. In non-ammoniacal solutions containing thiosulphates, Cu(II) is maintained in solution at concentrations above 50 mg/L only at relatively low pH values (pH<7). Cu(I) forms much stronger complexes with thiosulphate and can be maintained in solution at levels between 790 and 3500 mg/L in the whole pH range between 6.5 and 10.5.

In the present work the experiments were carried out in ammonia free solutions. Based on the above thermodynamic considerations, the rapid decrease of copper concentration from the initial value of 50 mg/L to 2.1-3.1 mg/L (Figure 6) is probably due to the precipitation of Cu(OH)2. To maintain copper (II) in solution the pH should be regulated at values below 7. The residual copper 2-3 mg/L is probably monovalent copper. According to Zang et al. (2013), Cu(II) is reduced to Cu(I) after mixing with thiosulphate in non-ammoniacal solutions, and the measured copper in solution exists only as a Cu(I)-TS complex [26].

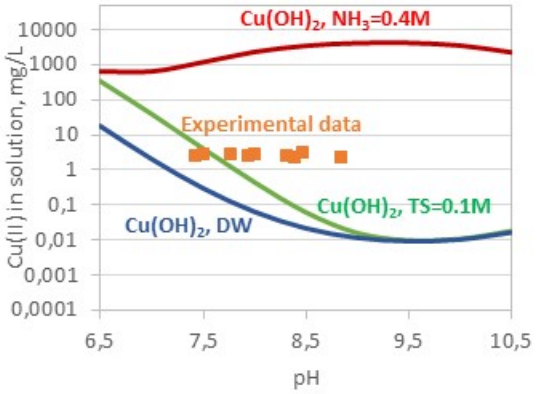

(a) Cu(II)

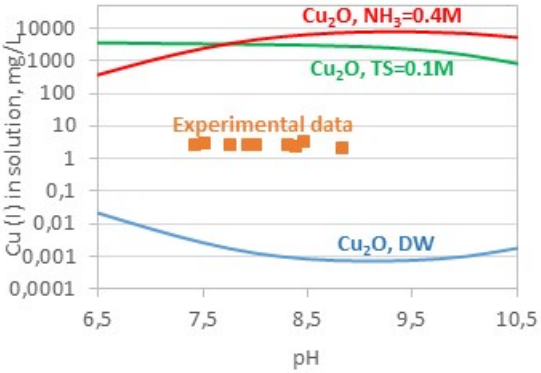

(b) Cu(I)

Fig. 6. Solubilities of Cu(II) and Cu(I) vs pH in deionized water (DW), in a solution containing 0.1 M Ca-thiosulphate, and in a solution containing 0.4 M NH_3. Thermodynamic calculations carried out with Visual Minteq and assuming as possible solid phases $Cu(OH)_2$ for Cu(II) and Cu_2O for Cu(I).

Redox potential and oxygen concentration

The values of redox potential in all the tests varied in the range 100-180 mV (reference electrode Ag/AgCl/KClsat) and the concentration of aqueous oxygen was between 6 and 9.5 mg/L.

Effect of CaTS concentration

Gold extraction

The effect of CaTS concentration on gold leaching is presented in Figure 7. The maximum gold extraction, 65%, was obtained at 6 hours, using 0.15 M CaTS. At the same time interval gold extraction was 25.5% with 0.05 M CaTS and 44.3% with 0.1 M CaTS.

The dissolution of gold was lower when the duration of treatment increased from 6 to 24 hours. This can be attributed to the reprecipitation or adsorption of dissolved gold, a phenomenon which has been often reported in the literature [26-30]. According to Daenzer et al. (2016) the stability of dissolved gold in CaTS solutions is negatively affected by the presence of pyrite, activated carbon or gypsum [30]. The pressure oxidized residue POX-mixed, used as feed material in this work, does not contain any pyrite or carbonaceous material, but the gypsum content is high, i.e. close to 15%, and may explain the observed decrease of gold extraction at longer treatment times.

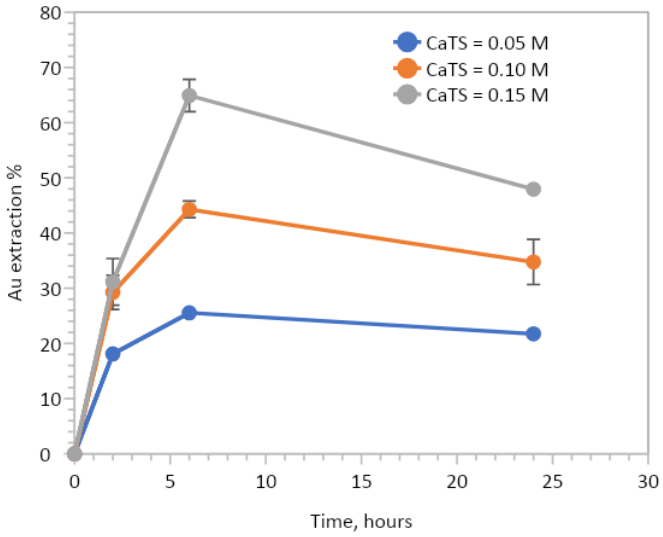

Fig. 7. The effect of CaTS concentration on gold extraction (pH 7, 40°C, S/L 20%).

Evolution of pH, As and Cu

All the experiments with different CaTS concentrations were conducted with initial pH 7. The evolution of pH followed a similar trend, regardless of the CaTS level. A similar trend was also observed for the evolution of As and Cu (Figure 8a and 8b).

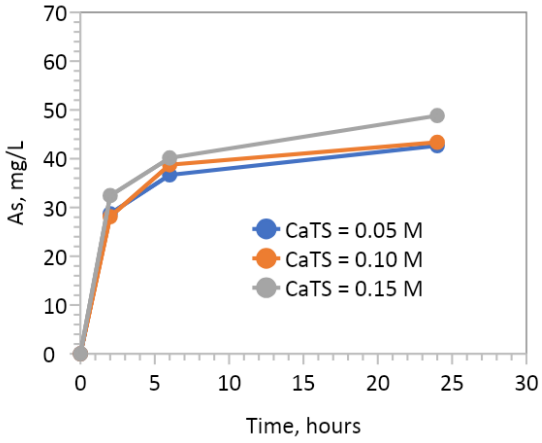

(a)

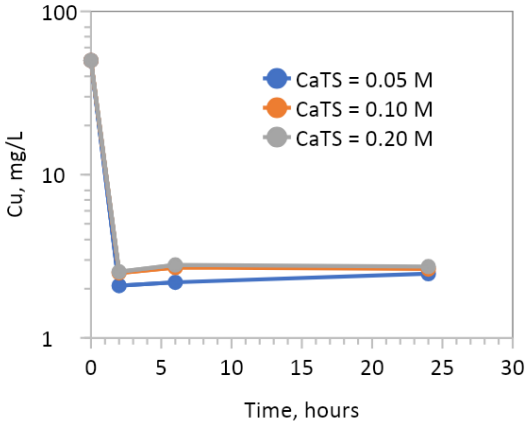

(b)

Fig. 8. Evolution of As (a) and Cu (b) in the tests carried out with different CaTS concentrations.

Effect of solid to liquid ratio

As shown in Figure 9, the increase of solid to liquid ratio from 100 to 300 g/L has limited effect on the percentage of gold extraction. The maximum extraction is observed at 6 hours and the observed variation of values, 37%-44%, was not very different from the variation between reproducibility experiments.

The trend of pH evolution, as well as the evolution of Cu concentration is similar in all three S/L ratios, namely the pH was increased to around 8.2 and the concentration of Cu was 3g/L after 24h. The concentration of As after 24 hours of treatment increased from 36.6 to 58.9 mg/L, when the S/L ratio increased from 100 to 300 g/L.

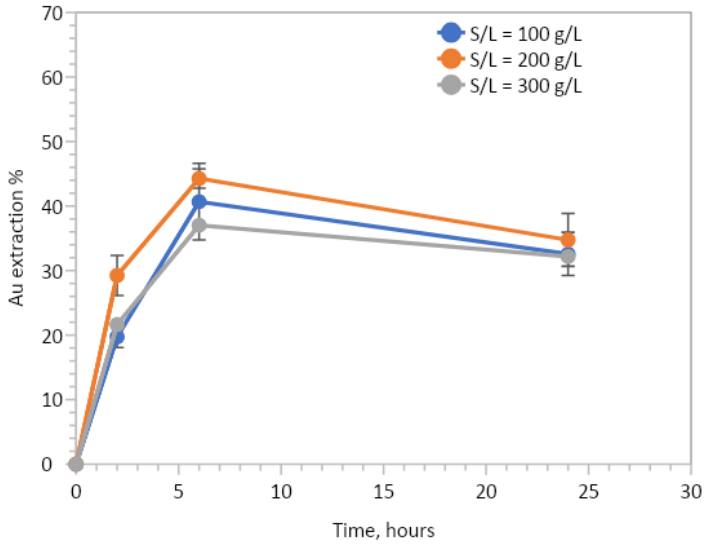

Fig. 9. The effect of solid to liquid ratio on gold extraction (pH=7, CaTS=0.1 M, T=40oC)

Effect of temperature

The increase of operating temperature had a positive effect on the kinetics of gold extraction (Figure. 10.). Increasing the temperature from 30 to 40 and 50oC, gold extraction after 6 hours was equal to 31%, 44% and 50%, respectively. After 24 hours gold extraction was equal to 42% at 30oC (still at increasing trend), dropped from 44% to 35% at 40oC, and dropped from 50% to 47% at 50oC.

The operating temperature had no effect on the evolution of pH and on Cu concentration. Similarly, the dissolution of As after 24 hours of treatment was not affected by the operating temperature and ranged between 37 and 43 mg/L.

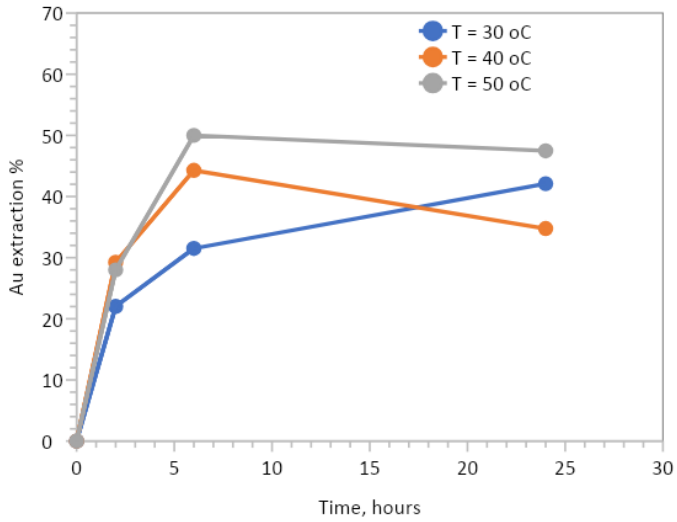

Fig. 10. The effect of temperature on gold extraction (pHin=7, CaTS=0.1 M, S/L=20%)

Resin in Leach test

The resin in leach (RIL) test was carried out at central experimental conditions by adding the anionic resin Purogold MTA5011 in the pulp (100 g/L), during the leaching of POX-mixed with CaTS. The results regarding gold extraction are presented in Figure 11. The addition of resin was found to decelerate the process of gold extraction. At 6 hours the dissolution of gold was equal to 25% with the resin against 44% without resin. However, gold extraction at 24 hours was higher in the presence of the resin, 52% against 35% without resin.

The addition of the resin has caused an important decrease of thiosulphate concentration as shown in Figure 12.(a). Namely, the concentration of CaTS dropped from 0.1 M to 0.05 M after 6 hours and 0.035 M after 24 hours. Moreover, the concentration of copper dropped below detection limit. It seems that the thiosulphate anions, either free or complexed with Ca or Cu(I), are strongly adsorbed by the resin and this may explain the slower kinetics of gold extraction.

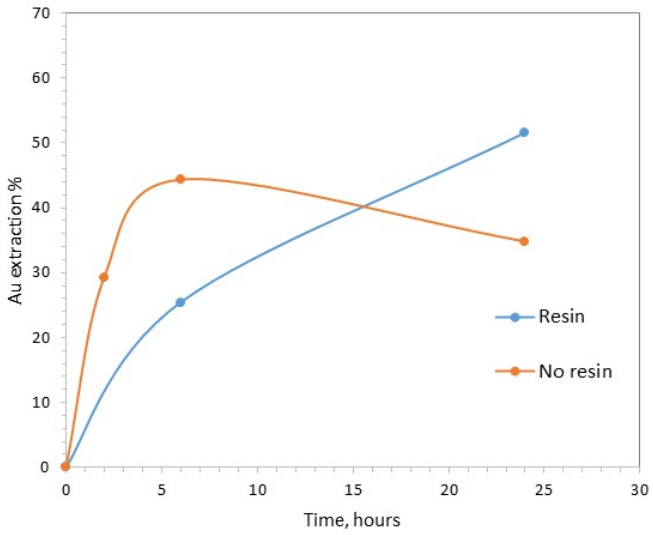

Fig. 11. Comparison of gold extraction with and without resin (pHin=7, CaTS=0.1 M, S/L=20%, T=40°C).

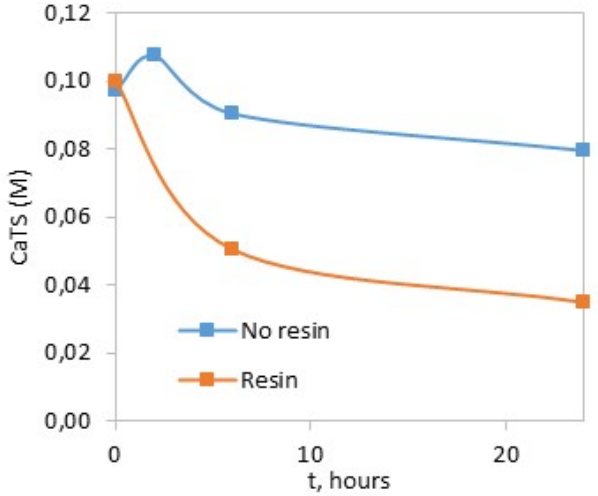

(a)

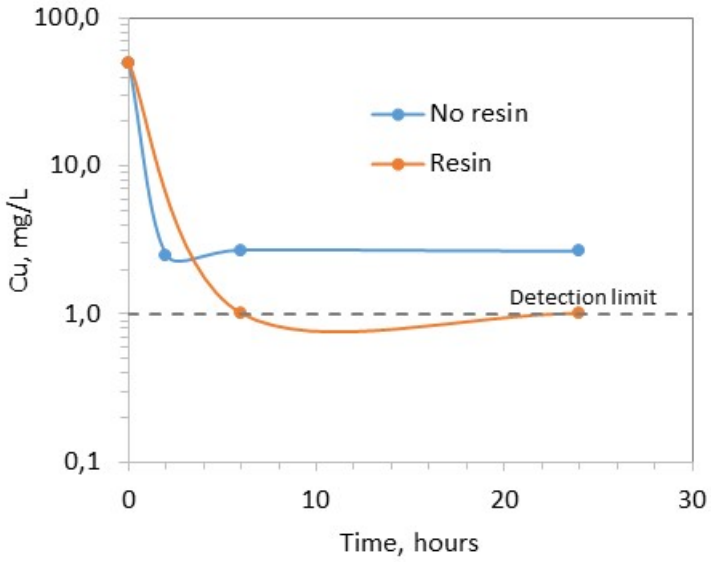

(b)

Fig. 12. Effect of resin addition on the concentration of (a) thiosulphate and (b) copper in the leachate

4 Discussion

Comparison of CaTS performance with published data

Published data regarding gold extraction using CaTS in ammonia free solutions are summarized in Table 4.

Table 4. Published data regarding gold extraction using CaTS in ammonia free solutions

Reference	Gold bearing material	Max Au extraction. Conditions	Extraction, t=6h	Comments
[26]	Oxidized ore, Au 4.4 g/t (NaCN leachable Au >95%)	35.1%, CaTS=0.3M, Cu=10 mM, O_2, pH=10, T=50°C, t=48h	8.2%	Only 9.2% Au extraction, with air instead of pure O_2.
[26]	Cu-Au conc. (S 28%), Au 7.7 g/t. (NaCN leachable Au 62%)	71.4%, CaTS=0.3M, Cu=2-10 mM, O_2, pH=10, T=50°C, t=48 h	38.9%	Dissolution of Cu from the conc. Decrease of TS from 0.3 to 0.067 M at 48 h
[26]	Cu-Au conc., Au 15 g/t (NaCN leachable Au 98%)	74.0%, CaTS=0.3M, Cu=2-36 mM, O_2, pH=10, T=50°C, 24 h	23.1%	Dissolution of Cu from the conc. Decrease of TS from 0.3 to 0.117 M
[26]	Pyrite conc., Au 45 g/t (NaCN leachable Au 90%)	52.4%, CaTS=0.3M, Cu=2 mM, O_2, pH=10, T=50°C, t=48h	21.8%	Decrease of TS from 0.3 to 0.147 at 48 h
[30]	Oxidized preg-robbing ore, Au 2.96 g/t	62.5% (45% in 6h) CaTS=0.1M, Cu=0.8 mM, air, pH=8.5, T=50°C, t=74h	~45%	
[31]	Alkaline POX, Au 2.3g/t. Quartz 59.3%, dolomite, 23.1%, calcite 4%, gypsum 2.5%, TCM 1.9%, Fe_2O_3 0.8%, FeS_2 0.8%	65.3%, CaTS=0.2M, air, pH=10, T=50°C, t=24h		Negligible TS consumption due to the presence of CO_3.Possible dissolution of Cu from POX
[31]	Acidic POX, Au 2.5 g/t. Quartz 88.8%, gypsum 7.5%, Fe_2O_3 1%, FeS_2 0.1%	75.5%, CaTS=0.2M, air, pH=10, T=50°C, t=24 h		10% TS consumption in 24 hours
Present study, 2024	Acidic POX, Au 45.4% g/t. Quartz 20%, gypsum 14.5%, BFAS 52%	65%, CaTS=0.15M, Cu=0.8 mM, air, pH=7-8, T=40°C, t=6 h.	65%	

TCM: Total carbonaceous matter

Zhang et al. (2013) performed experiments with 4 different samples, one oxidized ore, two Cu-Au concentrates and one pyrite concentrate [26]. The gold content varied from 4.4 g/t in the oxidized ore up to 45 g/t in the pyrite concentrate and the percentage of NaCN leachable gold varied in the range 62%-98%. The maximum gold extraction,

74%, was obtained from a Cu-Au concentrate under the following conditions: CaTS=0.3 M, initial Cu 2 mM, injection of pure O2, pH=10, T=50oC, t=24h. The concentration of copper increased from 2 to 36 mM during the treatment due to dissolution from the concentrate. The use of pure oxygen, in combination with the presence of copper, caused the oxidation of thiosulphate and the decrease of TS concentration by almost 60% within 24 hours.

Daenzer et al. (2016) applied the treatment on a sample of oxidized preg-robbing ore with Au 2.96 g/t, provided by Barrick Gold. The treatment was carried out with CaTS=0.1 M, Cu=0.8 mM, supply of air, pH=8.5, T=50oC, t=74 h. The extraction of gold was equal to 62.5% [30].

Soleymani et al. (2021) performed experiments with the pressure oxidized residues, produced in the Barrick's acidic and alkaline POX units of the CaTS process [31]. The conditions used were as follows: CaTS=0.2M, air, pH=10, T=50oC, t=24 h. There was no reference to any external addition of Cu, but it was assumed that there was dissolution of copper at least from the alkaline POX. The obtained gold extraction was 65.3% from the alkaline POX and 75.5% from the acidic POX. The lower extraction from the alkaline POX was attributed to the fact that an important amount of gold was locked in iron oxides and hydroxides (14%) and in FeS2 (13%), while in the acidic POX only 5% of gold was locked in these phases.

In the present study the maximum extraction of gold was 65%, obtained at conditions similar to the above studies (CaTS=0.15 M, Cu=0.8 mM, air, pH=7-8, T=40oC), within a relatively short treatment time, i.e. t=6 h. According to the available published data the extraction obtained at 6 hours was lower, ranging between 8.2% and 45%, but the increase of treatment time had in all cases a positive effect with final extraction rates up to 74% [26, 30]. In this study the extension of treatment duration from 6 to 24 hours caused reprecipitation of dissolved gold. The main drawback of the thiosulphate process in the system, seems to be the instability of gold-TS complexes, probably related with the high content of gypsum and oxidized Fe(III) phases.

5 Conclusions

This study investigated the feasibility of utilizing a thiosulfate (TS) system for gold extraction from pressure oxidation residue under controlled conditions. The maximum gold dissolution achieved was 65% at 0.15 M CaTS, 40°C, pH 7.5, and 6 hours of leaching. Increasing the concentration of CaTS from 0.05 to 0.15 M had a clear positive effect on Au extraction, while the increase of pH from 7 to 10 negatively impacted gold extraction. Increasing the solid to liquid ratio from 100 to 300 g/L has a minimal impact on the percentage of gold extraction, whereas raising the temperature from 30 to 50°C enhances gold extraction. The estimated release of arsenic ranged from 0.12% to 0.16%, for pH 7-10.

Purogold MTA5011SO4 resin successfully enhanced gold recovery to 52% within 24 hours while also adsorbing a significant amount of TS (60%). However, the absence of NH3 prevented Cu(II) from catalyzing gold extraction, and thermodynamic calculations suggest lower pH values are necessary for stabilizing Cu(II) in solution. While the

process proved partially successful, the main limitation appears to be the instability of gold-TS complexes, potentially due to the high content of gypsum and oxidized Fe(III) phases in the studied system. Further research is needed to address these limitations and optimize the thiosulfate system for efficient gold extraction in such environments.

References

1. Environmental Protection Agency (EPA). (1979, August 16). Final rule for control of cyanide used in or near surface waters. Federal Register, 44(161), 47398-47411. https://www.epa.gov/smartsectors/mining-sector-information
2. Environmental Protection Agency (EPA). (2006, December 13). Final rule for control of cyanide used in or near surface waters: Revisions to the cyanide rule. Federal Register, 71(244), 75619-76026. https://www.epa.gov/sites/default/files/2015-12/documents/9013a.pdf
3. Hilson, G. and Monhemius A.J.: Alternatives to cyanide in the gold mining industry: what prospects for the future?, Journal of Cleaner Production 14 (12–13), 1158-1167 (2006)
4. Zhu, Y. Liang, X. & Zhang, M.: Thiosulfate leaching of gold: A review. Journal of Hazardous Materials, 336, 174-184 (2017)
5. Aylmore, G.M. Chapter 28: Thiosulfate as an Alternative Lixiviant to Cyanide for Gold Ores Adams, M.D. (Ed.), Gold Ore Processing, second ed., Elsevier, 2016, 485-523
6. Senanayake, G. Gold leaching in non-cyanide lixiviant systems: critical issues on fundamentals and applications. Minerals Engineering 17, 785-801 (2004)
7. Aylmore, M.G. Chapter: 21: alternative lixiviants to cyanide for leaching gold ores. In: Adams, M.D. (Ed.), Gold Ore Processing, first ed. Elsevier B.V., Amsterdam, Netherlands, 501-539 (2005)
8. Patent US11639540B2, Method for carbon-catalysed thiosulfate leaching of gold-bearing materials, Published 2 May 2023, Barrick Gold Corp (2023)
9. Wan, R.Y. Importance of solution chemistry for thiosulfate leaching of gold. In: Proceedings, World Gold ’97. The Society for Mining, Metallurgy and Exploration, Inc., Littleton, CO, USA, 159- 162 (1997)
10. White, H.A. The solubility of gold in thiosulphate and thiocyanate. J. Chem. Metall. Min. Soc. S. Afr., 6, 109-111 (1905)
11. La Brooy, S.R., Fixing the cyanide issue – Alleviation or replacement? ALTA 2017, 2-27 (2017)
12. Senanayake, G. Gold leaching in non-cyanide lixiviant systems: critical issues on fundamentals and applications. Minerals Engineering, 17, 785-801 (2004)
13. Senanayake, G. Kinetic model for anodic oxidation of gold in thiosulfate media based on the adsorption of MS2O3 -ion-pair. Hydrometallurgy 76, 233-238 (2005a)
14. Senanayake, G. The role of ligands and oxidants in thiosulfate leaching of gold. Gold Bull. 38 (4), 170-179 (2005b)
15. Senanayake, G. Catalytic role of ammonia in the oxidation of gold in copper free thiosulfate solutions. Hydrometallurgy 77, 287-293 (2005c)
16. Senanayake, G., Zhang, X.M. Gold leaching by Cu(II) in ammoniacal thiosulfate solutions in the presence of additives. Part II: effect of residual Cu(II), pH and redox potentials on reactivity of colloidal gold. Hydrometallurgy 115-116, 21-40 (2012)
17. Lam, A.E., Dreisinger, D.B. The importance of the Cu(II) catalyst in the thiosulfate leaching of gold. In: Young, C.A., Alfantazi, A.M., Anderson, C.G., Dreisinger, D.B.,

Harris, B., James, A. (Eds.), Hydrometallurgy, Leaching and Solution Purification, vol. 1. TMS, Warrendale, 195-211 (2003)
18. Chen, J., Deng, T., Zhu, G., Zhao, J. Leaching and recovery of gold in thiosulfate based system - a research summary at ICM. Trans. Indian Inst. Met. 49 (6), 841-849 (1996)
19. Zhang, S., Nicol, M.J. An electrochemical study of the dissolution of gold in thiosulfate solutions. Part I - Alkaline solutions. J. Appl. Electrochem 33, 767-775 (2003)
20. Baron, J.Y., Mirza, J., Nicol, E.A., Smith, S.R., Leitch, J.J., Choi, Y., Lipkowski, J. SERS and electrochemical studies of the gold-electrolyte interface under thiosulfate based leaching conditions. Electrochim. Acta 111, 390-399 (2013)
21. Feng, D., van Deventer, J.S.J., . Effect of thiosulfate salts on ammoniacal leaching of gold. Hydrometallurgy 105, 120-126 (2010)
22. Braul, P. Thiosulfate going commercial. CIM Mag. 8 (1), 42-45 (2013)
23. Choi, Y., Baron, J.Y., Wang, Q., Langhans, J., Kondos, P. Thiosulfate processing e from lab curiosity to commercial application. In: World Gold Conference Proceedings, Brisbane, Qld, 26-29th September 2013 45-50 (2013)
24. Smith, R.M., Martell, A.E., Motekaitis, R.J. Critically Selected Constants of Metal Complexes Database, Version 5.0 Software. National Institute of Standards and Technology (1998)
25. Zhang, H., Dai, X., Breuer, P. Factors affecting gold leaching in thiosulfate-O2 solutions. In: Proceedings of the ALTA Gold Conference Perth WA, 30-31st May 2014. ALTA Metallurgical Services, Melbourne, Australia, 9 (2014)
26. Zhang, H., Dai, X., Breuer, P. Factors affecting gold leaching in thiosulfate-O2 solutions. ALTA 2013 May 30-31st; Perth, Australia: ALTA Metallurgical Services Publications (2013)
27. Zhang, H. and Jeffrey M. A study of pyrite catalysed oxidation of thiosulfate. Hydrometallurgy Proceedings of the Sixth International Symposium 2008 Phoenix, AZ: Society for Mining, Metallurgy, and Exploration (SME) (2008)
28. Dai, S., Li, P., Wang, Q., Feng, D. Effect of additives on thiosulfate leaching of a gold ore. Bulgarian Chemical Communications, Volume 49, Special Edition K2, 48 – 53 (2017)
29. Zhang H, Jeffrey M, A study of pyrite catalysed oxidation of thiosulfate. Hydrometallurgy 2008 Proceedings of the Sixth International Symposium; 2008; Phoenix, AZ: Society for Mining, Metallurgy, and Exploration (SME) (2008)
30. Daenzer R.; Dreiseinger, D. and Choi Y. Role of polythionates on the stability gold in the leaching of double refractory ores in the calcium thiosulfate-air leaching system. ALTA 2016 Gold Pm Proceedings, pp. 282-298 (2016)
31. Soleymani M., Sadri F., Ghahreman A. Effect of mixing acidic and alkaline pressure oxidation discharges with different ratios on gold thiosulfate leaching efficiency. Hydrometallurgy 205, 105744 (2021)

Critical Review of the Metallurgical Operation of the Greek Nickel Industry and Perspectives, based on the recent Industrial Experience on Smelting Reduction Process

Charalabos Zografidis[1], Konstantinos Betsis[2] and Anthimos Xenidis[2]

[1]Hellenic Survey of Geology and Mineral Exploration 1, Spyrou Loui St, Acharnes, 13677 Athens, Greece
[2]National Technical University of Athens, 9, Iroon Polytechniou St., 15780 Athens, Greece
chzografidis@eagme.gr

Abstract. The mining and industrial production of Greek ferronickel industry LARCO have ceased since 30.07.2022. The last LME nickel price crisis, exclusion from bank loaning, extremely high cost of electrical energy, management issues, resulted inter alia, in a prohibitive operational cost. Nevertheless, LARCO faces the challenge of adapting to the demands of a modern industrial operation as well as administration, given that privatization is in progress.
Within this framework, the current paper aims to critically comment on the quite recent industrial data concerning smelting reduction, being presented and analyzed, in order to contribute to the research for optimizing the applied pyrometallurgical process. Based on industrial experience concerning open bath submerged arc electric furnaces, focus is made on the critical factors of raw materials' management, maintenance strategy and a totally new human resources management strategy that should be adopted by a new ownership, so that the optimal techno-economic result of such an investment could be reached. Moreover, taking for granted the need for Ni-rich 'foreign' ores to increase the recovery and reduce the cost of the process, the extent of dependence on Fe-rich domestic ores is investigated, in order a safe and stable operation to be ensured.

Keywords: laterites; ferronickel; optimization, reductive smelting

1 Introduction

Ferronickel (Fe-Ni) with a Ni % analysis among 20 and 40%, and Nickel Pig Iron (NPI), constitute the predominant Nickel Class II category products, which meet an outstanding demand growth since 2006, with a widespread production in China and Indonesia. Nickel demand is still predominantly driven by the stainless steel industry, accounting for almost 70% of the total primary nickel consumption [1]. Furthermore, as seen in Figure 1, the primary nickel production (including Nickel Class I products) reached an outstanding increase of almost 40% within the last three years, taking for

granted the forecast that it will overcome 3.370.000 t by the end of 2023 [2], despite the negative challenges of COVID-19 pandemic and the energy crisis in the meantime.

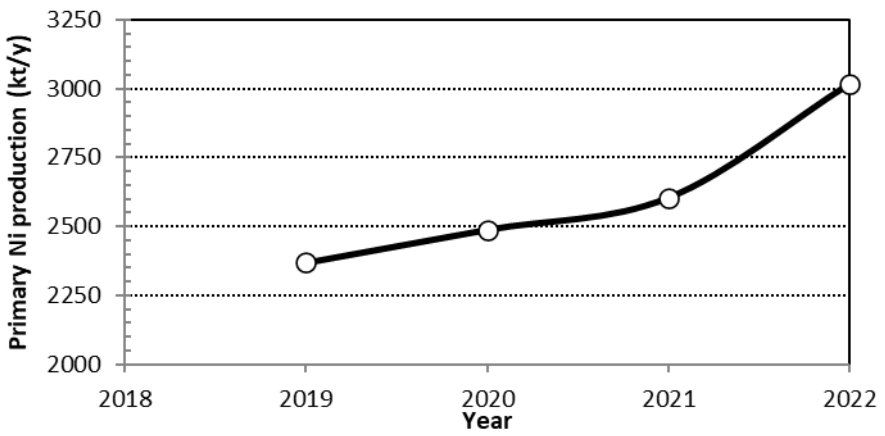

Fig. 1. Primary nickel production evolution

Nevertheless, as seen in Figure 2, the primary nickel production trend in China and Indonesia (C&I) is opposite in comparison with nickel production in Europe (not including Russia). Moreover, it can be clearly seen in Figure 3, that Europe's smelter Fe-Ni production in 2022 faced an enormous 57% decline, which can be safely attributed to the soaring energy costs. More specifically, based on INSG world statistics published, apart from Greece, the smelters' production for Fe-Ni production in Kossovo and Ukraine has been ceased in 2023, while in North Macedonia the production has been declined by 54.2%. The overall primary nickel production in Europe, including the sole nickel sulfide smelter in Finland (Harjavalta) has been declined by over 20% within the last two years.

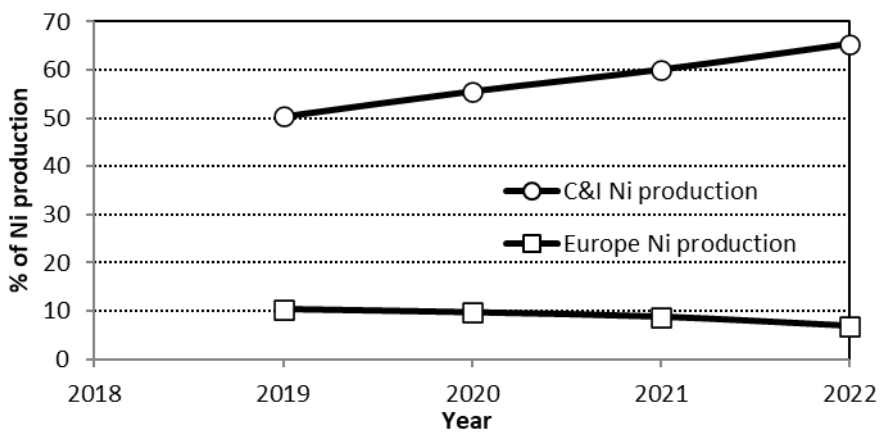

Fig. 2. Ni production as a percentage in China & Indonesia vs Europe

In any case, the forecast for the significant increase of nickel demand for usage in the battery sector within the next 15 years, challenges the European governments, apart from motivating nickel producers with more viable energy supplying prices in order to remain competitive in the Class II nickel production market, to seriously invest in R&D costs for enhancing greenfield projects for the production of nickel-matte or intermediate products, such as nickel sulfate or Mixed Hydroxide Precipitate (MHP). Furthermore, the absolute need for the nickel producers world-wide to alter their operational flowsheets targeting to meet the requirement for products more easily integrated in the lithium ion batteries market, enhance the research efforts for NPI or Fe-Ni conversion to nickel matte or other similar intermediate products, which can be further refined [4]. Within this framework, Hellenic Minerals Ltd. in Cyprus, is in the commissioning state of a Heap Leaching-Solvent Extraction-Crystallizer (HL-SX-CR) unit for NiSO4.6H2O production [3].

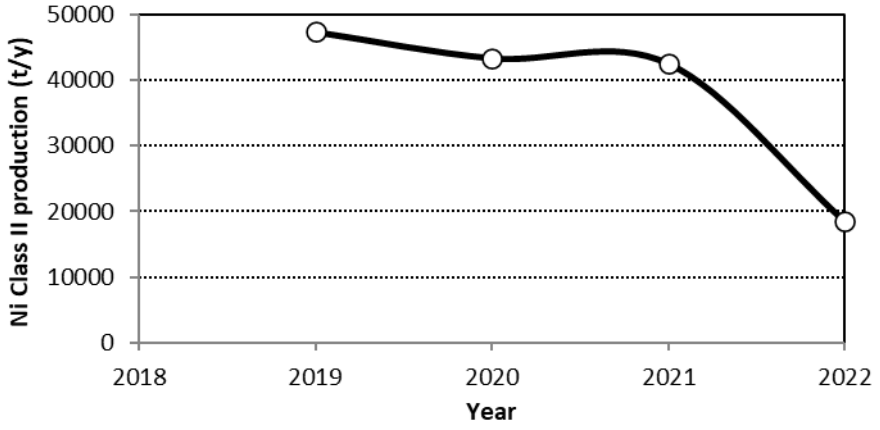

Fig. 3. Europe Ni Class II Production within the period 2019 – 2022

1.1 The Greek Ferronickel Industry

Considering the last 14 years, since 2010, the operation of the Greek Ferronickel Industry LARCO General Mining and Metallurgical Company, passed through many stages. The period 2011 – 2014, when the LME nickel prices as seen in Figure 4 fluctuated among 16.000 – 28.000 USD/ t, the Greek Ferronickel Industry managed to have annual production over 18.000 t of nickel, being historically among the best production performances. The subsequent nickel price crisis period 2015-2020, when the prices reached even 8.000 USD/t, was critical for the further progress of the industrial operation. Key parameters, such as the low nickel price, which resulted in cuts in maintenance and ore mining expenses, the exclusion from bank loaning due to conviction by the European Court for receiving in the past incompatible state aid, and structural and management malfunctions, resulted in a prohibitive operational cost. The extremely high cost of electrical energy (> 200 Euros/MWh) during the last two years, was the 'deathblow' for the industrial operation, which finally ceased in 30/7/2022. In the meantime, since 28/2/2020, LARCO is placed under a special administration regime,

in accordance with the provisions of article 21 of Law 4664/2020. Furthermore, the Greek Ferronickel industry faces the challenge of restructuring and reoperation in the future, given that privatization procedure is in progress, being in the stage of the acquisition of the company's assets to a joint venture enterprise, after its participation in an international open tender for the transfer of LARCO's assets.

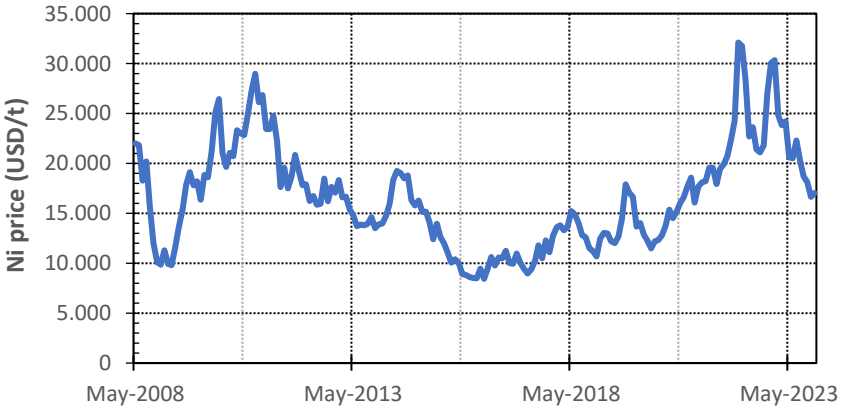

Fig. 4. Ni LME price within the period May 2008 – December 2023

2 Pyrometallurgical Processing of Greek Laterite Ores

Nickel is extracted pyrometallurgically from the domestic laterite (oxidized) ores via the LARCO metallurgical process, having finally succeeded the Krupp-Renn, the LM and the MLar methods, after certain technological and physicochemical modifications [3]. The Larco process [5] having already been presented elsewhere, is based on the application of the Rotary Kiln – Electric Arc Furnace (R/K – E/F) method for the production of Fe-Ni alloy 12-14% which is further enriched to 18-25% Ni in OBM converters.

The Greek nickeliferous laterite ores which comprise the main feed of the R/Ks in the Greek Fe-Ni industry are: Evia island ore (Ore A), Lokrida ore (Ore B) and Kastoria ore (Ore C). Based on the classification of the laterite ores according to their Fe and MgO % content [3], all the different deposits of Ore B are typical B1 type of limonites (Fe > 32%, MgO < 10%). The various deposits of Ore A can be classified among B1 and B2 type of limonites (25% < Fe < 32%, MgO < 10%). On the contrary, Ore C clearly belongs to Intermediate type C2 laterite ore (12% < Fe < 25%, 10% < MgO < 25%).

Temporarily for a short period of time in the past, imported high grade Ni ores were used in the Greek nickel industry, in order to enrich the metallurgical mixture fed in the R/Ks, increase the productivity and decrease the special electrical energy consumption, including: i) Indonesian and Guatemala laterite ores (Ni %>1.6 on a dry basis), which are typical Intermediate type C2 ores, and ii) Turkish laterite ores (Ore T) from different

deposits which are typical B2 type of limonites, having significantly higher Ni grade in comparison with the Greek limonitic laterites Ores A&B (Ni %>1.2 on a dry basis).

The case study of the laterite ore material fed in the Greek Fe-Ni industry, can be characterized as extremely rare, taking into consideration that high content of iron in the slag produced in the smelting reduction step (Fe > 28%), results in a lower melting point of the slag than the melting point of Fe-Ni, which means that smelting of the alloy is achieved through slag superheating. Thus, the smelting reduction process with open bath submerged arc E/F operation is method prerequisite for pyrometallurgical processing. Moreover, the critical parameter of SiO2/MgO content of the Greek laterites (or the slag produced) is greater than 7, while it does not exceed 3 in the case of all the other nickel smelters. Although the Fe/Ni ratio of the Greek laterites is almost 30 (in comparison with not higher than 12 in case of foreign laterites), only about 22% of iron is recovered in the crude Fe-Ni produced in E/Fs, which means that the LARCO method is classified in the low iron reduction category [6].

3 Critical Parameters for the Optimization of smelting reduction of Nickeliferous Laterites

It is clearly deduced by the industrial experience concerning open bath submerged arc electric furnaces, that the factors which constitute the prerequisite for a safe and cost-effective metallurgical process, are presented in Figure 5.

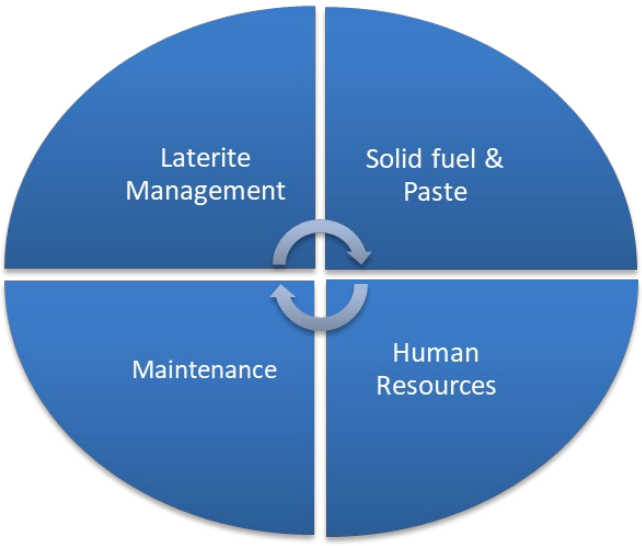

Fig. 5. Critical factors for the optimization of smelting reduction process in the Greek Fe-Ni industry

Within this framework, taken into account that the Greek Fe-Ni industry is on a transitional period, when the reoperation under a new regime, free from the restrictive

structural issues of a former public enterprise, should be accompanied by a general management strategy reassessment, the current paper aims to contribute to the former issue, focusing on the step of smelting reduction. Furthermore, the industrial experience of the last 13 years is utilized, in order critical parameters affecting the optimization of smelting reduction to be highlighted, by means of case studies presentation and statistical analysis of operational data.

3.1 Laterite Ores

The Ni % content of the laterite ore mixture (Laterite Mixture – L.M.) fed in the R/K-E/F system of the metallurgical plant is out of doubt the most critical factor affecting the recovery rate and the productivity of the process. The Ni grade of the laterite ore mixture after 2014, has gradually fallen in 2019 (the last year of operation of all the metallurgical equipment of the plant), into level (0.91% on a dry basis) that marginally can be characterized as economic [3] or viable in literature. Additionally, another vital parameter significantly affecting smelting reduction is the difference of iron and SiO2 content (Fe – SiO2 %) in the laterite ore mixture and consequently in the slag produced. Its decreasing trend in the last eight years is seen in Figure 6. This is very important, since it intimately affects both: i) the melting point of the laterite mixture, thus the specific energy consumption and ii) the viscosity of the E/F slag, which is related with the intensity of slag foaming phenomena.

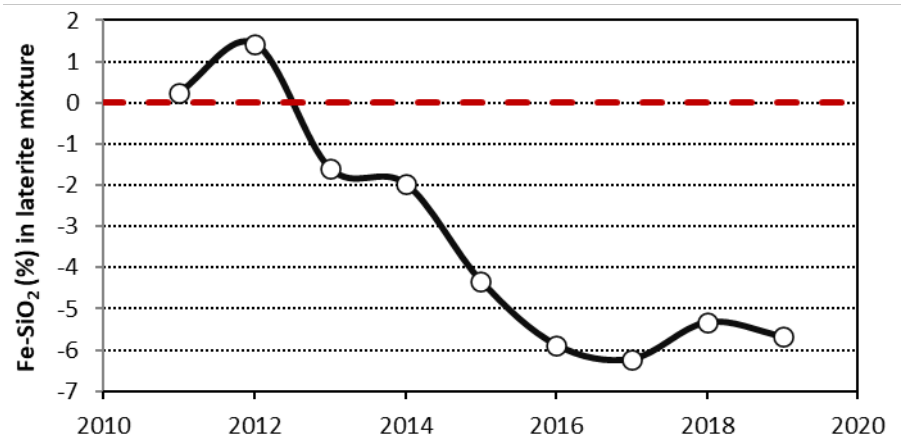

Fig. 6. Difference of iron and SiO_2 content (Fe – SiO_2, %) in the Laterite Mixture (L.M.)

The Operational Index (O.I. %), defined as Uptime × Speedfactor of the E/F equipment, constitutes probably the most critical index of the economic viability of the process, as seen in Figure 7, since it takes into consideration both the parameters: i) time of equipment operation (Uptime) and ii) % utilization of the E/Fs maximum power capability. Moreover, it is deduced that an E/F O.I > 70%, which is a prerequisite for high Ni production, is obtained having ensured an average Fe-SiO2 (%) content greater than -3% in L.M. feed.

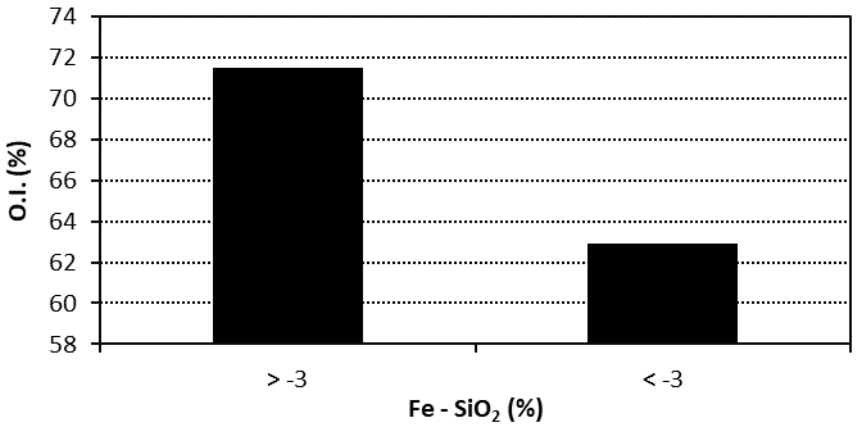

Fig. 7. Operational Index (O.I. %) vs. the difference of iron and nickel content in the laterite ore mixture

In Table 1 that follows, laterite mixtures of both domestic and foreign ores are presented, in order to assess and explain the effect of the raw material qualitative and quantitative characteristics in the smelting reduction step operation, in terms of the viscosity of the slags produced, related with foaming phenomena, as well as the SiO2/MgO ratio of either the ores or the slags produced, which is related with the slag melting point and the electrical energy consumption. The Greek industrial operation experience of open bath submerged arc E/Fs, including imported laterite ores utilization of C2 type (of Indonesia, Guatemala –Ore G- or Ivory Coast origin), has shown that a SiO2/MgO ratio no lower than 3.5 and a (Fe-SiO2) % content of no lower than -5% or even better no lower than -3% can be characterized as safe and economically viable. Moreover, lower SiO2/MgO ratio increases the slag melting point in values that render the open bath operation forbidden, due to its higher melting point in comparison with the alloy's melting point and the energy consumption index even higher than 600 kWh/t of calcine, in comparison with a mean value of 450 – 460 kWh/t of calcine applied for smelting reduction of domestic ores.

Table 1. Properties of various laterite mixtures

Laterite Mixture (L.M.)	Ni (%)	Fe-SiO_2 (%)	SiO_2/MgO
L.M.1: Ore A–Ore B-Ore C (%) = 65-25-10 (%)	1.04	2.4	7.3
L.M.2: Ore A–Ore B-Ore G(%) = 45-25-30 (%)	1.17	-4.5	3.8
L.M.3: Ore A–Ore B-Ore C (%) = 50-25-25 (%)	0.96	-7.1	4.8
L.M.4: Ore A–Ore B-Ore C (%) = 45-25-30 (%)	1.22	-1.3	3.6
L.M.5: Ore A–Ore B-Ore C (%) = 45-25-30 (%)	1.25	-0.4	3.3
L.M.6: Ore A–Ore B-Ore D* -Ore G (%) = 45-15-10 -30 (%)	1.26	1.2	3.8
L.M.7: Ore A–Ore B-Ore T -Ore G (%) = 40-15-20 -25 (%)	1.26	-1.7	4.6

*Ore D: Albanian ferrous ore

Taken for granted the quite stable quality of intermediate type domestic Ore C, the quantitative characteristics of the various deposits of the limonitic type domestic ores A and B, are of vital importance for the operational stability. Moreover, participation of an intermediate type ore more than 30% in the Laterite Mixture, results in a SiO2/MgO ratio < 3, rendering the open bath operation impossible. Apart from that, the percentage of Fe and SiO2 content of the limonitic type ores blended in order to form the rest 70% of the L.M., is critical in order the viscosity of the produced slag to be regulated according to the (Fe – SiO2) % relationship, so that foaming phenomena are controllable and do not result in high height of slag insight the furnace and low E/F power operation, for safety management issues.

L.M. 1 of Table 1 can be characterized as a Baseline scenario for the Greek nickel industry, since it constitutes a typical example that corresponds to a stable operation. On the contrary, L.M. 3 can be characterized as a Slag High Viscosity scenario (SHV), and it constitutes a typical example of ore blending corresponding to an unstable operation in Greek Fe-Ni industry. More particularly, Ore B was up to 2014 the regulatory factor of the L.M formation, taken for granted that its higher Fe content rendered its participation of not higher than 25% enough in order to assure satisfactory viscosity of the produced slag. At the same time, due to its lower Ni content compared to ore A, its participation at higher than 25% values was not possible due to the decrease of the total Ni content in the feed. The Baseline scenario (year 2012), resulted in the production of an industrial slag (FeO = 40.57%, SiO2 = 36.73%) with a viscosity of 72.5 poise, based on the Urbain Model. On the contrary, LME nickel price crisis after 2015, resulted in drastic cuts in mining costs, something that predominantly altered the chemical character of the Ores A and B fed in the metallurgical plant, as depicted in Figure 8. Difficulties in supply of the plant with the required quantities of Ores A and B, as well as the very low Ni (%) content of Ore B (<0.85%), resulted in the mandatory increase of Ore C participation, with L.M 3 (High Slag Viscosity scenario, December 2019) a typical example of such a case. The production of an industrial slag (FeO = 31.9%, SiO2 = 43.81%) with a viscosity of 138.0 poise, caused serious increase in the energy consumption index MWh/t Ni, due to the decrease of the O.I.

L.M.2, is a typical example of blending domestic limonitic type ores with intermediate type laterite ore of Guatemala origin (Ore G, Ni% = 1.79 on a dry basis). Even within the period of crisis (August 2019), where the Ni content of Ores A and B were considered as low (0.95 and 0.78%, respectively), the total Ni content of the mixture was significantly increased (1.17 %). Additionally, the period of time of almost a month that high Ni grade ore participated in the L.M., the operation was generally stable, with no serious slag foaming phenomena, low energy consumption indexes and high recovery rate, indicating that this should always be the strategic operational plan for the Greek Fe-Ni industry. Moreover, the specific energy consumption indexes (MWh/ t Ni, GJ/ t Fe-Ni) were reduced by almost 10%, which is indicative of the importance of the use of such a feed apart from the economic viability of the process, also for its environmental footprint, as it has been investigated in LCA analysis concerning the ferronickel industry in literature [7,8].

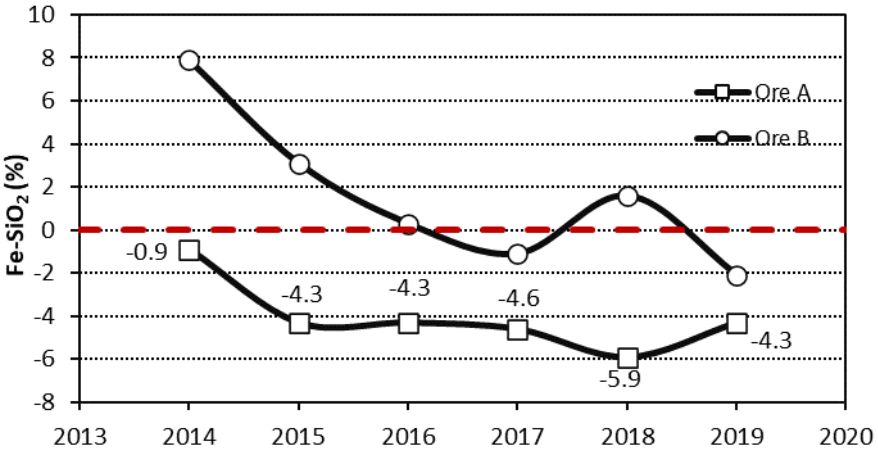

Fig. 8. (Fe – SiO_2) % values of ores A&B vs. time

Based on the study of the database of various proven deposits of the Greek Mines in Evia island and Ag. Ioannis, theoretical laterite mixtures were created, only with participation of domestic deposits (L.M. 4 & 5), as well as with the participation of imported ores: Ore G, Turkish ore (Ore T, limonitic type) and Albanian ore (Ore D, Ni (%) = 0.97, Fe = 35.3%, SiO2 = 21.0%) [9], which is a high iron limonitic type ore able to replace Ore B in a considerable extent. In all the aforementioned cases, which can be characterized as the Optimal Scenario (OS), the goal is as seen in Table 1, the indexes for obtaining the optimal laterite's feed management Fe-SiO2 (%) and SiO2/MgO not to be lower than the critical values -5 and 3, respectively. Moreover, the highest possible Ni grade obtained in such a way is approximately 19% higher (1.26-1.3%) compared to a typical annual average of the period 2011-2014 (1.04 – 1.06%).

Typical phase diagrams were created via the equilibrium module in FactSage7.0 professional software, mainly to determine the melting points of typical industrial slags produced by Laterite Mixtures similar with those of Table 1. It is noted that the effect of the refractory Cr-bearing spinel mineral phases has not been taken into consideration for the calculation of the melting points. The temperature determined each time as 'melting point' was the liquidus temperature, at which all the mineral phases of the industrial slags are melted, apart from the Cr-bearing solid spinel minerals that still co-exist, even at 1.600 oC. In case of the phase diagrams of slags produced by partial substitution (30%, SiO2/MgO = 4.18) or total substitution (100%, SiO2/MgO = 2.1) of intermediate type foreign laterite (Ore G) in the L.M., the mineral phases orthopyroxene, clinopyroxene (Mg,Fe)2Si2O6 and olivine (Mg,Fe)2SiO4 co-exist in equilibrium with liquid slag at significantly higher temperatures and at higher contents. Moreover, when the SiO2/MgO ratio is decreased at levels lower than 3, the melting point of the slag was increased up to 1,432 oC, in comparison with 1,220 oC, as seen in Figure 9. In Figure 10, the melting points of typical industrial slags, defined as solidus temperatures, are depicted by the use of FactSage7.0 software and the Phase Diagram module in a ternary system FeO – MgO – SiO2.

In the plotted area DS (Domestic Laterites) melting points of typical industrial slags are depicted (FL_A and FL_B, solidus temperature 1,256 oC, with SiO2/MgO 5 and 7, respectively), produced by different blend ratios of domestic laterite ores. Moreover, the melting point with the code name TS (Tropical Scenario) is also depicted (solidus temperature 1,380 oC, with S/M 2), which corresponds to the slag produced by a 100% foreign (Ore G) tropical origin ore feed. It is verified the trend that the low Fe content and the high MgO and SiO2 content of ferronickel slags produced by the total participation of intermediate type laterite ores (like Ore G) in the L.M., results in an increase of the slag melting temperature by almost 200 oC. A critical parameter for this is the remarkable presence of the olivine mineral phase in such a case, and especially forsterite (Mg2SiO4). On the contrary, the remarkable presence of the Fe – bearing spinel mineral phases (such as MgFe2O4) and magnesiowustite (Mg,Fe)O is a critical parameter for the low-melting point ferronickel slags produced by domestic laterite ores.

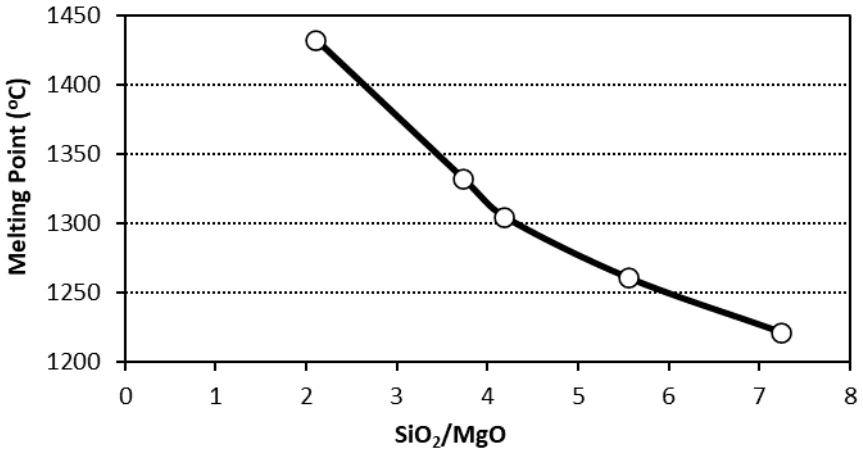

Fig. 9. Melting point of industrial slags v/s SiO_2/MgO ratio

In Figure 11, the correlation between the basicity of the same industrial slags and their viscosity calculated by the Urbain model is depicted. Moreover, increase of the viscosity of a low basicity slag in higher levels than 110 poise, close to that of the slag produced by the L.M 3 fed in the R/K-E/F system, with a Fe-SiO2 (%) ratio lower than -7, corresponds to intensive foaming phenomena, low operational index and high energy consumption.

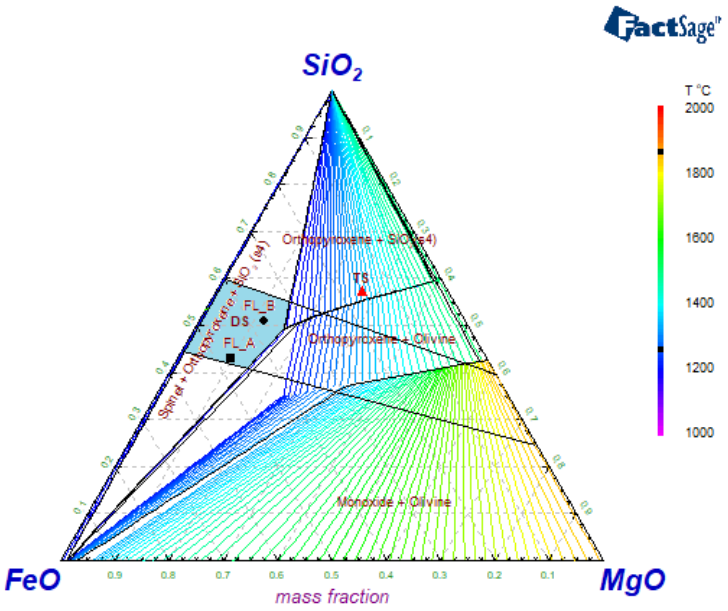

Fig. 10. Melting point of laterite slags in a ternary system FeO – MgO – SiO_2

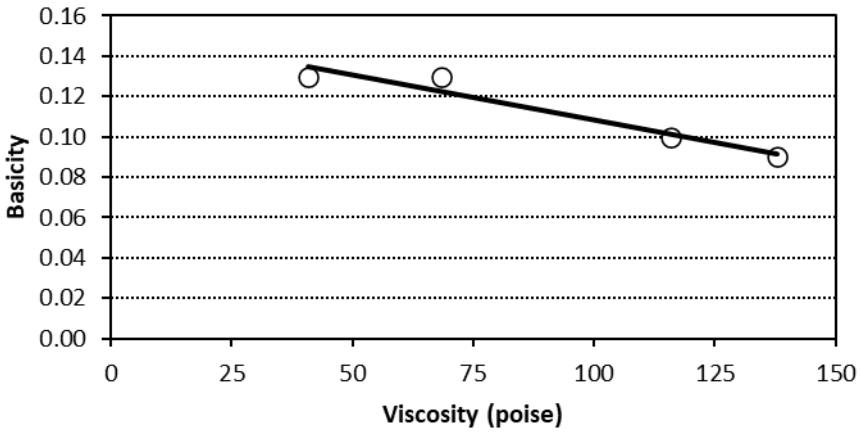

Fig. 11. Basicity vs viscosity of industrial slags

Within this framework, making the assumption of the linear fitting of the historical Ni (%) – O.I. (%) and MWh/t Ni data from the Greek industrial operation database, a quite conservative prediction for obtaining an energy consumption index of 58 – 59 MWh/t Ni could be made. Taking as bases of the consideration: i) the upper limit of

processing no more than 2,350,000 t of calcine annually by the R/K – E/F system and ii) the cost of the electrical energy is approximately 30% of the total cost of the nickel extraction, assuming that the energy prices will at least come back to the level before 2022 (70 €/MWh), an annual Ni production of 7.000 t is regarded as absolutely realistic for operation of two E/Fs, just for a potential beginning of the reoperation period of the Greek Fe-Ni industry. In such a case, a selling price of 15,000 €/t of Ni, could be very close to the marginal cost of the industry.

In any case, the conclusion that can be clearly drawn is that increase of the FeO content of the E/F slag, which is intimately related with the Fe content of the Laterite Mixture, as well as increase of the slag basicity, also intimately related with the decrease of SiO2 (%) content, results in considerable decrease of intensive slag foaming phenomena [10,11] and a series of operational problems. This can be clearly seen in Figure 12, where the evolution of ratio of energy consumed/energy loss due to operational problems caused by the poor quality of the laterite feed (Ni grade, Fe – SiO2), is presented. The aforementioned ratio in 2019, a year which was the worst concerning the quality of the laterite feed, fell from 8.7 in 2011 to 5.6, with the respective negative results in Ni production of the plant. The loss of income due to the energy losses due to operational problems caused by the poor laterite ore quality, was almost 22 M€ in 2019. The extent of the serious operational problems that the Greek Fe-Ni industry faced, affecting both the collapse of the E/F O.I. and the safety of personnel and equipment, due to the poor laterite feed quality (mainly regarding the quite negative Fe – SiO2 relationship) during the period 2015-2019, is concisely presented by means of case studies.

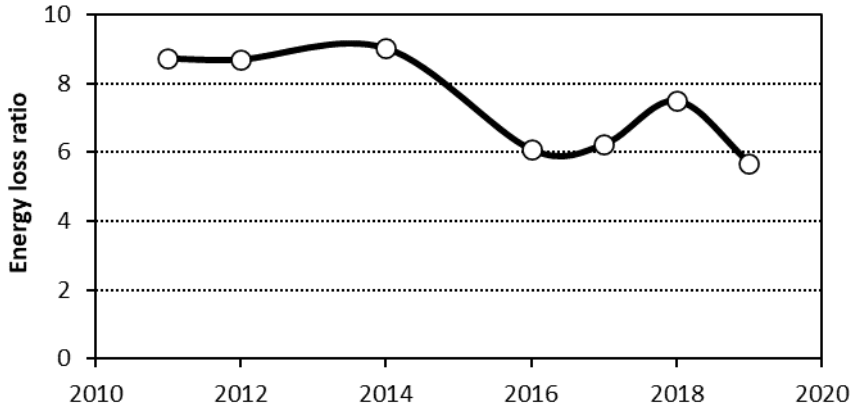

Fig. 12. Evolution of the energy loss ratio (energy consumed/energy loss due to operational problems caused by the poor quality of the laterite feed) in the period 2011-2019

Uncontrolled E/F operational case studies. A typical case study of an extremely dangerous and unstable E/F operation, due to very bad quality of laterite feed, is that of 2017. Based on operational data, the Fe-SiO_2 (%) content of limonitic type Ores A and B was -6 and -3, respectively, resulting in a two-days operation of the E/F which demands the difficult management of intensive slag foaming phenomena, current

fluctuations, power loss due to intensive electrode consumption, very high flames around the freeboard surface, very high slag viscosity that renders slag tapping very difficult and inability of maintaining calcine side-wall protection, because of the high slag level inside the E/F. The aforementioned serious operational problems, resulted in an uncontrolled metal tapping from the E/F side-wall shell the second day, which caused in addition to the other big decrease of the plant O.I., as well as increased cost of maintenance. In Figure 13, a typical picture from the E/F PLC operation is presented.

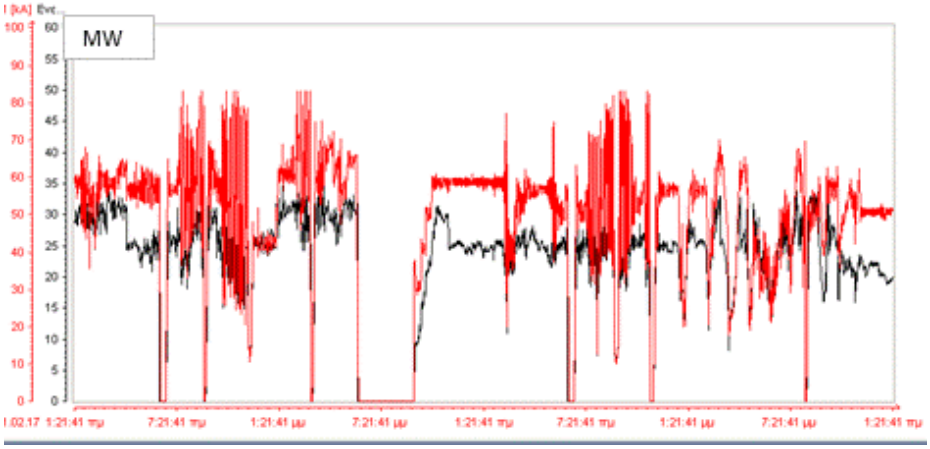

Fig. 13. PLC data of E/F unstable operation due to low quality laterite feed

3.2 Solid Fuels

The stable quality of the solid fuels used for roasting reduction in the Greek Fe-Ni industry plays a very important role in the final result of the smelting reduction step [12]. More precisely, either the combination of three solid fuel types (lignite, coal and coke) or two types (coal and coke), depending on the international fuel prices, should assure the retention of the needed temperature profile in the R/Ks, in order a calcine of the highest possible temperature to be fed in the E/Fs. In such a way, electric energy consumption is decreased and the operational problems in the smelting step due to slag foaming and intensive reduction phenomena, are minimized. A prerequisite for the aforementioned is a solid fuel mixture fed in the R/Ks with the optimum ratio of volatiles and fixed carbon (C^{fix}).

During 2010, there were periods of time when for cash management reasons, it was selected not the stable long-term co-operation with coal suppliers, who have the proved ability for supplying a certain quality of coal adjusted to the needs of the Greek Fe-Ni industry. Instead of this, it was selected the supply of spot ship loads of two different types: 'hard coal', with volatile content <25% and 'soft coal', with volatile content >35%, in order to be mixed in ratios that would lead to the achievement of the stable temperature profile inside the R/Ks. Nevertheless, it was proved by the industrial experience that especially the lack of lignite feed in such case, causes the inability to manage the optimum volatile combustion along the R/Ks, causing extremely dangerous operational situations for the E/Fs. The most typical case study was that of an E/F in 2010, that after almost a month fed with calcine of very low temperature with excessive

content of C^{fix}, its O.I. was dramatically decreased to lower than 59% on a three – month basis (almost 30% lower than the annual average). Moreover, intensive slag foaming and reduction phenomena finally led to such an uncontrolled slag height inside the E/F, that all the freeboard was covered by slag.

Solid fuels' granulometry also was proved by the industrial experience that is critical for the result of the smelting reduction step. As seen in Figure 14 at periods of utilization in the R/Ks of spot ship loads of coal with -1 mm (%) grain size higher than 25%, instead of 16-20% when the best operational results were achieved, the E/F recovery rate was significantly decreased by almost 12%. This can be attributed to the fact that more fine grained coal in the R/Ks, due to its easier combustion, cause a higher than required exit temperature of the calcine fed in the E/Fs. The former results in significantly higher Ni% grade in the E/F alloy phase (>14% on average), which is intimately related with lower recovery rates.

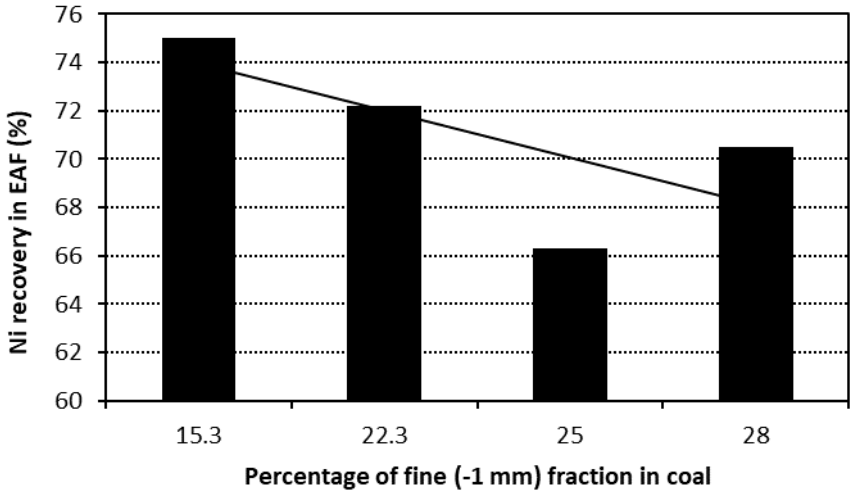

Fig. 14. Nickel recovery rate (R%) in E/Fs vs the percentage of fine (-1 mm) fraction in coal

3.3 Maintenance

Within the nickel price crisis period 2015-2020, tremendous cuts in the maintenance expenses program took place as well, being respectively critical for the disappointing result of the industrial operation. Nonetheless, apart from the objective problem of funding the Greek Fe-Ni industry the period 2015-2019, there should be a shift from the philosophy of corrective maintenance to the preventive maintenance one, being incorporated into a holistic maintenance management system [13]. Moreover, the lack of replacement of very low-cost spare parts, either due to lack of funding or within the framework of just corrective and no preventive management strategy, resulted in great production loss as well as dangerous operational situations.

Further emphasizing on such a typical case study, non - replacement of flexible conduits of E/F transformer within the framework of the shutdown of the furnace few months before for the annual general maintenance, resulted in the non – uniform conduction of the electrical current to each of the EAF conduct clamps. Thus, permanent

overheating of a certain contact clamp resulted in the wear of the clamp, water leakage inside the E/F, danger for the safety of personnel and equipment, melting of steel behind the clamp (Figure 15) and removal of the electrode baking zone considerably higher. Additionally, there was an income loss of 3M€ and a 30 days shutdown of the E/F, due to the lack of spare parts with a cost of just 5,000 €.

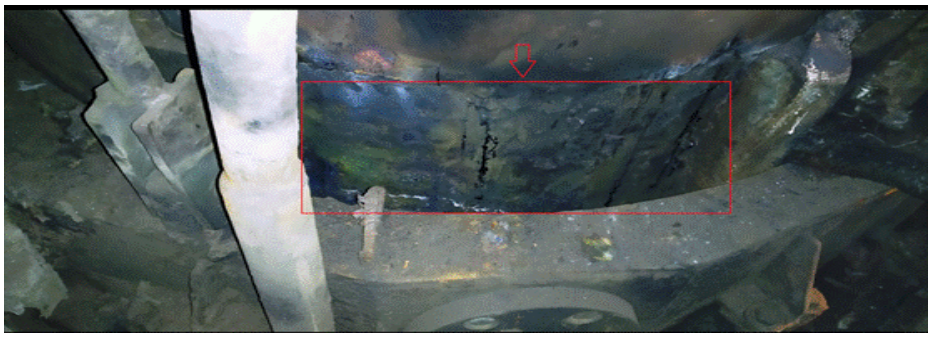

Fig. 15. Case study of melted casing steel due to overheating

3.4 Human resources and Knowledge operationalization

Despite the fact that the Greek Fe-Ni industry operates for over 70 years, mainly due to structural malfunctions, it is true that there is an absolute need for the application of a new management strategy concerning human resources management and process formalization - standardization. Experience can be characterized as a very essential knowledge asset for a metallurgical company, which therefore is quite difficult to be quantified [14]. Moreover, a sustainable and techno-economically optimal operation is difficult to be obtained, without a combination of applying a knowledge management system with the standarization of policies and procedures [15]. Thus, within the framework of planning to restructure the administrative philosophy of a privatized company in the future, it is quite essential to emphasize on the following parameters:

- **Culture of sharing responsibility for collecting and transferring the important knowledge**: loss of experience results in productivity decrease and lack of a sustainable competitive advantage of the Greek Fe-Ni industry. Within this framework, incentives should be given to skilled and experienced workers to remain to the metallurgy and assure successful troubleshooting in difficult -to - handle situations.
- **Tacit knowledge transfer** through organizing internal learning events, enhancing innovation through rewarding out of the box imaginative efforts, or conducting regular internal knowledge exchange forums.
- **Establishment of standarization procedures** for every single metallurgical process, including troubleshooting procedures, instructions with certain guidelines enriched with policies at which all the personnel should adhere. There were many cases were the lack of clearly described step-by-step procedures resulted in lost unit operation time, with respecting loss of thousands of Euros.
- **Introduction of modern IT systems**, for thorough cost monitoring management.

- **Implementation of best practices and best available techniques on health and safety training**, including safety seminars and establishment of modern on-the-job-training techniques.

4 Conclusions

The perspective of re-operation of the Greek nickel industry is a big challenge not only for the raw materials sector but also for the export character of our national economy, in general. Assessment of the big database of Greek nickel industry's operational data of the E/Fs from a techno-economic point of view, constitutes a useful tool for the required management planning, concerning the enterprise operation under a new ownership structure. It is clearly deduced by the current work that it is absolutely critical for achieving the optimum and cost-effective productive result of the pyrometallurgical process, the application of a strategic plan emphasizing on the following:

- **Assurance of the supply of the plant with high Ni grade (Ni%> 1.8 % on a dry basis)** imported laterite ores, with a participation of 35-40% to the laterite mixture and at the same time supply with domestic limonitic type laterite ores with the highest Ni (%) content and Fe (%) and SiO_2 (%) content fluctuating among certain marginal values. The aforementioned, in combination with the stable quality of critical raw materials, such as solid fuels and electrode paste, are the prerequisite for obtaining an Operational Index 75% at least and a special energy consumption lower than 60 MWh/Tn Ni. Therefore, an updated detailed study of the proven domestic ore reserves is very important to confirm that a laterite feed with approximately 1.26 % Ni content on a dry basis, is possible to be practically obtained.
- **SiO_2/MgO percentage ratio higher than 3 and difference of Fe-SiO_2 content higher than -5%**, constitute one of the basic pillars for assuring a stable and safe operation in open bath E/Fs.
- A strategic administrative decision for long-term contracts with suppliers of solid fuels (coke, coal and lignite in addition to the domestic sources of lignite if needed), is a parameter that significantly enhances operational stability and safety in the E/Fs. Industrial experience has shown that occasional co-operations with suppliers in order to face cash flow problems, accompanied by feeding of R/Ks with either fine-grained coal or different qualities of coal with less than the required volatile content, especially in the absence of lignite as a regulatory agent, result in a big decrease of Operational Index in E/Fs, even 30% lower than the expected and significantly lower recovery rates (>10% decrease)
- **Introduction of a holistic maintenance management system with the introduction of modern IT tools for cost analysis**, as well as the shift from the philosophy of corrective maintenance to preventive maintenance, is very essential, increase decisively the E/Fs Operational Index.
- **There is a need for application of modern HR management tools and techniques**, such as tacit and explicit knowledge transfer management strategy, incorporated in a holistic total quality long – term management plan.

Acknowledgments

The authors acknowledge LARCO General Mining and Metallurgical Company under special administration

References

1. Fraser, J., Anderson, J., Lazuen, J., Lu, Y., Heathman, O., Brewster, N., Bedder, J., Masson, O.: Study on future demand and supply security of nickel for electric vehicle batteries, Publications Office of the European Union, Luxembourg, 2021, ISBN 978-92-76-29139-8, doi:10.2760/212807, JRC123439
2. International Nickel Study Group, Lisbon, 26 April 2023, Press Release, Available online: https://insg.org/wp-content/uploads/2023/04/pressrel_INSG-Press-Release-April_2023-kr9tr21a.pdf, (accessed on 07/06/2023).
3. Zevgolis, E.N., Daskalakis, K.: The Nickel production methods from laterites and the Greek Ferronickel production among them, Mater. Proc.2021, 5(1), International Conference on Raw Materials and Circular Economy, 104; Available online: https://doi.org/10.3390/materproc2021005104
4. Sherrit: Does Matte Matter? Is nickel pig iron the answer to EV battery demand? Available online: https://s2.q4cdn.com/343762060/files/doc_downloads/2021/Does-Matte-Matter-Sept-2021.pdf.
5. Zevgolis, E.N., Zografidis, C., Gaitanos, J., Kostika, I.P., Halikia, I.: Energy requirements in nickeliferous laterite treatment, EPD Congress, San Antonio, Texas, 12-16 March 2006, pp. 487-496.
6. Solar, M.Y., Candy, I., Wasmund, B.: Selection of optimum ferronickel grade for smelting nickel laterites, CIM Bulletin 101, 1107 (2016).
7. Bartzas, G., Komnitsas, K: Life cycle assessment of ferronickel production in Greece, Resources, Conservation and Recycling 105, 113-122 (2015).
8. Haque, N., Norgate, T.: Estimation of greenhouse gas emissions from ferroalloy production using life cycle assessment with particular reference to Australia, Journal of Cleaner Production 39, 220-230 (2013).
9. Shefik, I., Gaitanos, I., Tahiraj, N., Rizaj, M., Kongoli, F.: Optimization of technological Fe-Ni production process in NEWCO FERRONIKELI in Kosovo. In: Fray International Symposium, Metals And Materials Processing In A Clean Environment, Vol.1: Sustainable Non-Ferrous Smelting In 21st Century, July, 2013, Edited by Florian Kongoli, FLOGEN.
10. Ma, Y.T. et al.: Effect of FeO content on melting characteristics and structure of Nickel slag. J. Min. Metall. Sect. B-Metall. 58(3), 427-438 (2022).
11. Xueming L. et al: Viscosity of SiO2-MgO-Al2O3-FeO slag for Nickel laterite smelting process. In: The Fourteenth International Ferroalloys Congress May 31-June 4, 2015 Energy efficiency and environmental friendliness are the future of the global Ferroalloy industry, Kiev, Ukraine, pp. 561-566.
12. Zevgolis E.N., Tzamtzis A.: The role of solid fuels used for reduction in Rotary Kilns, Techn. Chron. - C 7(2), 5-19 (1987) (in Greek).
13. Nikolaou, I.: Current trends and prospects for methods and tools in Maintenance Management Systems. Implementation in the Greek Industry, Thesis for Bachelor Degree, University of West Attica, Department Of Mechanical Engineering, 2021.

14. Coetzee, J.C., van Beek W.S.B., Buys, A.: A practical knowledge management framework within the pyrometallurgical industry. The Journal of The Southern African Institute of Mining and Metallurgy 112, 621-630 (July 2012).
15. Requisite Organization International Institute, Challenges to Knowledge Operationalization: Example of Metallurgy Knowledge Operationalization at Metallurgical Operations, Available online: https://www.requisite.org/wp-content/uploads/2019/08/Metallurgical-Knowledge-Operationalization-by-ROII.pdf.

Resin-supported nanoiron: A powerful tool for heavy metal decontamination - Elucidating the mechanism through column studies

Christiana Mystrioti[1], Nymphodora Papassiopi[1] and Anthimos Xenidis[1]

[1]Sch. of Mining and Metallurgical Eng., National Technical University of Athens, 15780, Greece
chmistrioti@metal.ntua.gr

Abstract. The significance of removing heavy metal ions from wastewater treatment plant effluents cannot be overstated in preserving a clean environment and protecting human health. Various methods, including adsorption, membrane-based processes, chemical treatments, electrical methods, and photocatalysis, have been documented for the effective removal of heavy metal ions from different wastewater sources. Nanoparticles, with their strong affinity, show promise in wastewater treatment, particularly in efficiently extracting heavy metals. This study aimed to evaluate the effectiveness of an iron nanocomposite (R-nFe), in eliminating various heavy metals from effluents of wastewater treatment plants through column tests. R-nFe is composed of nano zero valent iron (nZVI) supported in an inert cationic resin, produced using green tea extract as a reducing agent for Fe(III) to Fe(0). The introduced feed solution to the columns contained a mixture of heavy metals, including Cr(VI), As, Ni, Pb, Cu, Cd, and Zn. The study investigated the impact of contact time on the sorption and reduction rates of the selected compounds, varying contact times to 2.4, 4.8, and 6 minutes. R-nFe demonstrated high efficiency in removing Cr(VI) and As, with effluent concentrations meeting environmental limits when the contact time exceeded 5 minutes. However, the performance of R-nFe was less effective for divalent metal contaminants due to the strong competitive effect of coexisting Ca. The study provided a succinct exploration of the mechanisms involved in using the R-nFe nanocomposite for the removal of metals and metalloids.

Keywords: heavy metals, wastewater stream, water pollution, nano zero valent iron, resin, iron nanocomposite, flow conditions, removal mechanism, metal decontamination.

1 Introduction

As the global population steadily grows, the demand for freshwater resources for household, agricultural, and industrial use is on the rise [1]. Concurrently, industrial activities significantly contribute to the deterioration of water quality through the discharge of pollutants, leading to reduced availability and compromised suitability of

clean water sources [2,3]. The effluents of wastewater treatment plants can be used for various purposes, such as agriculture irrigation, landscape irrigation and industrial uses etc.

The use of treated wastewater for irrigation offers a sustainable solution, especially in regions facing water scarcity. However, the quality of the treated water is crucial, and it must meet specific standards to ensure it is safe for the intended use. Low concentrations of heavy metals and micropollutants are detected in the effluents of wastewater treatment plants (WWTPs) [4]. In a study by Du et al. (2020) [4], the concentrations of heavy metals in wastewaters were found to be Pb: 45 ± 15 μg/L; Cd: 5.2 ± 5.1 μg/L; Cr: 57 ± 13 μg/L; Hg: 0.28 ± 0.12 μg/L; and As: 2.6 ± 1.4 μg/L. In 2011, Karvelas and colleagues reported pertinent data on heavy metal concentrations in wastewater effluents from secondary sedimentation tanks, including Pb at 27 ± 3.6 μg/L, Cd at 1.5 ± 0.74 μg/L, Cr at 20 ± 3.5 μg/L, Zn at 270 ± 53 μg/L, and Ni at 430 ± 97 μg/L [5]. Agoro et al. 2020 [6] conducted research on the dispersion of five heavy metals (Cd, Pb, Cu, Zn, and Fe) in wastewater and sewage sludge within their waterbodies in the Eastern Cape Province, South Africa.

The presence of heavy metals in waterbodies and soils can lead to various health problems for both humans and ecosystems. Chromium, cadmium, and arsenic are classified as carcinogenic, while lead is designated as a potential carcinogenic metal by the International Agency for Research on Cancer (IARC) [7,8].

It is evident that the removal of heavy metals is crucial from wastewater effluents to reuse these effluents for irrigation or other uses. Several established technologies address this challenge, each with its unique strengths and weaknesses [9]. Activated carbon [10], biochar [11], and clay minerals [10] offer versatile and cost-effective options, but their effectiveness varies depending on the specific metal. Chemical precipitation and membrane technologies, such as reverse osmosis, excel in removal efficiency but can be energy-intensive or generate waste [12]. Biological approaches like biosorption are eco-friendly but slower and less widely applicable. Advanced oxidation processes like photocatalysis and the Fenton process boast broad contaminant removal but require careful handling and may have limited scalability [9,12].

Over the last two decades, iron nanoparticles have been investigated as promising agents for removing contaminants from soils, groundwater, and other sources [13-16]. Their high surface area allows for efficient adsorption and transformation of harmful metals into less toxic forms through reduction [17, 18]. Additionally, their potential for in-situ remediation offers exciting possibilities for direct water treatment [19]. However, the potential mobility and fate of iron nanoparticles should be considered for in-situ applications. To minimize risks, incorporating them into an inert porous matrix and using them as a water treatment filter is suggested.

In this study, an iron nanocomposite containing iron nanoparticles supported in a cationic resin (Amberlyst 15 H^+) was evaluated for cleaning up a polluted water stream containing heavy metals (Cr(VI), As, Ni, Pb, Cu, Cd, and Zn). Resin-supported nano-iron (R-nFe) is a nanocomposite material with high potential for remediating contaminated waters [20]. The resin can remove cationic metal contaminants through cation exchange or chelation processes, while nano zero-valent iron (nZVI) can also eliminate anionic contaminants, such as Cr(VI), by reducing it to Cr(III), or adsorb As(V) onto

the oxidized outer shell of nZVI. The experimental work involved a series of column tests with different contact times of the feed solution with the nanocomposites, namely 2.4, 4.8, and 6 minutes. To evaluate the potential use of effluents from a wastewater treatment plant (WWTP) as treated wastewater for various applications (e.g., irrigation, industrial use, or potable water), it was crucial to add it in the feed solution. The composition of the feed solution simulated the effluents of wastewater treatment plants contaminated with heavy metals, and the removal mechanisms were described in detail.

2 Materials and Methods

2.1 Synthesis of R-nFe

This study describes the synthesis of a resin-nZVI nanocomposite, R-nFe. Amberlyst 15 H+ (Sigma-Aldrich, China), a macro reticular polystyrene based ion exchange resin with strongly acidic sulfonic groups, was used as the host matrix. Iron chloride (FeCl3·6H2O) served as the iron source, and dry leaves of green tea (Twining of London) provided polyphenols. The detailed synthesis procedure is illustrated in Fig. 1.

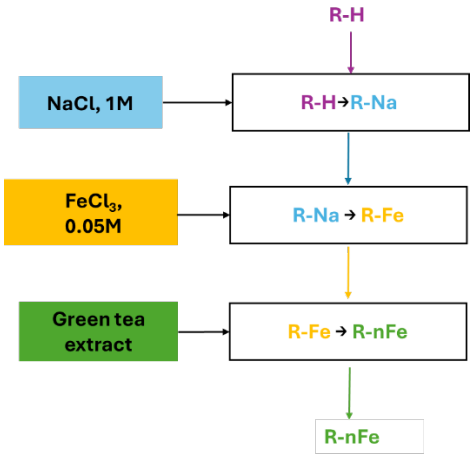

Fig. 1. The main steps of R-nFe synthesis procedure

A pre-conditioning step to improve the reactivity of the resin-iron nanoparticle composite (R-nFe) towards pollutant capture was implemented. This involved stirring the R-nFe in a 1 M NaCl solution for 24 hours at 200 rpm with a 1:10 R-nFe -to-solution ratio. This NaCl pre-treatment enhances the reactivity of R-nFe with target pollutants, possibly due to the corrosion of nZVI particles [21]. The total iron content of R-nFe was determined to be 0.50 mmol/g, while the reactive elemental iron content, responsible for pollutant removal, was estimated at 0.35 mmol/g.

2.2 Column experiments

The performance of the R-nFe nanocomposite for pollutant removal was evaluated through column experiments conducted over a period of 12 days, with experiments paused during weekends. Polyethylene columns with an internal diameter of 2.63 cm and a length of approximately 10 cm were employed. These columns were filled with varying amounts of the R-nFe nanocomposite: 12.5 g, 25.0 g, and 34.9 g, corresponding to volumes of 16.3 mL, 32.6 mL, and 43.5 mL, respectively. The nanocomposite was manually packed into the columns with gentle vibration at intervals to ensure homogenous packing. Table 1 provides detailed information regarding the properties of the three columns. The final bulk density in the columns, a measure of packing efficiency, ranged from 0.79 to 0.86 g cm-3 (as shown in Table 1). The packed columns were then connected to a pump and a reservoir containing the test solutions (Fig. 2). A schematic diagram of the experimental setup is presented in Figure 2.

Table 1. Properties of columns

	Columns		
Properties	**I**	**II**	**III**
Resin Mass weight, M (kgx10^{-3})	12.50	25.00	34.9
Column diameter, d (cm)	2.63	2.63	2.63
Column height, L (cm)	3	6	8.0
Bed Volume, BV (cm^3)	16.3	32.6	43.5
Particle density, ρ_p (g/cm^3)	1.21	1.21	1.21
Bulk density, ρ_b[(a)] (g/cm^3)	0.77	0.77	0.80
Porosity, θ[(b)]	0.37	0.37	0.34
Pore volume, V_{PV} (cm^3)	6	12	14.47
Flow rate, Q (mL/min)	2.5	2.5	2.5
Pore Volume Contact Time, τ[(c)] (min)	2.4	4.8	5.9
Empty Bed Contact Time, EBCT[(d)] (min)	6.5	13	17.3

(a) Dry bulk density calculated based on this equation $\rho_b=M/BV$

(b) Porosity calculated based on this equation $\theta=1-\rho_b/\rho_p$

(c) $\tau=Q/V_{PV}$

(c) EBCT=Q/BV

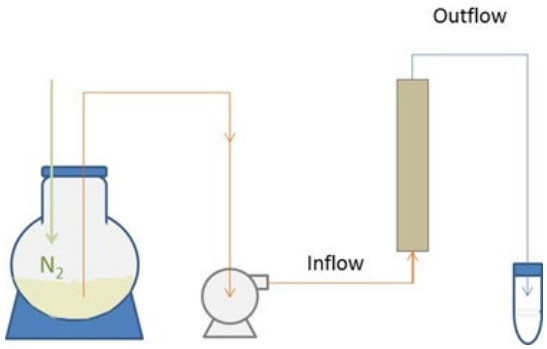

Fig. 2. Experimental set up [20]

The three columns were fed with a solution consisting of 44.4 mL/L Psyttalia WWTP effluents (2nd stage treatment) diluted with tap water of National Technical University of Athens (supplied by a drilling in the campus). The Psyttalia WWTP is the main wastewater treatment plant in Athens, Greece, receiving an average wastewater flow of approximately 730,000 m3/d). The solution was also spiked with a concentrated solution of a mixture of heavy metals (5 mL/L) to obtain the predetermined level of metal contaminants, i.e. 500 μg L-1 Cr(VI), 2 mg L-1 Ni, 1 mg L-1 Pb, 2mg L-1 Cu, 100 μg L-1 Cd, 20 mg L-1 Zn and 2 mg L-1 As (Table 2). The metal concentrations in the feed solution were selected to be approximately ten times higher than the limits which were established by the Greek legislation for recycling the WWTP effluents in other uses [22]. The pH of the solution was adjusted to 3.5 using concentrated HCl. The flowrate was constantly 2.5 mL/min and was the same for the three columns. Taking into consideration the bed volume and the porosity of the 3 packed beds, the contact time of the solution with the R-nFe beads was 2.2 min, 4.8 min, and 5.9 min, in the shortest, middle and highest size bed, respectively. The main physicochemical properties of tap water (TW) and feed solution are presented in Table 2.

2.3 Sampling and analyses

Column effluents were sampled and analyzed for pH, EC and concentrations of hexavalent chromium, Cu, Cd, Zn, As, Ca, Mg. Cu, Ca, Mg and Zn concentrations were determined by atomic absorption spectroscopy-flame emission, AAS-FE. Cd concentrations were determined by graphite absorption spectroscopy-flame emission Hexavalent chromium was analyzed by using the USEPA 7196a method, at a HACH DR-1900 spectrophotometer. Arsenic concentrations were analyzed applying ASTM D5673:2016 method at EAGME laboratory. pH values were measured using a pH meter Metrohm 827 pH Lab. Ni and Pb will be analyzed by ICP-OES.

Table 2. Quality of tap water (TW) and feed solution.

Parameters	Units	Tap water (NTUA Campus)	Feed Solution	WWTP effluents reuse limits [22]
pH		7.3	3.5	
TOC	mg/L	8.6	2.6	
Alkalinity	mg $CaCO_3$/L	409	--	
Cr(VI)	μg/L	<15	500	
Ca	mg/L	106.1	116	
Mg	mg/L	36.2	24	
Na	mg/L	44.1		
K	mg/L	1.44		
Ni	mg/L	<0.2	2	0.2
Cu	mg/L	<0.1	2	0.2
Cd	mg/L	<0.04	0.1	0.01
Zn	mg/L	0.11	20	2
Pb	mg/L	<0.5	1	0.1
Cr	mg/L	<0.3		0.1
As	mg/L	<0.2	2	0.1

3 Results

3.1 Evolution of pH

Figure 3 shows the pH values in the effluent solutions as a function of the hours of operation. The pH of feed solution was adjusted at 3.5. As shown in Fig. 3 the solution was strongly acidified when passed through the R-nFe beads. During the operation with the contaminated solution the pH in the outlet increased slowly from 1.5 to 3.5 at the end of the experiment (Fig. 3). The decrease of pH values observed at 75 and 170 hours is due to the interruption of operation during the weekends, which caused the acidification of the solution remaining in contact with the R-nFe beads inside the columns.

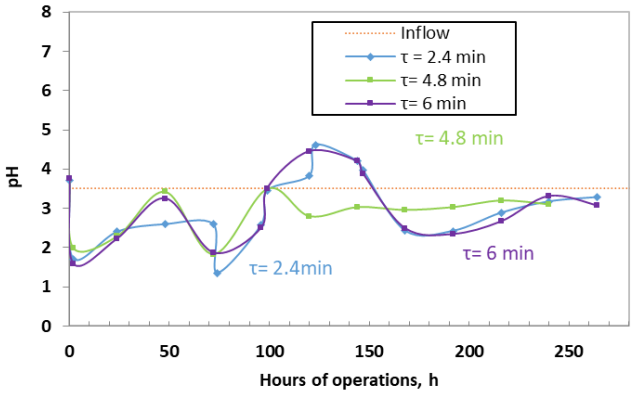

Fig. 3. Evolution of pH in the effluents of the three columns in comparison with the pH of inflow solution

3.2 Removal of Cr(VI)

The concentration of Cr(VI) in the feeding solution of columns was 500 μg/L. The effect of contact time on the Cr(VI) concentration in the effluent can be seen in Fig. 4. During the initial stages of operation, measurable amounts of Cr(VI) occurred after 50 hours of operation for column I (τ= 2.4min). The concentration of Cr(VI) in the effluents increased and reached a plateau at 325 μg/L, which is lower than the initial concentration of the feed solution. When the contact time of the polluted solution with the R-nFe was equal to 4.8 min (Column II), the Cr(VI) content in the effluent was constantly below detection limit for 74 hours of operation. Detectable values of Cr(VI), between 25 and 50 μg/L, appeared in the effluent for operation time from 74 to 144 hours. The concentration remained quasi constant, close to 200 μg/L, between 144 h and 264 h of operation. When the contact time of solution with R-nFe beads increased to 5.9 min (Col. III), all Cr(VI) was removed and the effluents did not contain any detectable amount for 216 hours. Measurable amounts of Cr(VI), from 50 to 185 μg/L, were observed after the 10th day (240 h) of operation.

From the results shown in Figure 4, it can be estimated that a column filled with the nanocomposite R-nFe is able to reduce the concentration of Cr(VI) from 500 to less than 50 μg/L for a total amount of solution equivalent to 2400 bed volumes, if the contact time is at least equal to 5.9 minutes. The total volume is reduced to 1750 and 1250 bed volumes if the contact time is reduced to 4.8 and 2.4 minutes, respectively. It is seen however that the concentration of Cr(VI) in the effluent is lower than the inflow concentration even in the column with the lower contact time after 280 hours of operation.

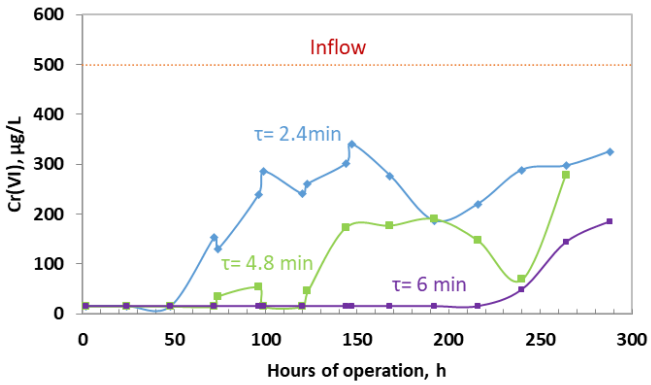

Fig. 4. Evolution of Cr(VI) concentration in the effluents of the three columns

The cumulative removal of Cr(VI) per gram of R-nFe, q_i, was calculated according to equation (2) and the corresponding curves are shown in Figure 5.

$$q_i = \frac{Q}{M_R} \sum_{1}^{i} (C_f - C_{e,i})\, \Delta t_i \qquad (2)$$

where Q is the flowrate (ml/min), M_R is the mass of R-nFe in the column (g), C_f is the concentration of Cr(VI) in the feed solution (mg/mL), $C_{e,i}$ is the mean concentration of Cr(VI) in the effluents between the sampling events i-1 and i (mg/mL), and Δt_i is the time interval between sampling events i-1 and i (min).

In a previous publication by our team, the effectiveness of R-nFe for chromate removal was evaluated through batch experiments. All tests were conducted by mixing 100 mL of Cr(VI) solution with the appropriate amount of R-nFe in 250 mL shaking flasks. The experimental parameters examined included agitation rate, particle size of R-nFe beads, initial chromate concentration, nZVI content in resin, resin dose per liter of solution, and solution pH. Based on these batch tests, the maximum removal capacity of the nanocomposite was equal to 0.43 mmol Cr(VI)/g or 22.36 mg Cr(VI)/g [23]. It should be noted that the batch experiments in that study were carried out using deionized water, while in the present study the experiments took place using a more complex matrix containing competitive cations and anions. The results from that study are presented here for comparison with the current findings, which focus on chromate removal using a column study approach. As shown in Figure 5, it is evident that the maximum removal capacity was not exhausted, and the process is still in progress with a continuous increasing trend. The Cr(VI) removal after 288 hours of operation was equal to 1.0 mg/g, 6.3 mg/g and 5.7 mg/g for the columns with contact time 2.4, 4.8 and 6 min respectively.

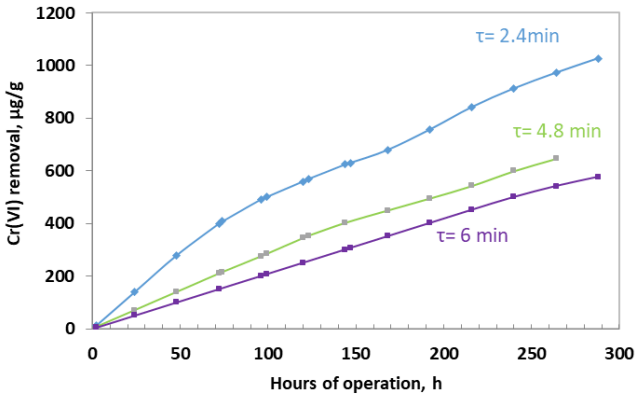

Fig. 5. Cumulative removal of Cr(VI) in the three columns

3.3 Removal of As

The evolution of arsenic in the effluent of the three columns is presented in Fig. 6a. High arsenic concentrations were detected in the 1st day of operation in Col. I and III. The arsenic concentrations decreased significantly after the 2nd day of operation in all three columns. Arsenic concentration in the effluents remained at low levels, <5-68 μg/L, till the end of experiment in Column III (τ=6 min). In Column II (τ=4.8 min), the concentrations were between <5 and 50 μg/L till 200 h and there was a slight increase above the limit of 100 μg/L at 264 h. The concentration of As in the effluents of Column I increased above the environmental limit after 150 h of operation.

The present work was carried out using pentavalent arsenic. As previously mentioned, the removal of arsenate using nZVI could be attributed to the precipitation of ferrous or ferric arsenates, such as Fe2(AsO4)3.8H2O or FeAsO4.2H2O. However, the relatively low pH (3.5-4.5) excludes the precipitation of symplesite (Fe2(AsO4)3.8H2O). Symplesite is a compound with very low solubility (pKso=33.25) but precipitation starts above pH 5 and the minimum As concentration is observed at pH close to 8 [24]. Precipitation of scorodite FeAsO4.2H2O occurs at acidic pHs but requires higher temperature conditions. During these experiments the most probable retention mechanism is chemisorption on the surface layer of Fe(III) oxides. A relative delay in the formation of oxidized surface layer around the nZVI particles could be the reason for the high concentrations of As observed in the first samples of effluents.

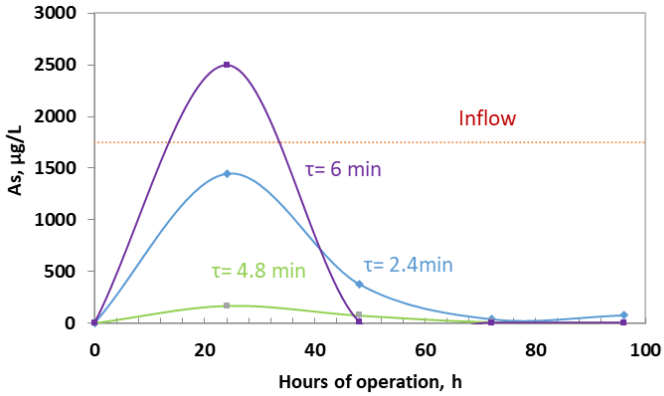

(a)

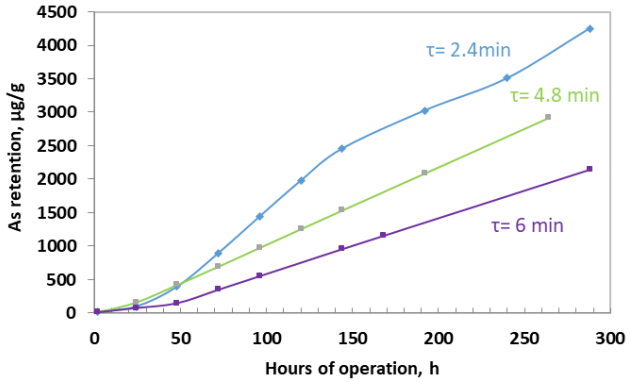

(b)

Fig. 6. Evolution of As removal in the 3 columns: (a) arsenic concentration in the effluents (µg/L), (b) cumulative retention in R-nFe (µg/g)

The cumulative retention of As by the R-nFe in the 3 columns is shown in Figure 6b. The retention increases almost linearly, indicating that the capacity of R-nFe to adsorb As is not exhausted. After 288 hours of operation the retention in column I (τ=2.4 min) is equal to 1026 µg/g.

3.4 Removal of divalent metal contaminants

The evolution of Cu concentration in the effluents of the 3 columns is shown in Figure 7a and the cumulative removal is shown in Figure 7b. As seen in Figure 7a, the concentration of copper in the effluents was maintained below the environmental limit 0.2 mg/L, only in column III (τ=6 min) and only for 24 hours of operation. This performance corresponds to the treatment of solution volume equivalent to 81.6 bed volumes.

In the other 2 columns with lower contact times Cu concentration exceeds the limit in the first sample taken at 24 hours.

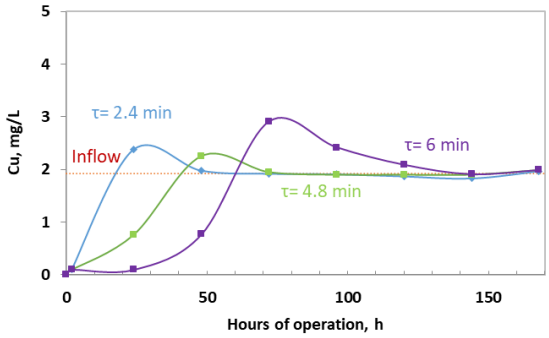

(a)

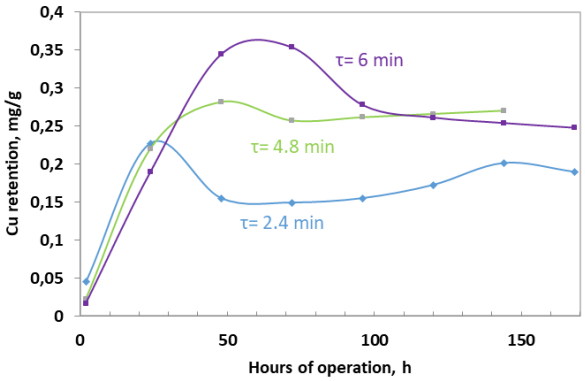

(b)

Fig. 7. Evolution of Cu removal in the 3 columns: (a) concentration in the effluents (mg/L), (b) cumulative retention in R-nFe (mg/g)

As shown in Figure 7b, the maximum cumulative retention of Cu by R-nFe in column III is equal to 0.35 mg/g, but there is a desorption effect, and the retention is finally stabilized close to 0.25 mg/g. A similar effect is observed in Column II (τ=4.8 min). In Column I (τ=2.4 min) the retention observe is lower in the order of 0.2 mg/g.

The results of Cd removal are shown in Figure 8. Concentrations below the limit of 10 μg/L were observed only in Column III and for the 24 initial hours of operation (Fig. 8a), similarly to the case of Cu. The final retention by R-nFe ranged between 14 and 18 μg/g (Fig. 8b).

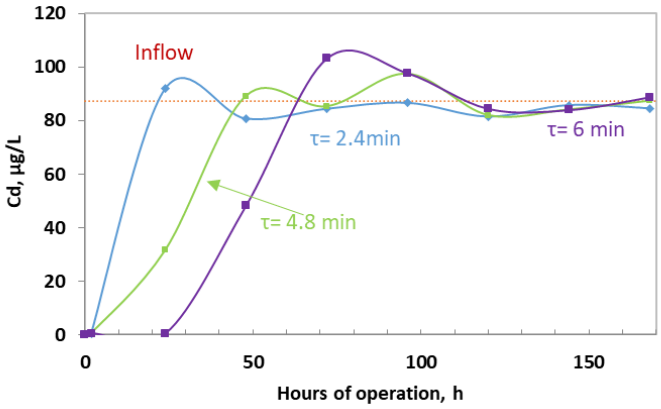

(a)

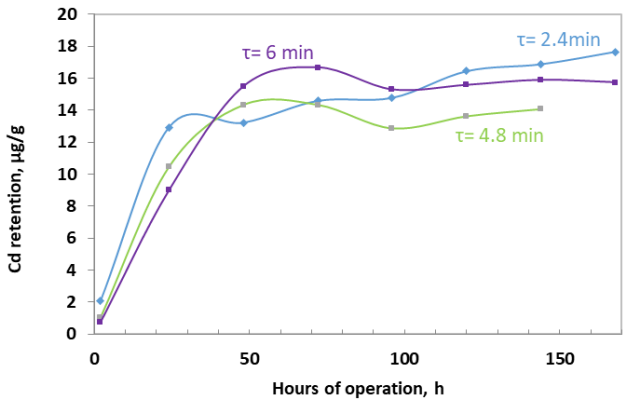

(b)

Fig. 8. Evolution of Cd removal in the 3 columns: (a) concentration in the effluents (µg/L), (b) cumulative retention in R-nFe (µg/g)

Zinc removal is presented at Figure 9. As previously observed a satisfactory performance was recorded only with column III (τ=6 min) for 24 hours (Fig. 9a). The appearance of a maximum value followed by a desorption effect was also very clear in the curves describing the cumulative retention of zinc by the R-nFe beads (Fig. 9b).

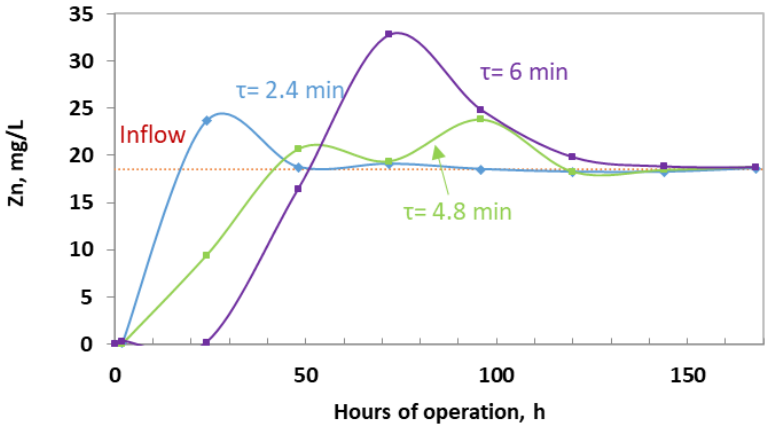

(a)

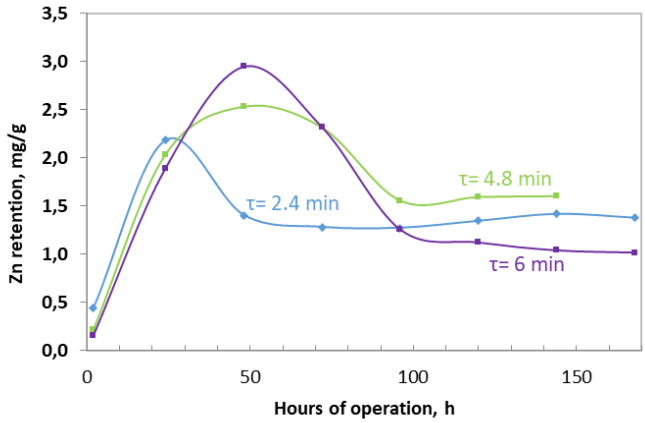

(b)

Fig. 9. Evolution of Zn removal in the 3 columns: (a) concentration in the effluents (mg/L), (b) cumulative retention in R-nFe (mg/g)

3.5 The effect of major divalent metals, Ca and Mg

The natural waters as well as WWTP effluents contain Ca and Mg at concentrations much higher than the concentration of usual metal contaminants (see Table 2). The water hardness is approximately 388.40 mg/L as $CaCO_3$ based on the calcium and magnesium concentration in the feed solution. To evaluate the effect of their presence, all the effluent solutions were also analyzed for these two metals. The results are presented in Figures 10 and 11 for Ca and Mg respectively.

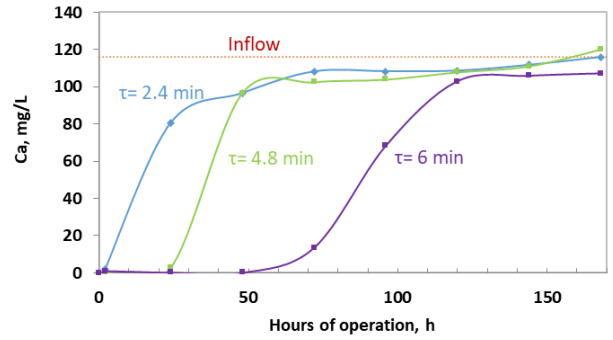

(a)

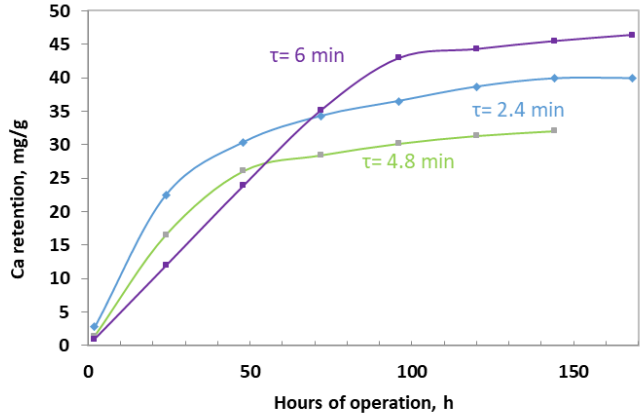

(b)

Fig. 10. Evolution of Ca removal in the 3 columns: (a) concentration in the effluents (mg/L), (b) cumulative retention in R-nFe (mg/g)

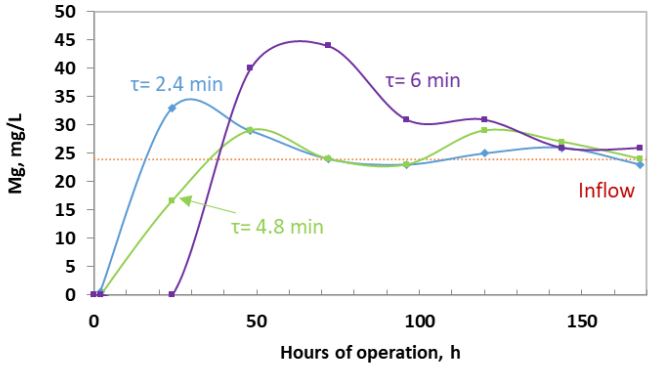

(a)

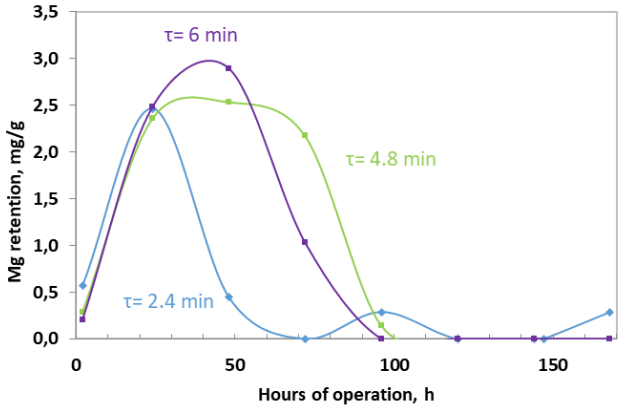

(b)

Fig. 11. Evolution of Mg removal in the 3 columns: (a) concentration in the effluents (mg/L), (b) cumulative retention in R-nFe (mg/g)

The breakthrough curves in Fig. 10a indicate that Ca is also retained by R-nFe. The concentration in the effluents approaches the value in the feed solution after 48 hours in Columns I and II and after 120 hours in Column III. The curves representing the cumulative retention of Ca follow a monotonic increasing trend, as seen in Figure 10b.

The removal of Mg follows a different trend. The charts in Figures 11a and 11b show that Mg is initially retained in the R-nFe, but after 72-96 hours of operation is completely repelled out of the resin beads.

The repulsion of Mg, as well as of other divalent metals, is obviously caused by the competitive adsorption of Ca. This is illustrated in Figure 12 for the case of Mg and Zn in the effluents of Column III in comparison with the levels of Ca. It is seen that all three elements are retained in R-nFe beads during the initial 24 hours. Between 24 and 96 hours, Ca continues to be retained and replaces Mg and Zn in the cation exchange

matrix of the resin. This effect can explain the fact that the concentrations of Zn and Mg in the effluents are higher compared to their concentration in the feed solution.

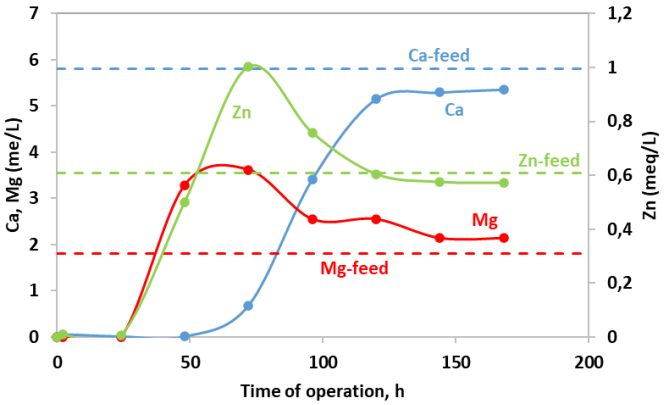

Fig. 12. The evolution of Mg, Zn and Ca concentration in the effluents of Column III

3.6 Selectivity factors for the retention of divalent cations on the strongly acidic cation exchange resins

The host matrix of R-nFe material is a strongly acidic cation exchange resin with sulphonic functional groups. According to Amberlite and Dupont manufacturers this type of resins exhibits high selectivity of Ca towards most heavy metals. A typical selectivity scale is shown in Table 3.

Table 3. Typical selectivity scale of sulphonic resins for divalent metals

Mg^{++}	Zn^{++}	Co^{++}	Cu^{++}	Cd^{++}	Ni^{++}	Mn^{++}	**Ca^{++}**	Pb^{++}
0.63	0.67	0.71	0.73	0.75	0.75	0.79	1	1.9

The high affinity of the resin for Ca can explain the trend of breakthrough curves and the poor performance of R-nFe material for Zn, Cu, Ni and Cd removal from treated waters.

The total cation exchange capacity of the host matrix is equal to 2.7 meq/g. It calculated the milli-equivalents of divalent and trivalent cations retained in R-nFe after 168 hours of operation in the three columns. Due to the low pH (2.5-3.5), we have assumed that the reduced Cr(III) and the Fe(III) generated from the oxidation of nZVI do not precipitate but are simply retained electrostatically by the sulfonic groups. The percent distribution of retained metal equivalents is shown in Figure 13.

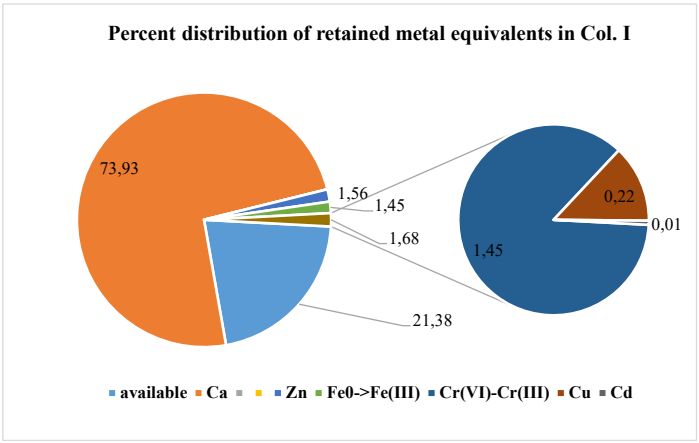

(a)

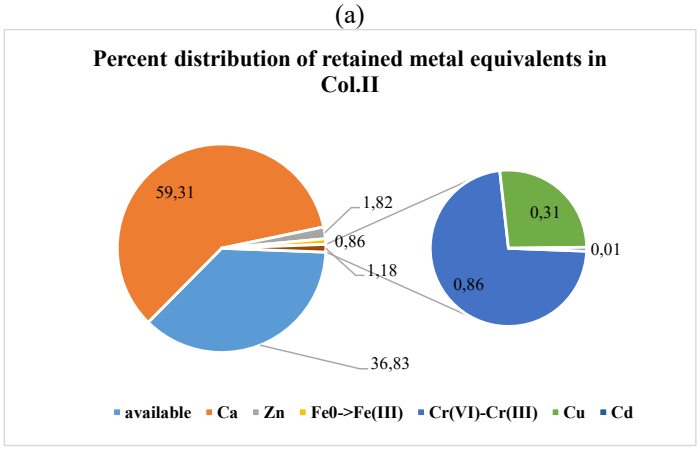

(b)

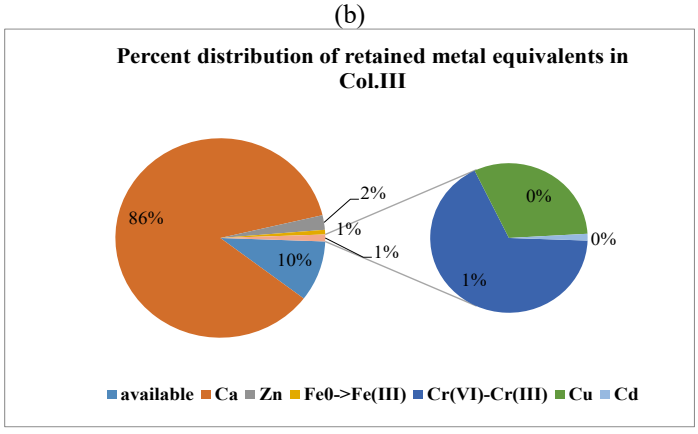

(c)

Fig. 13. Percent distribution of retained metal equivalents in the 3 columns after 168 hours for Columns I and III, and 144 hours of operation for Column II

As seen in Fig. 13 a major part of cation exchange capacity is occupied by Ca cations, followed by Zn. Magnesium was completely expelled for all three columns.

4 Discussion

4.1 Mechanisms involved in the removal of metal contaminants by R-nFe

Nanocomposite R-nFe consists of elemental iron nanoparticles (nZVI) incorporated in a cation exchange resin. Both the host matrix and nZVI particles contribute in the removal of metals and a brief description of the mechanisms is given below.

Reactivity of nZVI

The reactivity of nZVI is primarily related with the strong reducing capacity of metallic iron. Data for selected redox reactions involving characteristic inorganic and organic contaminants are given in Table 4. Two columns with values of standard reduction potential are included in the table. The first corresponds to the standard potential, Eh0, where proton activity is considered equal to one molar. The values in the second column, Eh0 (pH=7), were calculated assuming pH equal to 7. This series of values is considered to be more representative of the conditions prevailing in natural waters. Data are presented in order of decreasing Eh0 (pH=7). The reducing strength of the species to the left side of the reactions tends to increase towards the bottom of the Table. As seen elemental iron is situated very low in this order and theoretically can reduce all the oxidized species situated above, i.e. with higher Eh0 (pH=7) values.

Table 4. Standard reduction potential for characteristic metal contaminants

Half reactions	E_h^0 (V)	E_h^0 (pH=7)(V)
$Hg^{2+} + 2e^- \leftrightarrow Hg$	0.86	0.86
$Ag^+ + e^- \leftrightarrow Ag$	0.80	0.80
$CrO_4^{2-} + 8H^+ + 3e^- \leftrightarrow Cr^{3+} + 4H_2O$	1.51	0.41
$Cu^{2+} + 2e^- \leftrightarrow Cu$	0.34	0.34
$Pb^{2+} + 2e^- \leftrightarrow Pb$	-0.13	-0.13
$H_2AsO_4^- + 3H^+ + 2e^- \leftrightarrow H_3AsO_3 + 3H_2O$	0.42	-0.20
$Ni^{2+} + 2e^- \leftrightarrow Ni$	-0.25	-0.25
$Cd^{2+} + 2e^- \leftrightarrow Cd$	-0.40	-0.40
$Fe^{2+} + 2e^- \leftrightarrow Fe$	**-0.44**	**-0.44**
$Zn^{2+} + 2e^- \leftrightarrow Zn$	-0.76	-0.76
$Ba^{2+} + 2e^- \leftrightarrow Ba$	-2.92	-2.92

Among the metals presented in Table 4, Hg+2, Ag+1, Cu+2, Pb+2, Ni+2 and Cd+2 are cations which theoretically can be reduced by metallic iron to the elemental state.

On the contrary Zn2+ cannot be reduced because it is situated below iron in the reduction potential scale.

Hexavalent chromium, Cr(VI), exists in the form of anions, CrO42-, and when reduced in the trivalent state under the action of elemental iron precipitates in the form of low solubility solid compounds, such as mixed Fe-Cr hydroxides as shown in equation (1):

$$Fe^0 + HCrO_4^- + 2H_2O + H^+ \rightarrow Fe(OH)_3Cr(OH)_3 + H^+ \quad (1)$$

Arsenic is a metalloid and its usual forms in aquatic media are the pentavalent and trivalent oxyanion species, H2AsO4- and H3AsO3. Pentavalent arsenic in the presence of Fe(II) and Fe(III) precipitates in the form of ferrous and ferric arsenate phases like symplesite, Fe3(AsO4)2·8H2O and scorodite, FeAsO4·2H2O. Trivalent arsenic does not form any stable solid compound, but it is known to adsorb on the surface of iron oxyhydroxides.

When the metals have a redox potential more negative or close to that of iron, e.g. Zn, Cd, the preponderant removal mechanism is adsorption or co-precipitation with Fe(II) and Fe(III). It should be noticed that a second very important mechanism related with the reactivity of nZVI is due to its core-shell structure. When the metallic iron nanoparticles come in contact with the aquatic environment, their surface is oxidized and a layer of iron oxides is rapidly formed around the metallic core. The iron-oxides shell provides a very efficient substrate for the adsorption of contaminants.

Contribution of the cation-exchange resin

The matrix used for the incorporation of nZVI is a cation exchange resin. The cations retained in the resin after the synthesis procedure are primarily monovalent, e.g. H+ or Na+. It is known that during the cation exchange processes, cations with higher ionic charge are stronger bound to the resin and can replace cations with lower charge. It thus expected that divalent metals will be removed from the aqueous phase by replacing H+ and Na+ in the resin. However, natural waters, as well as WWTP effluents, contain also alkaline earth metals such as Ca+2 and Mg+2, which may compete with the metal contaminants in the cation exchange process.

5 Conclusions

This study focused on the effectiveness of a novel nanocomposite material, resin-supported nanoiron (R-nFe), for remediating water contaminated with heavy metals, including Cr(VI), As, Ni, Pb, Cu, Cd, and Zn. The experimental results revealed that the iron nanocomposite exhibited significant potential in removing Cr(VI) and As from the water stream. The column experiments demonstrated varying degrees of efficiency depending on the contact time between the feed solution and the nanocomposite. Particularly noteworthy was the efficient removal of Cr(VI) from the water, with concentrations dropping to less than 50 μg/L when the contact time is 6min. The study also highlighted the dynamic interactions between R-nFe and various heavy metals, elucidating mechanisms involving reduction, adsorption, and cation exchange facilitated by the resin matrix. Additionally, the research shed light on the intricate competition

between divalent metals, such as Ca and Mg, and the targeted contaminants during the cation exchange process within the resin-supported nanocomposite. Overall, the findings underscore the promising potential of R-nFe for water treatment applications, offering insights into its mechanisms and selectivity factors critical for future advancements in water remediation technologies.

References

1. World Bank Group, UNICEF. State of the World's Drinking Water report (2022)
2. WWAP. The United Nations World Water Development Report 2023: Water Security for Humanity. UNESCO Publishing (2023)
3. UN DESA. World Population Prospects 2022. United Nations Department of Economic and Social Affairs (2022)
4. Du, P., Zhang, L., Ma, Y., Li, X., Wang, Z., Mao, K., Wang, N., Li, Y., He, J. Zhang, X. Occurrence and Fate of Heavy Metals in Municipal Wastewater in Heilongjiang Province, China: A Monthly Reconnaissance from 2015 to 2017. Water 12, 728 (2020)
5. Karvelas, M., Katsoyiannis, A., Samara C. Occurrence and fate of heavy metals in the wastewater treatment process. Chemosphere, 53 1201–1210 (2003)
6. Agoro, M.A., Adeniji, A.O., Adefisoye, M.A. and Okoh, O.O. Heavy Metals in Wastewater and Sewage Sludge from Selected Municipal Treatment Plants in Eastern Cape Province, South Africa. Water, 12, 2746 (2020)
7. EPA. Volume I: Human Health Evaluation Manual (Part a) Washington, DC, USA: EPA. Risk assessment guidance for superfund (2004)
8. IARC. IARC Monographs on the Identification of Carcinogenic Hazards to Humans: Volumes 1–125. Bristol, UK: IOP Publishing PhysicsWeb (2012)
9. Hashim, M.A., Mukhopadhyay, S., Sahu J. N., Sengupta, B. Remediation technologies for heavy metal contaminated groundwater, Journal of Environmental Management, 92, 10, 2355-2388 (2011)
10. Karnib, M., Kabbani, A., Holail, H. and Olama, Z. Heavy Metals Removal Using Activated Carbon, Silica and Silica Activated Carbon Composite, Energy Procedia, 50, 113-120 (2014)
11. Wang, Y., Li, H., Lin, S. Advances in the Study of Heavy Metal Adsorption from Water and Soil by Modified Biochar. Water, 14, 3894 (2022)
12. Qasem, N. A. A., Mohammed, R. H. D. U. and Lawal D.U. Removal of heavy metal ions from wastewater: a comprehensive and critical review npj Clean Water 4, 36 (2021)
13. Dave, P.N. and Chopda, L. V. Application of Iron Oxide Nanomaterials for the Removal of Heavy Metals. Journal of Nanotechnology. 398569, 14 p. (2014). http://dx.doi.org/10.1155/2014/398569
14. Vijaya Bhaskar Reddy, A., Moniruzzaman, M., Madhavi, G. Removal of Heavy Metal Pollutants from Wastewater Using Zerovalent Iron Nanoparticles. Water Pollution and Remediation: Heavy Metals. Environmental Chemistry for a Sustainable World, 53 (2021)
15. Mohamed, A., Atta, R.R., Kotp, A.A. Green synthesis and characterization of iron oxide nanoparticles for the removal of heavy metals (Cd^{2+} and Ni^{2+}) from aqueous solutions with Antimicrobial Investigation. Scientific Reports 13, 7227 (2023)
16. Xu, W., Yang, T., Liu, S., Du, L., Chen, Q., Li, X., Dong, J., Zhang, Z., Lu, S., Gong, Y., Zhou, L. Liu, Y., Tan, X. Insights into the Synthesis, types and application of iron

Nanoparticles: The overlooked significance of environmental effects, Environment International, 58, 106980 (2022)
17. Dermatas, D., Mpouras, T., Papassiopi, N., Mystrioti, C., Toli, A. and Panagiotakis, I. Adsorption of Groundwater Pollutants by Iron Nanomaterials. Iron Nanomaterials for Water and Soil Treatment. 1st edn. Jenny Stanford Publishing (2018)
18. Tarekegn, M. M., Hiruy, A. M. and Dekebo, A. H. Nano zero valent iron (nZVI) particles for the removal of heavy metals (Cd^{2+}, Cu^{2+} and Pb^{2+}) from aqueous solutions. RSC Advances, 11, 18539 (2021)
19. Mondal, A., Dubey, B. K., Arora, M. and Mumford, K. Porous media transport of iron nanoparticles for site remediation application: A review of lab scale column study, transport modelling and field-scale application, Journal of Hazardous Materials, 403, 123443, (2021)
20. Toli, A., Mystrioti, C., Avgoustidis, I., Papassiopi, N., Fixed-bed flow experiments with supported green nZVI for the remediation of contaminated waters: Effect of pH and background solution composition, Chemosphere, 279, 130472 (2021)
21. Panagou, I., Noutsopoulos, C., Mystrioti, C., Barka, E., Koumaki, E., Kalli, M., Malamis, S., Papassiopi, N., Mamais, D. Assessing the Performance of Environmentally Friendly-Produced Zerovalent Iron Nanoparticles to Remove Pharmaceuticals from Water. Sustainability, 13, 12708 (2021)
22. Common Ministerial Decision No. 145116, 2011 (FEK 354/B/2011)
23. Toli, A., Varouxaki, A., Mystrioti, C., Xenidis, A. and Papassiopi N. Green Synthesis of Resin Supported Nanoiron and Evaluation of Efficiency for the Remediation of Cr(VI) Contaminated Groundwater by Batch Tests. Bulletin of Environmental Contamination and Toxicology 101:711–717 (2018)
24. Johnston, R. and Singer, P. Solubility of Symplesite (Ferrous Arsenate): Implications for Reduced Groundwaters and Other Geochemical Environments. Soil Sci. Soc. Am. J. 71:101-107 (2007)

Europe's economic geology potential enables reducing its geopolitical dependence on critical and strategic minerals

Nikolaos Arvanitidis, Dr Economic Geologist, Chair of the Mineral Raw Materials Committee, Association of Greek Geologists

Skeppstavägen 15, 12430 Bandhagen, Stockholm, Sweden
Nikolaos.Arvanitidis@gmail.com
greenminerals@nikolaosarvanitidis.eu

Abstract. For many years mineral raw materials were the missing link in the climate debate. A significant number of critical and strategic minerals (CSM) in continuously increasing quantities will be needed to achieve the global economy's need to become free of hydrocarbons. CSMs are utilized in the production of semiconductors, wind turbines, photovoltaics, and lithium batteries, which are employed to store and transfer renewable energy. Nonetheless, the EU depends 75–100% on imports for the majority of CSMs. Additionally, a lot of CSMs are produced and processed in a single nation or region, which puts their geopolitical supply and accessibility at risk. The goal of the Critical Raw Materials Act (CRMA) is to increase Europe's progressive autonomy in CSMs and long-term self-sufficiency. Recycling does not currently generate a substantial amount of resources for several of the CSMs. Europe's geology and metallogenic evolution have considerably favoured the fruitful use of its own CSM resources, which turns out to be the main factor enabling the continent to become resilient, self-sufficient, self-sustaining, and sustainable. Europe will have to establish its channels and means of obtaining the necessary amounts of resources due to China's geopolitical dominance, use of corporate partnerships, collaboration agreements, and investments made globally regarding the exploitation of other nations' CSMs. The predominant targets for the EU are to develop new mineral supply chains, become less dependent on China, and strengthen key technology value chains, including processing, refining, and metallurgy facilities.

Keywords: Critical and strategic minerals, European economic geology, Geopolitical shifts

1 Background

The imperative for a hydrocarbon-free global economy will require a large number of mineral raw materials in steadily growing amounts [1]. It is therefore important to know which and in what quantities they are needed to understand and assess the implications of insufficient access or their inadequacy for the European, and therefore the Greek, economy. During the last twelve years, the "criticality assessment" at the

European level aimed to identify those mineral raw materials that are generally evaluated to be at risk of mineral inaccessibility and insufficiency, and to be of great technical, economic, and social importance for several key value chains [2]. For these reasons, they were considered to be critical and strategic minerals (CSM) in terms of meeting and targeting the needs of new challenging technologies.

aluminium/bauxite*	antimony	**arsenic**
baryte	beryllium	bor/borate
flourspat	phosphate rock	phosphorus
feldspar	gallium	germanium
natural graphite	hafnium	**helium**
rare earth elements: HREE and LREE	silicon metal	cobalt
coking coal	copper*	lithium
magnesium	**manganese**	nickel*
niobium	platinum group metals: PGM	scandium
strontium	tantalum	titanium
vanadium	bismuth	tungsten

*=Strategic but not critical raw material

Synthetic graphite*

Fig. 1. The EU has listed 34 minerals and metals as critical and/or of strategic importance for European society and welfare. Copper and nickel are only strategic. Recently, aluminium and synthetic graphite were added to the strategic ones (Source: Geological Survey of Sweden)

Strategic and critical mineral raw materials (Fig. 1) are the foundation upon which modern technology is built [3] from photovoltaics to semiconductors, wind turbines, and lithium batteries to transport and store the renewable energy produced. In addition to lithium, batteries also need cobalt, graphite, nickel, and manganese, while the electrification of cars requires neodymium magnets, which also use other rare earth elements (REE), such as dysprosium and praseodymium, but also increased use of copper, zinc, and lead (Fig. 2, 4, 5), which together with nickel are of special ore geological interest for Greece. CSMs are also essential in the digital technology and electronics

industry. Simply put, there can be no energy and digital transition, and no scale-up in the use of e-mobility, without CSMs, which is why the resilience of the relevant value and supply chains are increasingly a priority for most advanced economies [2, 4, 6]. Recent reports by the International Energy Agency [7] and the World Bank indicate that global production of cobalt, lithium, and graphite needs to increase by 500% in the coming decades to enable the transition to a green and digital economy [8]. For example, the EU would need up to 18 times more lithium and 5 times more cobalt by 2030, and almost 60 times more lithium and 15 times more cobalt by 2050, to cope with the increase in electric vehicle battery production, and 10 times more REE for permanent magnets [1].

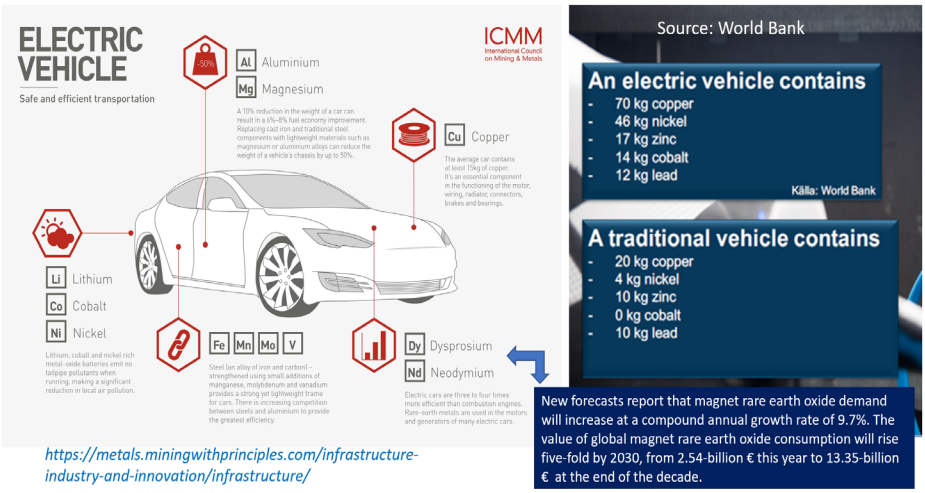

Fig. 2. An electric car produced in Europe contains on average 141 kg of mineral raw materials, compared to just 44 kg in a conventional car. Corresponding quantities of aluminium are 283 kg and 169 kg, respectively, whereas an electric car also requires 2 kg of REE (Source: ICMM)

2 China's geopolitical dominance

The above forecasts are seen as alarming if it is considered that the EU depends by 75 to 100% on imports for most of the CSMs. It also happens that the production and processing of many CSMs is geographically controlled, making their geopolitical access and supply vulnerable, which is accompanied by a series of social, economic, environmental, and other risks. Therefore, some CSMs, along with their related value chains, largely tend to be productively monopolized by specific regions of the planet, sometimes by just one country. For example, about 60% of the world's cobalt comes from the Democratic Republic of the Congo (Fig. 3). In terms of REE, China mines nearly 60% of the raw materials, supplies 85% of related processed/metallurgical products, and domestically consumes nearly 70% of global production.

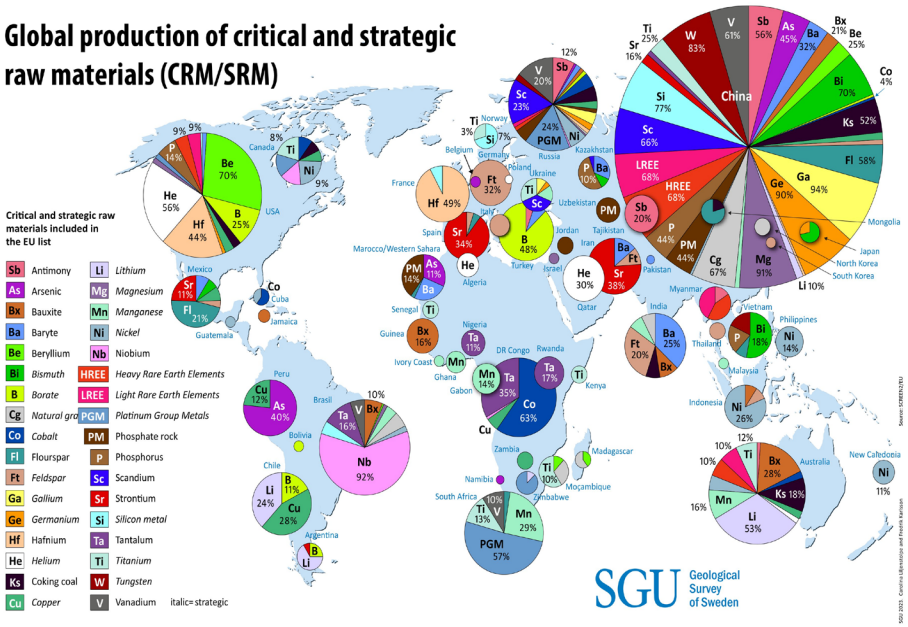

Fig. 3. Map of global CSM production according to the current European list (Source: Geological Survey of Sweden/9)

Many of the countries that mine CSMs choose China as a strategic trading partner since the majority of these countries lack an integrated operation of pertinent key technological value chains which results in the industrial production of neodymium magnets or lithium batteries, among other products that contribute to electrification (Fig. 4). It is clear that contrary to the strategies of the USA and the Soviet Union after the Second World War and until about 1990, which connected their technological research, almost exclusively with the military industry, China chose to invest its technological development in consolidating its geopolitical dominance and position in the global economy.

However, given that the planned battery factories in Europe are expected to start production within the next 12 to 36 months, the continuation of these trade routes may create obstacles to the supply of certain metals, notably lithium, and cobalt, which may cause a slowdown in the production of lithium batteries.

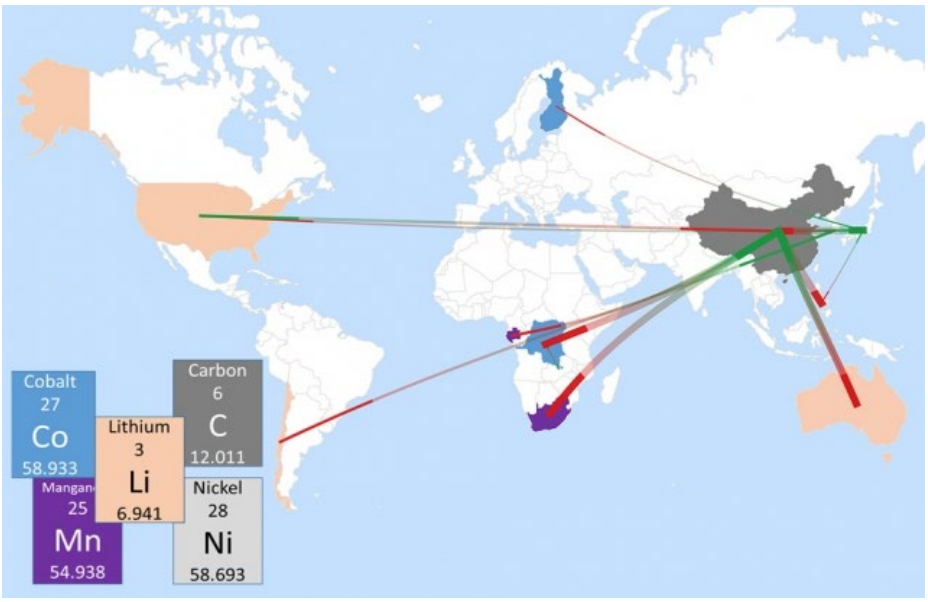

Fig. 4. The map shows today's battery mineral routes, which, while mined in Chile, Australia, Congo, the USA, Finland, South Africa, and others (red), end up in China, where industrial lithium battery production takes place (green) (Joule, 2017/42)

3 EU critical raw materials act

The Critical Raw Materials Act (CRMA) [11, 12, 13, 14] will become the political and strategic tool, but also the operational platform, that will seek to promote and accomplish the implementation of the European Green Deal [16, 17], the new industrial strategy [18, 19] the implementation plan of the European Innovation Partnership on Raw Materials [19], EU strategies around the energy transition, the circular economy and the resource-efficient intra-European mineral exploitation [20, 21, 22, 23], with the primary objective of achieving a climate-neutral Europe. The recent approval of the CRMA Regulation by the European Parliament [24, 25] will trigger a series of actions, decisions, and practices that are expected to lead to ensuring access to and supply of the increased amounts of CSMs that the European industry will need to achieve a green economy. This regulatory and "potential" legislative initiative is very timely and necessary in the formulation of a policy for the mining of the European CSM raw materials, which will contribute to the creation of investment interest in the direction of dynamic ore deposits exploitation of relevant primary [26, 27] and secondary (e.g. mining waste) [28] resources, including those that may result from the recycling of end-of-life (EoL) products, such as batteries, magnets, but also electronic waste in general.

The main targets and benchmarks of the CRMA until 2030 are (Fig. 5):

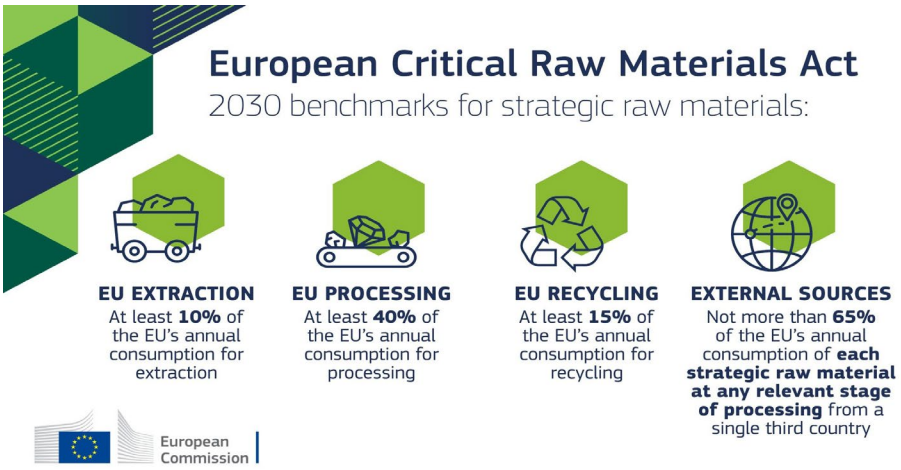

Fig. 5. The first tripartite political decision by the European Commission, the European Council, and the European Parliament that the EU needs to secure the supply of CSMs and the domestic implementation of related strategic value chains (Source: European Commission)

- At least 10% of the annual CSM consumption comes from European deposits.

The reliable, unimpeded, and immediate production of intra-European CSMs is a key condition for technological innovation, green industry, and sustainable development. The problem with insufficient and incomplete CSM mining and production in Europe is neither geological nor metallurgical. Europe's ability to become self-sufficient, self-sustaining, resilient, and sustainable, based on productive exploitation of its own CSM deposits, is greatly favored by its geology and metallogenetic evolution. Economic geological and mineral exploration technologies about [29] CSM deposits must be further developed to have reliable techno-economic approaches, but also relevant estimates for exploitation potential. The national Geological Survey agencies and institutes of the member states have largely re-examined the economic geology of the CSM systems with the aim of more justified and updated ore assessment. Comprehensive economic geological data are now available that 'map' lithium [21] and rare earth mineralisation occurrences in various regions of Europe.

- At least 40% of processed CSMs are produced within the EU.

Increasing Europe's long-term self-sufficiency and gradual autonomy in CSMs, as well as developing sustainable beneficiation and metallurgical downstream technologies, are a prerequisite for the integrated operation of resilient strategic value chains for the energy transition in Europe.

- At least 15% of the annual demand in CSMs should come from recycling.

Most CSMs are found primarily as minor components associated with base metal sulfide and oxide deposits (e.g., copper, lead, zinc, nickel, aluminium, and iron). With mining, production focused overtime on the extraction and processing of base metal minerals, any accompanying CSM concentrations ended up in the various types of mining wastes, such as waste rocks, processing tailings, and metallurgical residues. The historical mining wastes, as they are more broadly called, together mainly with the EoL

products (electronic, electrical, batteries, and others), make up secondary raw material resources that through their recycling can potentially lead to the recovery of the CSMs they respectively contain. The EU is at the forefront of the circular economy and has already increased the value of non-mining secondary sources, namely end-of-life consumer products such as waste electronic and electrical waste. In this case, access to environmentally friendly and economically viable recycling technologies and methods is crucial. For example, more than 50% of some metals, such as iron, zinc, or platinum, are recycled and contribute more than 25% of consumer needs in the EU. However, for CSMs needed in renewable energy technologies or high-tech applications, such as REE, lithium, gallium, or indium, the recovery rate from secondary sources is below 1% and thus contributes only very little (Fig. 6) to cover the rapidly growing demand. Even if they were to become more efficient, by 2050 recycling alone would not be able to close the large gap that exists today between the future demand and supply of CSMs.

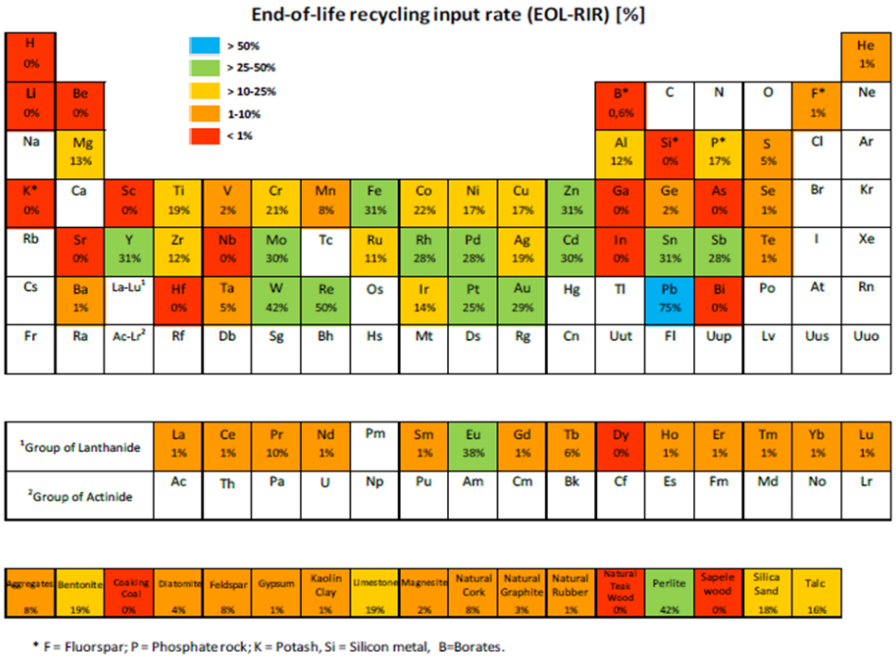

Fig. 6. Some of the CSMs, such as lithium and REE, have recovery rates that are currently sub-1 % [31]

- Less than 65% dependence of each CSM on one country.

CSMs have been the missing link in the climate debate for many years. It is now clear that the EU's climate targets cannot be achieved without them. More specifically, any disruptions to the access and adequacy of CSMs have implications for ensuring the energy transition and the achievement of climate goals. Addressing the growing demand for strategic and critical mineral raw materials requires diligence inside the EU, as well as international cooperation, in matters of exploring new ore mineral sources and resource potential. The reliable, unimpeded, and immediate production of intra-

European CSMs is a key condition for technological innovation, green industry, and sustainable development.

- Strengthening the resilience of strategic value chains for more effective implementation of the energy and digital transition.

CSM value chains differ from their supply chains. A CSM value chain is the set of activities that add value at each stage and step of their production cycle, thus improving relative competitiveness. The value chains for CSM include upstream exploration, prospecting and mining, midstream processing (concentration, metallurgy), and downstream industrial manufacturing and recycling, with environmental restoration foreseen in each case, at the post-closure stage of the mining cycle. Unfortunately, in Europe today there are limited possibilities for the sustainable and holistic operation of CSM value chains, especially those characterized as strategic for the technologies that support the energy transition, such as, for example, the lithium battery and neodymium magnet value chains (Fig. 7). To create competitive and autonomous value chains in the EU, all the production stages and steps included in them need to operate at a European level. That is, to mine CSMs, produce the required metallurgical products, and manufacture the batteries and magnets within Europe, with the final end-users being the industrial ecosystems of e-mobility, wind turbines, photovoltaics, and digital technology. Such a development creates further dynamic conditions for additional economic growth and employment.

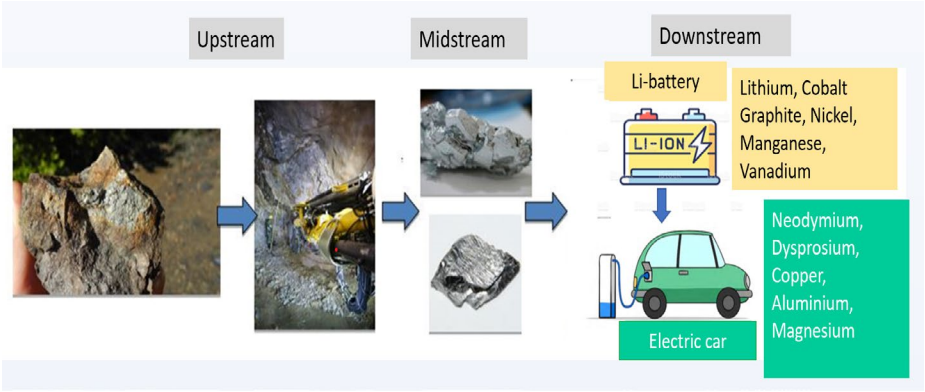

Fig. 7. The mineral value chain spans from upstream geological exploration and mining, midstream processing, and refining, to downstream manufacturing (2)

- Reduction of bureaucracy, and simplification and acceleration of licensing procedures.

The rapidly growing demand for mineral raw materials has also increased the need to update mining policy, as well as research and innovation projects. The CRMA Regulation aims to drastically reduce licensing time, and the Member States will ensure that the licensing process related to such projects becomes faster. The question is how EU countries will respond to this in practice.

- Development of alternative materials and more environmentally friendly mining and production methods.

The Raw Materials Supply Group (RMSG, an expert group including Member States representatives, regional authorities, industry associations, civil society, social partners, and research organisations) and the European Commission have developed and agreed upon a set of voluntary, non-mandatory EU principles for sustainable raw materials [33]. This will serve to create a common European understanding of best practices in the processing and responsible extraction of CSMs [30] in Europe in terms of social, environmental, and economic commitments and applications, and to set a trajectory toward the UN Sustainable Development Goals (SDG/Sustainable Development Goals) [34]. The achievement of many of the goals is highly dependent on relevant activities and uses of CSMs.

- Channeling strategic partnerships between the EU and third countries to ensure sustainable and resilient CSM supply chains.

The CRMA aims to pave the way for long-term partnerships, with knowledge and technology transfer, training, and skills development for new jobs with better working conditions and income, as well as mining and processing according to better ecological standards in the partner countries from which Europe will be able to access and import some of the CSMs needed.

4 "Critical" need for highly capital- and resource-intensive mineral exploration

Increasing the degree of self-sufficiency in CSM supply from 2-3% to 10% in the EU by 2030 means a 300–40% increase in domestic production in 7 years, which is about the time it takes on average to get a permit in place. This means that massive efforts and an increase in investment in exploration to at least an equivalent degree are required if we are to even come close to that degree of self-sufficiency. It also follows that we need to apply innovative and sustainable approaches, using breakthrough technologies, to improve economic efficiency and obtain information that could not be obtained by conventional methods.

4.1 Exploration as part of Economic Geology

The EU exploration and mineral industry needs to have access to harmonized knowledge-based mineral data and information for both primary (Fig. 8) and secondary mineral resources. With this data currently becoming more available and the innovative research carried out by the Geological Surveys of Europe, there is a better understanding today of the geological setting of CSM systems. Moreover, CSM-fitting exploration technologies and methods (e.g., 3D models integrating geology, geophysics, and geochemistry), have been developed and applied in recent years, which also consider the challenges of brownfield and/or greenfield exploration targets, e.g., the location of deeper-seated ore bodies, and re-mining historical wastes in the case of brownfield exploration. Knowledge about the implementation of the UNFC resource classification system is improving at a rapid rate and is now a dominant priority for the mining authorities and industry in Europe. A full-scale economic geological approach also includes beneficiation testing, suggesting possible processing technology options, and

considering the CRMA target that by 2030, 40% of the EU's annual consumption of each CSM, should be refined within the Union. In each case, the mineral exploration activity is completed by considering the possible options of open-pit and/or underground mining and drawing up a pre-feasibility study.

Mineral exploration efforts targeting CSMs must consider the fact that most of them are directly linked to known sulfide and oxide ore deposits. Examples of CSM found associated with known mineral systems are Co with Ni and Cu ores (Fig. 9); Ga, Ge, In, and Sb with base metal sulfides; Platinum Group Metals with Cr, Ni, and Cu; Ga, REE, and Sc with Al deposits; W, Nb, In, and Ta with Sn; and REE with P-minerals. Exploration activities in such cases might be a matter of (i) a feasibility study when it comes to active mines, addressing the volume, grades, and recovery rate of potentially associated CSMs, or (ii) brownfield, often deep, exploration of historical mining fields [Fig. 10], including mining wastes, this time prospecting also for exploitable CSM concentrations (Fig. 11). About this, it is appropriate to mention that brownfield exploration is less expensive, more time-efficient, provides better conditions for permitting, benefits the environment, and might be considered more socially acceptable. As we also deal with historical, currently abandoned mining fields, any stockpiled mining waste makes a secondary mineral resource and a new mineral deposit target.

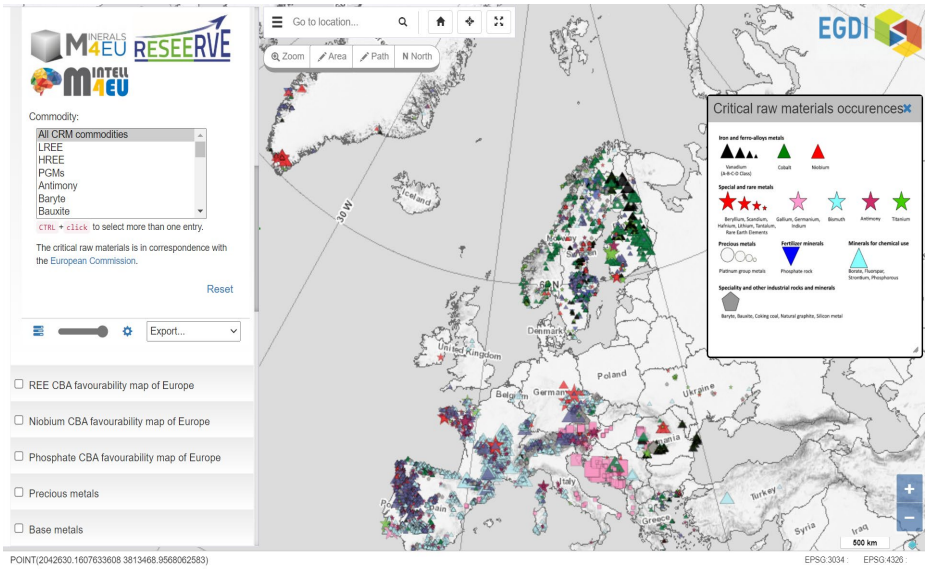

Fig. 8. The Geological Surveys of Europe provide regularly updated information on CSMs. EGDI is EuroGeoSurveys' European Geological Data Infrastructure (Source: EGDI/EuroGeoSurveys)

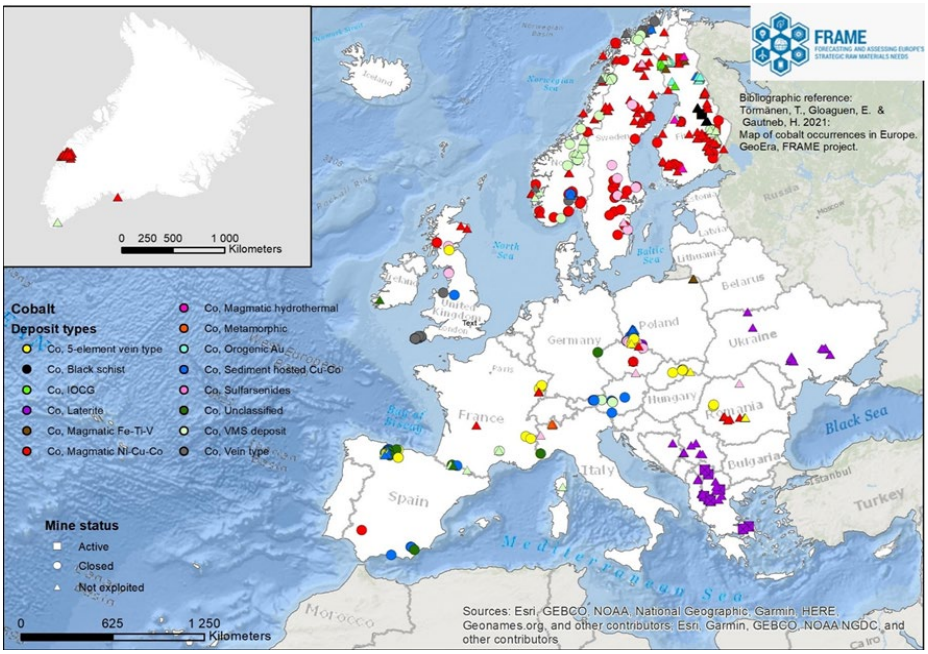

Fig. 9. Potentially exploitable cobalt concentrations in Europe are mainly associated with magmatic nickel sulfide mineral systems in Finland and with lateritic Ni deposits in Greece and other West Balkan countries (Source: FRAME/GeoERA project)

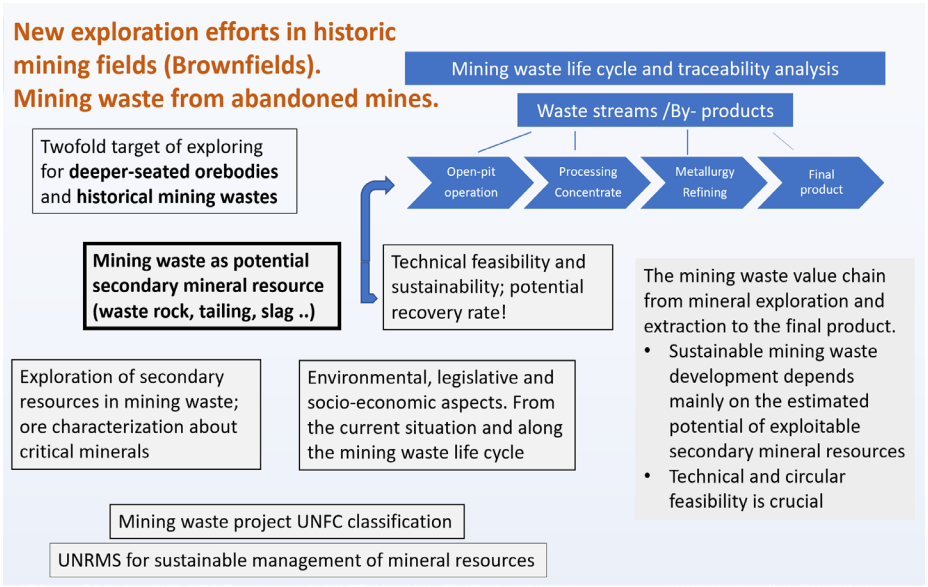

Fig. 10. Proposed methodology when addressing brownfield exploration targeting deeper-seated orebodies and mining wastes in historical mining fields (26)

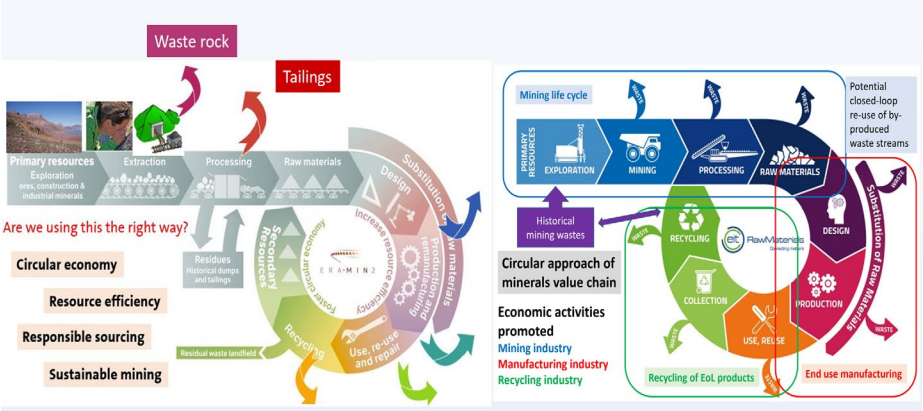

Fig. 11. The potential of recycled CSMs refers to three secondary "feedstock" sources: (1) mining waste, (2) industrial waste, and (3) EoL products. Waste rocks and processing tailings as a potential secondary source for CSMs also need to be further explored (2, 4)

5 European initiatives for geopolitical balance and the gradual autonomy of CSMs

As it follows from the CRMA, the implementation of a multidimensional search strategy for new supply markets for CSMs is a dynamic European objective. For example, with the significant CSM reserves that they have and sustainably and responsibly mine, countries such as Canada and Australia can be safe and reliable CSM production partners and related value-added products for global markets, including the EU. Improving the holistic and resource-efficient exploitation of CSMs is part of the action plan for the circular economy and the current EU directive on mining waste. In addition, the directive provides for compliance with specific terms for both the minimization and recycling of mining waste. The EU considers that the implementation of circularity through the strengthening of recycling will have a significant contribution to the geopolitical balance and will strengthen the strategic autonomy of CSMs. All new mining and mineral production projects should, from the very beginning, be designed based on the circular economy and the holistic recovery of main and by-products within the loop of the same production cycle before they are sent to waste.

Given China's geopolitical dominance and the extent of corporate partnerships, collaborations, and investments that it has launched (Fig. 4) around the world about the exploitation of other countries' CSMs, Europe will be tasked with finding its roads and ways of accessing the resources it needs. In fact, at a time when the Russian invasion of Ukraine is ongoing, a difficult geopolitical reality has become even more difficult since some of the minerals that are today characterised as strategic and critical for the EU are mined from the Russian and Ukrainian bedrock basements [16]. Russia, for example, produces 8% of the world's nickel, 23% of vanadium, 41% of palladium, 5% of cobalt, 4% of copper, and 6% of aluminium, while Ukraine mines 3% of the world's iron ore and is respectively the eighth largest producer of manganese. It also produces

smaller amounts of other CSMs, such as titanium, graphite, and silicon, and mines zircon and uranium.

Faced with these particularly difficult and determined geopolitical conditions, which have been "largely" shaped and controlled by China, the EU, as well as other countries dealing with problems of access to CSMs, are undertaking dynamic initiatives to build stronger partnerships at the global level, based on trust, openness, and mutual benefit. On its behalf, the EU has recently concluded trade agreements with Chile, while upcoming agreements are underway with Indonesia and other countries (Fig. 12), which will help support sustainable and resilient supply chains. The goal is to create a global gathering for CSMs with trusted partners who also wish to develop their own CSM value chains as well as related CSM industries. Closer and more diversified commercial ties and partnerships will help the EU to reduce dependencies, which currently exist mainly from China, but also any weaknesses that this entails. What is required for the EU is to secure the CSMs, which are of fundamental importance for its competitiveness, focusing on its aim to be a pioneer in the green industries of the future.

More broadly, globally, the US, Canada, and Australia are collaborating on CSM exploration and resource characterization and classification [35]. Japan and the US have signed an agreement that is expected to create strong and sustainable CSM value and supply chains in cooperation with other countries as well [36]. Particularly dynamic and important is the international Mineral Security Partnership (MSP) initiative, which involves the cooperation of 13 countries and the EU to promote and implement public and private investments in responsible mineral security value and supply chains worldwide. This partnership aims to accelerate the development of diverse and sustainable CSM supply and value chains but also to support diplomatically and economically related strategic projects through government and industry collaboration. The 13 participating partners include Australia, Canada, Finland, France, Germany, India, Italy, Japan, Norway, the Republic of Korea, Sweden, the United Kingdom, the United States, and the European Union (represented by the European Commission] [37].

The EU and other countries that rely on CSM imports must act quickly and effectively to reduce their dependence primarily on China, which currently geopolitically dominates CSM supply and value chains globally. If nothing else, to diversify today's trade "routes" to their advantage. A typical example of the influence that China continues to have on global CSM markets is its recent decision to restrict exports of gallium and germanium [38, 39, 40]. So given that China produces about 80% of the world's gallium (primary gallium production in China is a by-product of bauxite or zinc processing) and about 60% of the germanium, and the fact that the two elements are used in a large range of applications and products, including semiconductors, computer chips, and photovoltaics, their zero export in August had major implications for the respective EU, Japanese, and US industries. For example, as far as Japan is concerned, about 40% of its gallium supply depends on China. Also, China's announcement of limited exports in early July led to a nearly 20% increase in the price of gallium in the US and Europe.

So, the answer to the question, of whether the EU and other affected countries will succeed in working together to remove or better reduce their dependence on China, is

difficult for the moment to give concretely and clearly when it comes mainly to the time it will take.

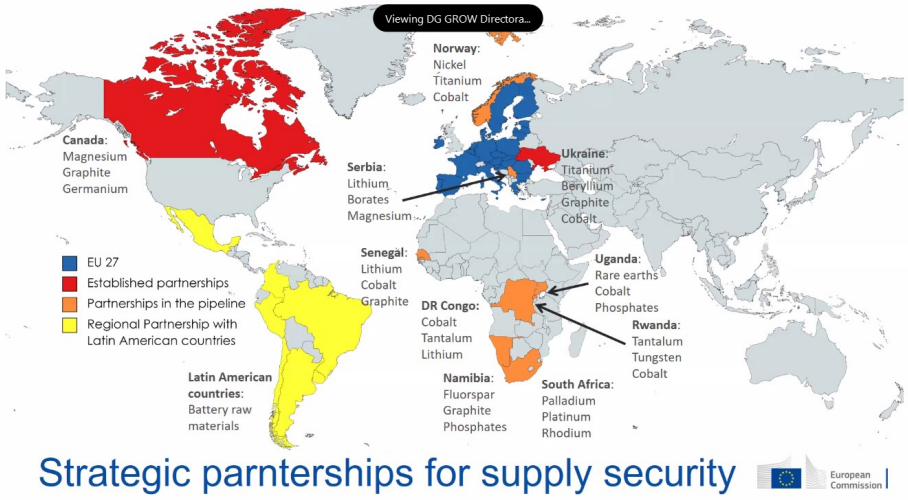

Fig. 12. EU Strategic Partnerships to Secure CSM Supply Chains and thereby Strengthen the Resilience of Domestic Value Chains (Source: European Commission)

5.1 CSM availability challenging EU 2030 goals

There are growing global and EU concerns regarding CSM availability, considering that.

- Mineral intensity issues about Green Deal targets to be achieved by 2030, e.g., cutting greenhouse gas emissions by at least 55%.
- The EU estimates that the penetration of electric cars amounts to 7-8 million per year. This means that by 2030, more battery and magnet minerals will be needed in terms of large quantities of manganese, lithium, cobalt, graphite, rare earths, nickel, and copper if car manufacturers are to hit their very ambitious production targets.
- Lithium demand has risen very strongly in the last few years, and it is expected to go higher, especially as the planned battery giga factories appear to be coming online in the next 12 to 36 months.
- By 2030, demand for graphite is expected to reach 4 m.t. per year, with 75% going to lithium battery anodes. A shortfall of around 780,000 tons per year is estimated by 2030. Most of the graphite comes from China.
- According to CRMA, by 2030, 10% of the Union's consumption of strategic mineral raw materials should be mined in the EU.
- 2030 is only seven years away. Just about 10 years or so is the amount of time it takes to bring a new mine into production. Consider also that almost 1% of mineral occurrences found will become mines.

So, the central question is: where will all these battery and magnet minerals need to come from? Will the EU manage to reach the 10% target? Because, certainly, the CSM

of batteries and magnets is not enough to ensure the increasing production of wind energy and electric cars.

6 EU's economic geology sets the spot for exploitable resources in CSMs

- Europe's opportunity to become self-sufficient, resilient, and sustainable in critical and strategic mineral supply from its resources is strongly favoured by its geological setting and metallogenetic evolution.
- Predictive mapping, along with updated geological knowledge and improved mineral intelligence, results in areas of high regional-scale exploration potential to enable targeting prospective mineral resources of REE, lithium, cobalt, graphite, and nickel in Europe. Sweden, Norway, and Finland have undertaken joint efforts to provide a common approach and assessment on raising the exploration and resource potential of battery and magnet minerals in the Fennoscandian mineral belt.
- EU Member States (MS) should promote national and/or transboundary CSM exploration, focusing on brownfield areas with the twofold target of exploring deeper-seated orebodies and historical mining wastes.
- Recycling alone is not yet sufficient to meet the EU's and the world's current growth in demand for mineral raw materials. However, it constitutes a potential exploration target, considering the CRMA target that by 2030, 15% of the EU's annual consumption of each CSM should come from recycling.
- The fast-growing demand for mineral raw materials has also raised the need for policy updates and innovation. For example, it will take at least 10–15 years before the Swedish company LKAB can begin mining and delivering REE products to the market.
- The CRMA aims at reducing the permitting time drastically, as MS ensures that the permit-granting process related to such projects will get faster. The question is, how will MS respond to this?
- Strategic projects addressing CSM will be identified and financed by the EC, together with a European Critical Raw Materials Board that is about to be established. It has been drafted that "private investment alone is not sufficient" and that the effective roll-out of projects along the CRM value chains may require public support (so-called state aid).

7 Concluding remarks

Upon these particularly difficult geopolitical conditions, which have been "largely" shaped and controlled by China, the EU is facing CSM access problems, and apart from relying on its own CSM resources, is undertaking dynamic initiatives to build stronger partnerships at the global level, based on trust, openness, and mutual benefit. In this respect, the EU has recently concluded trade agreements with Chile, Argentina, Canada, Greenland, Ukraine, Kazakhstan, DRC, Zambia, and Namibia while upcoming agreements are underway with Norway, Indonesia, Australia, and other countries, which will help support sustainable and resilient supply chains. The goal is to create a global gathering for CSM, with trusted partners who also wish to develop their own CSM value chains as well as related CSM industries. With closer and more diversified commercial routes and partnerships, designed to reduce dependencies, which currently exist mainly from China (42), this will help to reduce any weaknesses and risks that these dependencies entail. What is required for the EU is to secure the CSMs, which are of fundamental importance for its competitiveness, focusing on its aim to be a pioneer in the green industries of the future. At the same time, the improvement of the holistic and resource-efficient exploitation of CSM is part of the action plan for the circular economy. The EU considers that the implementation of circularity through the strengthening of recycling will have a significant contribution to the geopolitical balance and will strengthen the strategic autonomy of CSM. All new mining and mineral production projects should, from the very beginning, be designed based on the circular economy and the holistic exploitation of main and by-products.

References

1. European Commission, Directorate-General for Internal Market, Industry, Entrepreneurship and SMEs (2021): 3rd Raw Materials Scoreboard – European innovation partnership on raw materials, Publications Office, 2021, https://data.europa.eu/doi/10.2873/567799
2. Arvanitidis N. and Constantinides D. (2023): Exploitation of critical mineral deposits in the EU: The key to indigenous, holistic and sustainable value chains (in Greek). Newsletter, RAWMATHUB. https://rawmathub.gr/epistimonika-kai-epixeirimatika-afieromata/krisimes-oryktes-protes-yles-ena-stoixima-gia-tin-evropi/ekmetallefsi-koitasmaton-kopy-stin-ee-to-polykleido-gia-gigeneis-olistikes-kai-viosimes-alysides-aksias
3. European Commission, Directorate-General for Internal Market, Industry, Entrepreneurship and SMEs (2023): Critical Raw Materials. https://single-market-economy.ec.europa.eu/sectors/raw-materials/areas-specific-interest/critical-raw-materials_en
4. Arvanitidis N. (2021): Lithium batteries and neodymium magnets renew the energy in electromobility (in Greek). Newsletter, Greek Association of Mining Enterprises. https://www.sme.gr/bataries-lithiou-kai-magnites-neodymiou-ananeonoun-tin-energeia-stin-ilektrokinisi/
5. Arvanitidis N. (2021): The new age of copper is also "courting" Greece (in Greek). Newsletter, Greek Association of Mining Enterprises. https://www.sme.gr/h-nea-epochi-tou-chalkou-flertarei-kai-tin-ellada/

6. Dimitriadis D. and Arvanitidis N. (2023): Considerations and views on the Greek Mining Policy (in Greek). Newsletter, RAWMATHUB. https://rawmathub.gr/synentefkseis-kai-arthra-gia-protes-yles/arthra-gia-protes-yles/oi-nees-energeiakes-texnologikes-prokliseis-antimetopizontai-me-viosimes-oryktes-protes-yles
7. International Energy Agency (2022): Global Supply Chains of EV Batteries. https://iea.blob.core.windows.net/assets/4eb8c252-76b1-4710-8f5e-867e751c8dda/GlobalSupplyChainsofEVBatteries.pdf
8. Kirsten H. La Porta D., Fabregas T. P., Laing T. and Drexhage J. (20209: Minerals for Climate Action: The Mineral Intensity of the Clean Energy Transition. The World Bank Group. World Bank Publications. https://pubdocs.worldbank.org/en/961711588875536384/Minerals-for-Climate-Action-The-Mineral-Intensity-of-the-Clean-Energy-Transition.pdf
9. Geological Survey of Sweden (2023): Critical and strategic raw materials. Mineral Resources. https://www.sgu.se/en/mineral-resources/critical-raw-materials/
10. U.S. Department of Energy (2022): Rare Earth Permanent Magnets. Supply Chain Deep Dive Assessment. U.S. Department of Energy Response to Executive Order 14017, "America's Supply Chains".https://www.energy.gov/sites/default/files/2022-02/Neodymium%20Magnets%20Supply%20Chain%20Report%20-%20Final.pdf
11. European Commission, Directorate-General for Internal Market, Industry, Entrepreneurship and SMEs (2023): Critical Raw Materials Act. https://single-market-economy.ec.europa.eu/sectors/raw-materials/areas-specific-interest/critical-raw-materials/critical-raw-materials-act_en\
12. Arvanitidis N. (2022): Critical Raw Materials Act. Practical application or another theoretical rhetorical approach? (in Greek). Newsletter, Greek Association of Mining Enterprises. https://www.sme.gr/protovoulia-gia-tis-krisimes-oriktes-protes-iles/
13. Arvanitidis N. (2022): Critical Raw Materials Act. Practical application or another theoretical rhetorical approach? (in Greek). Newsletter. RAWMATHUB. https://rawmathub.gr/synentefkseis-kai-arthra-gia-protes-yles/arthra-gia-protes-yles/protovoulia-gia-tis-krisimes-oryktes-protes-yles-praktiki-efarmogi-i-alli-mia-theoritiki-ritoriki-proseggisi
14. Arvanitidis N. (2023): Views on the sustainable operation of the National Committee on strategic and critical minerals (in Greek). Newsletter. RAWMATHUB. https://rawmathub.gr/synentefkseis-kai-arthra-gia-protes-yles/arthra-gia-protes-yles/dr-n-arvanitidis-skepseis-sxetika-me-ti-viosimi-leitourgia-ethnikis-epitropis-opy
15. European Commission, Strategy and Policy (2021). The European Green Deal. https://commission.europa.eu/strategy-and-policy/priorities-2019-2024/european-green-deal_en
16. Arvanitidis N. (2022): Ukraine and Russia can contribute to the realization of the European Green Deal (in Greek). Newsletter. RAWMATHUB. https://rawmathub.gr/synentefkseis-kai-arthra-gia-protes-yles/arthra-gia-protes-yles/dr-n-arvanitidis-me-rosia-kai-oukrania-i-evropaiki-prasini-symfonia-kerdizei-edafos
17. European Commission, Directorate-General for Internal Market, Industry, Entrepreneurship and SMEs (2021): European industrial strategy. https://single-market-economy.ec.europa.eu/industry/strategy_en
18. European Commission, Strategy and Policy (2021): The European Commission's priorities. https://commission.europa.eu/strategy-and-policy/priorities-2019-2024/europe-fit-digital-age/european-industrial-strategy_en
19. European Commission, Directorate-General for Internal Market, Industry, Entrepreneurship and SMEs (2020): Strategic implementation plan (SIP). European Innovation

Partnership (EIP) on raw materials. https://single-market-economy.ec.europa.eu/sectors/raw-materials/eip/strategic-implementation-plan-sip_en
20. SCRREEN project (2023): European Union's Horizon Europe Research and Innovation Programme under Grant Agreement N° 101138060. https://scrreen.eu/
21. GeoERA project (2021): Forecasting and Assessing Europe's Strategic Raw Materials needs (FRAME). European Union's Horizon 2020 research and innovation program under grant agreement No 731166. https://geoera.eu/projects/frame2/
22. European Geological Data Infrastructure (EGDI) (2024): Geological Service for Europe. EuroGeoSurveys (EGS). .https://www.europe-geology.eu/
23. GSEU project (2023): Geological Service for Europe. European Union's Horizon Europe. https://www.geologicalservice.eu/
24. European Parliament (2023): Critical raw materials: MEPs back plans to secure EU's own supply and sovereignty. Press Releases. News. https://www.europarl.europa.eu/news/en/press-room/20230904IPR04618/critical-raw-materials-meps-back-plans-to-secure-eu-own-supply-and-sovereignty
25. Arvanitidis N. (2023): The European Parliament votes in favor of the Critical Raw Materials Act Regulation (in Greek). Newsletter. RAWMATHUB. https://rawmathub.gr/synentefkseis-kai-arthra-gia-protes-yles/arthra-gia-protes-yles/dr-n-arvanitidis-to-evropaiko-koinovoylio-psifizei-yper-tou-kanonismoy-gia-tis-skopy
26. Arvanitidis N. (2023): Geopolitical developments and sustainable EU access to Strategic and Critical Mineral Raw Materials (in Greek). Greek Mineral Wealth. https://rawmathub.gr/synentefkseis-kai-arthra-gia-protes-yles/arthra-gia-protes-yles/dr-n-arvanitidis-epistameni-kai-estiasmeni-geologiki-erevna-gia-koitasmatologiki-aksiopoiisi-endoevropaikon-apothematon-kopy
27. Arvanitidis N. (2022): United Nations system for universal classification of mineral deposits (in Greek). Newsletter, Greek Association of Mining Enterprises. https://www.sme.gr/sistima-inomenon-ethnon-gia-oikoumeniki-taxinomisi-koitasmaton/
28. Arvanitidis N. (2021): Mining wastes- the new mineral exploration challenge (in Greek). Newsletter, Greek Association of Mining Enterprises. https://www.sme.gr/metalleftika-apovlita/
29. Arvanitidis N. (2022): Intensified and focused mineral exploration of intra-European critical raw materials resources (in Greek). Newsletter. RAWMATHUB. https://rawmathub.gr/synentefkseis-kai-arthra-gia-protes-yles/arthra-gia-protes-yles/dr-n-arvanitidis-epistameni-kai-estiasmeni-geologiki-erevna-gia-koitasmatologiki-aksiopoiisi-endoevropaikon-apothematon-kopy
30. Arvanitidis N. (2019): Europe's dependence on Critical Raw Materials (CRM) and growing supply needs for battery minerals-based value chains. Newsletter, Greek Association of Mining Enterprises. https://www.sme.gr/europes-dependence-on-critical-raw-materials-crm-and-growing-supply-needs-for-battery-minerals-based-value-chains/
31. Arvanitidis N., J. Boon, P. Nurmi, G. Di Capua (2017): White Paper on Responsible Mining. IAPG Task Group on Responsible Mining. With the contribution of V. Correia, R. Lencina, D. Ovadia, M. Rachovides and I. Thomson. International Association for Promoting Geoethics. https://www.researchgate.net/publication/321715310_White_Paper_on_Responsible_Mining
32. European Commission, Directorate-General for Internal Market, Industry, Entrepreneurship and SMEs (2023): Critical Raw Materials. https://ec.europa.eu/growth/sectors/raw-materials/specific-interest/critical_en
33. Bobba, S., Carrara, S., Huisman, J., Mathieux, F. and Pavel, C (2020): Critical Raw Materials for Strategic Technologies and Sectors in the EU -A Foresight Study. European

Commission, Joint Research Centre. https://rmis.jrc.ec.europa.eu/uploads/CRMs_for_Strategic_Technologies_and_Sectors_in_the_EU_2020.pdf
34. European Commission, Raw Materials Supply Group (2021): EU principles for sustainable raw materials. Publications Office of the European Union. https://tem.fi/documents/1410877/2851374/EU_principles_for_sustainable_raw_materials+–+kopio.pdf/4687cf52-7ca7-bb90-854b-832ea19d24c5/EU_principles_for_sustainable_raw_materials+–+kopio.pdf?t=1639642622731
35. United Nations (2015): The 2030 Agenda for Sustainable Development. Department of Economic and Social Affairs. https://sdgs.un.org/goals
36. USGS (2020): Critical Cooperation- How Australia, Canada and United States are working together to support critical mineral discovery. https://www.usgs.gov/news/featured-story/critical-cooperation-how-australia-canada-and-united-states-are-working
37. Ministry of Foreign Affairs of Japan (2023): Signing of the Japan-U.S. Critical Minerals Agreement (CMA). Press Releases. https://www.mofa.go.jp/press/release/press1e_000400.html
38. US Department of State (2023): Minerals Security Partnership. State for Economic Growth, Energy and the Environment. https://www.state.gov/minerals-security-partnership/
39. Reuters (2023): China exported no germanium, gallium in August after export curbs. https://www.reuters.com/world/china/china-exported-no-germanium-gallium-aug-due-export-curbs-2023-09-20/
40. Center for Strategic and International Studies (2023): Understanding China's Gallium Sanctions. https://www.csis.org/analysis/understanding-chinas-gallium-sanctions
41. Cytera C. (2023). Gallium, Germanium, and China — The Minerals Inflaming the Global Chip War. Center for European Policy Analysis (CEPA). https://cepa.org/article/china-gallium-and-germanium-the-minerals-inflaming-the-global-chip-war/
42. Elsa A. Olivetti, Gerbrand Ceder, Gabrielle G. Gaustad, Xinkai Fu, (2017): Lithium-Ion Battery Supply Chain Considerations: Analysis of Potential Bottlenecks in Critical Metals, Joule, Volume 1, Issue 2, 2017, Pages 229-243, ISSN 2542-4351, https://doi.org/10.1016/j.joule.2017.08.019; https://www.sciencedirect.com/science/article/pii/S2542435117300442

Author Index